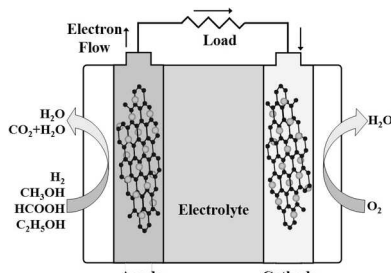


Graphene-Supported Nanoelectrocatalysts for Fuel Cells: Synthesis, Properties, and Applications

Minnin Liu,^{†,‡,§} Ruizhong Zhang,^{†,‡,§} and Wei Chen*,[†]

[†]State Key Laboratory of Electroanalytical Chemistry, Changchun Institute of Applied Chemistry, Chinese Academy of Sciences, Changchun 130022, Jilin, China

[‡]University of Chinese Academy of Sciences, Beijing 100039, China



CONTENTS

1. Introduction
2. Synthesis of Functionalized Graphene and Graphene-Supported Electrocatalysts
 - 2.1. Synthesis of Graphene and Heteroatom-Doped Graphene Electrocatalysts
 - 2.1.1. Chemical Vapor Deposition (CVD)
 - 2.1.2. Arc-Discharge Approach
 - 2.1.3. Thermal Annealing Method
 - 2.1.4. Plasma Treatment
 - 2.1.5. Solvothermal and Hydrothermal Treatments
 - 2.2. Graphene-Supported Pt and Low-Pt Nanocatalysts
 - 2.2.1. Graphene-Supported Pt Nanocrystals (Pt/Graphene)
 - 2.2.2. Graphene-Supported Low-Pt Alloy Nanocrystals
 - 2.3. Graphene-Supported Non-Pt Nanocatalysts
 - 2.3.1. Pd-Based Nanocatalysts/GNs
 - 2.3.2. Au- and Ag-Based Nanocatalysts/GNs
 - 2.3.3. Fe-Based Nanocatalysts/GNs
 - 2.3.4. Co-Based Nanocatalysts/GNs
 - 2.3.5. Ni-Based Nanocatalysts/GNs
 - 2.3.6. Other Non-noble Nanocatalysts/GNs
 - 2.4. Graphene-Supported Metal-Free Electrocatalysts
3. Structural Characterization and Properties of Graphene-Supported Nanoelectrocatalysts
 - 3.1. Structural Characterization
 - 3.1.1. Electron Microscopy (TEM, HRTEM, SEM, and STEM)
 - 3.1.2. Scanning Probe Microscopy (AFM and STM)
 - 3.1.3. Raman Spectroscopy
 - 3.1.4. X-ray Photoelectron Spectroscopy (XPS)
 - 3.1.5. X-ray Diffraction (XRD)

3.1.6. UV–Vis Spectroscopy	5142
3.1.7. X-ray Absorption Near-Edge Structure (XANES)	5142
3.1.8. Other Characterization Methods	5143
3.2. Catalytic Properties	5143
3.2.1. Intrinsic Catalytic Properties of Heteroatom-Doped Graphene	5143
3.2.2. Catalytic Properties of Graphene-Supported Nanoelectrocatalysts	5144
3.3. Other Unique Properties	5145
4. Applications of Graphene-Supported Nanoelectrocatalysts	5146
4.1. Electrooxidation of Small Organic Molecules at Anode of Fuel Cells	5146
4.1.1. Methanol Oxidation Reaction (MOR)	5146
4.1.2. Formic Acid Oxidation Reaction (FAOR)	5147
4.1.3. Ethanol Oxidation Reaction (EOR)	5148
4.1.4. Hydrogen Oxidation Reaction (HOR)	5149
4.2. Oxygen Reduction Reaction (ORR) at Cathode	5149
5. Conclusions and Future Outlook	5151
Author Information	5152
Corresponding Author	5152
Author Contributions	5152
Notes	5152
Biographies	5152
Acknowledgments	5153
Abbreviations	5153
References	5153

1. INTRODUCTION

With the rapid increase of energy demand in people's daily life and the depletion of fossil fuel reserves, research on new environment-friendly energy sources and their practical applications has attracted increasing attention in the past decades.^{1–3} Ensuring clean and efficient energy sources is one of the biggest challenges that we face in the 21st century. Among the proposed clean energy sources, fuel cells, such as proton exchange membrane fuel cells (PEMFCs), direct methanol fuel cells (DMFCs), direct formic acid fuel cells (DFAFCs), etc., have been considered a class of the most promising power sources with high energy density and high efficiency.^{4–7} A fuel cell is an electrochemical device that can convert the chemical energy of a fuel into electrical energy

Received: October 6, 2013

Published: March 25, 2014

through chemical reactions on the interface of electrode and electrolyte. The main reactions in a fuel cell include the fuel oxidation on anode and the oxygen reduction on cathode. Among the metal catalysts for anode and cathode reactions, platinum (Pt) exhibits the highest electrocatalytic activities for electro-oxidation of small organic fuels on the anode and the oxygen reduction on the cathode. However, with Pt alone as catalyst, several obvious disadvantages largely limit its application in fuel cells. First, for small organic fuels oxidation on Pt, the self-poisoning originated from the strong CO adsorption on the surface of Pt will decrease its catalytic performance. Second, with Pt as cathodic catalyst in DMFCs, the methanol crossover from anode to cathode may reduce the ORR performance due to the mixed potentials formed from the simultaneous methanol oxidation and oxygen reduction at cathode. Third, the limited reserve in nature and the resulting high-cost hinders the wide commercialization of fuel cells. According to the annual report of the U.S. Department of Energy (DOE) in 2008, the Pt-based catalyst ink accounts for 27–43% of the cost of a direct H₂ PEM fuel cell stack.⁸ The total cost of a fuel cell stack can be largely reduced by lowering the catalyst loading and using low- or non-Pt-based electrocatalysts. Therefore, how to improve the catalytic activities and lower the costs of anode and cathode catalysts are the critical issues to realize the real commercialization of fuel cells.⁹

To obtain ideal electrocatalysts for fuel cells with high catalytic performance and low price, much effort has been devoted to designing novel structured catalysts. Especially, the nanostructured materials meet excellently the requirements of a catalyst candidate with large surface area, increased surface active sites, and low metal loading. Up to now, various chemical and physical methods have been well-developed for preparing nanocrystals with desired surface facets. So far, the developed electrocatalysts can be mainly classified into the following categories: (1) The first is Pt-based nanocatalysts.¹⁰ By incorporating transition metals into Pt, various Pt-based bimetallic and ternary nanocatalysts, such as PtRu,^{11,12} PtFe,^{13–17} PtNi,¹⁸ PtCu,¹⁹ PtCo,²⁰ PtMn,²¹ and PtIr,²² etc., have been designed to improve their catalytic performance and reduce the costs.^{10,23} It should be pointed out that, as compared to the Pt alone catalysts, Pt-based electrocatalysts have enhanced catalytic performance and improved tolerance toward CO poisoning due to the so-called bifunctional mechanism and/or ligand effect.^{24–28} (2) The second is Pd-based nanocatalysts.^{29,30} Because of the similar intrinsic properties but lower cost as compared to Pt, Pd-based nanostructured materials have been constructed and used as fuel cell electrocatalysts. Moreover, *in situ* spectroelectrochemical investigations revealed that there is little CO poisoning during organic small molecule oxidation on Pd-based electrocatalysts, which can enhance their electrocatalytic performance. The catalytic activity of Pd-based catalysts can be effectively manipulated by alloying with different transition metals^{31–37} and by fabricating different nanostructures.^{38–47} (3) The third is non-noble metal nanoelectrocatalysts. To further reduce the costs of electrocatalysts, Pt- and Pd-free nanostructured materials have also been studied as catalysts, for instance, coinage metal nanoclusters,^{48–52} transition metal oxides and sulfides,^{53–58} transition metal macrocyclic complexes,^{59,60} metal-containing porphyrin compounds,⁶¹ carbon-supported iron- and cobalt-based catalysts,^{62,63} metal nitrides,⁶⁴ and so on. (4) The final category is metal-free and heteroatom-doped carbon materials. In recent years, it has been found that single,

binary, or ternary N, P, B, and S-doped carbon materials, such as graphene, carbon nanotubes (CNTs), nanofibers, exhibit enhanced electrocatalytic activity for oxygen reduction due to the conjugation between the π electrons of carbon and the lone pair electrons from dopants.^{65–67} Such metal-free materials have promising applications in fuel cells as cathode catalysts with high activity, low price, and high methanol tolerance.

Besides the considerations of the catalytic activity and cost, the stability and lifetime of a catalyst are also the critical issues for its practical applications in fuel cells. When the above materials are used as fuel cell catalysts, they are usually dispersed on a catalyst support. A good catalyst support should meet some requirements, such as large surface area for catalyst dispersion, highly electric conductivity, and high electrochemical stability in acidic or alkaline electrolytes. At present, the state-of-the-art commercial catalysts are usually prepared by dispersing catalyst nanoparticles (2–5 nm) on carbon supports. However, previous studies showed that, except for the metal catalyst degradation because of the dissolution and aggregation of metal nanoparticles, the severe corrosion and oxidation of carbon support materials under the real fuel cell operating environment could also lead to the quick activity loss of the catalysts. In recent years, various catalyst support materials have been proposed to address the challenges. In addition to the traditional carbon materials, noncarbon materials, such as metal oxides, electronically conductive polymers, carbides, and nitrides, etc., have also been proposed as catalyst supports in the past decades.⁶⁸

In the carbon material family, graphene is a new star member discovered in 2004 by Geim et al.⁶⁹ Graphene has a unique two-dimensional and single-atom thick structure with sp²-bonded carbon atoms densely arranged in a honeycomb crystal lattice. Heteroatom-doped graphene has been found to show high electrocatalytic activity for ORR. On the other hand, graphene nanosheets (GNs) have exhibited promising wide applications as 2-D catalyst support due to the following properties. First, graphene possesses a large theoretical specific surface area (SSA) of ~2600 m²/g, which is twice that of single walled CNTs. Second, graphene has a fully conjugated sp² hybridized planar structure, giving rise to ultrahigh electrical conductivity, excellent mechanical properties, and high thermocconductivity. Third, the chemically converted graphene with interlayer structure contains lattice defects (vacancies, holes) and surface functional groups (carbonyls, epoxides, hydroxyls, etc.), which can anchor and immobilize metal nanoparticles on its surface. Because of the strong metal–substrate interaction, the stability of nanocatalysts can be improved by dispersing on graphene.^{70,71} For instance, by using density functional theory (DFT) and bond-order potential calculations, Fampiou and Ramasubramaniam⁷⁰ found that the surface defects in graphene support can act as strong binding traps for Pt nanoclusters, which leads to the long-term stability toward sintering of Pt–graphene composites. Moreover, the catalytic activity of the graphene-supported catalysts can be enhanced because of the increasing charge transfer from catalysts to graphene substrate. From the above, the unique properties of graphene meet very well the basic requirements of an ideal catalyst support. Therefore, notable effort has been devoted to the design of novel nanostructured catalysts dispersed on graphene support. Our recent study⁷² showed that, as compared to Pt/C commercial catalyst and unsupported PtPd nanoparticles, graphene-supported PtPd alloy nanocrystals exhibited higher catalytic performance and much higher durability for methanol

Table 1. Heteroatom-Doped Graphene Materials and Their Applications in Electrocatalysis

material	preparation method	precursor	dopant	ref
B-graphene	CVD	CH ₄ /B ₂ H ₆ polystyrene/boric acid	boron	99 100
	arc discharge	graphite/H ₂ /B ₂ H ₆	boron	87
	thermal annealing	GO/B ₂ O ₃	boron	117
		graphite/H ₃ BO ₃	boron	118
N-graphene	CVD	CH ₄ /NH ₃ acetonitrile/NH ₃ pyridine H ₂ /ethylene/NH ₃ polystyrene/urea	nitrogen	88, 94 95 96, 98 97 100
	arc discharge	graphite/H ₂ /pyridine(ammonia)	nitrogen	87
	thermal annealing	graphene/NH ₃ GO/melamine GO/NH ₃ GO-silica/NH ₃ Ni(C)/B(N) GO/S-aminotetrazole	nitrogen	105, 106 116 107, 109, 119 121 110 385
	pyrolysis	sugar/urea GO/polypyrrole	nitrogen	115 114
	plasma treatment	graphene/nitrogen GO/hydrogen/nitrogen gaphene/NH ₃ GO/H ₂ and NH ₃ PMMA ^a /N ₂ and H ₂	nitrogen	129–131 132 133 134 135
	solvothermal	Li ₃ N/CCl ₄ or N ₃ C ₃ Cl ₃ /Li ₃ N/CCl ₄ GO/hydrazine hydrate	nitrogen	140 141
	hydrothermal	GO/hydrazine/ammonia	nitrogen	142
	thermal annealing	GO, triphenylphosphine	phosphorus	112
	pyrolysis	toluene, triphenylphosphine	phosphorus	113
	CVD	hexane/sulfur powder	sulfur	101
S-graphene	thermal annealing	GO/benzyl disulfide GO-silica/H ₂ S	sulfur	120 121
I-graphene	thermal annealing	GO/iodine	iodine	111
B,N-graphene	thermal annealing	GO/H ₃ BO ₃ /NH ₃	boron and nitrogen	122
S,N-graphene	thermal annealing	GO, melamine, benzyl disulfide	nitrogen and sulfur	123
P,N-GNs	hydrothermal	GO, ammonium thiocyanate	nitrogen and sulfur	124
	pyrolysis	GO, dicyandiamide, phosphoric acid	nitrogen and phosphorus	125

^aPMMA: polymethylmethacrylate.

oxidation. It is anticipated that graphene-supported nanomaterials represent a promising class of electrocatalysts for fuel cells.

Despite that great efforts have been dedicated to the investigation of graphene-based nanomaterials and a number of reviews on graphene have been published,^{73–81} a comprehensive overview on the graphene-based nanoelectrocatalysts for fuel cells is still absent. To keep up to date with the rapidly increasing advances in this field, it is time to review the recent progress and the challenges of the graphene-supported nanoelectrocatalysts. In this Review, we summarize first the developed synthetic techniques for the preparation of doped graphene and graphene-supported nanoelectrocatalysts. The structure-dependent properties then will be presented. In the following section, the application of graphene-based nanoelectrocatalysts in fuel cells as anode and cathode catalysts will be discussed in detail. Finally, a brief conclusion and an outlook on the development of graphene-based elecrocatalysts will be provided. We hope that this Review is helpful to push forward the advancement of this research field.

2. SYNTHESIS OF FUNCTIONALIZED GRAPHENE AND GRAPHENE-SUPPORTED ELECTROCATALYSTS

Overall, graphene-based electrocatalysts include heteroatom-doped graphene and graphene-supported nanocomposites. It is well-known that the activities of catalysts are strongly dependent on their surface properties. Especially for the graphene-supported nanocomposites, their electrocatalytic properties can be largely influenced by the composition, particle size and the exposed surface planes of the composites and the interfacial interactions between composites and graphene support. Up to now, different physical and chemical methods have been successfully used to prepare heteroatom-doped graphene and graphene-supported nanocomposites. In this section, the synthetic methods for preparation of graphene-based electrocatalysts are outlined on the basis of the catalyst composition, that is, graphene and heteroatom-doped graphene catalysts, graphene-supported non-Pt nanocatalysts, and graphene-supported Pt and low-Pt nanocatalysts.

2.1. Synthesis of Graphene and Heteroatom-Doped Graphene Electrocatalysts

Since graphene was obtained by a manual mechanical cleavage of graphite with Scotch tape the first time, a wide range of techniques have been developed for synthesizing graphene sheets. These methods can be divided into top-down and bottom-up strategies. Top-down methods include micro-mechanical cleavage of highly oriented pyrolytic graphite (HOPG), intercalation/exfoliation from graphite by means of oxidation,^{82,83} oxidative splitting or unzipping of CNTs via etching for the fabrication of nanoribbons,^{84,85} and chemical oxidation of graphite to graphite oxide to obtain mildly oxidized graphene. Bottom-up approaches have been widely employed to fabricate large, continuous graphene or heteroatom-doped graphene films for practical applications, including arc-discharge approach,^{86,87} chemical vapor deposition (CVD) on catalytically active metals,^{88,89} epitaxial growth on single-crystal SiC,⁹⁰ etc. Especially, chemical doping with foreign atoms is an effective approach to manipulate the electronic and chemical properties of graphene. Recent studies have shown that heteroatom-doped graphene materials have potential applications in fuel cells as metal-free electrocatalysts. Under certain conditions, carbon atoms in the hexagonal honeycomb lattice of graphene can be replaced by foreign atoms, such as nitrogen, boron, sulfur, etc. The most commonly used methods for the preparation of graphene, especially heteroatom-doped graphene, are summarized in Table 1 and discussed in detail below.

2.1.1. Chemical Vapor Deposition (CVD). CVD is a kind of common and popular method for controllably synthesizing various types of nanomaterials. In recent years, CVD has also been widely used as an efficient method to synthesize mono- or multilayer graphene or B-, N-, S-, and P-doped graphene nanosheets with high quality. The previous studies found that with the CVD method, the nucleation and growth of graphene occur via arranging carbon and foreign atoms on surfaces of transition metal catalysts.^{89,91,92} In CVD methods, graphene sheets can be obtained by using CH₄ and hydrocarbon gases as carbon sources under high deposition temperatures (e.g., 1000 °C). Ruoff and co-workers reported a typical CVD method to grow large-area graphene films in the order of centimeters directly on the surface of copper foils using a mixture of methane and hydrogen as carbon resources at temperatures up to 1000 °C.⁹¹ The electron microscopy (SEM, TEM) and Raman spectroscopy characterizations showed that the formed graphene films are highly uniform and predominantly single-layer products. It was found that on Cu substrate the graphene growth is a surface-catalyzed and self-limited process. In another work, Kim et al.⁹³ synthesized large-scale graphene films with high quality by using CVD method on thin nickel layers. More importantly, the graphene monolayer can be transferred to various arbitrary substrates while maintaining their low sheet resistance (~280 Ω per square) and high optical transparency (80%), which makes them perfect applications in electronic devices.

As for the preparation of N-doped graphene (denoted as N-graphene) with CVD method, a similar process is used except for introducing nitrogen-containing precursors as nitrogen source.^{88,94–98} In the previous reports, NH₃ and other organic compounds have been used as nitrogen sources. For example, Dai and co-workers⁹⁴ developed a CVD method for synthesizing N-graphene films on nickel film. In the synthesis, Ni film was first deposited on a SiO₂/Si substrate. After the Ni film was

heated to 1000 °C under argon atmosphere, a gaseous mixture with the composition of NH₃:CH₄:H₂:Ar = 10:50:65:200 was introduced, followed by a flow of NH₃ and Ar for another 5 min. After treatments with aqueous HCl solution, the N-graphene film can be transferred onto different substrates. From the digital photo image shown in Figure 1a, the as-

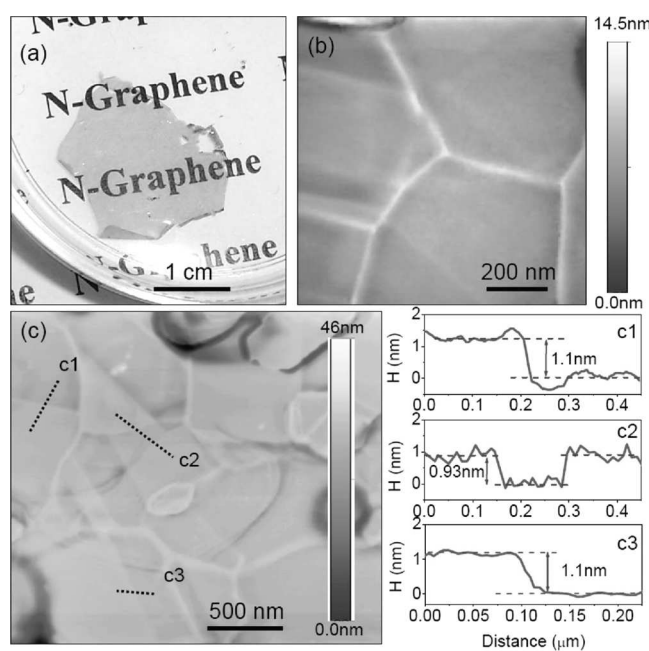


Figure 1. Characterizations of the N-doped graphene film. (a) A digital photo image of a transparent N-doped graphene film floating on water; (b,c) atomic force microscopy (AFM) images of the N-graphene film and the corresponding height analyses along the lined marked in the AFM image (c1–c3 in panel c). Reprinted with permission from ref 94. Copyright 2010 American Chemical Society.

synthesized N-graphene film is flexible and transparent. The atomic force microscopy (AFM) measurements (Figure 1b and c) showed that the formed N-graphene film is highly uniform with a smooth surface. The height analyses indicated that the N-graphene film is 0.9–1.1 nm in thickness, consisting of only one or a few layers of carbon atoms. The X-ray photoelectron spectroscopic (XPS) measurements indicated the presence of both pyridine-like and pyrrolic nitrogen atoms in the product. In addition to NH₃, liquid N-precursors such as acetonitrile and pyridine have also been used as nitrogen sources for the synthesis of N-graphene. Jin et al.⁹⁸ successfully synthesized monolayer N-graphene in centimeter-scale sheets by CVD process with pyridine as the sole source of both carbon and nitrogen. Imamura and Saiki⁹⁶ found that the substrate temperature and N-containing source materials have strong effects on the formation of N-graphene. In their study, when pyridine was used as precursor, N-graphene can be formed on a Pt(111) surface at the substrate temperature (T_s) higher than 500 °C, while nitrogen can not be doped into graphene at T_s higher than 700 °C. However, with the same substrate, only graphene but not N-graphene can be obtained by using acrylonitrile as precursor at any temperature. On the basis of the proposed N-doping mechanism of “bond breaking and bonding reforming” two processes, the weak single C–C bond in acrylonitrile is preferentially broken, resulting in the formation of CN fragments. Because of the formation of

other molecules from CN fragments, N can not be doped into the formed graphene sheets.

In addition to nitrogen, other heteroatoms have also been successfully doped in graphene through CVD process. Cattelan et al.⁹⁹ synthesized single layer boron-doped graphene (B-graphene) on polycrystalline copper foil through CVD method by using methane and diborane as carbon and boron sources. In the synthesis, a two-step process was adopted to prepare the B-graphene. As shown in Figure 2, large graphene patches were

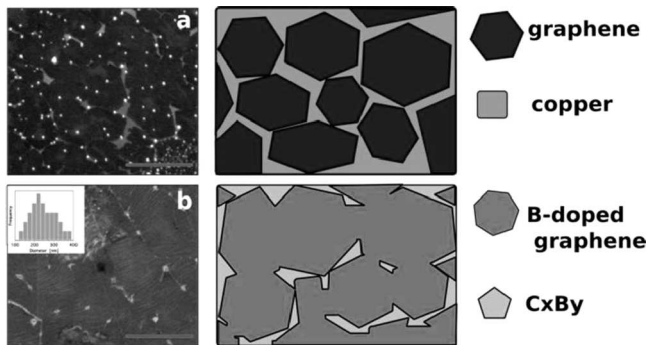


Figure 2. SEM micrographs of the boron-doped graphene synthesized by CVD method on copper polycrystalline foils and schematic diagram of the two-step growth. (a) First step of the synthesis of large graphene domains covered about 80% of the copper surface; (b) second step with the further growth of graphene islands and the nucleation of some 3D clusters of nonstoichiometric boron carbide on bare copper surface areas. Both scale bars are 3 μm . Reprinted with permission from ref 99. Copyright 2013 American Chemical Society.

first formed by exposing Cu substrate in methane and hydrogen at 1000 °C. At this stage, about 85% of the copper surface is covered by single layer graphene. In the second step, with the further growth of graphene islands and introduction of B_2H_6 , nonstoichiometric boron carbides were formed on the bare Cu surface area between graphene domains, which can migrate by diffusion into the graphene patches to produce boron-doped graphene films. With CVD approach, Wu et al.¹⁰⁰ synthesized nitrogen- and boron-doped graphene on Cu foil substrate by using polystyrene, urea, and boric acid as C-, N-, and B-containing precursors, respectively. By changing the ratio of the precursors, the doping concentration of N can be tuned from 0.9% to 4.8% and B can be modulated from 0.7% to 4.3%. It was found that the nitrogen types vary with the doping concentration of N in graphene films. For the N-graphene with doping of about 2.1%, the N-binding configuration is predominated by pyridinic N. However, for the N-graphene with doping of about 4.8%, 60.2 at. % pyridinic N and 39.8 at. % pyrrolic N are presented in the product. Such a result indicates that the properties of N-graphene can be manipulated by controlling the doping concentration. With CVD technique, Gao et al.¹⁰¹ synthesized sulfur-doped graphene sheets by using sulfur powder and hexane as the growth precursors. On the basis of the XPS, high-resolution TEM, and elemental mapping characterizations, it was proposed that S atoms tend to form linear nanodomains in graphene lattice. The S-graphene exhibited p-type semiconductor behavior.

However, it should be noted that CVD or ultrahigh vacuum (UHV) CVD techniques usually require transition metals as substrate materials. The high cost of the single crystal substrates, special synthetic instruments, and the extreme

conditions, such as high temperature (1000 °C), ultrahigh vacuum, greatly limit its large-scale application.

2.1.2. Arc-Discharge Approach. In the past two decades, the arc-discharge method has been widely utilized to prepare carbon-based nanomaterials, such as carbon nanotubes and fullerenes, by evaporating carbon sources at high temperature. This method has also been used in the synthesis of graphene and heteroatom-doped graphene. The properties of graphene more or less depend on the heating modes. Wu et al.¹⁰² developed a hydrogen arc-discharge exfoliation method for the synthesis of graphene. In the method, the presynthesized graphene oxide (GO) was rapidly heated by arc discharge in a mixed buffer atmosphere of H_2/Ar ($\text{H}_2:\text{Ar} = 10:90$ kPa pressure) with graphite rod as cathode and a rotatable graphite cylinder as anode. The obtained exfoliated graphite was then dispersed in *N*-methylpyrrolidone by ultrasonication to produce graphene sheets. The obtained graphene sheets exhibited higher electric conductivity and thermal stability than those of graphene synthesized by argon arc-discharge exfoliation and thermal exfoliation processes. The excellent properties of graphene may be ascribed to the high plasma temperature and hydrogen atmosphere, which can result in efficient exfoliation, considerable deoxygenation of GO, and defect elimination.¹⁰² With a similar method, Rao's group⁸⁶ synthesized 2–4 layer graphene flakes by arc discharge between graphite electrodes under a relatively high pressure of hydrogen (above 200 Torr). In their study, with the presence of a mixture of H_2 and diborane or H_2 and pyridine during arc discharge, boron-doped (1–3 wt %) graphene or nitrogen-doped (0.6–1.0 wt %) graphene can be produced. Chen and co-workers¹⁰³ developed an arc-discharge method for efficient and large-scale synthesis of few-layered graphene by using a gas mixture of He/ CO_2 . Volotskova et al.¹⁰⁴ reported a one-step approach for simultaneous preparation and separation of graphene flakes and carbon nanotubes via the arc-discharge method by splitting the high-temperature growth and low-temperature separation zones and depositing nanotubes and graphene in different areas.

The arc-discharge method has also been used to synthesize N- and B-doped graphene. Panchakarla et al.⁸⁷ studied the effects of the precursors on the structure and doping degree of the N- and B-graphene. They synthesized two B-graphene samples by using graphite electrodes in the presence of $\text{H}_2 + \text{B}_2\text{H}_6$ (BG1) or boron-stuffed graphite electrodes (BG2). The electron energy loss spectroscopy (EELS) measurements showed that boron is bonded to sp^2 carbon in both samples. However, the XPS results indicated that the boron doping concentration in BG2 (3.1 at. %) is much higher than that of BG1 (1.2 at. %). They also prepared three N-graphene samples by using graphite electrodes in the presence of $\text{H}_2 + \text{pyridine}$ (NG1), $\text{H}_2 + \text{ammonia}$ (NG2), and by using the transformation of nanodiamond in the presence of pyridine (NG3). The N-doping concentrations are 0.6 (NG1), 1.0 (NG2), and 1.4 at. % (NG3), respectively. The in-plane crystallite sizes of the undoped graphene, BG1, BG2, NG1, NG2, and NG3 were calculated to be 64, 30, 26, 43, 41, and 19 nm, respectively. The results indicate that the precursors can influence the structure and doping concentration of the heteroatom-doped products.

2.1.3. Thermal Annealing Method. With the presence of heteroatom-containing precursors, doped graphene can be obtained easily through high-temperature annealing graphene or graphene oxide. Up to now, N, S, I, P, and B-doped graphene have been synthesized via different thermal annealing methods.^{105–115} Xia and co-workers¹¹⁶ developed a catalyst-

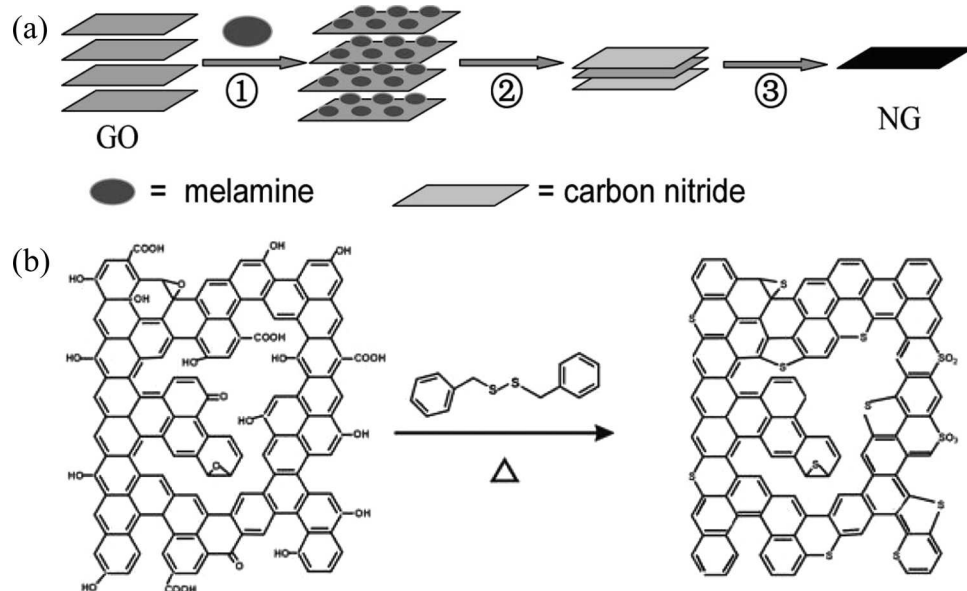


Figure 3. N- and S-doped graphene sheets synthesized by thermal annealing methods. (a) Illustration of the formation of N-doped graphene with melamine as precursor. (1) Melamine adsorption on the surface of GO with a temperature lower than 300 °C; (2) melamine condensed and carbon nitride formed at temperature lower than 600 °C; (3) carbon nitride decomposed and doped into graphene layers at temperature higher than 600 °C. Reprinted with permission from ref 116. Copyright 2011 American Chemical Society. (b) Schematic illustration of S-doped graphene synthesis by using benzyl disulfide as precursor. Reprinted with permission from ref 120. Copyright 2012 American Chemical Society.

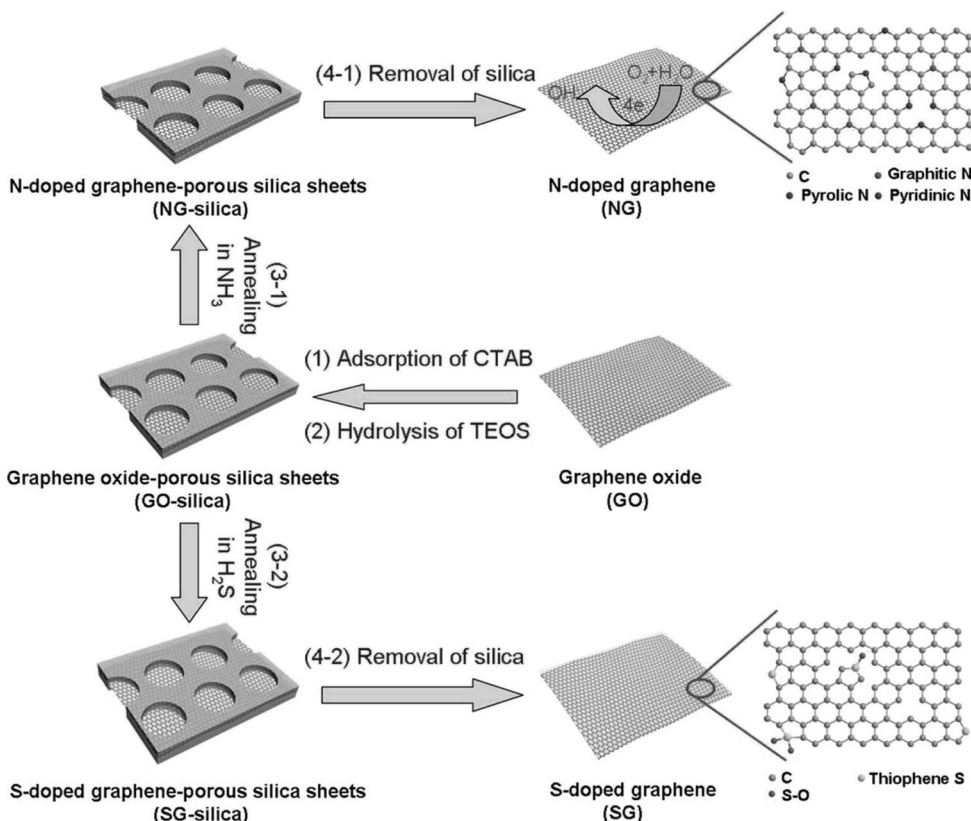


Figure 4. Schematic illustration of the synthesis of N- and S-doped graphene. (1,2) Hydrolysis of tetraethyl orthosilicate (TEOS) on GO surface with the presence of cetyltrimethyl ammonium bromide (CTAB). (3-1) Thermal annealing of GO-silica sheets in ammonia at 600, 800, 900, and 1000 °C, respectively. (3-2) Thermal annealing of GO-silica sheets in H₂S at 500, 700, and 900 °C, respectively. (4-1 and 4-2) Removal of silica by HF or NaOH solution. Reprinted with permission from ref 121. Copyright 2012 Wiley-VCH.

free synthetic method to prepare N-graphene by thermal annealing graphite oxide with melamine as the nitrogen source. As shown in Figure 3a, the method includes three steps. First,

melamine molecules were adsorbed on the presynthesized GO. Melamine was then condensed to carbon nitride at high temperature (<600 °C). Finally, with the removal of oxygen

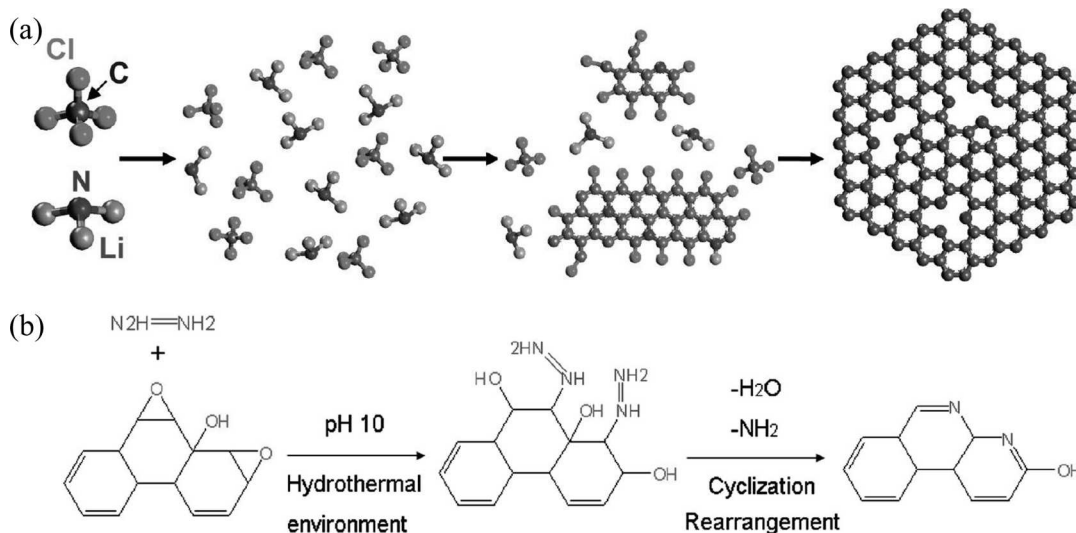


Figure 5. (a) Scheme of the proposed mechanism for solvothermal synthesis of N-doped graphene based on the reaction between CCl_4 and Li_3N . Reprinted with permission from ref 140. Copyright 2011 American Chemical Society. (b) Schematic illustration of the synthesis of nitrogen-doped graphene by a hydrothermal process. Reprinted with permission from ref 142. Copyright 2010 American Chemical Society.

groups on graphene nanosheets at high temperature, nitrogen atoms can be doped in the provided active sites. The nitrogen doping concentration can be adjusted by changing the mass ratio of GO to melamine and the annealing temperature. N-graphene with the highest nitrogen doping level of 10.1% was obtained with a GO/melamine mass ratio of 1/5 at 700 °C. Such synthetic strategy can be applied to the preparation of other heteroatom-doped graphene with appropriate precursors. For instance, a similar approach has been used to synthesize boron-doped graphene multilayers as metal-free electrocatalysts in fuel cells.¹¹⁷ Boron-doped single-layer graphene was prepared by mixing boric acid and graphite and thermally treating at 2450 °C in an argon atmosphere.¹¹⁸ Li et al.¹¹⁹ prepared N-graphene by thermal annealing GO in ammonia atmosphere. They found that the oxygen-containing groups on GO surface are essential for the C–N formation from the reaction between GO and NH_3 . In the study, the highest N-doping concentration of 5% was achieved at 500 °C. In another work, Yang et al.¹²⁰ synthesized sulfur-doped graphene through thermal annealing method at 600–1050 °C by using benzyl disulfide as precursor (Figure 3b). It was found that the S doping level decreases with increasing annealing temperature (1.53%, 1.35%, and 1.30% at 600, 900, and 1050 °C, respectively). Recently, Mullen and co-workers¹²¹ developed a novel method to prepare N- and S-doped graphene by thermal reaction. As shown in Figure 4, sandwich-like GO-porous silica sheets were first fabricated by hydrolysis of tetraethyl orthosilicate with the presence of cetyltrimethyl ammonium bromide. The formed hybrids were then annealed at high temperature (500–1000 °C) under NH_3 or H_2S atmosphere. N- or S-graphene can be finally obtained after removal of the silica template by etching. XPS measurements showed that S and N have been doped into graphene sheets with a major form of thiophene-like S and three types of nitrogen, including pyridinic-N, pyrrolic-N, and graphitic-N. Also, the doping levels of S and N are in the ranges of 1.2–1.7% and 2.4–2.6%, respectively.

Besides single-doping, codoping of graphene has also been achieved through thermal annealing treatment. Wang et al.¹²² reported a facile approach to prepare boron and nitrogen

codoped graphene by thermal annealing GO in the presence of boric acid under ammonia atmosphere. Tunable B/N codoping levels can be achieved by changing annealing temperature and time. In the study, $\text{B}_7\text{C}_{87}\text{N}_6\text{H}_{26}$, $\text{B}_{12}\text{C}_{77}\text{N}_{11}\text{H}_{26}$, and $\text{B}_{38}\text{C}_{28}\text{N}_{34}\text{H}_{26}$ were obtained with the annealing times of 0.5, 1, and 2 h, respectively at the annealing temperature of 1000 °C. In another work, Liang et al.¹²³ successfully prepared mesoporous N-, S-dual-doped graphene (N-S-G) via heating treatment of the mixture of GO/ SiO_2 , melamine, and benzyl disulfide (BDS) at 900 °C. Other dual- or tridoped graphene, such as N,S,¹²⁴ N,P,¹²⁵ and N,S,Se-GNs,¹²⁶ have also been synthesized as ORR electrocatalysts.

2.1.4. Plasma Treatment. In recent years, substrate-free gas-phase synthesis of graphene has been achieved through plasma treatment.¹²⁷ Hazra et al.¹²⁸ reported a method to transform multilayer graphene to single-layer graphene in a hydrogen and nitrogen plasma environment. As compared to the harsh conditions, plasma treatment can be realized at relatively ambient conditions. As a kind of energy-efficient and eco-friendly alternative method to synthesize carbon materials, plasma treatment has been used to prepare heteroatom (mainly N)-doped graphene or GO.^{129–133} In N_2 or NH_3 plasma atmosphere, carbon atoms of graphene may be replaced by nitrogen. Wang et al.¹²⁹ prepared N-graphene by plasma treatment of graphene nanosheets supported on glassy carbon electrode in a nitrogen atmosphere. The nitrogen percentage doped in graphene can be manipulated in the range of 0.11–1.35% by controlling the exposure time. In this study, it was also found that the plasma treatment can not only lead to the doping of nitrogen in graphene but also increase the oxygen content, which increased from ~15% in graphene to ~27% in N-graphene. Recently, Kumar et al.¹³⁴ reported a scalable approach to simultaneously reduce GO and introduce nitrogen into GO near room temperature by plasma treatment in a mixed gas atmosphere of H_2 and NH_3 . The synthesis can produce gram-scale quantities of N-graphene with high nitrogen doping level of 5.8%. In another study, Wang et al.¹³⁵ synthesized single- or double-layer graphene sheets on copper foils through microwave plasma using polymethylmethacrylate as carbon source. N-Graphene with around 5%

Table 2. Graphene-Supported Noble Metal Electrocatalysts and Their Applications

material	preparation method	precursor	application	ref
Pt/GNs	chemical reduction	N-GN, H ₂ PtCl ₆ ·6H ₂ O, EG GN, Pt salt, NaBH ₄ GO, H ₂ PtCl ₆ , NaBH ₄ GO, H ₂ PtCl ₆ , EG GO, PDDA, ^a H ₂ PtCl ₆ , NaBH ₄	MOR ORR MOR/ORR MOR MOR/ORR	109 131 163, 170 165 190
	self-assembly	3D GN, K ₂ PtCl ₄	MOR	159
	electrodeposition	3D GN, H ₂ PtCl ₆ GO, Cu foil, H ₂ PtCl ₆	MOR MOR	175 176
	microwave-assisted process	GO, H ₂ PtCl ₆ , EG	MOR	180
	impregnation/thermal reduction	GN, Pt(NO ₂) ₂ (NH ₃) ₂ , H ₂ /Ar	MOR/HOR	184, 458
	chemical reduction	GO, PVP, ^b Pt(acac) ₂ , Pd(acac) ₂ PVP ^b -GN, K ₂ PtCl ₄ , PdCl ₂	MOR MOR	72 200
	electrodeposition	GO, H ₂ PtCl ₆ , PdCl ₂	MOR/EOR	202, 203
	hydrothermal	GO, K ₂ PtCl ₄ , Na ₂ PdCl ₄ , NaI, PVP ^b	MOR	204
	chemical reduction	GO, H ₂ PtCl ₆ , HAuCl ₄ , EG PDDA ^a -GO, H ₂ PtCl ₆ , HAuCl ₄ , NaBH ₄	FAOR FAOR	154 206
	electrodeposition	GN, H ₂ PtCl ₆ , HAuCl ₄	MOR/ORR	207
PtPd/GNs	microwave-assisted process	N-GN, H ₂ PtCl ₆ , HAuCl ₄	MOR	208
	chemical reduction	GO, H ₂ PtCl ₆ , RuCl ₃ , EG GO, Pt(acac) ₂ , Ru(acac) ₃	MOR/EOR MOR	212 216
PtAu/GNs	electrodeposition	3D GN-CNTs, H ₂ PtCl ₆ , RuCl ₃ , EG	MOR	219
	microwave-assisted process	GN-N-CNTs, H ₂ PtCl ₆ , RuCl ₃ , NaBH ₄	MOR	220
PtRu/GNs	chemical reduction	PMo ₁₂ -GN, H ₂ PtCl ₆ , RuCl ₃ , EG GN-Vulcan C, H ₂ PtCl ₆ , RuCl ₃	MOR MOR	218 221
	electrodeposition	GO, Co(NO ₃) ₂ , K ₂ PtCl ₄ , CTAB, ^c NaBH ₄	MOR	222
	microwave-assisted process	GO, H ₂ PtCl ₆ , Co(NO ₃) ₂ , EG GO, H ₂ PtCl ₆ , CoCl ₂ , NaBH ₄	ORR MOR/ORR	225 227, 228
	chemical reduction	CTAB ^c -GN, K ₂ PtCl ₄ , CoCl ₂ , EG	ORR	229
	electrodeposition	GN, H ₂ PtCl ₆ , (Co(NO ₃) ₂	MOR	224
	chemical reduction	PDDA ^a -GO, H ₂ PtCl ₆ , NiCl ₂ , EG	MOR	230
	electrodeposition	GN, H ₂ PtCl ₆ , NiCl ₂ , NaBH ₄	MOR	231
	chemical reduction	GO, K ₂ PtCl ₄ , NiC ₄ H ₆ NiO ₄ , NaBH ₄	ORR	233
	electrodeposition	GO, H ₂ PtCl ₆ , NiCl ₂ , hydrazine	MOR	234
	chemical reduction	GO, K ₂ PtCl ₆ , NiCl ₂ , PVP, ^b NaBH ₄	MOR	236
PtFe/GNs	chemical reduction	GO, Pt(acac) ₂ Fe(CO) ₅	ORR	237
PtCu/GNs	chemical reduction	GO, H ₂ PtCl ₆ , Fe(NO ₃) ₃ , hydrazine	MOR	239
PtSn/GNs	chemical reduction	GN, H ₂ PtCl ₆ , CuCl ₂ , NaBH ₄	MOR	241
PtCr/GNs	chemical reduction	GO, H ₂ PtCl ₆ , SnCl ₂ , EG	MOR	242
PtAg/GNs	chemical reduction	GO, H ₂ PtCl ₆ , SnCl ₆ , EG	MOR	243
PtPdAu/GNs	chemical reduction	GO, H ₂ PtCl ₆ , CrCl ₃ , EG, Ar-H ₂	ORR	244
PtPdCu/GNs	chemical reduction	GO, K ₂ PtCl ₄ , HAuCl ₄ , NaBH ₄ , AA ^d	MOR	245
Pd/GNs	chemical reduction	GO, H ₂ PtCl ₆ , PdCl ₂ , HAuCl ₄ , EG	MOR	251
Pd-MnO ₂ /RGO	impregnation/thermal treatment	graphene, H ₂ PtCl ₆ , PdCl ₂ , CuSO ₄ , EG	EOR	252
	electrochemical deposition	GO, K ₂ PdCl ₄	FAOR/EOR	262
	chemical reduction	GO, PdCl ₂ , NaBH ₄	FAOR	263
	impregnation/thermal treatment	GO, pyrrole, H ₂ PdCl ₄ , NaBH ₄	MOR	266
	electrochemical deposition	GO, H ₂ PdCl ₄ /PdCl ₂ , N ₂ , H ₂	ORR/FAOR	182, 278
	chemical reduction	GO, Na ₂ PdCl ₄	FAOR	270
	impregnation/thermal treatment	GO, KMnO ₄ , EG, (NH ₄) ₂ PdCl ₆ , NaBH ₄	MOR	267
	electrochemical reduction	GO, HAuCl ₄ , PdCl ₂	ORR	269
	polyol reduction	GNs, PdCl ₂ , RuCl ₃ , EG	MOR	257
	polyol reduction	GNs, PdCl ₂ , SnCl ₂ , EG	MOR	273
PdAu/GNs	galvanic displacement reaction	GO, CoCl ₂ , C ₆ H ₅ Na ₃ O ₇ , NaBH ₄ , HAuCl ₄ , Na ₂ PdCl ₄	FAOR	275
PdAg/GNs	galvanic displacement reaction	GO, C ₆ H ₅ Na ₃ O ₇ , AgNO ₃ , Pd(NO ₃) ₂	ORR	276
PdRuSn/GNs	polyol reduction	GO, NaBH ₄ , RuCl ₃ , PdCl ₂ , SnCl ₂ , EG	MOR	277
Pd ₃ Y/GNs	impregnation/thermal treatment	GO, Pd(NO ₃) ₂ , Y(NO ₃) ₃ , N ₂ /H ₂	ORR/EOR	281
Au/Pd/GNs	chemical reduction	GO, polyallylamine, HAuCl ₄	ORR	303
Au/GNs	chemical reduction	GO, PTCDA, ^e N ₂ H ₄ , NH ₃ , HAuCl ₄	ORR	306
Au/GNs	electrochemical deposition	GO, N ₂ H ₄ , NH ₃ , HAuCl ₄	ORR	290

Table 2. continued

^aPDPA: poly (diallyldimethylammonium chloride). ^bPVP: polyvinylpyrrolidone. ^cCTAB: hexadecyltrimethylammonium bromide. ^dAA: ascorbic acid. ^ePTCDA: 3,4,9,10-perylenetetracarboxylic dianhydride.

doping concentration was then obtained by treatment in N₂/H₂ plasma. The XPS measurements showed that most of the doped nitrogen atoms are present with pyridine-like structure, which was attributed to the polycrystalline nature of graphene sheets and the easy formation of carbon vacancies by N₂/H₂ plasma treatment.

2.1.5. Solvothermal and Hydrothermal Treatments.

Much work has been done to develop the solvothermal and hydrothermal approaches for the preparation of graphene and N-doped graphene.^{136–139} Such method is accepted to be a green method for graphene preparation without using hazardous reducing agents. Recently, Deng et al.¹⁴⁰ developed a one-pot solvothermal method to prepare 1–6 layered N-graphene with gram scale production. As shown in Figure 5, N-graphene can be produced by solvothermal reaction between lithium nitride (Li₃N) and tetrachloromethane (CCl₄) at 250 °C for 10 h (denoted as NG-1) or between cyanuric chloride (N₃C₃Cl₃), Li₃N, and CCl₄ at 350 °C for 6 h (denoted as NG-2). It was proposed that dichlorocarbene, free –C=C–, and –C=N– groups are likely the intermediates during the change from sp³ carbon in CCl₄ to sp² carbon in graphene. In comparison with the low N doping concentration in graphene with the synthetic methods mentioned above, high N doping levels at 4.5 and 16.4 at. % have been achieved in NG-1 and NG-2 products, respectively. In another work, Wang et al.¹⁴¹ reported a hydrazine-assisted solvothermal method to synthesize N-graphene. By the proposed process, ~3% nitrogen was introduced into the reduced graphene oxide (rGO).

Yoon and co-workers¹⁴² synthesized N-graphene through a hydrothermal reduction of GO in the presence of NH₃ and hydrazine. It was found that the hydrothermal temperature has an obvious effect on the N-doping level. For instance, N-graphene with 5.21 wt % nitrogen content can be obtained at low temperature (80 °C). However, with increasing temperature, the nitrogen content decreases gradually, and only 4.01 wt % nitrogen is present in graphene at 200 °C. The XPS measurements showed that more pyridine N was incorporated into the graphene at higher temperature. On the basis of the proposed mechanism shown in Figure 5b, under hydrothermal environment, the reaction between hydrazine and epoxides may readily open the ring of epoxide and form hydrazine alcohols. During the deoxygenation and reconstruction of the carbon network, nitrogen atoms can be incorporated spontaneously.

In addition to the methods listed above, the synthesis of high-quality and large-area graphene sheets can also be achieved by other techniques, such as epitaxial growth on single-SiC carbide or metal surface,^{143–145} micromechanical exfoliation from graphite,^{69,146} electrochemical methods,^{147,148} microwave-assisted methods,¹⁴⁹ unzipping carbon nanotubes,^{85,150} and so on. Currently, these methods are usually applied to the synthesis of graphene or GO but not heteroatom-doped graphene. Interestingly, recent studies showed that GO can be effectively reduced to graphene by taking advantage of the bacterial respiration.^{151,152} Generally, through physical processes, high-quality graphene nanosheets can be obtained with few defects, which are suitable for the fabrication of electric devices. On the other hand, graphene sheets prepared by chemical methods usually have a number of

surface defects and functional groups, which can serve as anchoring sites for metal/graphene formation.

2.2. Graphene-Supported Pt and Low-Pt Nanocatalysts

Graphene-supported noble metal nanoparticles are one class of the most widely used hybrid electrocatalysts for fuel cells. Although Pt-free catalysts have been investigated extensively in recent years, Pt and Pt-based nanocatalysts are still mainly used in practical applications due to their high catalytic performance. By depositing Pt and low-Pt nanomaterials on graphene nanosheets, high dispersity of metal nanocatalysts can be achieved. Previous studies have showed that graphene-supported Pt and low-Pt nanocatalysts exhibited enhanced catalytic activity and long-term durability. It is well-known that the catalytic performance of hybrid electrocatalysts is strongly dependent on the size, composition, shape, dispersion states of noble metal nanocrystals, and their interactions with graphene support.^{14,49,153,154} Up to now, various synthetic strategies have been developed for the preparation of high-quality graphene-supported nanocatalysts.^{155–159} In this section, the syntheses of graphene-supported Pt and low-Pt nanocatalysts are summarized (Table 2).

2.2.1. Graphene-Supported Pt Nanocrystals (Pt/Graphene). To prepare Pt/graphene hybrids, the most frequently used method is reducing Pt-containing precursors in the presence of graphene or graphene oxide.^{160–162} By using NaBH₄ as reducing agent, Li et al.¹⁶³ prepared Pt/graphene nanocomposites via the coreduction of H₂PtCl₆ and presynthesized GO in water with pH = 10. With the process, Pt nanoparticles with the average diameter of 5–6 nm were dispersed on the graphene surface. In addition to the strong reducing agent, mild reductants, such as ethylene glycol (EG), sodium citrate, etc., have also been used to prepare Pt/graphene composites.^{164–169} Wang and co-workers¹⁶⁵ reported a simple approach of depositing Pt nanoparticles (1–5 nm) onto surfaces of GO nanosheets by EG reduction at 120 °C under stirring. Modified polyol method has also been used to synthesize rGO-supported Pt nanoparticles (~2.9 nm).¹⁷⁰ In the method, under the refluxing at 120 °C, NaBH₄ dissolved in EG was added dropwise into the mixed solution of GO and H₂PtCl₆. On the other hand, it has been found that GO and rGO themselves can serve as reducing agents. Therefore, metal nanoparticles could be directly reduced on GO or r-GO nanosheets without addition of any reducing agent. In the process, the electrons in negative-charged graphene sheets can be transferred to positive-charged metal precursors to produce zerovalent metal nanoparticles.

In addition to chemical reduction methods, Pt/graphene composites can also be prepared by other synthetic routes. As a traditional electrochemical technique, electrodeposition is a useful approach to prepare metal nanocrystals with the advantages of simplicity, free of templates, and easy shape control of metal particles.^{171–174} For instance, Maiyalagan et al.¹⁷⁵ have successfully electrodeposited Pt nanoparticles on 3D graphene nanosheets as an anode electrocatalyst toward methanol oxidation in fuel cells. 3D graphene foams were first synthesized by chemical vapor deposition with nickel foam as the template and ethanol as precursors. The morphology and

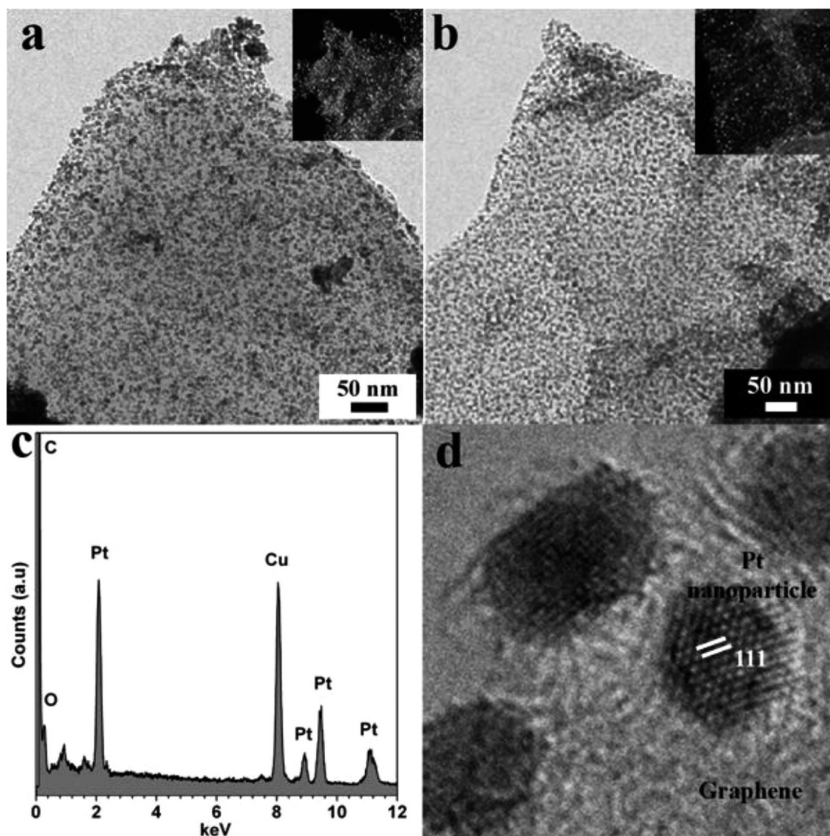


Figure 6. TEM bright-field images of (a) Pt/graphene-1 (20 mL of EG) and (b) Pt/graphene-2 (50 mL of EG) with corresponding dark-field images as insets. (c) EDS of the hybrid Pt/graphene-1. (d) HRTEM image of Pt nanoparticles dispersed on the rGO sheets. Reprinted with permission from ref 180. Copyright 2011 American Chemical Society.

size of Pt nanoparticles can be controlled by electrodeposition potential and time in H_2PtCl_6 solution. It was found that 200 pulses with the profile of 0 mV (500 ms)–1000 mV (200 ms)–0 mV (500 ms) (vs Ag/AgCl/3 M KCl) can produce spherical 10–30 nm Pt nanoparticles, which uniformly dispersed on the 3D graphene support. Recently, Liu et al.¹⁷⁶ developed a simple electroless deposition method to synthesize metal–graphene hybrid materials by taking advantage of the different redox potentials between a substrate and metal ions. In the synthesis, graphene sheets were first deposited on a Cu substrate by immersing a piece of copper foil into a graphene suspension. After being dried, the substrate was immersed into metal ion solution, resulting in nanoparticle-decorated graphene. In the process, due to the work function difference between Cu (4.67 eV) and graphene (4.7–5.0 eV), and the redox potential difference between Cu^{2+}/Cu and $\text{PtCl}_4^{2-}/\text{Pt}$, H_2PtCl_6 can be reduced to nanoparticles on graphene nanosheets. Moreover, the size and density of Pt nanoparticles dispersed on graphene can be tuned by changing the deposition time. Multilayer assemblies of hybrid Pt/graphene can also be obtained by repeating the graphene-coating and Pt-depositing processes.

In recent years, microwave-assisted process has also been applied to the synthesis of metal nanoparticle/graphene hybrids. Microwave irradiation can generate homogeneous and rapid heating, which has been used to prepare unsupported or supported metal nanoparticles.^{177–179} Ravishankar and co-workers¹⁸⁰ reported a rapid method to synthesize graphene-supported Pt nanoparticles by the coreduction of GO and PtCl_6^{2-} (H_2PtCl_6) using ethylene glycol as reducing agent under microwave irradiation. It was proposed that under

microwave irradiation, the platinum ions were first reduced to Pt^{2+} by EG, which can reduce GO. The defect sites generated from the removal of functional groups on GO surface during the reduction process can serve as anchoring centers for the formation of Pt nanoparticles. As shown in Figure 6a and b, the produced Pt nanoparticles with sizes of 2–3 nm are uniformly dispersed on the graphene surface. The authors also studied the effect of the amount of EG on the morphology of products. By comparing Figure 6a,b and insets, larger interparticle spacing was obtained when more EG (Figure 6b) was used. Figure 6c,d clearly shows the presence of Pt nanoparticles with (111) planes.

Impregnation methods or thermal reduction process were found to be useful for the synthesis of small and even subnanometer-sized Pt clusters.^{181–183} Yoo et al.¹⁸⁴ synthesized graphene-supported Pt nanoclusters with diameter smaller than 1 nm. In the synthesis, the mixture of presynthesized graphene sheets and $\text{Pt}(\text{NO}_2)_2(\text{NH}_3)_2$ was dispersed in ethanol and then dried in air at 40 °C for 1 h. Pt/graphene can be obtained by thermal reduction of the mixture in a hydrogen/argon stream at 400 °C for 2 h. In the mechanism study,¹⁸⁵ the authors found that when strong reductant of NaBH_4 was used instead of ethanol, no subnanometer Pt cluster but only large Pt nanoparticles were obtained. Therefore, only the gradual reduction process of Pt^{4+} , Pt^{2+} , and finally Pt^0 by weak reductant can produce tiny Pt clusters.

It should be pointed out that the experimental conditions have considerable effects on the morphologies and properties of Pt/graphene products. Although the above developed methods have been successfully applied to the syntheses of Pt/graphene

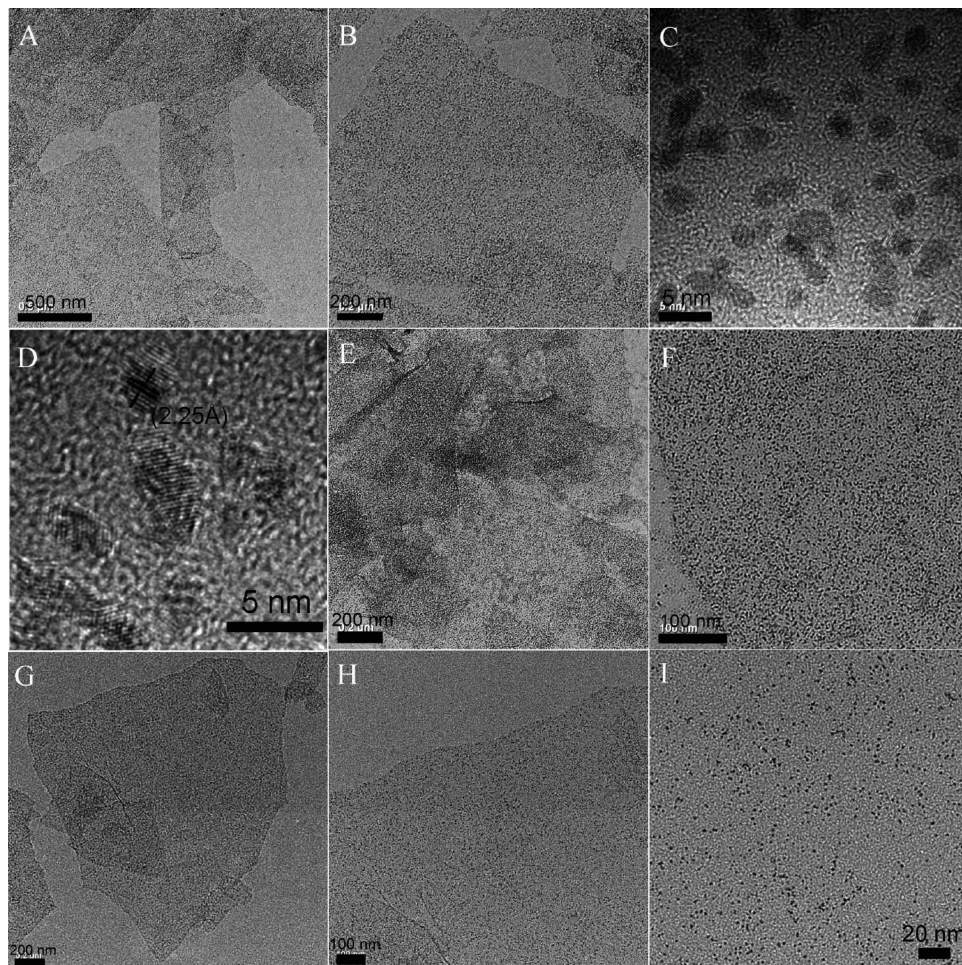


Figure 7. (A–C) TEM images of Pt/graphene (1 mL Pt precursor) at different magnifications. (D) HRTEM image of the Pt nanoparticles dispersed on graphene. (E,F) TEM images of Pt/graphene with relative high density of Pt nanoparticles (2 mL of Pt precursor) at different magnifications. (G–I) TEM images of Pt/graphene with relative low density of Pt nanoparticles (0.5 mL of Pt precursor) at different magnifications. Reprinted with permission from ref 186. Copyright 2010 American Chemical Society.

hybrids, some critical issues of the hybrids still remain, especially for their practical applications in fuel cells, including the poor distribution and aggregation of Pt nanoparticles on graphene surface, and the durability of the hybrids. To achieve the homogeneous distribution and improve the stability of Pt nanoparticles, surface-treatments of graphene by covalent or noncovalent functionalization have been proposed. Guo et al.¹⁸⁶ synthesized Pt/graphene hybrids by heating a water/EG solution of H_2PtCl_6 and graphene oxide in the presence of poly(methacrylic acid sodium salt) (PMAA). Figure 7A–D shows that 2.6 nm Pt nanoparticles were homogeneously dispersed on the graphene nanosheets. In this work, the PMAA plays an important role for the formation of uniform Pt nanoparticles with small size. PMAA can not only improve the stability of graphene sheets due to the strong hydrophobic interaction between them, but also stabilize the Pt nanoparticles as a protecting agent. Moreover, as shown in Figure 7E,F and G–I, the mass loading (density) of Pt nanoparticles deposited on graphene can be easily controlled by changing the ratio of Pt precursor to PMAA.

Poly(diallyldimethylammoniumchloride) (PDDA) is a widely used cationic polyelectrolyte, and it can be adsorbed on the surface of carbon nanotubes and graphene through $\pi-\pi$ and electrostatic interactions.¹⁸⁷ Previous studies found that

PDDA can be used as a kind of unique stabilizer for controlled synthesis of Pt/graphene.^{166,188,189} Graphene nanosheets with negative charge can be easily functionalized by positively charged PDDA through the electrostatic interaction, which can increase the stability of graphene in solution. On the other hand, PtCl_6^{2-} ions can be confined in the positively charged surface of PDDA-functionalized graphene and then be in situ reduced to Pt nanoparticles upon the addition of reducing agents. With this strategy, controllable deposition of Pt nanoparticles on graphene was realized by Qiu et al.¹⁹⁰ From the TEM characterization in Figure 8, the formed Pt nanoparticles are uniformly dispersed on graphene surface. The Pt loading density can be effectively adjusted by changing the ratio of PDDA-GO to the Pt precursor. As shown in Figure 8a–f, the Pt/graphene with Pt loading from 30 to 78 wt % was obtained when the ratio of PDDA-GO to H_2PtCl_6 varies from 1:1 to 1:8.5, whereas the particle size was maintained at ~4.6 nm. In another work,¹⁹¹ by using PDDA as both reducing agent and stabilizer, soluble graphene nanosheets were obtained from graphite oxide. The PDDA-functionalized graphene facilitated the in situ growth of highly dispersed Pt nanoparticles to produce Pt/graphene nanocomposites. Besides PDDA, thiolated graphene,¹⁹² poly(sodium styrene sulfonate),¹⁹³ and perfluorosulfonic acid-functionalized graphene¹⁹⁴ have also

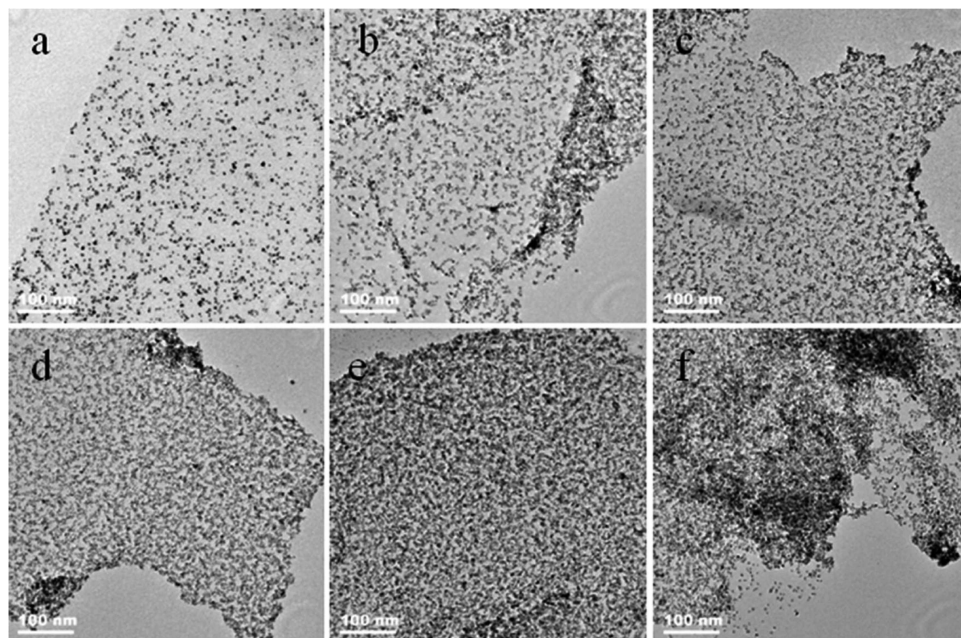


Figure 8. TEM images of the Pt/graphene-PDDA nanocomposites synthesized at different mass ratios of PDDA-GO to H_2PtCl_6 : (a) 1:1, (b) 1:1.5, (c) 1:2.5, (d) 1:3.5, (e) 1:6.0, and (f) 1:8.5. Reprinted with permission from ref 190. Copyright 2011 American Chemical Society.

been fabricated to improve the dispersion of Pt nanoparticles on graphene surface and their electrocatalytic performances.

To improve the catalytic properties, especially the stability of graphene-based nanocomposites, some recent research focused on the unique interfacial construction between Pt nanoparticles and graphene nanosheets. Kou et al.⁷¹ proposed an interesting route to deposit Pt nanoparticles and metal oxides on graphene surface to form stable metal–metal oxide–graphene triple junctions. The experimental and theoretical calculations indicated that the Pt nanoparticles supported at the Pt–indium tin oxide (ITO)–graphene triple junctions are more stable than those only dispersed on graphene. Such unique Pt–ITO–graphene junctions with large surface area, good particle distribution, and high electrical conductivity exhibited better catalytic properties than Pt/graphene and commercial Pt/C catalysts. Meanwhile, Huang and co-workers¹⁹⁵ found that by inserting carbon black (CB) into Pt/graphene, the formed Pt/rGO/CB hybrid structure showed greatly enhanced catalytic activity for oxygen reduction in comparison with the simple Pt/rGO hybrids. It was proposed that the presence of CB can effectively prevent the stacking of rGO sheets and thus improve the diffusion of O_2 molecules through rGO, resulting in the high electrocatalytic activity toward ORR.

2.2.2. Graphene-Supported Low-Pt Alloy Nanocrystals. Because of the low loading of Pt metal and bifunctional mechanism or the so-called ligand effect, graphene-supported Pt-based nanomaterials attract much attention. The synthetic strategies for Pt/graphene have also been applied to the preparation of Pt-based bimetallic or trimetallic nanostructure supported on GNs. Up to now, several kinds of important PtPd alloys/GNs have been prepared as efficient electrocatalysts for fuel cells.

2.2.2.1. PtPd/GNs. Among the Pt-based nanostructured materials, PtPd alloys are among the most interesting cathode catalysts because of their excellent stability and catalytic performance. In previous studies, various structured PtPd alloys have been synthesized.^{196–199} To synthesize PtPd/

graphene nanocomposites, methods similar to those described above for the preparation of Pt/graphene are usually used. To improve the dispersity of PtPd nanocrystals on graphene surface, GNs can be prefunctionalized with stabilizers. Guo et al.²⁰⁰ reported a wet-chemical method to prepare high-quality three-dimensional Pt-on-Pd bimetallic nanodendrites supported on polyvinylpyrrolidone (PVP)-functionalized graphene sheets, which can be used as an advanced electrocatalyst toward the methanol oxidation. In this method, PVP-functionalized graphene was first obtained under the reduction of hydrazine. Pd/GNs hybrids were then synthesized using HCOOH as reducing agent at room temperature. Finally, Pt-on-Pd nanodendrites supported on GNs were produced by heating the mixture of Pd/GNs suspension and Pt precursor in the presence of ascorbic acid as reducing agent. In another work, by using PDDA-functionalized GNs as supports, PtPd alloys with controlled compositions (Pd_4Pt_1 , Pd_3Pt_1 , Pd_2Pt_1 , and Pd_1Pt_1) have been synthesized under the reduction of EG.²⁰¹ The highly dispersed alloy particles on GNs exhibited composition-dependent catalytic activity for the ORR, higher performance from the alloys with higher Pt content. Meanwhile, a simple two-step electrodeposition method was also developed to construct PtPd/GNs nanostructures directly on electrode surface.^{202,203} In the first step, graphene oxide was chemically or electrochemically reduced and deposited on a glassy carbon electrode surface. PtPd alloy nanoparticles were then electrodeposited on the graphene-modified electrode. The as-synthesized hybrid catalysts exhibited high catalytic activities and stability for alcohol oxidation in alkaline media.

The electrocatalytic activity of nanoparticles is very sensitive to the surface electronic structure and the arrangement of surface atoms. Therefore, it is of great importance to synthesize Pt-based alloy nanoparticles with specific morphology and narrow size distribution. In the reported syntheses, most produced metal nanoparticles supported on graphene are spherical. Designing and synthesizing highly active Pt–Pd alloy nanoparticles templated by graphene with desirable structures

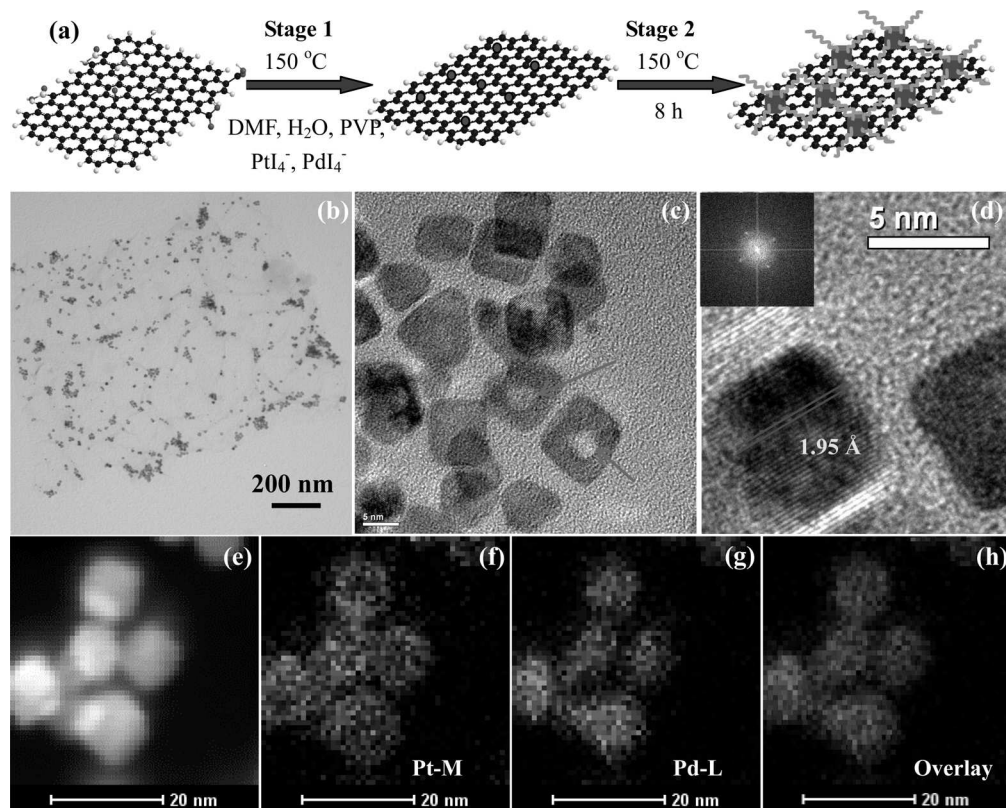


Figure 9. (a) Schematic illustration of the one-pot hydrothermal synthesis of PtPd alloy nanocubes supported on rGO. (b) TEM and (c,d) HRTEM images of the PtPd alloy nanocubes dispersed on rGO at different magnifications. The inset in (d) shows the FFT pattern of an individual PtPd nanocrystal. (e) The high-angle annular dark-field (HAADF)-STEM image of PtPd/rGO, and the corresponding elemental mapping of (f) Pt, (g) Pd, and (h) the overlay. Reprinted with permission from ref 72. Copyright 2013 American Chemical Society.

are still challenging. Recently, we developed a facile and general hydrothermal approach that could allow the one-pot fabrication of water-soluble and uniform single-crystalline PtPd alloy nanocubes supported on the reduced graphene oxide nanosheets (PtPd/rGO).⁷² This method could also be used to synthesize other water-soluble Pt- or Pd-based alloy nanocrystals with desirable morphology supported on rGO. As shown in Figure 9a, the synthesis includes two steps: (1) the reduction of GO and the nucleation of nanocrystals attached onto the surface of rGO sheets because of the strong interaction between them; and (2) the nuclei grew gradually into the cubic shape under the protection of PVP. From the TEM characterizations and element mapping shown in Figure 9b–h, PtPd nanocrystals with 82% nanocubes are uniformly distributed on the rGO surface. With a similar hydrothermal method, PtPd alloy concave nanocubes can also be in situ formed on the graphene surface.²⁰⁴

2.2.2.2. PtAu/GNs. Because of the inert property of gold in acid electrolyte and its excellent catalytic activity for CO oxidation, Pt–Au bimetallic catalysts can not only improve the adsorption/dissociation of alcohol in acid media and enhance the catalytic performance toward the oxidation of alcohol fuels, but also promote the durability of the catalysts.²⁰⁵ Therefore, binary PtAu nanomaterials are of special interest and importance as fuel cell electrocatalysts. Rao et al.¹⁵⁴ reported an EG reduction method to synthesize graphene-supported Pt–Au alloy nanoparticles with an average size of 4.5 nm. The Pt–Au alloys are well-dispersed on graphene surface and exhibit high electrocatalytic performance toward formic acid oxidation. By using PDDA-modified graphene as support, Pt–

Au alloy nanoparticles with a mean diameter of 3.2 nm were also synthesized by the NaBH₄ reduction method.²⁰⁶ With the electrodeposition method, Pt–Au nanoparticles were electrodeposited on graphene-decorated glassy carbon (GC) electrode at –0.4 V (versus SCE).²⁰⁷ The composition, size, and morphology of the formed Pt–Au particles can be easily controlled by adjusting the ratio of Pt and Au precursors in the reaction mixtures. As described above, nitrogen-doped graphene exhibit higher catalytic activity and thermal stability as compared to graphene. Therefore, N-graphene may be an excellent support for the deposition of metal nanocatalysts. Zhu and co-workers²⁰⁸ synthesized Pt₃Au/N-graphene with a wet-chemistry method under the assistance of microwave heating. The electrochemical measurements showed that the Pt₃Au/N-graphene nanocomposites have much higher electrocatalytic activities for methanol oxidation than do the Pt₃Au/graphene and commercial Pt/C catalysts.

2.2.2.3. PtRu/GNs. Among the bimetallic catalysts for fuel cells, PtRu alloys are considered to be the best anode catalysts for DMFCs, and they have been used in commercial fuel cells.^{209,210} Besides the intrinsic catalytic properties of catalysts, the used support also plays important roles in determining their catalytic performance. The dispersion and durability of catalysts can be improved by using a good support. Carbon materials, such as carbon black, carbon nanotube, and carbon nanofiber, are the traditional supports in fuel cells for the dispersion of electrocatalysts. Because of the high electronic conductivity and large surface area, graphene has also been studied as an efficient support for PtRu catalysts.^{211–214} Dong et al.²¹² synthesized graphene-supported PtRu nanoparticles by using the EG

reduction method, and they found that the PtRu/GNs exhibited enhanced efficiency for methanol and ethanol oxidation in comparison with the PtRu catalysts supported on Vulcan XC-72R carbon black. Under the assistance of supercritical carbon dioxide, Zhao et al.^{215,216} prepared graphene-supported ultrafine PtRu nanoparticles at low temperature. With the proposed route, the PtRu nanoparticles (~ 2.87 nm) can be uniformly distributed on the surface-functionalized GNs. Highly dispersed PtRu nanoparticles with an average size of 1.8 nm supported on graphene were prepared by a simple surfactant-free process,²¹⁷ in which the mixture of hydrogen hexachloroplatinate(IV) hexahydrate, ruthenium(III) chloride hydrate, and graphene nanosheets was treated at 300 °C under $N_2 + H_2$ (4%) atmosphere. To improve the dispersion and stability of PtRu nanoparticles on graphene sheets, Li et al.²¹⁸ prepared PtRu catalyst (ca. 2.0 nm) supported on PMo_{12} -functionalized graphene nanosheet by microwave irradiation method in ethylene glycol (EG) solution. Because of the negatively charged nature of PMo_{12} , the resulted hybrid catalyst exhibited higher catalytic activity and better cycle stability for methanol electrooxidation as compared to that of the unmodified PtRu/graphene catalyst.

Before the discovery of graphene, carbon black and carbon nanotubes were the main supports for electrocatalysts. Although graphene and carbon nanotubes have excellent properties as catalyst supports, their disadvantages will be present obviously when they are used singly. For example, the surface area of graphene sheets will be decreased during the electrochemical cycling due to the aggregates of nanosheets from van der Waals force and $\pi-\pi$ interaction. On the other hand, with CNTs alone as support, only the external surface of CNTs can be efficiently utilized for dispersing metal catalysts due to the small inner diameter and the usually closed tips. Recently, several studies focused on the hybrid supports composed of graphene and CNTs. Wang et al.²¹⁹ constructed a 3-D porous GNs-CNTs architecture as support for the deposition of PtRu nanoparticles. In the carbon hybrid, CNTs act as nanospacers to efficiently decrease the face-to-face aggregation of GNs. The porous structure provides large surface area for the immobilization of PtRu nanoparticles and facilitates the electrolyte and reactant diffusion, and thus increases the catalytic performance of the catalysts. In another study, Lv et al.²²⁰ synthesized an interesting GNs-N-doped CNTs (NCNTs) hybrid with graphene sheets grown inside the large inner cavities of the NCNTs through a one-step water-assisted CVD process. Figure 10a,b shows the TEM images of PtRu nanoparticles formed on multiwalled CNTs and GNs-NCNTs, respectively. Clearly, the aggregates of PtRu nanoparticles can be easily formed on CNTs (indicated by the circles). With the same reduction process, the produced PtRu nanoparticles in the size range of 2–4 nm are well dispersed on the GNs-NCNTs hybrid. The improved dispersion of PtRu nanoparticles was attributed to the nitrogen doping and the presence of graphene inside the carbon nanotubes.²²⁰ Benefiting from the hybrid structure, the PtRu/GNs-NCNTs exhibited enhanced catalytic performance and better long-term operation stability for methanol oxidation as compared to CNTs-supported PtRu catalysts. Woo et al.²²¹ designed another graphene–Vulcan carbon hybrid as support for PtRu nanoparticles. In the sandwich structure, the Vulcan carbon serves as a nano spacer to decrease the aggregation of graphene sheets and improve the electrocatalytic activity of the PtRu catalyst.

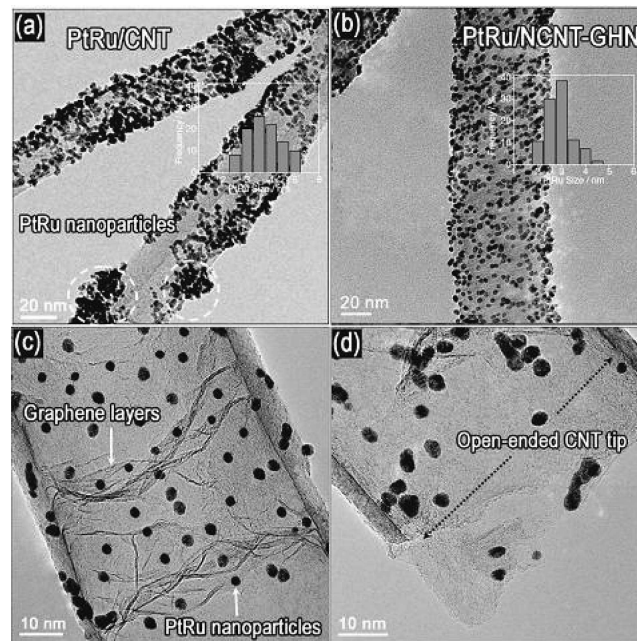


Figure 10. TEM images of PtRu nanoparticles supported on multiwalled CNTs (a) and GNs-NCNTs (b–d). The white circles in (a) show the PtRu aggregates on CNTs. The insets in (a) and (b) are the corresponding size-distribution histograms of the PtRu nanoparticles supported on CNT and NCNTs-GNs. Reprinted with permission from ref 220. Copyright 2011 Wiley-VCH.

2.2.2.4. Other Pt-Based Bimetallic Catalysts Supported on Graphene. In addition to the above Pt-based catalysts, other Pt-transition metal alloys supported on graphene have also been fabricated by the methods described above, such as PtCo/graphene,^{222–229} PtNi/graphene,^{230–236} PtFe/graphene,^{237–239} PtCu/graphene,^{240,241} PtSn/graphene,^{242,243} PtCr/graphene,²⁴⁴ PtAg/graphene²⁴⁵ PtIr/graphene,²⁴⁶ PtW, and PtMo/graphene,²⁴⁷ etc. For example, Guo et al.²³⁷ found that the annealing process can improve the catalytic activity of FePt/graphene composites for ORR. The ORR activity of FePt/graphene annealed at 100 °C for 1 h showed 2 times higher catalytic activity than that of the unannealed sample. The study demonstrated that graphene is indeed an effective support to improve the activity and durability of electrocatalysts. To avoid the aggregation and increase the stability of nanoparticles, Choi and co-workers²²⁹ prepared PtCo nanoparticles via an EG reduction method by using hexadecyltrimethylammonium bromide (CTAB)-functionalized graphene sheets as support. Similar to the unsupported Pt-based electrocatalysts, all of the studies showed that the Pt-based bimetallic nanocomposites supported on graphene exhibited higher catalytic activities than those of single Pt catalysts because of the synergistic effect.

2.2.2.5. Ternary Metal Composites Supported on GNs. Because of the catalytic activity and stability superior to that of bimetallic alloys, ternary metal catalysts have attracted much attention in recent years. Several methods have been reported to synthesize graphene-supported ternary metal composites as efficient catalysts for fuel cells.^{248–250} For instance, PtPdAu ternary alloy nanoparticles were synthesized on graphene nanosheets by a simple EG chemical reduction method.²⁵¹ As compared to the Pt/GNs and the bimetallic composites of PtPd/GNs and PtAu/GNs, the ternary nanoparticles have higher catalytic activity and stability for methanol oxidation. Qu and co-workers²⁵² developed a novel dual-solvothermal process

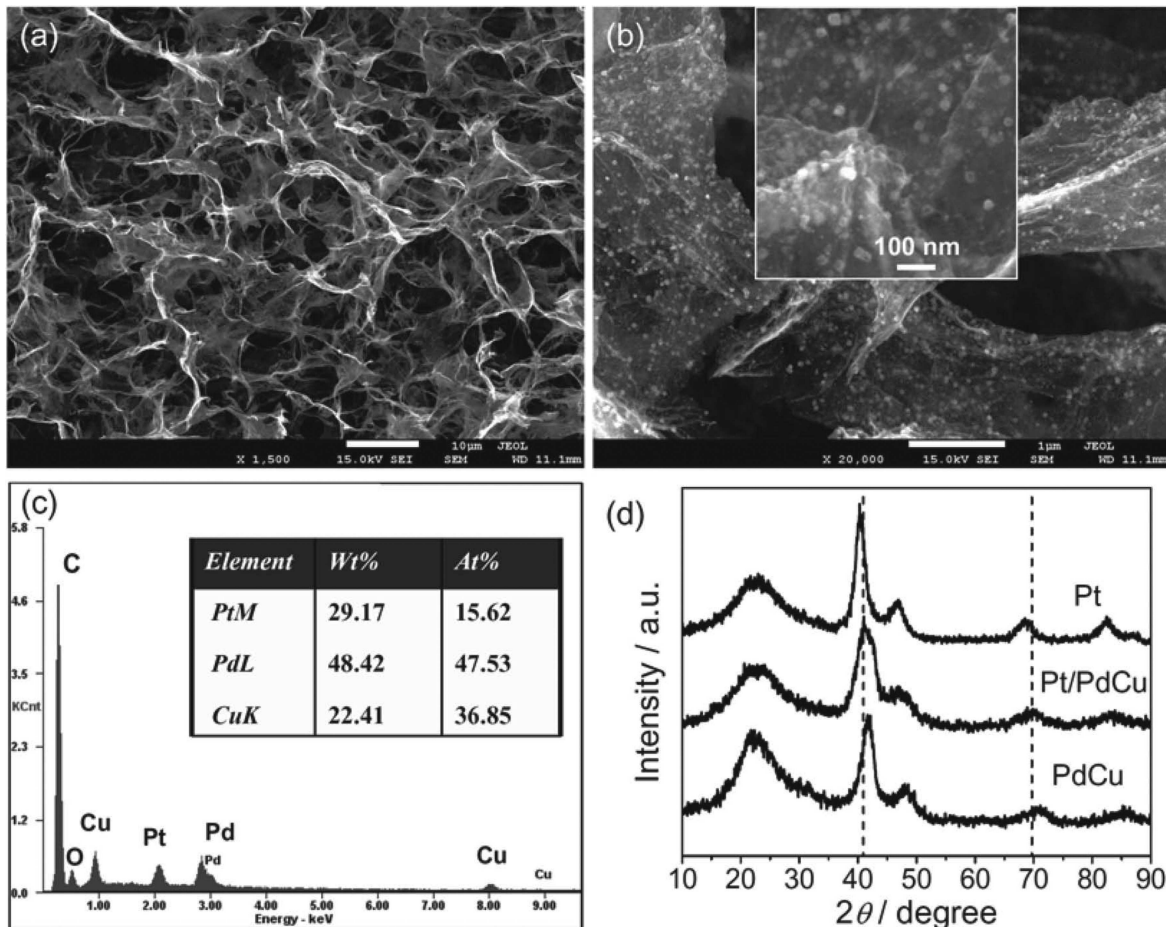


Figure 11. (a,b) SEM images of Pt/PdCu nanocrystals supported on a 3D graphene framework (3DGF). The inset in (b) is a magnified SEM image of the cubic Pt/PdCu on graphene nanosheets. (c) EDS and (d) XRD patterns of Pt, PdCu, and Pt/PdCu anchored on the 3DGF. Reprinted with permission from ref 252. Copyright 2012 Wiley-VCH.

to synthesize ternary Pt/PdCu nanoboxes supported on 3D graphene framework (3DGF), which can be used as an efficient anodic electrocatalyst for ethanol oxidation. In the reported method, hollow PdCu nanocubes on 3DGF were first synthesized by solvothermal treatment in EG at 160 °C. Ternary structure was then achieved by mixing the PdCu/3DGF with EG solution of H₂PtCl₆ and heating at 160 °C for another 3 h. As shown in Figure 11a,b, the formed Pt/PdCu nanoboxes with an average size of 30 nm are dispersed on the interconnected 3D porous network of graphene sheets. The energy dispersive spectroscopy (EDS) and XRD measurements shown in Figure 11c and d further indicate the presence of Pt/PdCu ternary nanocrystals.

2.3. Graphene-Supported Non-Pt Nanocatalysts

From above, Pt-based nanocrystals supported on graphene have been extensively studied because of their excellent catalytic properties and resistance to corrosion and oxidation. However, the high cost and limited reserve hinder the large-scale application of Pt-based catalysts and the wide commercialization of fuel cells. To reduce the cost of electrocatalysts and fuel cells, many studies on fuel cell electrocatalysts focus on the fabrication and development of nonprecious metal alternatives. Previous studies found that for graphene-supported non-Pt nanocatalysts, there exists a charge transfer process across the graphene–metal interface, which depends on the distance and the Fermi level difference between graphene and the supported

catalysts. Such charge transfer may be beneficial for the enhanced catalytic activities of graphene-supported catalysts, as exemplified by the catalysts of Co₃O₄/graphene,²⁵³ Fe₃O₄/graphene,²⁵⁴ Co_xS_{1-x}/graphene,²⁵⁵ MnCo₂O₄/graphene²⁵⁶ for ORR, and PdRu/graphene²⁵⁷ for methanol electrooxidation, etc. Graphene-supported noble and nonprecious metal electrocatalysts and their applications are summarized in Tables 2 and 3, respectively.

2.3.1. Pd-Based Nanocatalysts/GNs. Among the potential metal catalysts, Pd stands well as the Pt substitute, because it has similar properties, lower cost, and greater resistance to CO poisoning in comparison with Pt. First-principle calculations revealed that, as compared to Pt, Pd can interact with and bind more strongly to graphene surface because more interaction states and transmission channels can be produced between Pd and graphene, and Pd tends to grow into three-dimensional structures on GNs.^{258,259} During recent years, various methods have been developed to synthesize Pd-based nanocatalysts on graphene with different size, composition, and morphology. Similar to the preparation of nanocatalysts on other supports, Pd and Pd-based alloy nanocatalysts supported on graphene can be generally prepared through numerous synthetic routes, such as chemical reduction, electrochemical reduction, impregnation, and heat treatment, etc. Most of the syntheses are carried out by first preparing GO (or functionalized GO), followed by reducing GO and metal ions simultaneously with different strong or weak reducing agents,

Table 3. Graphene-Supported Nonprecious Metal Electrocatalysts and Their Applications

catalyst	preparation method	precursor	application	ref
FeTsPc ^a /GNs	chemical reduction	GO, N ₂ H ₅ OH, FeTsPc ^a	ORR in PBS	331
Fe/N-graphene	thermal treatment	GO, cyanamide, FeCl ₃	ORR in acid and alkaline	332
FePc ^b /N-graphene	thermal treatment	GO, ammonia, FePc ^b	ORR in alkaline	334
Fe/N-graphene	thermal treatment	GO, pentaethylenehexamine, FeCl ₃	ORR in acid	335
FeCN/N-graphene	thermal treatment	GO, NH ₃ , Fe(OAc) ₂ , phenanthroline	ORR in acid	336
Fe–N/rGO	thermal treatment	GO, NH ₃ , N ₂ H ₄ , dicyandiamide, FeCl ₃	ORR in acid/PBS	337, 338
(Fe–P) _n -MOF/rGO	solvothermal	GO, 4-(4-aminostyryl)pyridine sodium nitrite, TCPP, ^c FeCl ₃	ORR in alkaline	340
Fe ₃ O ₄ /N-graphene	hydrothermal/heat treatment	GO, iron acetate, polypyrrole	ORR in alkaline	254
Co(OH) ₂ /graphene	electrodeposition	GO, NH ₃ , N ₂ H ₄ , Co(No ₃) ₂	ORR in alkaline	348
Co ₃ O ₄ /(N–)rGO	hydrothermal	GO, Co(Ac) ₂ , NH ₄ OH	ORR/OER in alkaline	253
Co _{1-x} S/rGO	heat treatment	GO, TAA, ^d Co(OAc) ₂	ORR in acid	255
MnCo ₂ O ₄ /N-rGO	solvothermal	GO, Co(OAc) ₂ , Mn(OAc) ₂ , NH ₄ OH	ORR/OER in alkaline	256
Co–CoO/GNs	thermal decomposition	GO, Co ₂ (CO) ₈	ORR in alkaline	341
CoTAPP ^e /GNs	diazonium salt reaction	graphene, CoTAPP ^e	ORR in acid	353
Ni/GNs	chemical reduction/thermal treatment	GO, NiCl ₂	MOR in alkaline	366
Ni–Co/GNs	chemical reduction	GO, NiSO ₄ , Co(No ₃) ₂ , NH ₃ , N ₂ H ₄	EOR in alkaline	350
Ni(Co)O _x /GNs	chemical reduction	GO, Ni(No ₃) ₂ , CoCl ₂ , NaBH ₄ or N ₂ H ₄	MOR in acid	367
Ni(Cu)-α-MnO ₂ /GNs	hydrothermal	rGO, MnSO ₄ , KMnO ₄ , Cu(No ₃) ₂ , Ni(No ₃) ₂	ORR in alkaline	368
NiCo ₂ S ₄ /graphene	solvothermal	GO, Co(OAc) ₂ , Ni(OAc) ₂ , thiourea,	ORR in alkaline	363
Cu ₂ O/rGO	polyol reduction	GO, copper acetate, diethylene glycol	ORR in alkaline	373
CuO/N-rGO	aqueous process	GO, NH ₃ , CuCl ₂	ORR in alkaline	371
MnO ₂ /rGO	chemical reduction	GO, PSS, ^f MnSO ₄ , NH ₃ , H ₂ O ₂ , N ₂ H ₄	ORR in alkaline	378
MnO _x /GNs	hydrothermal	GO, N ₂ H ₄ , KMnO ₄ , MnSO ₄	ORR in alkaline	380
Ir _x V/rGO	polyol reduction	GO, IrCl ₃ , NH ₄ VO ₃ , ethylene glycol	ORR in alkaline	381

^aFeTsPc: iron tetrasulfophthalocyanine. ^bFePc: iron(II) phthalocyanine. ^cTCPP: 5,10,15,20-tetrakis(4-carboxyl)-21H,23H-porphine. ^dTAA: thioacetamide. ^eCoTAPP: cobalt[tetrakis(*o*-aminophenyl)porphyrin]. ^fPSS: poly(sodium 4-styrene sulfonate).

such as NaBH₄, trisodium citrate, polyol, K[Bet₃H], hydrogen gas, hydrazine hydrate, etc. A variety of Pd/graphene composites could be prepared by these processes.^{260–265} For example, Zhao and co-workers²⁶⁶ synthesized Pd nanoparticles supported on polypyrrole (PPy)-functionalized GNs. In the synthesis, the PPy-graphene was first prepared by an in situ radical polymerization method with graphene, pyrrole, and (NH₄)₂S₂O₈ precursors, and PdCl₄²⁻ was chemically reduced to Pd nanoparticles on the support by NaBH₄. In another case, Giovanni et al.¹⁸² prepared Pd/graphene hybrids by thermal exfoliation method in nitrogen or hydrogen atmosphere. In a typical process, the graphite oxide presynthesized by Hofmann method was dispersed in water containing palladium(II) chloride under ultrasonication. The mixed suspension was consequently dried in a vacuum oven to yield the metal doped-graphite oxide precursor powders. The thermal exfoliation of the dry precursor was carried out at 1000 °C for 12 min. The obtained product was then flushed repeatedly with pure nitrogen and subsequently inserted into a preheated reactor in nitrogen or hydrogen atmosphere to produce Pd/graphene hybrid material.

To improve the stability and dispersion of Pd nanoparticles, graphene or GO can be modified by functional groups before deposition of Pd nanoparticles. Liu et al.²⁶⁷ prepared Pd nanoparticles supported on manganese dioxide-modified rGO (MnO₂/rGO) by a chemical reduction method. The formed Pd nanoparticles are well-dispersed on the MnO₂/rGO support without aggregation, and the as-synthesized catalyst exhibited much higher electrocatalytic activity and stability as compared to the Pd/rGO, indicating the promoting effect of the MnO₂ functionalized on rGO. More recently, Chen and colleagues²⁶⁸ developed a facile aqueous-based method for well-dispersion of

~2 nm Pd nanoparticles on phosphonic acid calyx[8]arene functionalized graphene. Here, *p*-phosphonic acid calyx[8]-arene acts as both a noncovalent stabilizer for suspending 2D materials in water and also a surfactant for the decoration of Pd nanoparticles. In the chemical reduction methods, undesirable excessive reducing agents may increase the cost in mass production and contaminate the chemically reduced GO, which will also affect the electrocatalytic performance of the nanocomposite. Alternatively, electrochemical reduction is a facile and environmentally friend approach for the syntheses of Pd-based alloy nanocomposites.^{269,270} For instance, Yang et al.²⁶⁹ electrochemically prepared Au–Pd/GNs composites without the aid of any reducing reagent. The electrochemical reduction process can efficiently remove the oxygen-containing groups in GO, which was then modified with homogeneously dispersed AuPd nanoparticles in a good size distribution.

Nanomaterials with clean surface are very beneficial for their applications as active catalysts in fuel cells. However, nanocrystal surface is usually protected by stabilizer to keep them from agglomeration, which may heavily block their surface catalytically active sites and therefore lower the catalytic performance. Chen et al.²⁶² successfully prepared ultrafine Pd nanoparticles monodispersed on GO surface through a surfactant-free process. By taking advantage of the difference between the reduction potential of PdCl₄²⁻ and the oxidation potential of GO, Pd nanoparticles can be spontaneously produced on GO without the presence of additional reducing agent. From the TEM images shown in Figure 12, Pd nanoparticles with a uniform size of ~3.5 nm are monodispersed on the surface of GO, although no additional stabilizer was used. It was suggested that the strong anchoring effect between the Pd nuclei and the GO surface plays a key

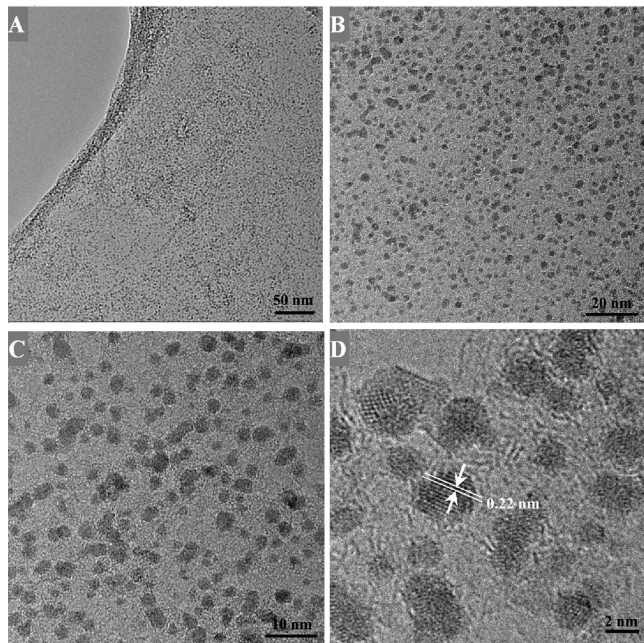


Figure 12. TEM images (A–C) at different magnifications and HRTEM micrographs (D) of Pd nanoparticles supported on GO. Reprinted with permission from ref 262. Copyright 2011 American Chemical Society.

role during the formation of Pd nanoparticles. Recently, highly dispersed Pd nanoparticles supported on graphene were also successfully synthesized by a one-step electrochemical codeposition approach.²⁷⁰ The as-synthesized hybrid composite provides a “clean” surface as a result of the reductant- and surfactant-free synthesis process. The electrochemical studies showed that the clean Pd/graphene materials have desirable catalytic performance for formic acid oxidation.

Similar to the Pt-based nanocatalysts, interesting behaviors have also been exhibited by the Pd-based alloys, which often provide better electrocatalytic properties than the pure metal alone due to the synergistic effect. On the basis of the density functional theory, Wang and Balbuena²⁷¹ predicted that ORR catalytic activity could be enhanced by coupling a metal M (M = Co, Ni, Cr, V, and others) with low occupancy of d-orbitals with another metal M' (such as M' = Pd, Au, and Ag) with fully occupied d-orbitals. The enhancement arises from decreasing the Gibbs free energy of the electron transfer steps with alloying. Meanwhile, previous studies indicated that palladium alone exhibits inert behavior toward alcohol oxidation in acidic medium, while it is highly catalytically active in alkaline solution.^{30,272} To improve the catalytic performance, Pd-based nanostructures have been designed by alloying Pd with other metals. Pd-based alloys supported on graphene could be prepared by chemical reduction procedure.^{257,273,274} For instance, Chai and co-workers²⁷⁵ prepared a novel hollow AuPd alloy nanostructure with a rough surface via a facile one-pot simultaneous reduction of Au(III) and Pd(II) with NaBH₄. The produced hollow nanospheres were then assembled on ionic liquid-grafted graphene sheets by electrostatic interaction to form AuPd/graphene hybrid nanomaterials under mild conditions. Recently, our group successfully synthesized PdAg nanorings supported on GNs by two steps.²⁷⁶ In the first step, Ag nanoparticles supported on graphene nanosheets (Ag/GNs) were prepared by refluxing an aqueous mixture of silver nitrate

and GO with sodium citrate as the reducing agent. In this process, the oxy-functional groups on GO surface can act as nucleation sites and facilitate seeding and growth of the silver nanoparticles. Taking advantage of the different standard reduction potential between Ag⁺/Ag (+0.7991 V vs NHE) and Pd²⁺/Pd (+0.915 V vs NHE), PdAg nanorings can be obtained through a galvanic replacement reaction between the Ag nanoparticles and Pd²⁺ on GNs. From the HRTEM images shown in Figure 13a,b, the highly crystalline ring-shaped

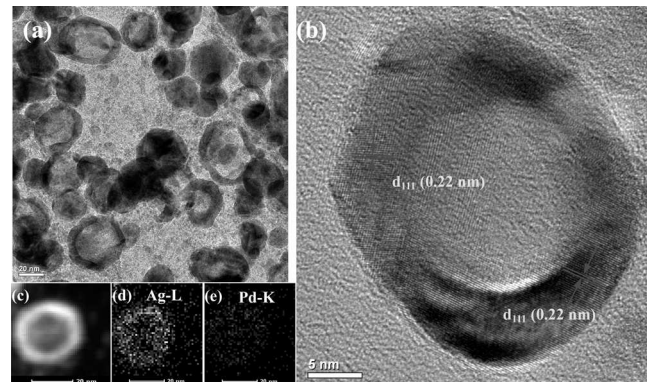


Figure 13. (a,b) HRTEM images of PdAg nanorings supported on GNs at different magnifications. (c) High-angle annular dark-field (HAADF) micrograph of single PdAg nanoring, and (d,e) the corresponding elemental mapping of Ag and Pd. Reprinted with permission from ref 276. Copyright 2013 Wiley-VCH.

nanocrystals can be observed clearly. The elemental mapping shown in Figure 12c–e indicates that Ag and Pd are evenly distributed in the shell of nanorings.

In addition, Pd-based ternary alloy composites supported on GNs have also been prepared via chemical reduction procedures. Awasthi²⁷⁷ reported a graphene-supported ternary Pd–Ru–Sn nanoalloy with a face centered cubic structure by a microwave-assisted polyol reduction method. Briefly, GNs, RuCl₃, PdCl₂, and SnCl₂·2H₂O were dispersed in ethylene glycol under ultrasonication. Ternary Pd–Ru–Sn/GNs composites were obtained by keeping the resulting mixture in a microwave oven for 5 min at 800 W power with a solution pH of 10. Meanwhile, impregnation and heat treatment (hydrogen atmosphere) provide simple, low-cost, high-efficient synthetic routes to synthesize highly dispersed Pd and Pd-based nanoparticles on GNs.^{278–280} Seo and co-workers²⁸¹ synthesized GNs-supported Pd and Pd₃Y nanoparticles through the impregnation method combined with a heat treatment under hydrogen gas. Both experimental and ab initio density functional theory calculations showed that the alloying with Y can significantly modify the electronic structures of Pd atoms. The up-shifted d-band center and thus enhanced bond strength of Pd–O in Pd₃Y/GNs make the Y-modified bimetallic Pd alloys good electrocatalysts for ethanol oxidation but not for ORR.

2.3.2. Au- and Ag-Based Nanocatalysts/GNs. Although Pt- and Pd-based nanomaterials are the most active catalysts, further exploring other noble metals, such as Au, Ag, and their alloys, as advanced catalysts is of significance in both fundamental research and practical applications in fuel cells. Bulk coinage metals are quite inert and show poor catalytic activity due to the filled d bands and thus the high activation barriers. Interestingly, it has been found that Au, Ag, and Cu

nanoclusters exhibit enhanced catalytic activities, which can be mainly ascribed to the high fraction of low-coordinated surface.^{48,49,51,282–284} However, the small size and high surface energy of metal clusters may induce their aggregation or dissolution during the practical applications as catalysts. Therefore, deposition of metal clusters on a stable support can improve their electrochemical stability. In recent years, increasing studies have been carried out on the Au- and Ag-based nanocatalysts supported on graphene.^{285–297} Among the used preparation methods, the most convenient way to prepare graphene-loaded Au or Ag nanocatalysts is based on the reduction of metal precursors' solution in the presence of graphene. Goncalves et al.²⁹⁸ prepared Au nanoparticles grown on graphene surface using a simple chemical method in aqueous medium. The study showed that the presence of oxygen functionalities at the graphene surface provide reactive sites for the nucleation and growth of gold nanoparticles; no gold nanoparticles can be formed at the totally reduced graphene surfaces. Pasricha et al.²⁹⁹ developed a facile method to prepare Ag/GNs through the reduction of metal precursors in graphene dispersion. In the synthesis, silver nanoparticles were first deposited on GO sheets via chemical reduction of silver ions in KOH aqueous solution. The formed Ag-GO films were then subjected to hydrazine treatment to remove the oxygen functionalities to reduce the defects and restore the sp^2 network. Ye's group³⁰⁰ used mixed reducing agents of EG and NaBH₄ to prepare Ag/graphene composites. The mixed reductants can not only keep the mild reaction environment, but also enhance the reducing strength to speed up the reaction. Moreover, by controlling the strength of the reducing agents, the chemical reduction of GO to graphene and the formation of Ag nanoparticles can be achieved simultaneously. Recently, Li and colleagues³⁰¹ reported a novel method for synthesizing a cylindrical piece of Au/graphene hydrogel with 1.08 cm in diameter and 1.28 cm in height through the self-assembly of Au/graphene sheets under hydrothermal conditions with GO as the graphene precursor, chloroauric acid as Au precursor, and triethylenetetramine as a reductant. Such 3D nanocomposites can improve the stability and the catalytic activity.

Metal nanoparticles produced by chemical reduction methods usually exhibit poor dispersion on GNs, and the hydrophobic GNs tend to aggregate through van der Waals interactions. With the assistance of positive charge polyelectrolyte and surfactant, noncovalent functionalization of GNs could be easily realized, which is favorable for the generation of Au or Ag nanoparticles uniformly dispersed on surface of GNs.^{188,302–304} Of them, Zhang et al.³⁰⁵ reported a facile one-pot method for synthesizing high-quality single-layer Ag-graphene composite by using commercially available poly-(N-vinyl-2-pyrrolidone) (PVP) as reductant and stabilizer. The size and loading of Ag nanoparticles can be tuned by changing the reaction time and the ratio between the precursors of AgNO₃ and GO. In another work, Li et al.³⁰⁶ synthesized 3,4,9,10-perylene tetracarboxylic acid (PTCA)-functionalized graphene/Au-ionic liquid through a chemical reduction route. In the first step, the conjugated ring of PTCA can interact with graphene sheets through the $\pi-\pi$ stacking and hydrophobic forces, and the –COOH groups on PTCA can separate the exfoliated graphene sheets and serve as uniformly distributed sites for nucleation of Au nanoparticles. The synthesized amino-terminated ionic liquid can interact with the –COOH of PTCA/graphene and in situ reduce HAuCl₄ to Au nano-

particles. The resulting hybrid nanocomposites showed high electrocatalytic activity for ORR. Different from the usual in situ growth of metal nanoparticles on graphene sheets from the corresponding metal salts, Huang et al.³⁰⁷ demonstrated a facile method to synthesize Au/GO(or rGO) composites just by mixing GO (or rGO) and presynthesized gold nanoparticles with surface functionalized by 2-mercaptopuridine. Through the noncovalent $\pi-\pi$ stacking and other molecular interactions, Au nanoparticles can be assembled on GO or rGO with controlled size, size distribution, and morphology. Cho et al.²⁹² reported an interesting procedure to synthesize gold nanostructures with well-defined shapes deposited on unfunctionalized rGO. First, a HAuCl₄ layer was coated on an rGO film supported on glass. The dried HAuCl₄ layer was reduced to gold nanocrystals with EG vapor at high temperature. The shape of the Au nanostructures can be tuned by changing the loading of HAuCl₄, triangular nanoplates produced at low Au loading, and hexagonal and pentahedron nanoplates formed at high Au loading.

In addition to the traditional chemical reduction method, other synthetic strategies, such as electrochemical deposition,^{290,308,309} photochemical synthesis,³¹⁰ and thermal reduction,¹⁸² have also used to synthesize Au (or Ag)/graphene composites. Fu and co-workers³¹¹ prepared Au/graphene nanocomposites by electrochemically reducing GO and Au (III) in ionic liquid, while Zhao et al.³¹² synthesized a novel 3D hybrid film composed of electrochemically reduced graphene oxide (ERGO)/silver nanoparticle via an electrochemical route. The formed nanocomposite has layer-by-layer structure decorated by Ag nanoparticles as separators. Electrochemical sensor fabricated from the nanocomposites demonstrated fast, stable, and reliable detection of hydrogen peroxide, which could be ascribed to the enlarged surface area of the 3D layered structure. Zhang's research group³¹⁰ developed a photochemical method for the one-pot synthesis and in situ assembly of fluorescent Au nanodots (AuNDs) on rGO sheets. In the method, the surface of rGO was prefunctionalized with 1-octadecanethiol (ODT), which served as template for the in situ synthesis and assembly of AuNDs. By using an electrostatic self-assembly and thermal annealing method, Zhou and co-workers³¹³ fabricated transparent and conductive Ag nanoparticles/rGO multilayer film. In the procedure, Ag nanoparticles with surface capped by poly-(diallyldimethylammonium-chloride) were first synthesized. Monolayer composite of Ag nanoparticles/GO was prepared by immersing a pretreated and hydroxylated quartz substrate in the silver and GO colloid solution successively. Multilayer composites can be synthesized by repeating the adsorption cycles. The obtained films were thermally reduced to Ag nanoparticles/rGO.

Graphene is an ideal support for dispersion of metal nanoclusters, even for the naked particles, which is very beneficial for their application as electrocatalysts. Tang and co-workers demonstrated a simple strategy to grow Au nanoclusters with clean surface on rGO sheets without any additional protecting and reducing agents.⁵⁰ In a typical reaction, 1.8 nm gold nanoclusters can be formed on rGO sheets by mixing HAuCl₄ and presynthesized rGO solution. From the SEM and TEM images shown in Figure 14, the produced Au nanoclusters with monodisperse size are uniformly dispersed on the surface of rGO sheets, and no clusters can be formed outside the rGO. According to the proposed mechanism, negative-charged rGO can adsorb

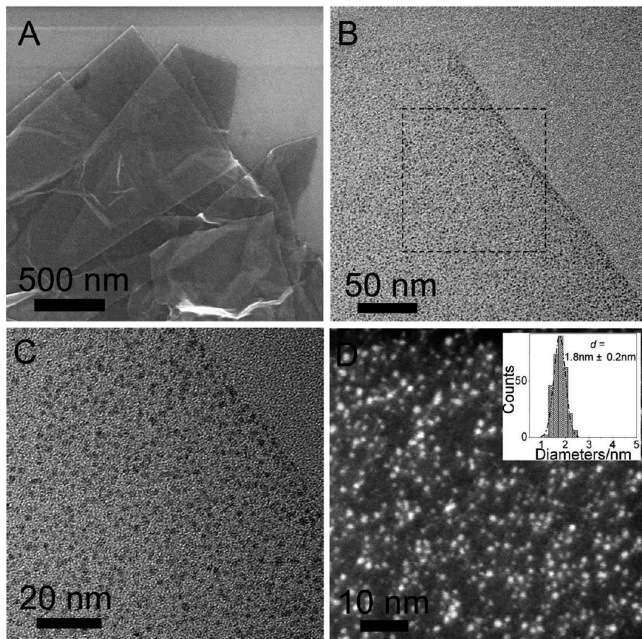


Figure 14. (A) SEM, (B,C) TEM, and (D)HAADF of Au nanoclusters supported on reduced GO. Inset in (D) is the size histogram of gold clusters with an average diameter of 1.8 ± 0.2 nm. Reprinted with permission from ref 50. Copyright 2012 American Chemical Society.

strongly the positive Au(III) ions, and most Au(III) ions may coordinate with the heteroatoms (N) at the defects of rGO sheets. Because of the electron-donor property of rGO sheets, the anchored Au(III) ions can be reduced to clusters on the surface of rGO. The prepared Au/rGO hybrid exhibited excellent electrocatalytic performance for ORR with onset potential comparable to that of commercial Pt/C catalyst.

The above syntheses are based on chemical processes. Recently, Chen and co-workers³¹⁴ reported a physical method for depositing aerosol Ag nanocrystals onto GO sheets by using electrostatic force directed assembly (ESFDA) technique. Figure 15 shows the schematic diagram of the preparation of aerosol Ag nanocrystals and the subsequent ESFDA process. Ag nanoparticles were synthesized with physical vaporization of Ag wire by using arc plasma source kept between a tungsten cathode and a graphite anode. The produced aerosol was carried by inert gases to an electric field between two electrodes. One electrode is the grounded metal tubing for

introducing the Ag aerosol. Another electrode composed of TEM grid containing GO sheets was applied with a direct current voltage. When a DC voltage was applied to the GO/TEM grid, the oppositely charged Ag aerosol nanocrystals can be assembled onto the GO surface.

2.3.3. Fe-Based Nanocatalysts/GNs. Advantages in low cost, recycling capability, and excellent catalytic activity of Fe-based nanomaterials dispersed on carbon supports render them good electrocatalysts for the ORR in fuel cells. FeN_x and FeC_x materials, including macrocycles and chelates supported on carbon materials, exhibited excellent catalytic activities for ORR in acidic media.^{63,315–321} In the early days, the iron-based catalysts were prepared by depositing macrocycles on a carbon support and pyrolyzing the product in inert atmosphere. In 1989, Yeager and co-workers³²² found that the compounds can be obtained from simple N- and metal-containing precursors. From then on, Fe-based catalysts have been successfully synthesized through high-temperature pyrolysis of iron complexes or procedures of iron salts and nitrogen-rich compounds.^{323–330} Since the discovery of graphene in 2004, monolayer or multilayer graphene or its oxide has been widely utilized as supports for FeN_x catalysts.

Noncovalent functionalization of GNs with iron tetrasulfophthalocyanine (FeTsPc) was achieved not only to prevent the aggregation of GNs but also form an efficient electrocatalyst with the maximum power density close to that of Pt/C cathode.³³¹ Parvez et al.³³² developed a cost-efficient synthesis of N-doped graphene (NG) by using cyanamide as a nitrogen source, with which high and controllable nitrogen contents can be realized after pyrolysis. They found that the NG decorated with 5 wt % Fe nanoparticles exhibited enhanced catalytic performance for ORR with $4e^-$ transfer process, large current density, superior stability, and high tolerance to methanol crossover in both alkaline and acidic solutions. Among the FeN_4 macrocycles, iron(II) phthalocyanine (FePc) attracted much attention due to its best catalytic performance for ORR.³³³ However, the poor electron conductivity and easy aggregation largely limit its practical application in fuel cells. Recently, Hou and co-workers³³⁴ studied the ORR catalytic activities of FePc supported on GO, rGO, and N-doped GNs(N-GNs) and found that the $\text{FePc}/\text{N-GNs}$ exhibited the best catalytic performance for ORR. It should be noted that most of the N-doped graphene and nonprecious catalysts supported on graphene are only catalytically active in alkaline media, which limits their application in acidic fuel cells. Therefore, developing efficient FeN_x/GNs catalysts working in acidic solutions is very important for their practical applications. Recently, Kamiya et al.³³⁵ reported a one-pot synthesis of graphene sheets modified by iron and nitrogen in a much shorter heat-treatment period (45 s) as compared to the long-duration heat treatment in the pyrolysis-based methods (\sim a couple of hours). In the electrocatalytic studies in 0.5 M H_2SO_4 , it was found that the synthesized Fe–N/graphene exhibited much enhanced catalytic activity for ORR as compared to the N-graphene and Fe-graphene. This study suggests that the atomic iron coordinated with N, that is, Fe–N/graphene hybrid, served as the active reaction center for ORR. In another study, Tsai and co-workers³³⁶ reported carbon-containing iron nitride nanoparticles (FeCN) supported on N-GNs, which were synthesized through a chemical impregnation and thermal treatment process. As compared to the N-GNs, FeN , and FeN/C , the $\text{FeCN}/\text{N-GNs}$ showed superb performance in ORR with the highest stability and

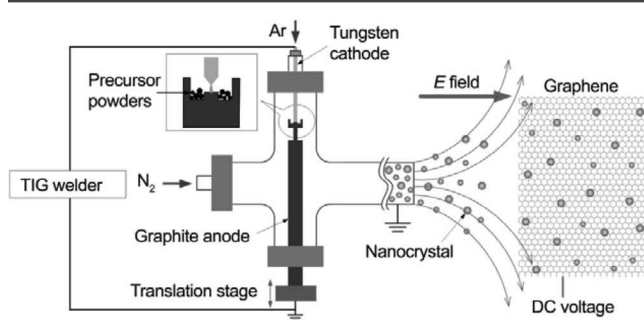


Figure 15. Schematic diagram of the synthesis of Ag aerosols using a mini-arc plasma reactor and the subsequent deposition of the Ag nanocrystals onto GO sheets through electrostatic force directed assembly (ESFDA) technique. Reprinted with permission from ref 314. Copyright 2009 Springer.

almost four-electron transfer reaction. The Fe–N–C catalytic active sites in the FeCN/N-GNs may be responsible for its enhanced catalytic activity. Through a thermal treatment of a mixture of iron salt, graphitic carbon nitride (gC_3N_4), and rGO, Fe–N-GNs nanostructures have also been successfully prepared and showed promising ORR activities.^{337–339}

Recently, Jahan et al.³⁴⁰ fabricated a hybrid metal organic framework (MOF) by reacting the pyridine-functionalized graphene with iron-porphyrin, which possesses high electrocatalytic activity for ORR. The synthetic routes to make graphene-porphyrin MOF are shown in Figure 16. In the first

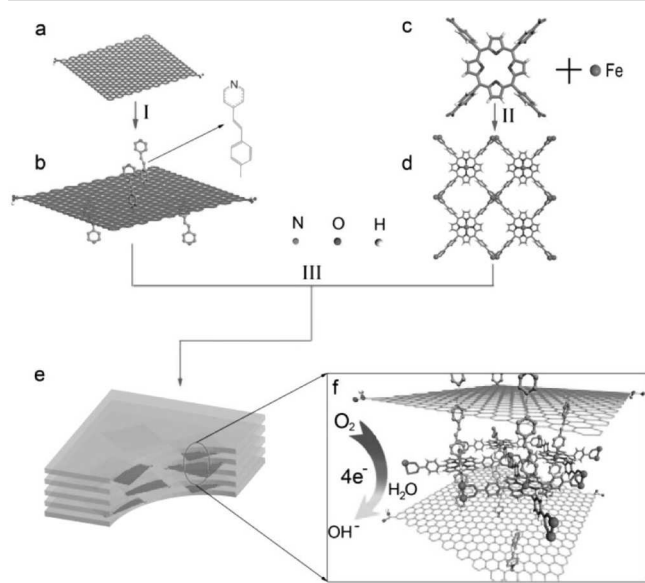


Figure 16. Schematic of the chemical structures and synthetic routes to prepare graphene-porphyrin MOF: (I) G-dye synthesized from rGO sheets via diazotization with 4-(4-aminostyryl) pyridine, (II) $(\text{Fe}-\text{P})_n$ MOF synthesized via reaction between TCPPs and Fe ions, and (III) $(\text{G-dye-FeP})_n$ MOF formed via reaction between $(\text{Fe}-\text{P})_n$ MOF and G-dye. Reprinted with permission from ref 340. Copyright 2012 American Chemical Society.

step, through diazotization with 4-(4-aminostyryl) pyridine, rGO was functionalized by donor- π -acceptor dye molecules terminated with pyridinium moieties. Meanwhile, MOF structure $((\text{Fe}-\text{P})_n$ MOF) was constructed via the reaction between 5,10,15,20-tetrakis (4-carboxyl)-21H,23H-porphyrin (TCPP) and Fe^{3+} ions. Finally, $(\text{G-dye-FeP})_n$ MOF was formed through the reaction between G-dye and $(\text{Fe}-\text{P})_n$ MOF. In the synthesis, the addition of rGO can change the crystallization process of iron-porphyrin in the MOF, and therefore increase its porosity, enhance the electrochemical charge transfer rate of iron-porphyrin, and show efficient four-electron ORR activity.

Besides iron complexes, iron oxide is also a class of effective alternative catalysts for ORR. By depositing on graphene support, the degradation of metal oxide catalysts suffering from the dissolution, sintering, and agglomeration in electrochemical operation can be significantly improved. Recent studies also revealed that the synergistic chemical coupling effects between graphene sheets and metal oxides are beneficial to their electrocatalytic activities.^{253,341} Wu et al.²⁵⁴ synthesized three-dimensional $\text{Fe}_3\text{O}_4/\text{N}$ -graphene networks via hydrothermal assembly and thermal treatment route. In the study, the novel 3D N-doped graphene aerogels can provide rich macroporosity

and multidimensional electron transport pathways, which is very beneficial for their application as catalyst supports. Actually, the electrochemical studies showed that the 3D $\text{Fe}_3\text{O}_4/\text{N}$ -graphene hybrid exhibited a more positive onset potential, higher cathodic current density, lower H_2O_2 yield, and higher electron transfer number for the ORR in alkaline electrolyte in comparison with the Fe_3O_4 nanoparticles supported on N-doped carbon black or N-doped graphene sheets.

2.3.4. Co-Based Nanocatalysts/GNs. Cobalt-based nanostructures supported on graphene have been proven to be a class of efficient electrocatalysts for ORR and have attracted tremendous attention in both experimental and theoretical scientific communities.^{342,343} From density functional calculations, Mao et al.³⁴⁴ found that after optimization the center of the hexagonal ring in graphene sheets is the most stable site for Fe, Co, Ni to stay, and the system of Co adatom on graphene exhibits metallic electronic structure. Recently, Olson and co-workers³⁴⁵ studied the selectivity of Co-based ORR catalysts in the presence of methanol and formic acid by using experimental and theoretical analyses. It was found that noncompetitive reaction adsorption process is present in the mixed methanol/ O_2 because O_2 is preferentially adsorbed on the $\text{Co}-\text{N}_x$ type sites, whereas the adsorption of methanol mainly occurs on graphitic type surface sites. However, there exists a competitive reaction adsorption process for the formic acid/ O_2 mixture as both O_2 and formic acid have a tendency to be adsorbed on the $\text{Co}-\text{N}_x$ type sites. As efficient ORR electrocatalysts, $\text{Co}_3\text{O}_4/\text{GNs}$ nanostructures have been studied recently from their electronic structures to their ORR catalytic performances. Wang et al.³⁴⁶ studied the chemical, electronic, and structural properties of Co_3O_4 nanocrystals supported on N-doped graphene sheets ($\text{Co}_3\text{O}_4/\text{N-GNs}$) by spatially resolved X-ray absorption near edge structure (XANES) spectroscopy and chemical imaging. The authors found that due to the strong covalent interaction between graphene sheets and Co_3O_4 , the Co^{3+} in the hybrid was partially reduced to Co^{2+} , and the reduction varies spatially on and among individual Co_3O_4 nanocrystal-graphene sheets. Meanwhile, nitrogen sites on graphene were found to be the major and important anchoring sites for Co_3O_4 nanocrystals in addition to the carbon and possibly oxygen sites.

Deposition of Co and Co-based nanoparticles onto graphene sheets as efficient electrocatalysts has been demonstrated theoretically and experimentally in recent years. The reported methods include pulsed laser deposition, chemical deposition, wet chemical and heat treatment, electrodeposition, etc. The various types of physical and chemical methods can provide different configurations and spaces to synthesize graphene-supported Co-based nanomaterials with desired morphology and tunable properties. As an important electrochemical active material, a great deal of interest has been focused on $\text{Co}(\text{OH})_2$ material. Zhu and co-workers³⁴⁷ designed a facile and straightforward soft chemical strategy to deposit $\text{Co}(\text{OH})_2$ nanoparticles on graphene sheets at a low temperature (approximately 83 °C) in a water-isopropyl alcohol system by utilizing Na_2S as a precursor. Wu et al.³⁴⁸ fabricated graphene–cobalt hydroxide composite by casting graphene suspension on a GC electrode first and subsequent electrodeposition of $\text{Co}(\text{OH})_2$ from $\text{Co}(\text{NO}_3)_2$ solution. The hybrid exhibited efficient four-electron O_2 reduction at lower overpotential as compared to the two successive two-electron processes of ORR on only graphene modified GC electrode.

Cobalt oxides (sulfides) are promising alternative electrocatalysts, but metal oxides frequently suffer from dissolution, sintering, and agglomeration during their electrochemical operation, which can result in catalyst degradation. When Co oxides are deposited on graphene nanosheets, the low intrinsic electrical conductivity of metal oxides can be remarkably improved, which favors their electrocatalytic activities. Meanwhile, the synergetic chemical coupling effects between graphene and the metal oxides (sulfides) are also beneficial to the enhanced electrocatalytic activity of the hybrid nanomaterials. The composites of flexible and electrically conductive graphene anchored with nanostructured Co_3O_4 particles can efficiently utilize the combinative merits of nanosized Co_3O_4 and graphene.³⁴⁹ On the other hand, the functional groups presented on the surface of GO, such as $-\text{OH}$, $-\text{COOH}$, and epoxides, can interact with metal precursors and thus facilitate the nucleation and formation of oxide nanoparticles. Dai's group has synthesized a series of nanocomposites consisting of Co_3O_4 ,²⁵³ Co_{1-x}S ,²⁵⁵ and MnCo_2O_4 ²⁵⁶ nanocrystals grown on GNs as excellent ORR electrocatalysts. For instance, controlled nucleation of Co_3O_4 on GO sheets was achieved by the slow hydrolysis $\text{Co}(\text{OAc})_2$ in ethanol/ H_2O system and subsequent hydrothermal reaction.²⁵³ It was found that the catalytic performance of the hybrid can be greatly enhanced by adding NH_4OH during synthesis to afford N-doping in graphene. Similar to ORR catalyzed by a commercial Pt/C catalyst, the obtained $\text{Co}_3\text{O}_4/\text{N}$ -doped graphene favored the efficient four-electron oxygen reduction process. They also successfully fabricated well-defined MnCo_2O_4 /graphene nanocomposite using the similar synthetic protocol mentioned above.²⁵⁶ The produced nanocomposites showed high electrocatalytic activity and long stability in alkaline media and therefore may be advanced electrocatalysts with low-cost for energy conversion and storage. The $\text{Co}_{1-x}\text{S}/\text{GNs}$ hybrids synthesized via a low-temperature solution-phase reaction followed by a high-temperature annealing step also showed unprecedented high ORR catalytic performance among all of the studied cobalt chalcogenide catalysts in acid medium.²⁵⁵

Recently, Sun and co-workers³⁴¹ synthesized Co nanoparticles assembled on graphene sheets with a layer of CoO formed on the surface of Co (Co-CoO/GNs). By controlling the oxidation extent, a series of Co-CoO/GNs were obtained with different particle size and thickness of CoO shell. The results demonstrated that the optimized Co-CoO/GNs hybrid has a comparative activity and better stability than the commercial Pt/C and may serve as a promising alternative catalyst for the ORR in alkaline solutions. The authors also found that the thickness of the CoO layer has an effect on the catalytic activity of the Co-CoO/GNs, and the hybrid with a 1 nm CoO shell exhibited the best activity. In addition to monometallic Co nanoparticles, bimetallic materials of cobalt and other metals were also reported as advanced non-noble electrocatalysts. For instance, Wang et al.³⁵⁰ synthesized non-noble Ni-Co/graphene electrocatalysts through a simple solution synthesis method by using hydrazine hydrate as a reducing agent and ethylene glycol as a solvent. As compared to the Ni/graphene catalyst, the Ni-Co/graphene has higher catalytic activity and better stability for ethanol electrooxidation.

Carbon-supported cobalt/nitrogen (Co-N/C) materials have attracted increasing attention due to their promising catalytic activity toward the ORR, along with the utilization of abundant, inexpensive precursor materials. Previous studies

indicated that the high temperature heating treatments during catalyst synthesis can remarkably enhance the electrocatalytic activity as well as the stability of the Co-N/C materials.^{351,352} Similarly, graphene functionalized with transition metal macrocycle compounds have been fabricated as good alternatives to Pt-based catalysts. Kim et al.³⁵³ prepared cobalt[tetrakis(*o*-aminophenyl)porphyrin] (CoTAPP) covalently anchored carbon nanomaterials (graphene, single-walled carbon nanotubes (SWCNTs), and multiwalled carbon nanotubes (MWCNTs)) via diazonium salt reactions and compared their electrocatalytic activity for the ORR. It was found that among the materials, graphene anchored with CoTAPP exhibited the most efficient electrocatalytic performance for ORR, further illustrating the advantage of graphene as carbon support.

2.3.5. Ni-Based Nanocatalysts/GNs. Nickel is a kind of low cost, relatively abundant material that is used extensively in numerous industrial applications. Among non-noble metals, Ni is a versatile catalytic material due to its electrochemical stability and resistance to poisoning. Ni can be easily converted to $\text{Ni}(\text{OH})_2$, and the $\text{Ni}^{2+}/\text{Ni}^{3+}$ redox centers show high catalytic activity toward oxidation of alcohols in alkaline media.^{354,355} As one of the alternatives of Pt, many Ni-based catalysts, such as pure nickel,^{356–358} nickel alloys,^{359–363} nickel complexes,³⁶⁴ and nickel hydroxides,³⁶⁵ have been successfully performed to fabricate new anode and cathode catalyst systems.

As compared to other carbon materials, graphene is more suitable to immobilize guest nanoparticles due to the large contact area from its planar structure. In recent years, chemical reduction and heat treatment have been used to synthesize Ni-based materials supported on graphene. For example, Zhang and co-workers³⁶⁶ prepared Ni nanoparticles anchored on graphene nanosheets by reducing GO and Ni^{2+} ions in one pot with hydrazine and the following heat treatment at high temperature (300–700 °C). The Ni/GNs obtained at 500 °C demonstrated the highest activity and stability for methanol electrooxidation in an alkaline electrolyte due to its small size and surface oxygen species. In another study, Elzatahry et al.³⁶⁷ synthesized nickel oxide and cobalt oxide-graphene nanocomposites and investigated their electrocatalysis for methanol oxidation in acidic media. Recently, Lambert et al.³⁶⁸ reported an interesting work on the simple syntheses of graphene-Ni- α - MnO_2 and graphene-Cu- α - MnO_2 nanowire blends. The specific activities and half-wave potentials of the hybrid materials for ORR exhibited values comparable to that of the commercial 20% Pt/C benchmark catalyst. However, the poor electrical conductivity of nickel oxides, hydroxides, and its oxidized NiOOH form may restrict their catalytic performance to some extent. Therefore, much work has been focused on using different additives to improve the electrocatalytic property of nickel, among which ethanol electrooxidation by Pd-Ni,³⁷ Cu-Ni,³⁶⁹ and Ni-Zn³⁷⁰ in alkaline solution has been reported.

2.3.6. Other Non-noble Nanocatalysts/GNs. Besides the Pt-free nanomaterials supported on graphene mentioned above, other non-noble nanocatalysts/GNs have also been investigated as electrocatalysts for fuel cells.^{371,372} Yan et al.³⁷³ reported a facile method to prepare ~4 nm Cu_2O nanoparticles dispersed on rGO by reducing copper acetate with diethylene glycol as both solvent and reducing agent. The $\text{Cu}_2\text{O}/\text{rGO}$ composite exhibited high ORR activity and excellent tolerance to CO and methanol in alkaline medium. MnO_x nanomaterials have also been found to be efficient ORR electrocatalysts.^{374–376} Cheng

et al.³⁷⁷ found that the catalytic activities of MnO_2 for ORR in alkaline solution depend strongly on the crystallographic structures, with the order of α - > β - > $\gamma\text{-MnO}_2$. Gao and co-workers³⁷⁸ synthesized MnO_2/rGO composites by a polymer-assisted chemical reduction method and found that the hybrid has excellent catalytic property for ORR in alkaline media with a $4e^-$ process. In another work,³⁷⁹ Mn_3O_4 nanoparticles were anchored in the ionic liquid-modified rGO nanosheets by a facile solution-based growth mechanism. Lee et al. found that the hybrid with a higher Mn_3O_4 (52.5%) content showed ORR catalytic activity with the inefficient two-step, two-electron pathway. The ORR mechanism of the hybrid with a lower Mn_3O_4 (19.2%) content, however, is similar to a Pt/C catalyst with a one-step, four-electron pathway. Here, the ionic liquid can not only improve the conductivity of the hybrid, but also enhance the electrocatalytic activity of the system. In the following study, Wu et al.³⁸⁰ synthesized graphene-supported manganese oxides (MnO_x) with different crystalline structures and morphologies. The authors found that the catalytic activities of the hybrid materials for ORR vary in the sequence: $\alpha\text{-MnO}_2$ nanowire > amorphous MnO_x nanoparticles > $\beta\text{-MnO}_2$ microprism. The $\alpha\text{-MnO}_2$ nanowire exhibited the highest catalytic property for four-electron reduction of O_2 in 0.1 M KOH solution and highest durability among the materials.

As an important transition-metal catalyst, Ir-based binary and ternary alloys have been studied as anode and cathode electrocatalysts for fuel cells. Recently, we synthesized iridium–vanadium bimetallic nanoclusters dispersed on rGO nanosheets through a facile “surfactant-free” method (Figure 17a) and studied their electrocatalytic activities for ORR in

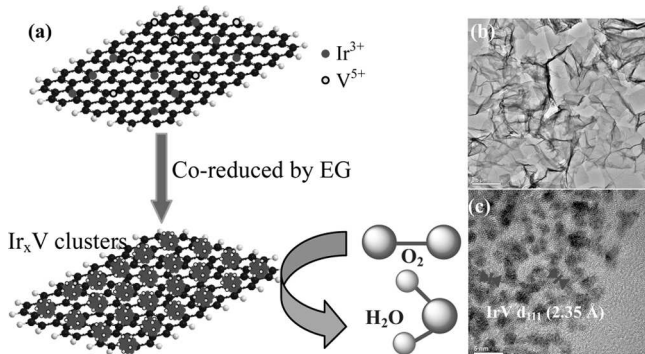


Figure 17. (a) Schematic illustration of the synthesis of IrV nanoclusters and their application for the oxygen reduction reaction. (b,c) HRTEM images of the Ir_2V bimetallic nanoclusters assembled on rGO sheets at different magnifications. The scale bars are 500 and 5 nm, respectively, in (b) and (c). Reprinted with permission from ref 381. Copyright 2013 Royal Society of Chemistry.

alkaline electrolyte.³⁸¹ As shown in Figure 17b and c, the as-synthesized IrV nanoclusters are uniformly dispersed on rGO sheets, and each IrV cluster has high-quality single-crystalline nature. The overall average core diameter of the clusters is 2.02 ± 0.02 nm, and the EDX showed the presence of both Ir and V. The electrochemical studies showed that the IrV/rGO hybrids exhibited composition-dependent catalytic activity for ORR and the $\text{Ir}_2\text{V}/\text{rGO}$ clusters displayed the highest catalytic performance.

2.4. Graphene-Supported Metal-Free Electrocatalysts

Metal-based hybrids have exhibited significantly high electrocatalytic activities in the aforementioned studies as anode and cathode catalysts. However, the metal-based electrocatalysts often suffer from some disadvantages, such as high cost, poor durability in strong acid or base, and so on. Therefore, developing fully metal-free electrocatalysts is of great importance for the wide commercialization of fuel cells. Graphene-supported metal-free electrocatalysts and their applications are summarized in Table 4. As discussed above, heteroatom-doped graphene is one of the most studied metal-free nanocatalysts for oxygen reduction reaction (ORR) in fuel cells.^{382–389} Although it is still a challenge to determine the exact active sites of heteroatom-doped graphene, many researchers have proved that the heteroatom doping can induce the charge redistribution of graphene. It was proposed that the dopant (regardless of whether it has a higher (like N, S) or lower (like B) electronegativity than carbon) could create charged sites favorable for O_2 adsorption, and thus induce the intramolecular charge transfer. Recently, carbon hybrid materials combining heteroatom-doped graphene with carbon nanotube (CNT) have been reported as an important class of metal-free nanocatalysts.³⁹⁰ For example, Yu and co-workers³⁹¹ designed a mildly hydrothermal process to synthesize the hybrid composite of nitrogen-doped carbon nanotube supported on nitrogen-doped graphene (NG-NCNT) by using graphene oxide (GO), oxidized multiwalled carbon nanotube (OCNT), and ammonia as precursors. In the work, the authors demonstrated that the nanocomposite has synthetically enhanced electrocatalytic activity for ORR, and the activity is much higher than those of the NG, NCNT, and the directly mixed product of GO and OCNT. In another case, Jin et al.³⁹² successfully fabricated the selenium-doped CNT/graphene composites (Se-CNT-graphene) through a facile thermal annealing process using CNTs, GO, and diphenyl diselenide (DDS) as precursors. The structure characterizations demonstrated that an interpenetrating network between CNTs and graphene has been formed, which can effectively accelerate reactant, ion, and electron transport and therefore synergistically improve the ORR catalytic activity. These studies suggest that fabrication of carbon hybrid materials will open a unique strategy to obtain novel metal-free catalysts with high activity, low cost for fuel cell applications.

In recent years, carbon nitride (CN) has attracted much attention in the studies of metal-free catalysts.^{393–398} As a kind of carbonaceous material enriched with nitrogen content including pyridinic and graphitic nitrogen moieties, carbon nitride has been theoretically and experimentally considered to have high electrocatalytic activity for ORR. However, the low electrical conductivity ($<10^{-2}$ S/cm) of CN materials significantly hampers the electron transfer as electrocatalysts for fuel cells. To overcome the disadvantage, Yang et al.³⁹⁹ successfully fabricated the graphene-based carbon nitride (G-CN) nanosheets by using graphene-based mesoporous silica nanosheet as template, and ethylenediamine and carbon tetrachloride as precursors. Through the synthetic process, the produced thin G-CN nanosheets not only exhibited high surface areas, high nitrogen content, but also showed improved electrical conductivity. These excellent properties are very favorable for the adsorption of oxygen molecules on the surface of G-CN catalysts, and can lead to the rapid diffusion of electrons during the ORR process. Accordingly, the electrochemical measurements indicated the outstanding electro-

Table 4. Graphene-Supported Metal-Free Nanocatalysts and Their Applications

catalyst	preparation method	precursor	application	ref
rGO	electrochemical reduction	GO	ORR in acid	147
B-GNs	thermal annealing	GO, B ₂ O ₃	ORR in alkaline	117
N-rGO	thermal annealing	GO, amines, EDC ^a	ORR in alkaline	436
N-GNs	CVD	CH ₄ , NH ₃	ORR in alkaline	94
		H ₂ , ethylene, NH ₃	ORR in alkaline	97
	solvothermal	Li ₃ N, CCl ₄ or N ₃ C ₅ Cl ₃ , Li ₃ N, CCl ₄	ORR in alkaline	140
	pyrolysis	GO, polypyrrole	ORR in alkaline	114
		sugar, urea	ORR in alkaline	115
N-C-GNs	hydrothermal	GO, melamine, formaldehyde, phenol	ORR in alkaline	433
N-GQDs	solution chemistry	benzene derivatives,	ORR in alkaline	434
		N-containing carbon fiber	ORR in alkaline	383
N-GNs	thermal annealing	graphene or GO, NH ₃	ORR in alkaline	384
		GO, melamine	ORR in alkaline	116
		GO, silica, NH ₃	ORR in alkaline	121
		N-containing polymer, rGO	ORR in alkaline	384
		GO, 5-aminotetrazole	ORR in alkaline	385
P-GNs	pyrolysis	toluene, triphenylphosphine	ORR in alkaline	113
	thermal annealing	GO, triphenylphosphine	ORR in alkaline	112
S-NGs	thermal annealing	GO, benzyl disulfide	ORR in alkaline	120
		graphene, CS ₂	ORR in alkaline	386
		GO, H ₂ S	ORR in neutral or alkaline	387, 388
I-NGs	thermal annealing	GO, iodine	ORR in alkaline	111
B,N-GNs	thermal annealing	GO, H ₃ BO ₃ , NH ₃	ORR in alkaline	122
S,N-GNs	thermal annealing	GO, melamine, benzyl disulfide	ORR in alkaline	123
P,N-GNs	hydrothermal	GO, ammonium thiocyanate	ORR in alkaline	124
N-CNTs, graphene	pyrolysis	GO, dicyandiamide, phosphoric acid	ORR in acid	125
N-graphene, N-CNTs	pyrolysis	Ni, rGO, pyridine	ORR in alkaline	389
rGO, CNTs	hydrothermal	CNTs, GO, ammonia	ORR in alkaline	391
Se-GNs, CNTs	electrostatic interactions	GO, PDAC ^b , MWNTs	ORR in alkaline	390
Se,S,N-GNs, CNTs	thermal annealing	CNTs, GO, diphenyl diselenide	ORR in alkaline	392
CN, GNs	thermal annealing	CNTs, GO, DCDA ^c , DDS ^d , DDSe ^e	ORR in acid	126
	thermal annealing	rGO, polypyrrole	ORR in alkaline	398
	pyrolysis	GO, tetraethylorthosilicate, ethylenediamine, carbon tetrachloride	ORR in alkaline	399
anthraquinone, GNs	hydrothermal	GO, phenol, melamine,	ORR in alkaline	433
EDOT, rGO	electroreduction	GO, Fast Red AL salt	ORR in PBS (pH 7.0)	400
functionalized G nanoplatelets	redox-mediated synthesis	GO, EDOT ^f	ORR in alkaline	401
TDMAC, rGO	ball milling	graphite, hydrogen, carbon dioxide, sulfur trioxide	ORR in alkaline	403
amino, GNs	physicochemical process	GO, TDMAC ^g , NaBH ₄	ORR in alkaline	404
	solvothermal	GO, ammonia	ORR in alkaline	493

^aEDC: *N*-ethyl-*N'*-(3-dimethyl aminopropyl)carbodiimide methiodide. ^bPDAC: poly(diallyldimethylammonium chloride). ^cDCDA: dicyandiamide. ^dDDS: diphenyldisulfide. ^eDDSe: diphenyldiselenide. ^fEDOT: ethylenedioxythiophene. ^gTDMAC: tridodecylmethylammonium chloride.

catalytic activity, long durability, and high selectivity when the G-CN nanosheets were employed as metal-free catalysts for ORR.

In addition, it has also been demonstrated that through the intermolecular charge transfer between graphene and modified molecules, net positive charge can be created on carbon atoms of graphene, which could be an effective way to develop metal-free electrocatalysts.^{400–403} For instance, through a simple physicochemical process, Ahmed et al.⁴⁰⁴ synthesized reduced graphene oxide with surface functionalized by tridodecylmethylammonium chloride (TDMAC-RGO). In the synthesis, TDMAC was modified onto the surface of graphene nanosheets during the reduction of GO into RGO (by sodium borohydride) in the presence of TDMAC. Here, the quaternary ammonium salt, TDMAC, could create net positive charge on the carbon atoms of graphene sheets via the intermolecular

charge transfer. Such TDMAC-functionalized/adsorbed RGO catalysts showed enhanced electrocatalytic activities toward ORR. This study suggests that the surface modification of graphene by certain molecules could be a general approach to design graphene-based metal-free ORR catalysts.

However, it should be noted that Pumera and co-workers⁴⁰⁵ recently found that some so-called graphene-based “metal-free” electrocatalysts probably contain trace metal impurities, which are actually responsible for the improved ORR catalytic activities. In the report, the authors demonstrated that trace levels of manganese oxide modified on glassy carbon electrode and doped in graphene can effectively enhance the ORR catalytic performance. Therefore, in the electrocatalytic studies with graphene-based metal-free catalysts, it is of importance to confirm the real metal-free samples by careful elemental analysis.

3. STRUCTURAL CHARACTERIZATION AND PROPERTIES OF GRAPHENE-SUPPORTED NANOELECTROCATALYSTS

3.1. Structural Characterization

Because the catalytic activities of graphene-supported nanomaterials are strongly dependent on their size, composition, morphology, and surface properties, various characterization techniques have been applied to their structural analyses. Moreover, detailed structural characterizations are needed for deeply understanding the structure–property–catalytic activity correlations, which further provide the fundamental basis for structural optimization and synthesis of nanomaterials for applications in electrocatalysts. For instance, it has been found that the electrocatalytic activities of metal nanoparticles are dependent on their structures, such as the core size, shell thickness, etc.^{14,22,49,341,381} On the basis of the structural characterizations and electrochemical measurements, the dependence of catalytic performance on structure can be determined, which could give experimental feedback for further goal-directed synthesis. In this section, we briefly summarize the commonly used techniques for structural characterization of graphene-supported nanocatalysts, mainly including X-ray (XRD, XPS, EDX) spectroscopy, electron microscopy (TEM, HRTEM, SEM), ultraviolet and visible spectroscopy, infrared spectroscopy, thermogravimetric analysis, and so on.

3.1.1. Electron Microscopy (TEM, HRTEM, SEM, and STEM). For metal nanocrystals, the particle size and exposed facets represent two of the most important parameters in the regulation of their electronic and catalytic properties. Transmission electron microscopy (TEM) and scanning electron microscopy (SEM) have traditionally been used to directly obtain the morphology information of the supported nanoparticles and graphene nanosheets. However, there is around a 0.2 nm size uncertainty for TEM measurement, and more or less melting effects of tiny nanoparticles under electron beam heating could occur during imaging. Therefore, TEM can not be used to identify the actual size of small nanoclusters supported on graphene and the internal atomic structure of graphene nanosheets. High-resolution TEM (HRTEM) is a powerful tool in the study of size and crystalline structure of relatively small metal nanocrystals. On the other hand, HRTEM can not only resolve the interesting structural features of graphene, such as individual carbon atoms, defects, adatoms, etc, but also can generate defects and edge reconstruction due to the high-energy electrons.^{406,407} Recently, Gomez-Navarro and co-workers⁴⁰⁸ reported the very clear atomic structure of a single layer rGO nanosheet by using phase-contrast HRTEM. As shown in Figure 18, the hexagonal lattice of the well-crystallized graphene sheet can be seen clearly. From the different color labeled in Figure 18b, except for the graphene facet, the various defects and deformations, such as disordered carbon networks, trapped carbonaceous adsorbates, and heavy atoms, isolated pentagon–heptagon pairs and clustered defects can also be identified. The number of layers of graphene flake can be detected from the nanobeam electron diffraction in TEM.⁴⁰⁹

Scanning transmission electron microscopy (STEM) has also been used to investigate the morphology, crystal structure, and composition distribution of graphene and graphene-based hybrids. By using the high-angle annular dark field (HAADF) mode, the atomic information of graphen-based hybrids can be identified. For example, Pasricha et al.²⁹⁹ prepared Ag-

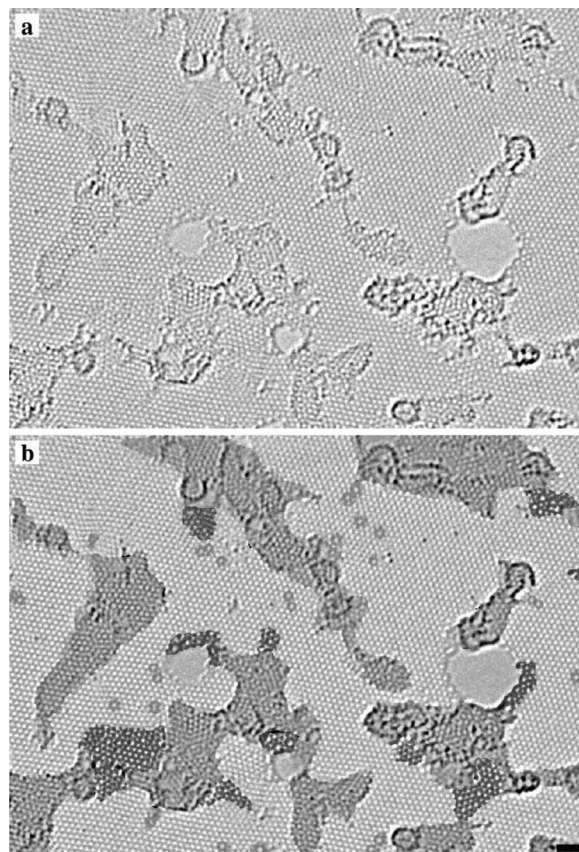


Figure 18. (a) Aberration-corrected TEM image of a single layer rGO nanosheet with atomic resolution. (a) Original image and (b) with color labeled to highlight the different features. The defect-free crystalline graphene area is displayed in the original light gray color. Contaminated regions are shaded in dark gray. Blue regions are the disordered single-layer carbon networks, or extended topological defects. Red areas highlight individual ad-atoms or substitutions. Green areas indicate isolated topological defects, that is, single bond rotations or dislocation cores. Holes and their edge reconstructions are colored in yellow. Scale bar 1 nm. Reprinted with permission from ref 408. Copyright 2010 American Chemical Society.

graphene-based hybrid and observed clearly the dispersion of Ag nanoparticles (bright) on graphene (dark) through the atomic-number contrast between Ag and carbon. Similarly, other graphene hybrids, such as Au nanoclusters, and PdAg nanorings supported on GNs have also been studied by HAADF-STEM.^{50,276}

3.1.2. Scanning Probe Microscopy (AFM and STM). Scanning probe techniques, including atomic force microscopy (AFM) and scanning tunneling microscopy (STM), are the most important tools for the structural characterization of solid surface with atomic resolution. The morphology of a solid surface can be mapped by AFM based on the strong interatomic forces between atoms of the surface and sharp probe tips at a very short distance. There are contact, noncontact, and tapping imaging modes in AFM measurements. AFM with a tapping mode is widely used to measure the thickness of graphene sheets on different substrates. The typical thickness of a pristine graphene is around 0.34 nm. Meanwhile, the thickness of a single graphene oxide nanosheet increases to around 1–1.5 nm, possibly due to the various functional group or adsorbed molecules present on the surface of GO.^{410,411} Practically, the measurement of exact thickness of grapheme

from AFM is still challenging, and repeated analyses on different substrates should be performed. To get the correct layer information, other characterization methods, such as Raman spectroscopy, should also be used to correlate the AFM measurements. On the other hand, STM can also be used to obtain the lattice structure and surface morphology of graphene at atomic resolution. Wintterlin and co-workers^{412,413} studied the growth mechanism of graphene on Ru (0001) substrate by *in situ* high temperature STM. They found that the large terraces on Ru (0001) surface that resulted from low pressure and high temperature can produce highly ordered graphene layers. For nanoparticles deposited on graphene sheets, AFM and STM can be used to characterize the size and distribution of particle on the graphene surface.

3.1.3. Raman Spectroscopy. Raman spectroscopy is a powerful tool for characterizing ordered and disordered crystal structures of carbon materials, and there have been many studies on Raman spectra of graphene sheets.^{414–416} From the Raman spectrum, the bonding configuration of carbon atoms in graphene sheets can be detected. As shown in Figure 19, the three typical Raman spectral peaks are the G band at around 1580 cm^{-1} , the D band at around 1350 cm^{-1} , and the 2D band at 2700 cm^{-1} .⁴¹⁴ The G band is from sp^2 carbon atoms domains, corresponding to the first-order scattering of the E_{2g} mode. The D-mode is a disorder-activated Raman mode and is related to the vibrations of sp^3 carbon atoms of disordered graphene nanosheets. D band is usually observed at graphene edge. The previous studies showed that the position and shape of the second-order 2D-band are sensitive to the layers of graphene sheets.^{414,417} On the basis of this, the 2D band can be used to evaluate the number of layers of a multilayer graphene. It can be seen from Figure 19b,c that the Raman spectra of graphene change significantly with the number of layers. Monolayer graphene exhibits a single sharp 2D band from the 2D_{1A} component. For bilayer graphene, the 2D band becomes broader and up-shifted in comparison with that of the single layer. From the 2D band of two-layer graphene shown in Figure 19e, the 2D band can be fitted to four components, 2D_{1B} , 2D_{1A} , 2D_{2A} , and 2D_{2B} , and the 2D_{1A} and 2D_{2A} have higher intensity than the other two. In double-layer graphene, the interaction between layers can lead to the splitting of π and π^* electronic bands into four peaks. Similarly, as indicated in Figure 19d, the D band of monolayer graphene exhibits a single sharp peak, while in bulk graphite the band splits into two peaks of D_1 and D_2 . With the further increase of the number of graphene layers (Figure 19b,c), the intensity of 2D_1 band decreases. For graphene with more than five layers, the Raman spectrum resembles that of the bulk graphite. Although multilayer non-AB stacked graphene also shows a single 2D peak,⁴¹⁸ the monolayer graphene can be distinguished from the full-width at half-maximum (fwhm). The fwhm of multilayer non-AB stacked graphene is 50 cm^{-1} , which is twice that of single layer graphene.

The Raman spectrum of graphene is also sensitive to the heteroatom doping and surface decoration of metal clusters.^{419,420} Increasing the electron doping concentration or decreasing the hole doping concentration in graphene can lead to the decrease of 2D band position, which can be used to identify the doping type, that is, electron or hole doping. The intensity ratio of the D- and G-bands ($I_{\text{D}}/I_{\text{G}}$) has been widely used to evaluate the quality of graphene nanosheets.

3.1.4. X-ray Photoelectron Spectroscopy (XPS). XPS is a powerful tool to investigate the oxidation states, chemical

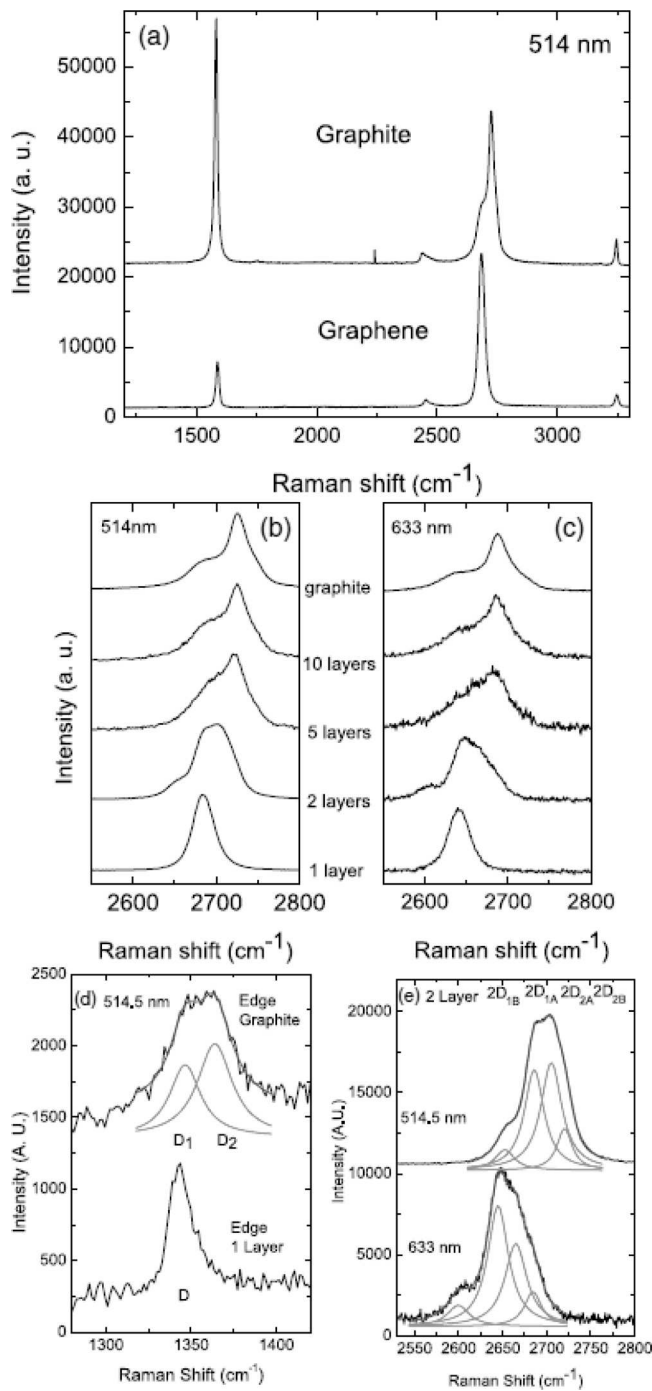


Figure 19. (a) Raman spectra of graphite and graphene. (b) Evolution of the Raman spectra at 514 nm with the number of layers of graphene. (c) Evolution of the Raman spectra at 633 nm with the number of layers of graphene. (d) Comparison of the D band at 514 nm from single layer of graphene and bulk graphite. (e) The four components of the 2D band in two-layer graphene at 514 and 633 nm. Reprinted with permission from ref 414. Copyright 2006 American Physical Society.

composition, and the nature of the bonds in graphene-supported composites. Moreover, the surface chemistry of nanocomposites can also be studied from XPS results. For example, in a recent report, the oxidation states of Ir and carbon of Ir_2V nanoclusters supported on rGO nanosheets were studied by XPS measurements.³⁸¹ As shown in Figure 20a, the peaks at 61.43 and 64.35 eV in the Ir 4f photoelectron

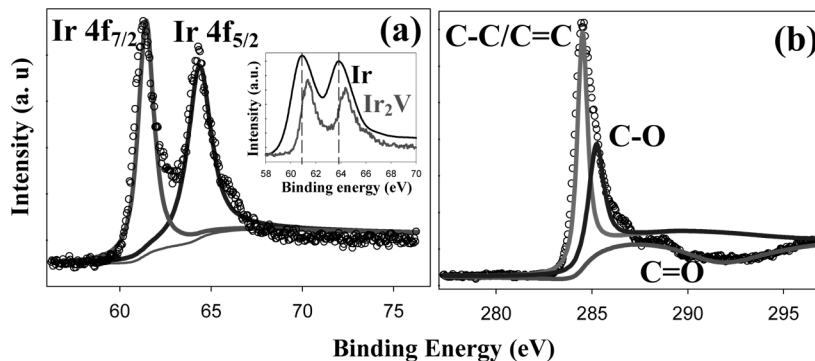


Figure 20. (a) Ir 4f and (b) C 1s XPS spectra of Ir₂V nanoclusters supported on rGO sheets (Ir₂V/rGO). The inset in (a) shows the Ir 4f XPS spectra from Ir and Ir₂V nanoclusters supported on rGO. Reprinted with permission from ref 381. Copyright 2013 Royal Society of Chemistry.

spectrum could be assigned to the binding energies of Ir 4f_{7/2} and Ir 4f_{5/2} of metallic Ir⁰. Moreover, by comparing the Ir 4f XPS spectra from Ir/rGO and Ir₂V/rGO samples (Figure 20a, inset), Ir 4f_{7/2} and 4f_{5/2} shift from 60.90, 63.90 eV on Ir/rGO to 61.43, 64.35 eV on Ir₂V/rGO, respectively, exhibiting upshift of Ir 4f binding energy from Ir to Ir₂V nanoclusters (0.53 and 0.45 eV for Ir 4f_{7/2} and Ir 4f_{5/2}, respectively). Such results strongly suggest the electronic interactions between Ir and V atomic orbitals, resulting in electron transfer from Ir to V. From the deconvoluted C1s XPS spectrum shown in Figure 20b, the three fitted peaks can be assigned to the binding energies of carbon in C=C/C—C, C—O (epoxy/hydroxyls), and C=O (carbonyl/ketone), respectively. The predominant intensity of C=C/C—C indicates that graphene oxide has been reduced to graphene by the ethylene glycol reduction treatment. These results clearly indicate that XPS measurements can provide valuable information about the bond structure of nanoparticles and the surface interaction between graphene support and the metals. On the other hand, from the ratio of the corresponding XPS peak intensities, the formula of metal nanoparticles or the average composition of alloy nanoparticles can also be identified.

3.1.5. X-ray Diffraction (XRD). XRD is usually used to study the crystal structure and evaluate the crystal size of nanomaterials based on the Debye–Scherrer equation. By XRD characterization, the formation of GO and rGO can be identified. When graphite powder is used as precursor for the synthesis of GO, there is a typical sharp diffraction peak at $2\theta = 26.4^\circ$ from the original graphite with the corresponding *d*-spacing of 3.38 Å. However, the XRD pattern of GO product shows no diffraction peaks of the parent graphite but a new broad peak at around $2\theta = 10.7^\circ$ (*d*-spacing of 8.27 Å).⁴²¹ The increased interlayer distance can be attributed to the hydroxyl and epoxy groups between the carbon sheets introduced and inserted by the oxidation course, which can lead to the decrease of van der Waals forces between the graphite sheets in the exfoliated GO. With NaBH₄ as reducing agent to obtain rGO, the diffraction peak position from GO will change with the concentration of NaBH₄. Shin et al.⁴²² reported that with the concentration of NaBH₄ increasing, the diffraction peak first shifted to $2\theta = 9.5^\circ$ and then to 9.1° . When the concentration of NaBH₄ further increased (150 mM), the peak of the large interlayer distance disappeared completely, and a broad peak near $2\theta = 23.9^\circ$ (*d*-spacing of 3.73 Å) became evident. The XRD pattern change reflects the formation of GO and the reduction process of GO to rGO. Moreover, for bimetallic or multimetallic nanoparticles supported on graphene, their XRD

pattern can also reveal the crystal structures and whether the nanoparticles have alloy structure or not.^{45,72,276}

3.1.6. UV–Vis Spectroscopy. Because of the different characteristic UV–vis absorption, graphene and its oxide can be identified from their UV–vis absorption spectra. For graphene, there is a characteristic adsorption peak at around 268 nm, and the ultraviolet absorption exhibits linear enhancement with the number of layers.⁴²³ As for graphene oxide, there are two main absorption peaks in the UV–vis absorption spectrum.⁴²⁴ The peak located around 230 nm and the shoulder peak around 300 nm are assigned to the $\pi-\pi^*$ transitions of aromatic C=C bonds and the n– π^* transitions of C=O bonds, respectively. On the other hand, metal nanoparticles exhibit unique optical characteristics with an exponential decay of the absorption profile with increasing wavelength. Meanwhile, the UV–vis absorption of coin metal nanoparticles (Au, Ag) is dominated by plasmon resonance peaks at around 420 and 520 nm for Ag, Au nanoparticles, respectively. During the deposition of metal nanoparticles on GO through chemical reduction method, the UV–vis absorption change can be observed clearly. For instance, during the deposition of Ag nanoparticles on graphene nanosheets by the chemical reduction process, there are two absorption peaks for the original GO at 226 and 305 nm.⁴²⁵ After the formation of Ag nanoparticles on graphene, the characteristic surface plasmon resonance absorption of Ag nanoparticles can be observed at 391 nm. Meanwhile, the absorption peak at 226 nm from GO red-shifted to 245 nm, and the shoulder peak at around 305 nm almost disappeared. The UV–vis absorption change indicated that after the chemical reduction process, Ag nanoparticles have been successfully deposited on graphene, and GO has also been reduced to rGO. Such study clearly indicates that UV–vis absorption measurements can provide valuable qualitative information about formation of nanomaterials on graphene and their interaction.

3.1.7. X-ray Absorption Near-Edge Structure (XANES). XANES, also named near-edge X-ray absorption fine-structure (NEXAFS), is a kind of powerful and nondestructive method to investigate the chemical bonding, local electronic structure, and interactions of graphene and adsorbates.³⁷² XANES analysis can also provide the structure information of the doped graphene, such as oxygen-containing groups.^{107,426–429}

By using NEXAFS and other characterization techniques, Zhao et al.⁴²⁸ studied the individual nitrogen doping in monolayer graphene and confirmed the presence of nitrogen in graphene. As compared to pristine graphene, two new peaks (400.7 and 408 eV) from the graphitic N were observed in the

N K-edge NEXAFS spectrum of N-doping graphene. For the graphene-supported Co_3O_4 catalyst, Dai and co-workers²⁵³ found that the C K-edge peak intensity of $\text{Co}_3\text{O}_4/\text{N-rGO}$ around 288 eV showed an obvious increase as compared to the N-rGO, indicating the interaction between Co_3O_4 and GO with the possible formation of Co–O–C and Co–N–C bonds in the hybrid. On the other hand, from the O K-edge NEXAFS, there is an obvious decrease of the unoccupied O 2p–Co 3d hybridized state and an increase in the Co L-edge NEXAFS. The strong coupled interactions between graphene sheets and Co_3O_4 nanocrystals and the modified chemical bonding environment may lead to the enhanced electrocatalytic activity of $\text{Co}_3\text{O}_4/\text{N-rGO}$ for ORR.

3.1.8. Other Characterization Methods. Besides the above techniques, other normally used characterization approaches have also been applied to the graphene-based materials. Energy dispersive X-ray (EDX) spectroscopy is also an efficient chemical tool for qualitative and quantitative element analysis of graphene-based materials. For monometallic or bimetallic nanoparticles supported on graphene sheets, EDX can be used to determine the composition of the composites.⁴³⁰ Thermogravimetric analysis (TGA) is a widely used technique to characterize the thermal stability and the loading amount of metal in graphene-based composites.^{72,431} In addition to Raman spectroscopy, the functional groups present on graphene (such as hydroxyl, carbonyl, carboxylic, and epoxy) can be characterized by Fourier transform infrared spectroscopy (FTIR) technique.⁴³² The change of surface chemistry of graphene can also be detected during the various reactions. Electron energy loss spectroscopy (EELS) is a very effective method for measuring electronic and optical properties of graphene-based nanomaterials. Combined with scanning transmission electron microscopy, the local chemistry and electronic structure of graphene can be analyzed through EELS.⁴¹⁰

3.2. Catalytic Properties

3.2.1. Intrinsic Catalytic Properties of Heteroatom-Doped Graphene. In recent years, it has been found that the heteroatom-doped graphene exhibited excellent electrocatalytic activity toward oxygen reduction reaction (ORR). For instance, N-, P-, or S-doped graphene sheets or graphene quantum dots have been studied as metal-free catalysts for ORR.^{94,113,120,433–436} Mullen reported that the N- or S-doped graphene exhibited excellent catalytic performance for ORR with long durability and high selectivity.¹²¹ Qiao's group found that the N,S- and N,B-dual doped graphene showed higher ORR catalytic activity than that of N-, S-, or B-singly doped graphene.^{123,437} All of these investigations indicated that the catalytic activity of graphene can be significantly enhanced through heteroatom doping. Besides the experimental studies, much effort has also been devoted to the mechanism explanation of the enhanced ORR catalytic properties of doped graphene by different theoretical calculations.

The density functional theory (DFT) calculations showed that the electrocatalytic activity of heteroatom-doped graphene is strongly dependent on the electron spin density and atomic charge density distribution on atoms.^{438–441} The catalytically active sites in doped graphene are usually the carbon atoms with high spin density. The doping of N, P, or B in graphene introduces unpaired electrons and causes local high spin density, resulting in high electrocatalytic performance for the ORR. According to the study from Zhang and Xia,⁴³⁸ the N-graphene containing either pyridine or pyrrole structure has

electrocatalytic property for ORR with four-electron process. It was found that, as compared to atomic charge density, spin density is the more important factor in determining catalytically active sites. Qiao and co-workers studied the synergistic effect of dual doping of B, N or S, N in enhancing the ORR performance by DFT calculations.^{123,437} For N-doped graphene, due to the greater electronegativity of N atoms (3.04) than that of C (2.55), the ORR activity mainly originates from the surrounding C atoms with high charge density. For S-doped graphene, there was negligible charge transfer between C and S because of their similar electronegativities. The positively charged S atoms were considered to be the catalytic centers. When graphene is dual-doped by N and S, as shown in Figure 21, the C1 has the maximum spin density (0.43), indicating

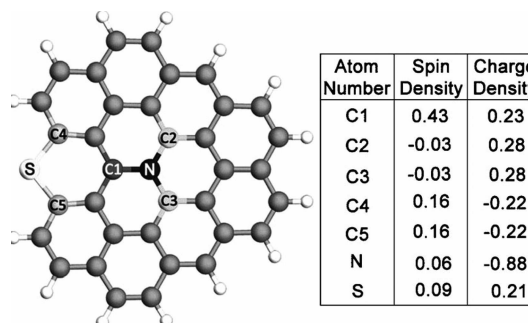


Figure 21. Spin and charge density of a graphene network (gray) dual-doped by N (black) and S (white). The table shows the spin and charge density of different C sites, S, and N. Reprinted with permission from ref 123. Copyright 2012 Wiley-VCH.

enhanced ORR catalytic activity. Moreover, due to the asymmetrical spin and charge density induced by dual-doping, other C sites (C2–C5) with high positive spin or charge density are also catalytically active. In the B,N dual-doped graphene, the authors analyzed the catalytic properties with the energy of HO_2 adsorption (E_{ad}), which is the rate-determining step of the ORR.⁴³⁷ The results showed that the dual-doped graphene exhibited higher E_{ad} than that from singly doped B- and N-graphene, suggesting the improved ORR catalytic activity of the dual-doped graphene. Interestingly, it was also found that in singly doped N-graphene, only the graphitic N atom can induce the HO_2 adsorption at the adjacent C atom, and 2-fold-coordinated pyridinic N dopant has a tendency to suppress the ORR. However, in the dual-doped graphene the inactive pyridinic N can improve the adsorption of HO_2 on the active B dopant, whereas graphitic N decreases the activity of B.

Recently, Dai and co-workers¹²² theoretically studied the ORR activities of N,B codoped graphene with different doping concentrations. From the first-principles calculations of energy gap between the highest-occupied molecular orbital (HOMO) and the lowest-unoccupied molecular orbital (LUMO), the N and B doping can result in a smaller energy gap than pure graphene and thus lead to improved catalytic activity. However, overdoping of B and N can result in significantly increased energy gap, lowering the catalytic capability of the materials. Meanwhile, the calculations showed that the pure and highly doped graphene do not have spin density at all. In contrast, graphene with modest N- and B-doping level exhibited relatively high spin and charge density. This study indicates that the energy bandgap, spin, and charge density strongly depend on the doping level, and only the modest doping can

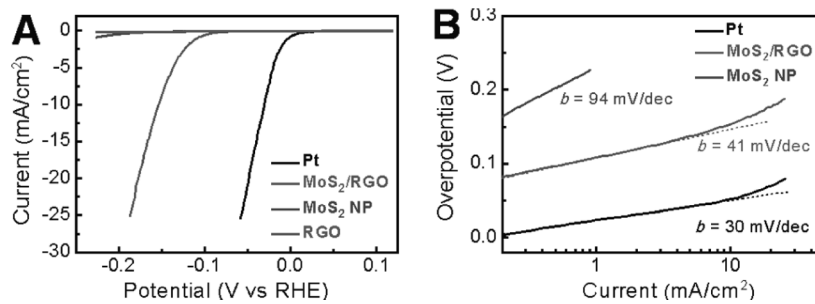


Figure 22. (A) Polarization curves of the hydrogen evolution reaction (HER) from MoS₂ nanoparticles supported on rGO and other catalysts. (B) Corresponding Tafel plots recorded on glassy carbon electrodes with a catalyst loading of 0.28 mg/cm². Reprinted with permission from ref 443. Copyright 2011 American Chemical Society.

enhance the electrocatalytic activity of graphene toward ORR. In another work, Kong and Chen⁴⁴¹ found that not all of the heteroatom doping can enhance the activity of graphene. P-substituted graphene exhibited a weak capacity of HO₂ adsorption and poor catalytic activity, which was ascribed to the large structural distortion and weakened spin density with P doping in graphene.

3.2.2. Catalytic Properties of Graphene-Supported Nanoelectrocatalysts. The enhanced electrocatalytic activities of graphene-supported nanocomposites might be partly due to the isolated sp² hybridized bonds (π electrons) and the strong interaction (charge transfer) between metal nanoparticles and graphene nanosheets. Johll and colleagues⁴⁴² investigated the interaction of graphene with transition-metal cluster by the plane-wave-based DFT program. They found that the charge transfer from the adsorbed clusters to graphene sheets can change the population of d and s orbitals of the metal atoms. Meanwhile, the binding energy between metal clusters and graphene depends on the adsorption site, adsorption configuration, and the composition of clusters. Dai and co-workers⁴⁴³ studied the electrocatalytic activities of free MoS₂ nanoparticles and rGO-supported MoS₂ nanoparticles (MoS₂/rGO) for the hydrogen evolution reaction (HER). From the polarization curve shown in Figure 22, the prepared free MoS₂ nanoparticles and rGO alone exhibited little HER activity. However, the MoS₂/rGO showed only a small overpotential (~0.1 V) and large cathodic current density. Moreover, the MoS₂/rGO exhibited a Tafel slope of 41 mV/decade, which is very close to that obtained from commercial Pt catalyst (30 mV/decade) but much smaller than that from free MoS₂ nanoparticles (94 mV/decade). The enhanced electrocatalytic performance of MoS₂/rGO was attributed the strong chemical and electronic coupling between rGO sheets and MoS₂, which can improve the dispersion of small MoS₂ particles and afford an abundance of accessible catalytically active edge sites for the HER. On the other hand, the electronic coupling can also promote the electron transfer from the less-conducting MoS₂ particles to electrode, which was reflected from the impedance measurements.

Okamoto theoretically studied the interface interaction between graphene and Pt₁₃ or Au₁₃ clusters by density-functional calculations.⁴⁴⁴ It was found that introducing a carbon vacancy into a graphene sheet can enhance the interaction between the metal clusters and graphene sheets, and the stability of the metal clusters on graphene with carbon vacancies is higher than that on defect-free graphene. Moreover, CO and H chemisorption energies become smaller on the graphene-supported metal clusters than on the clusters

without carbon support. On the basis of DFT, it was also found that single-carbon-vacancy defect in graphene can significantly improve the catalytic activity of Au₈ and Pt₄ clusters supported on graphene.⁴⁴⁵ For example, with Au₈ supported on defect-free graphene sheet, the reaction barrier of CO oxidation is around 3.0 eV, whereas the reaction barrier greatly reduced to around 0.2 eV on defective graphene. In another work, Groves et al.⁴⁴⁶ studied the binding energy between a single Pt atom and nitrogen-doped graphene by DFT. The authors found that the N doping in graphene can increase the binding energy of C–Pt bond. Although the nitrogen atoms do not bond with Pt atom directly, the more N atoms and the closer they are to the C atom, the stronger is the binding energy of the C–Pt bond. For N-graphene, the N doping disrupts the delocalized double bond in pure graphene sheets, and therefore the C–Pt bond in N-graphene focuses on 2s/6s orbitals rather than 5d/2p orbitals. Such results suggest that the increased binding energy of Pt to N-graphene can effectively improve the catalytic stability of Pt/graphene catalysts. As an important kind of catalyst, Akturk et al.⁴⁴⁷ studied the adsorption of Au_nPt_n nanoclusters on graphene surface by DFT. The calculations showed that the adsorption of Au_nPt_n nanoclusters on graphene can largely change the electronic properties, including the composition-dependent Fermi level and band gap.

At present, high overpotentials of ORR on most cathodic electrocatalysts arise mainly because of the sluggish electron-transfer kinetics caused by the strong adsorption of O on catalysts. Therefore, weakening the adsorption energy can improve the ORR efficiency. Recently, Liu et al.⁴⁴⁸ studied the electronic structures of MPd₁₂ (M = Fe, Ni, Cu, Zn, Pd) nanoparticles supported on defective graphene substrates and their reactivity for O adsorption by first-principles-based calculation. The defective graphene can provide anchoring sites for nanoparticle adsorption by forming strong metal–substrate interaction. The strong metal–graphene interaction can not only enhance the stability but also further tune the averaged d-band center of the deposited alloy nanoparticles, resulting in a strong effect on the O adsorption. As shown in Figure 23, as compared to the free MPd₁₂ particles, lower adsorption energies were obtained for O adsorbed on the MPd₁₂/SVG composites. Because O adsorption on these composites is weakened, the ORR kinetics over these composites may be promoted, and they are thus expected to have both enhanced stability and superior catalytic performance for ORR.

These theoretical calculations have predicted that metal nanoparticles supported on graphene could generate excellent catalytic activity by the increased charge transfer from the

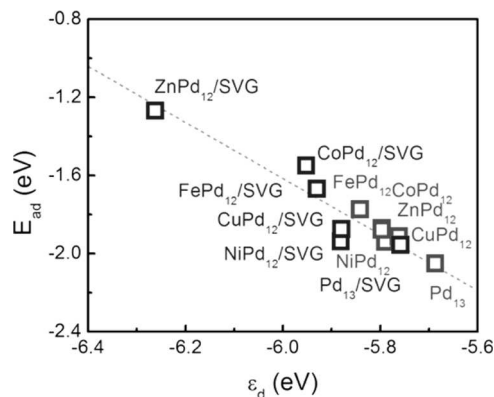


Figure 23. Calculated O adsorption energies (E_{ad}) on free MPd₁₂ and MPd₁₂ supported on single vacancy graphene (MPd₁₂/SVG) plotted versus d-band center with respect to vacuum (ϵ_d). Reprinted with permission from ref 448. Copyright 2013 American Chemical Society.

clusters to the substrates, while their stability could be simultaneously improved due to the hybridization between metal particles and sp² dangling bonds at the defect sites of graphene. The theoretical studies are useful in explaining the experimental results and helpful for the future design of graphene-based nanocatalysts.

3.3. Other Unique Properties

Besides the above catalytic properties, graphene nanosheets also possess unique electronic, optical, mechanical, thermal, and electrochemical properties. Carbon materials exhibit strong mechanical strength. For instance, diamond is the hardest

natural material, and carbon nanotube has excellent tensile strength. As for graphene, the Young's modulus of graphene has been measured by AFM.⁴⁴⁹ From the experimental evaluation, the Young's modulus and fracture strength of a defect-free graphene are 1.0 TPa and 130 GPa, respectively,⁴⁵⁰ which suggests that graphene is the strongest material ever measured. Meanwhile, the electronic property of graphene is very important for its application in electrochemistry. The previous studies showed that the electron mobility in suspended single layer graphene can reach around 2×10^5 cm²/(V·s) at room temperature,⁴⁵¹ which is higher than that of all other materials, including metals and carbon nanotubes.

Graphene-based catalysts have also been widely used in electrochemical sensors and enzyme biosensors.^{424,425,452} Graphene-based biosensors exhibit good sensitivity and selectivity toward the detection of glucose, H₂O₂, DNA, small biomolecules, cholesterol, Hb, heavy metal ions, and poisonous gaseous molecules.⁴⁵³ Graphene quantum dots (GQDs) possess strong quantum confinement and edge effects when their size is less than 10 nm, which induce new physical properties. GQDs have been applied in many fields, such as photovoltaics, bioimaging, light emitting diodes, sensors, and so on.^{454,455} On the other hand, due to the high specific surface areas (theoretically 2620 m²/g), excellent electron conductivity, and other properties, functionalized graphene or graphene-supported metal oxide composites have been used as advanced electrode materials in electrochemical capacitors and lithium ion batteries.⁴⁵⁶

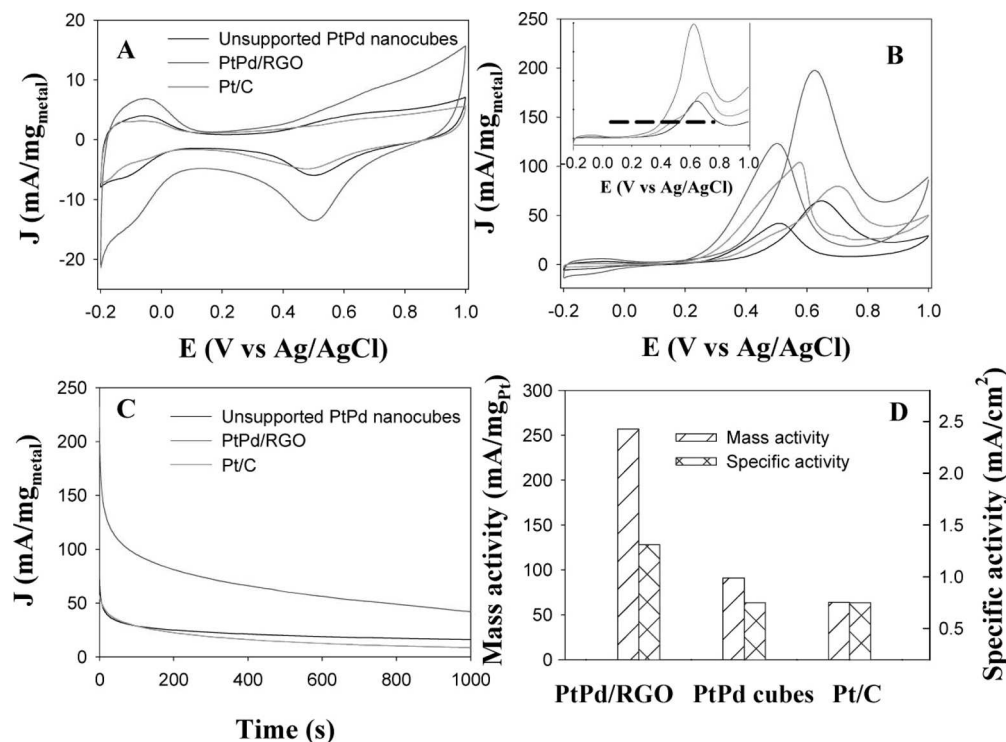


Figure 24. CVs of the unsupported and rGO-supported (PtPd/rGO) PtPd alloy nanocubes, and the commercial Pt/C catalysts in (A) 0.1 M HClO₄ solution, and (B) 0.1 M HClO₄ + 1.0 M CH₃OH solution. (C) Chronoamperometric curves of methanol oxidation at 0.62 V in 0.1 M HClO₄ + 1.0 M CH₃OH solution after the CO stripping treatment. Potential scan rate 50 mV/s. All currents were normalized to the total mass of noble metals (Pt and Pd). (D) Comparison of mass and specific activities of the three catalysts for methanol oxidation. Reprinted with permission from ref 72. Copyright 2013 American Chemical Society.

4. APPLICATIONS OF GRAPHENE-SUPPORTED NANOELECTROCATALYSTS

4.1. Electrooxidation of Small Organic Molecules at Anode of Fuel Cells

4.1.1. Methanol Oxidation Reaction (MOR). Direct methanol fuel cells (DMFCs) have attracted persistent attention due to their high energy density and low environmental pollution as compared to traditional energy sources. Meanwhile, among various fuel candidates, methanol has been considered as one of the most appropriate fuels for the direct alcohol fuel cells because of its low molecular weight, simplest structure, and very high energy density. The process of MOR includes the methanol adsorption and the subsequent dissociation into adsorbed intermediates.⁴⁵⁷ According to the dual-pathway mechanism, CO is a kind of poisoning intermediate species, which can largely reduce the catalytic activity of catalysts, especially Pt-based catalysts. To eliminate the CO poisoning to catalysts, oxygen-containing surface species (e.g., OH) formed on adjacent catalyst sites are usually needed to remove CO adsorbed (CO_{ad}) on the catalyst surface. Therefore, to catalyze the methanol oxidation efficiently, catalysts with multiple active sites are required for the adsorption of methanol and formation of OH species. Interestingly, Sharma et al.¹⁷⁹ found that the presence of oxygen groups on the graphene or rGO support can promote the oxidation of CO_{ads} formed on the active Pt sites via the bifunctional mechanism. By comparing the catalytic activity for methanol oxidation, the rGO-supported Pt nanoparticles with different size and loading exhibited higher catalytic performance than the commercial Pt/C catalyst. Because of the unusual catalytic properties, graphene-supported nanomaterials have attracted more attention in the catalytic applications for MOR over the past years.^{163,165,174,175,184,458–460}

To reduce the cost and improve the electrocatalytic performance of nanocatalysts, Pt-based nanomaterials supported on graphene have also been extensively investigated for MOR. Up to now, small Pt-based alloy nanoparticles well dispersed on graphene have been reported, and they displayed superior electrocatalytic activities toward methanol oxidation, such as PtRu/GNs,^{212,218,461} PtPd/GNs,^{72,200,202} PtNi/GNs,^{234,236} PtFe/GNs,²³⁹ PtSn/GNs,²⁴³ etc. Among the Pt-based anode electrocatalysts for DMFCs, Pt–Ru alloy exhibits the best electrocatalytic activity because PtRu alloy can reduce CO poisoning effectively. The adsorption of hydroxyls on the oxophilic Ru facilitates the removal of residual CO-like species adsorbed on the Pt surface and thus releases the occupied active sites. The experimental results from different research groups demonstrated that PtRu nanoparticles supported on graphene show much higher catalytic activity for methanol oxidation as compared to commercial PtRu/C catalyst.^{212,461,462} It is believed that the unique properties of graphene, such as large surface area and excellent electron conductivity, play key roles for the enhanced catalytic performance of PtRu/graphene for MOR. Recently, we studied the catalytic activities of rGO-supported PtPd nanocubes (PtPd/rGO) for methanol oxidation in acid electrolyte.⁷² As shown in Figure 24, as compared to the unsupported PtPd alloy nanocubes and commercial Pt/C catalyst, the PtPd/rGO exhibited enhanced electrocatalytic performance with increased electrochemically active surface area, more negative onset potential, and larger current density of MOR. Moreover, the PtPd/rGO exhibited high stability during the methanol

oxidation. This study indicates that graphene sheets are an excellent catalyst support for enhancing the catalytic performance and improving the stability of catalysts.

It has been well-documented that the catalytic activities of alloy nanoparticles are strongly dependent on their compositions. Ji et al.²⁰² found that graphene-supported PtPd nanoparticles with a molar ratio of 1:1 have the highest activity for electrocatalytic oxidation of methanol. Cai and co-workers²³⁴ reported that the Pt–Ni/graphene nanocatalysts with a molar ratio of 1:1 exhibited the highest catalytic activity toward methanol oxidation as compared to Pt/Ni supported on single-walled carbon nanotubes and Vulcan XC-72 carbon black. Multimetal alloy catalysts supported on graphene have also been reported for MOR. Feng et al.²⁴⁵ synthesized Au@PtAg nanorods/graphene hybrid materials via the self-organization of Au@PtAg nanorods on graphene. The composites showed higher catalytic activity with improved stability toward MOR than that of pure Au@Pt and Au@AgPt alloy nanorods. As carbon materials, carbon nanotubes and graphene have exhibited their potential applications as catalyst supports in fuel cells. In recent studies, carbon nanotube and graphene hybrids have been investigated as cosupports for electrocatalysts. Jha et al.⁴⁶³ studied the catalytic properties of nanostructured PtRu dispersed on graphene–carbon nanotube (CNT) hybrid support. The electrochemical measurements showed that the PtRu nanoparticles supported on the hybrid support have higher activity toward methanol oxidation as compared to either PtRu/CNT or PtRu/graphene. In another work, PtRuMo nanoparticles supported on graphene–CNT nanocomposites (PtRuMo/G-CNTs) were also studied as anode catalysts for MOR. It was found that the catalytic activity and stability of the PtRuMo/G-CNTs catalyst are higher than those of PtRuMo/GNs and PtRuMo/CNTs catalysts. In these studies, the hybrid GNs-CNTS supports not only prevent the graphene from restacking and thus provide more electrochemically active surface area, but also enhance the electronic conductivity and the mass transport, resulting in enhanced catalytic performance for MOR.

Pd is a promising alternative to Pt due to its properties similar to those of Pt but much lower cost and higher abundance. Moreover, as anode electrocatalysts for fuel cells, Pd-based materials have much higher CO-tolerance as compared to Pt. In addition to Pt-based nanomaterials, Pd-based nanocatalysts supported on graphene have also been studied in both acidic and alkaline solution. Zhao and co-workers²⁶⁶ investigated the activity of Pd/GNs-PPy catalysts for MOR in alkaline condition. The forward peak current density of MOR on Pd/GNs-PPy (359.8A/g Pd) is much higher than that of Pd/GNs (265.8A/g Pd) and Pd/C (205.3A/g Pd), indicating that Pd/GNs-PPy composite has the highest activity for methanol oxidation. Previous studies showed that OH_{ads} species can be produced at relatively lower potentials on Ru sites, which is beneficial for methanol oxidation at low onset potential. Awasthi et al.²⁵⁷ studied the Pd–Ru bimetallic nanoparticles dispersed on graphene nanosheets as anode catalysts for MOR. By comparing the CVs shown in Figure 25, the 40%Pd–5%Ru/GNs catalyst has significantly negative onset potential and the greatest oxidation current for methanol oxidation as compared to the Pd alone catalysts supported on graphene or carbon nanotubes. Moreover, it was found that the content of Ru in the bimetallic nanoparticles has an obvious effect on the catalytic performance, and the best activity was obtained at 5% Ru.

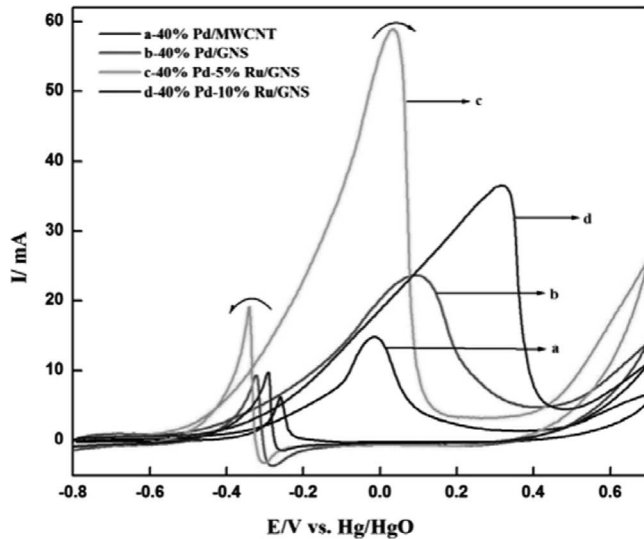


Figure 25. CVs of methanol oxidation on 40%Pd/MWCNT, 40%Pd/GNs, 40%Pd-5%Ru/GNs, and 40%Pd-10%Ru/GNs catalysts at potential scan rate of 50 mV/s in 1 M KOH + 1 M CH_3OH at 25 °C. Reprinted with permission from ref 257. Copyright 2013 Elsevier.

4.1.2. Formic Acid Oxidation Reaction (FAOR). Formic acid is liquid at room temperature, and diluted formic acid is recognized as a kind of safe fuel used in fuel cells. As compared to hydrogen fuel, aqueous solution of formic acid shows the advantages of the ease of handling, transportation, and storage. Meanwhile, direct formic acid fuel cells (DFAFCs) has a lower crossover of formic acid than that of methanol in DMFCs, which enables the use of thinner membranes and high concentration of fuel to improve the performance of fuel cells. In addition, the theoretical open circuit voltage (OCV) of DFAFC (\sim 1.48 or 1.45 V) is higher than hydrogen–oxygen (1.23 V) and methanol–oxygen (1.18 V) fuel cells.⁴⁶⁴ It has been generally accepted that the FAOR follows a dual-pathway mechanism: (I) direct dehydrogenation producing CO_2 pathway, which involves the removal of two hydrogen atoms (dehydrogenation) to form CO_2 directly $\text{HCOOH} \rightarrow \text{CO}_2 + 2\text{H}^+ + 2e^-$, and (II) indirect pathway, which involves the dehydration of formic acid to form a poisonous intermediate CO_{ads} species and then further oxidation to CO_2 . On the basis of such a mechanism, the materials on which the dehydrogenation pathway predominantly occurs or have high CO tolerance are ideal anode catalysts for formic acid oxidation. Graphene-based catalysts are endowed with excellent catalytic performance toward formic acid electrooxidation as they are able to overcome CO poisoning through the direct pathway, and graphene is propitious to not only maximize the availability of surface area of supported nanoelectrocatalysts but also provide efficient mass transport of reactants, products, and electrolytes.^{262,275} A number of mono-, bi-, and ternary metallic nanostructures supported on graphene have been fabricated as electrocatalysts for FAOR^{154,188,206,249,263,465–468}

The advantages of low cost, high tolerance to CO poisoning, and catalytic properties similar to those of Pt, Pd-based nanomaterials have been applied to FAOR as efficient anode catalysts.^{263,275,278,465,469–471} Wang and co-workers⁴⁶⁷ studied the catalytic activity of Pd nanoparticles supported on three-dimensional reduced graphene oxide (Pd/TRGO) for formic acid electrooxidation. From the CVs of formic acid oxidation shown in Figure 26, the Pd/TRGO exhibits much higher

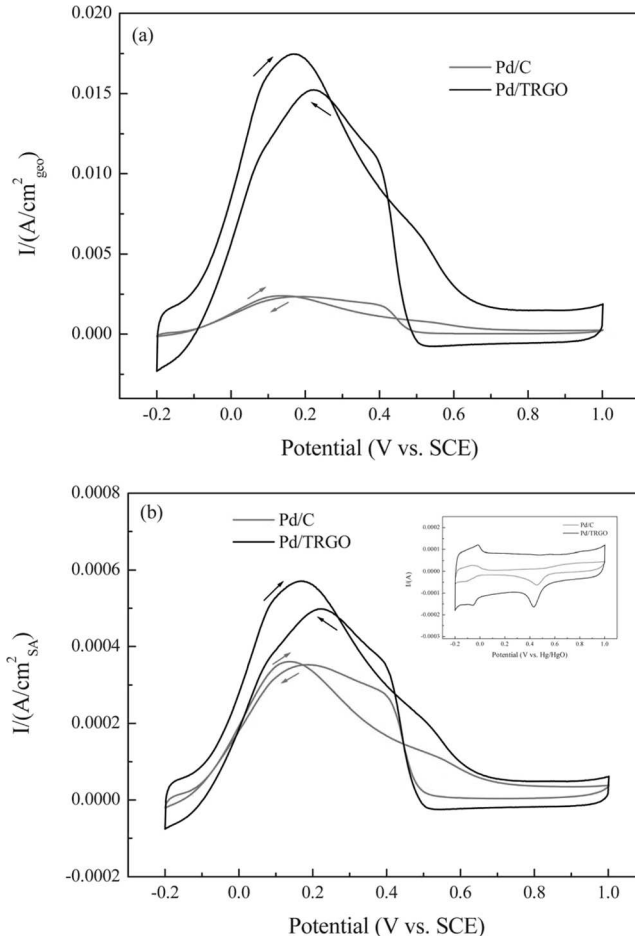


Figure 26. CVs of formic acid oxidation on Pd/C and Pd/TRGO catalysts in 0.5 M H_2SO_4 + 0.5 M HCOOH . (a) Normalized by the electrode surface area; (b) normalized by the Pd ECSC (inset: CVs in a 0.5 M H_2SO_4 solution). Reprinted with permission from ref 467. Copyright 2013 Royal Society of Chemistry.

current density of FAOR as compared to the Pd loaded on carbon black with the same amount of Pd. The enhanced catalytic activity of Pd/TRGO can be ascribed to the high specific surface area of 3D graphene oxide support, efficient Pd dispersion on the porous structured TRGO, and the improved efficiency of mass transport through the 3D graphene network with abundant macropores and mesopores. In another work, highly dispersed Pd nanoparticles supported on graphene were fabricated by a one-step electrochemical codeposition approach with reductant- and surfactant-free process.²⁷⁰ Because of the clean surface of the as-synthesized Pd nanoparticles, the Pd/GNs showed remarkably improved electrocatalytic performance for FAOR. Zhao et al.⁴⁷¹ prepared Pd nanoparticles supported on graphene via galvanic displacement between Pd ions and the presynthesized Cu nanoparticles anchored on graphene (g-Pd/GNs). From the CV measurements, the g-Pd/GNs catalyst exhibited much higher current density of 446.3 mA/ mg_{Pd} as compared to those for the Pd/GNs synthesized by direct reduction of Pd ions (213.0 mA/ mg_{Pd}) and Pd/C catalysts (191.9 mA/ mg_{Pd}). The chronoamperometric curves obtained at 0.15 V showed that the residual current of FAOR at g-Pd/GNs is about 6.9 times higher than those at Pd/GNs and Pd/C. The electrochemical measurements indicated that the g-Pd/GNs catalyst has excellent stability and activity, which can be ascribed to the small size (\sim 3 nm) and high dispersion of the

Pd nanoparticles, and the absence of stabilizers or surfactants on the particle surface.

Rao et al.¹⁵⁴ compared the electrocatalytic performance of graphene-supported Pt (Pt/GNs) and PtAu alloy (PtAu/GNs) toward FAOR. The voltammetric measurements indicated that the activity of PtAu/GNs for formic acid oxidation is about 10 times higher than that of Pt/GNs. Figure 27 shows the single-

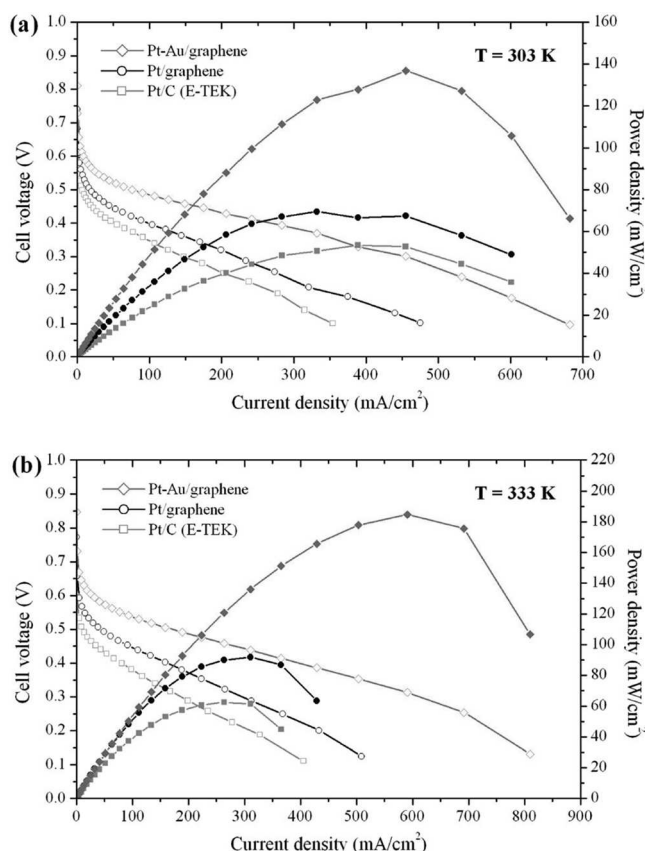
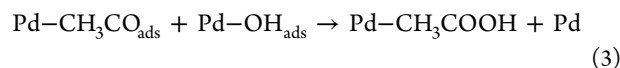
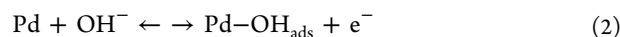
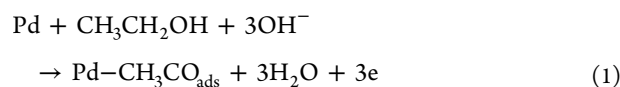


Figure 27. I - V polarization curves of Pt/GNs, PtAu/GNs, and Pt/C anodes under DFAFC conditions: (a) 303 K and 1 atm and (b) 333 K and 1 atm. Open and closed symbols corresponding to the cell voltage and power density, respectively. Reprinted with permission from ref 154. Copyright 2011 American Chemical Society.

cell DFAFC performance with the as-synthesized materials at 303 and 333 K. From the polarization curves shown in Figure 27, the Pt/GNs and PtAu/GNs show better fuel cell performance than the commercial Pt/C catalyst at both temperatures, and the PtAu/GNs anode exhibited the best performance. The open circuit voltages (OCV) of the membrane-electrode assembly (MEA) based on Pt/C, Pt/GNs, and PtAu/GNs were calculated to be 0.72, 0.77, and 0.85 V, respectively. At 303 K, the Pt/C, Pt/GNs, and PtAu/GNs showed limiting current densities of 354, 475, and 682 mA/cm², which correspond to the maximum power densities of 53, 70, and 136 mW/cm², respectively. This study clearly indicates that graphene support can enhance the catalytic performance of catalysts in a real fuel cell.

4.1.3. Ethanol Oxidation Reaction (EOR). Ethanol fueled direct alcohol fuel cells have been attracted much attention due to the higher theoretical energy density but less toxicity of ethanol as compared to methanol. For ethanol oxidation on Pt-based electrocatalysts, several reaction mechanisms have been proposed with complex processes.^{472,473} On the basis of the

mechanisms, acetaldehyde, acetic acid, or CO₂ can be formed through different reaction pathways. For Pd-based electrocatalysts, it has been found that they show catalytic activity for EOR only in alkaline media and on them ethanol is selectively converted to acetate. Previous studies on smooth Pt showed that the kinetics of EOR is strongly dependent on the pH value of electrolyte, and a peak current density was observed at pH = 14.⁴⁷⁴ In NaOH solution with concentration higher and lower than 1 mol/L, the activity will decrease. It was proposed that ethanol oxidation on Pd in alkaline media has the following reaction mechanism:



The removal of the adsorbed acyl by the adsorbed hydroxyl (the third step) has been suggested to be the rate-determining step.

Recently, metal nanoparticles supported on graphene have been used as catalysts for EOR. Dong et al.²¹² synthesized graphene-supported Pt (Pt/GNs) and Pt-Ru nanoparticles (Pt-Ru/GNs) and studied their catalytic activity for ethanol oxidation. The electrochemical results showed that, as compared to the Vulcan XC-72R carbon black support, graphene as catalyst support can more effectively enhance the electrocatalytic activities of Pt and PtRu for EOR. Moreover, as observed previously, the introduction of Ru into nanoparticles (PtRu) can efficiently improve the CO-tolerance during EOR. Jiang et al.⁴⁷⁵ synthesized Pt nanoparticles supported on electrochemically reduced and poly(3,4-ethylenedioxythiophene) (PEDOT) incorporated graphene oxide (ER-GO) sheets (Pt/PEDOT/ER-GO). From the CVs of ethanol oxidation on different catalysts, the forward peak current density (390 A/g) on the Pt/PEDOT/ER-GO is higher than that from the Pt/C catalyst, and 5 times greater than that of bare Pt/GC electrode. The high electrocatalytic activity of Pt/PEDOT/ER-GO is mainly due to the good electronic conductivity of PEDOT/ER-GO composites and the well-dispersed Pt nanoparticles, resulting in the large electrochemical active surface area of Pt (47.1 m²/g).

Besides Pt, EOR has also been studied on various graphene-supported Pd-based electrocatalysts.⁴⁷⁶ Fan and co-workers¹⁵⁷ reported the synthesis of Pd/GNs composites and studied their electrochemical properties toward alcohol electrooxidation in alkaline electrolyte. Figure 28 compares the CVs of ethanol oxidation on Pd/GNs and Vulcan XC-72R carbon-supported Pd nanoparticles (Pd/VXC). Obviously, higher catalytic performance of EOR was obtained on Pd/GNs with more negative onset potential (-0.65 vs -0.52 V on Pd/VXC) and 8.06 times larger peak current density than that from Pd/VXC. In another work, Chen et al.²⁶² reported the synthesis of “clean” and ultrafine monodispersed Pd nanoparticles on graphene oxide (PdNPs/GO) and their catalytic activity for ethanol oxidation in alkaline media. It was found that the onset potential of ethanol oxidation on PdNPs/GO is more negative than that on Pd/C. The peak current densities from the PdNPs/GO are ~3- and 1.6-fold larger than those of commercial Pd/C catalyst in the forward and reverse potential scans, respectively. Moreover, after 100 potential cycles, the

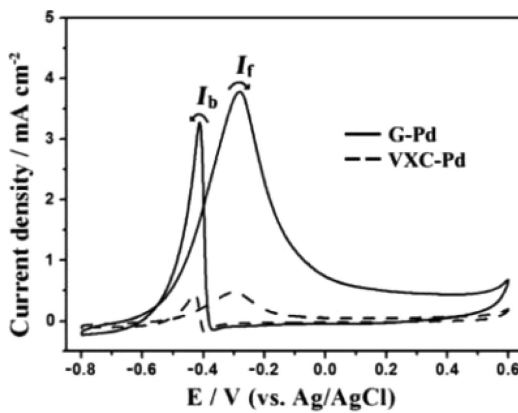


Figure 28. CVs of ethanol oxidation on Pd/GNs and Pd/VXC in 1.0 M $\text{C}_2\text{H}_5\text{OH}$ + 1.0 M NaOH. Reprinted with permission from ref 157. Copyright 2013 American Chemical Society.

drop of the current density is only ~6.3%, suggesting that the PdNPs/GO catalyst has great stability in EOR. Recently, Lee and co-workers²⁰³ synthesized bimetallic PtPd alloy nanoparticles on Nafion–graphene film by a simple electrochemical method. The hybrid exhibited efficient electrocatalytic activity and stability toward ethanol oxidation in alkaline media.

4.1.4. Hydrogen Oxidation Reaction (HOR). Hydrogen is a kind of zero-emission and high-energy fuel for fuel cells. A hydrogen-fed fuel cell can produce electricity, heat, and very clean product of water. Therefore, a lot of work has been done on the HOR with different electrocatalysts.^{477–484} Similar to other small organic molecular fuels, platinum-based catalysts show the best catalytic properties for HOR. It should be noted that the kinetics of HOR in a PEMFC is much faster than that of the ORR; therefore, only very low Pt loading is needed for the HOR. Although different types of carbon materials have been used as catalyst supports for HOR,⁴⁷⁹ only a few of studies have been reported about the graphene-supported catalysts for HOR.

For HOR, the CO tolerance is an important parameter to evaluate the properties of a catalyst. Graphene nanosheets show a high CO tolerance performance in HOR. Yoo et al.¹⁸⁴ reported that subnano Pt clusters supported on graphene nanosheets (Pt/GNs) showed a higher CO tolerance performance in the HOR than the Pt clusters dispersed on carbon black (Pt/CB). It was found that in pure H_2 atmosphere, Pt/GNs, Pt/CB, and PtRu/CB showed similar electrocatalytic activities for the HOR despite the different types of carbon material used. However, the activity of the Pt/GNs for the HOR can remain 52% in the presence of H_2 and 500 ppm CO, while that of the Pt/CB is only 11%.

4.2. Oxygen Reduction Reaction (ORR) at Cathode

Oxygen reduction reaction (ORR) on cathode plays a critical role in determining the performance of a fuel cell. Although substantial progress has been achieved on cathodic catalysts in the past decades, the sluggish electron-transfer kinetics of ORR and the large overpotential still remarkably limit the wide commercialization of fuel cells. The ORR has complicated reaction pathways and proceeds through an efficient four-electron reduction of O_2 to water as the end product ($\text{O}_2 + 4\text{H}^+ + 4\text{e}^- \rightarrow 2\text{H}_2\text{O}$), or a less efficient two-step, two-electron reduction pathway, involving the formation of hydrogen peroxide as an intermediate ($\text{O}_2 + 4\text{H}^+ + 2\text{e}^- \rightarrow \text{H}_2\text{O}_2 + 2\text{H}^+ + 2\text{e}^- \rightarrow 2\text{H}_2\text{O}$).⁴⁸⁵ Pt and Pt alloys have been accepted as

the most active and effective cathodic catalysts for ORR. However, a number of challenges remain for the Pt-based catalysts, such as low durability, easy poisoning from methanol crossover, high cost, and so on. To resolve these problems, low-Pt or non-Pt and metal-free electrocatalysts with low-cost, high electrocatalytic activity, and stability have been extensively studied as efficient ORR electrocatalysts in recent years (Tables 2–4).^{10,65,81,382,435}

The kinetic parameters of ORR can be determined using the rotating disk electrode (RDE) technique. The kinetic current density and the electron transfer numbers can be derived from the following equations:⁴⁸⁶

$$\frac{1}{J} = \frac{1}{J_K} + \frac{1}{J_L} = \frac{1}{J_K} + \frac{1}{B\omega^{1/2}} \quad (4)$$

$$B = 0.62nFC_{\text{O}}D_{\text{O}}^{2/3}\nu^{-1/6} \quad (5)$$

$$J_K = nFkC_{\text{O}} \quad (6)$$

where J is the measured current density, J_K and J_L are the kinetic and diffusion limiting current densities, respectively, ω is the electrode rotation rate, n is the overall number of electron transferred, F is the Faraday constant, C_{O} is the bulk concentration of O_2 dissolved in the electrolyte, D_{O} is the diffusion coefficient for O_2 , ν is the kinematic viscosity of the electrolyte, and k is the electron transfer rate constant. In addition, rotation ring-disk electrode (RRDE) can also be used to evaluate the ORR performance of a catalyst. Electron transfer number (n) can be obtained from the ring and disk current as the equation of $n = 4I_{\text{D}}/(I_{\text{D}} + (I_{\text{R}}/N))$. I_{D} and I_{R} represent the disk and ring current, and N is the RRDE collection efficiency. The H_2O_2 percentage generated at the disk electrode can also be calculated according to the equation of $\% \text{H}_2\text{O}_2 = (2I_{\text{R}}/N)/(I_{\text{D}} + (I_{\text{R}}/N))$.

As described above, graphene as substrate would enhance the catalytic performance of electrocatalysts supported on it due to its high surface area, excellent conductivity, and improved durability. In recent years, Pt-based catalysts supported on graphene nanosheets have been fabricated for ORR.^{166,170,181,194,201,225,237,244,487} Kou et al.¹⁸¹ found that Pt nanoparticles (~2 nm) supported on the functionalized graphene sheets exhibit enhanced electrochemical surface area (ECSA), higher ORR activity, and improved stability in acid solution as compared to commercial E-TEK catalyst. As is reported by Ha and co-workers in another work,¹⁷⁰ Pt nanoparticles (~2.9 nm) embedded on reduced graphene oxide platelets also showed much larger electrochemically active surface area and greater catalytic activity toward ORR in 0.1 M H_2SO_4 as compared to Johnson Matthey (JM) Pt/C (75 wt % Pt) catalyst. To improve the stability and reduce the chemical/physical defects of graphene support, Shao et al.¹⁶⁶ prepared Pt nanoparticles supported on poly(diallyldimethylammonium chloride) (PDDA)-functionalized graphene nanoplatelets as ORR electrocatalysts. It was found that the synthesized hybrid exhibited improved durability with 2–3 times over commercial Etek Pt/C and Pt/CNT catalysts. In a recent report from Huang's group,¹⁹⁵ the stacking of rGO can be effectively avoided by inserting carbon black (CB) particles between rGO sheets. The unique stable Pt/rGO/CN composite showed greatly enhanced ORR activity and durability as compared to the simple Pt/rGO hybrid. Because of the lower cost and greater resistance to CO over Pt catalysts, graphene-supported low-Pt bimetallic hybrids have also been studied as potential

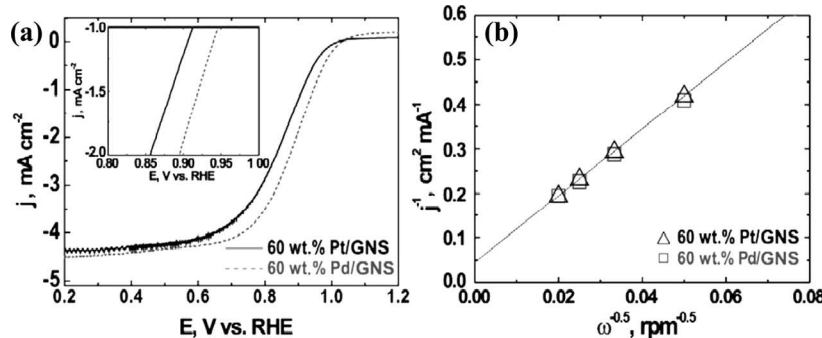


Figure 29. Polarization curves (a) and the Levich–Koutecky plots (b) of the ORR obtained from Pt/GNs and Pd/GNs in O₂-saturated 0.1 M NaOH solution with a sweep rate of 10 mV/s and rotating speed of 1600 rpm. Reprinted with permission from ref 265. Copyright 2011 Elsevier.

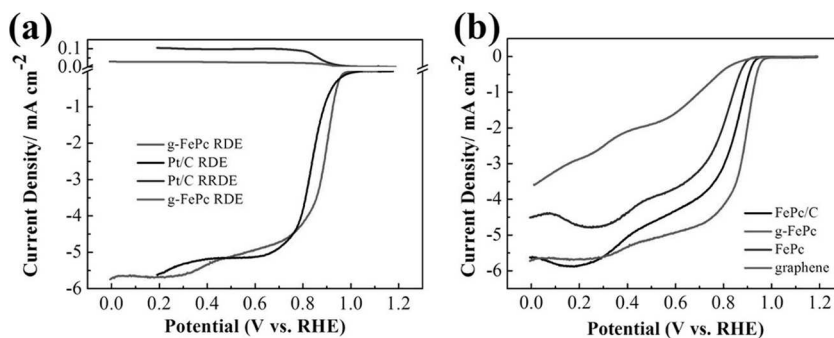


Figure 30. (a) RDE and RRDE measurements of ORR at graphene-supported iron phthalocyanine (g-FePc) and commercial Pt/C catalyst in O₂-saturated 0.1 M KOH. The ring electrode is polarized at 0.5 V (vs Ag/AgCl) with a rotation rate of 1600 rpm and a potential scan rate of 10 mV/s. (b) Comparison of the RDE polarization curves of FePc, graphene, g-FePc, and FePc supported on carbon (FePc/C) in O₂-saturated 0.1 M KOH at 1600 rpm. Reprinted with permission from ref 431. Copyright 2013 American Chemical Society.

ORR electrocatalysts. Yue et al.²²⁸ reported that the PtCo nanoparticles supported on graphene (PtCo/graphene) exhibited higher ORR catalytic activity over pure Pt in alkaline solutions. Moreover, the ORR activity of the PtCo/graphene and the generation of OH radicals showed a volcano dependence upon the alloy compositions. The authors also studied the ORR activity of the acid-treated PtNi alloy supported on graphene (PtNi/graphene) with different compositions.²³³ The PtNi/graphene catalysts were found to have higher ORR activity than that of pure Pt catalysts in both acidic and alkaline solutions, and the PtNi alloy with 50 atom % Ni content gave the highest ORR activity. It is interesting that after acid treatment, the composites demonstrated enhanced ORR catalytic performance.

To reduce the Pt loading and the cost of electrocatalysts in fuel cells, graphene-supported non-Pt catalysts were also developed in recent years. Pd-based nanomaterials have attracted special interest as cathode catalysts.⁴⁸⁸ For instance, Kim and co-workers²⁶⁵ studied the ORR electrocatalytic activities of Pt/GNs and Pd/GNs in alkaline solution. As shown in Figure 29, the uniformly dispersed Pd/GNS catalyst shows higher mass and specific catalytic activities toward ORR than does the Pt/GNS catalyst. Also, efficient four-electron reduction processes occur on both the Pt/GNs and the Pd/GNs catalysts. Recently, we prepared PdAg nanorings supported on graphene nanosheets (PdAg/GNs) and studied their ORR performance in alkaline solution.²⁷⁶ The graphene-supported PdAg nanorings demonstrated the advantages as ORR catalysts, including efficient usage of noble metals, high surface area, and high ORR electrocatalytic performance. Moreover, the prepared PdAg/GNs have higher methanol

tolerance even at a high concentration as compared to Pd/C and Pt/C catalysts.

Although bulk coinage metals, such as Au, Ag, are electrocatalytically inert for ORR, their materials on nanoscale exhibit relative high catalytic activities.⁴⁹ Tang and co-workers⁵⁰ synthesized small surfactant-free gold nanoclusters (less than ~2 nm) supported on rGO (Au/rGO) and studied their catalytic activity for ORR. It was found that the ORR onset potential on Au/rGO is at ca. -0.08 V (vs Ag/AgCl) with a reduction current peak at ca. -0.19 V, which are very close to those obtained from commercial Pt/C catalyst. The Au/rGO catalysts exhibited improved methanol-tolerance and electrocatalytic stability as compared to commercial Pt/C catalyst. Other studies also indicated that graphene-supported gold and silver nanoparticles have high electrocatalytic activities for ORR.^{285,290,306,489}

Because of the high cost of noble metal electrocatalysts, nonprecious metal-based catalysts supported on graphene or doped graphene sheets have been investigated extensively as efficient ORR catalysts.^{254,332,334–337,490} Fe (or Co)-N-C catalysts have been found to be a class of promising non-noble metal catalysts for ORR.^{63,491} Byon et al.³³⁷ prepared Fe-based catalyst on rGO (Fe-N-rGO), which contains the pyridinic N-dominant heterocyclic N. The Fe–N-rGO exhibited higher ORR mass activity and improved stability than the Fe–N–C catalysts prepared from carbon black (CB) or oxidized CB in acid solution. Recently, graphene nanosheets functionalized with iron phthalocyanine (g-FePc) through π – π interaction were studied as a kind of noble metal-free catalyst for ORR in alkaline media.⁴³¹ It can be seen from Figure 30 that the graphene support can remarkably improve the ORR perform-

ance of the FePc catalyst, and the g-FePc has better ORR activity than the carbon-supported FePc electrocatalyst (FePc/C). Moreover, the g-FePc exhibited comparable ORR activity, long-term operation stability, and better tolerance to methanol crossover and CO poisoning compared with commercial Pt/C. Transition metal oxides or sulfides supported on graphene have also been studied as non-noble metal catalysts for ORR.^{253,255,341,368,373,378,380} The strong and intimate electrical and chemical couplings between metal oxide nanomaterials and graphene can enhance the charge transport through interfaces. Moreover, the high intrinsic structural stability of graphene and the strong interactions among the hybrids can largely improve the stability and durability of the inorganic/graphene hybrids.³⁷²

In recent years, a large number of surface-functionalized graphene and heteroatom-doped graphene materials have been reported as metal-free electrocatalysts for ORR.^{81,116,131,404,435,439,492–498} Wang et al.⁴⁹² reported graphene modified with PDDA (PDDA-graphene) as metal-free catalyst toward ORR. The PDDA-graphene exhibited excellent ORR electrocatalytic performance with better selectivity, higher CO tolerance, and longer durability than that of graphene and the commercial Pt/C catalyst. In electrochemical studies, the ORR proceeds via a nearly four-electron pathway within the range of the electron transfer number from 3.5 to 4. The excellent ORR electrocatalytic activity of the PDDA-graphene is attributed to the intermolecular charge-transfer that creates a net positive charge on carbon atoms in the graphene sheets.⁴⁹²

For N-doped graphene, its ORR catalytic activity is strongly dependent on the nitrogen types and doping concentration. Geng et al.¹⁰⁶ prepared N-doped graphene with different content of three types of nitrogen at different temperatures (Figure 31). From the polarization curves of ORR at different

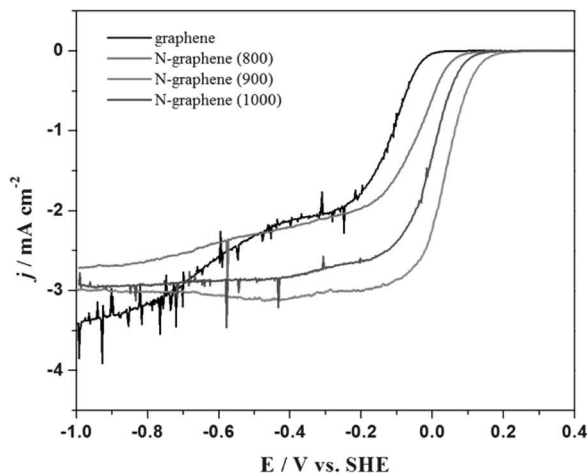


Figure 31. (a) Linear-sweep voltammograms of ORR on graphene and N-doped graphene prepared under different temperatures in O_2 -saturated 0.1 M KOH. Potential scan rate, 5 mV/s; rotation speed, 1600 rpm. Reprinted with permission from ref 106. Copyright 2011 Royal Society of Chemistry.

N-graphene, their catalytic performances are much different. On the basis of the detailed analysis, the authors found that there is no obvious dependence of the ORR activity on the content of pyridine-like and pyrrole-like N species. However, the quaternary type of nitrogen may play a decisive role for the ORR catalytic activity. In another study,⁶⁷ the N-graphene with

pure pyridinic nitrogen doping exhibited inefficient $2e^-$ ORR process, indicating that pyridinic N may not be an effective doping for ORR. Recently, Li et al.⁴³⁴ synthesized nitrogen-doped graphene quantum dots (N-GQDs) with oxygen-rich functional groups. The N-GQDs with N/C atomic ratio of ca. 4.3% exhibited electrocatalytic activity for ORR comparable to that of commercial Pt/C catalyst. The transferred electron number per O_2 molecule (n) was calculated to be in the range of 3.6–4.4, suggesting an efficient four-electron process.

5. CONCLUSIONS AND FUTURE OUTLOOK

Carbon materials are the most widely used supports for electrocatalysts in fuel cells. Since being obtained with Scotch tape for the first time, graphene has aroused an intense research interest due to its unique structure and novel chemical and physical properties. Although graphene is still a relatively new member in carbon material family, its novel properties, such as large surface area, ultrahigh electrical conductivity, excellent mechanical properties, and high chemical stability, render it an ideal electrocatalyst support for fuel cells. Moreover, the defects and functional groups present on graphene surface can immobilize the nanocatalysts, resulting in improved stability of the graphene-based hybrid catalysts. Graphene-based fuel cell catalysts at both anode and cathode have been very successfully fabricated and developed by many research groups in the past decade. Thanks to the efforts of researchers in the related fields, a huge increasing number of studies in the synthesis and characterization of graphene-based nanomaterials as electrocatalysts for fuel cells have been performed, and impressive progress has been achieved.

In this Review, the recent development of graphene-supported nanoelectrocatalysts for fuel cells, including synthesis, characterizations, properties, and application at anode and cathode of fuel cells, has been extensively reviewed. Up to now, graphene-based structures, such as zero-dimensional graphene quantum dots (GQD), two-dimensional graphene nanosheets (GNs), and three-dimensional graphene aerogel (GA) structures have been developed as catalyst supports. Overall, graphene-based nanoelectrocatalysts can be classified into the following types according to the composition of catalysts: (1) metal-free electrocatalysts, including surface-functionalized graphene and heteroatom-doped graphene; (2) graphene-supported non-noble metal electrocatalysts, including transition metal and their oxide, sulfide nanomaterials, and metal complex; (3) graphene-supported Pt-free electrocatalysts, including Pd, Au, Ag monometallic and alloy nanomaterials; and (4) graphene-supported Pt-based nanocatalysts. On the basis of the reported results, graphene-supported nanoelectrocatalysts exhibit excellent catalytic performance for fuel oxidation or oxygen reduction with optimized structures. Especially, single- or codoped graphene with N, S, B, and P is promising as a cost-efficient cathode catalyst for fuel cells. The nitrogen types and doping concentration in graphene have been found to significantly influence their catalytic performance in ORR.

It should be noted that, despite substantial progress that has been made in constructing graphene-based advanced electrocatalysts and understanding their electrocatalytic mechanism, a lot of scientific and technical challenges still remain to realize commercialization of graphene-supported electrocatalysts in fuel cells. First, shape-controlled synthesis methods should be developed for depositing metal nanocrystals on graphene nanosheets. It is well-known that the catalytic activity of metal

nanocrystal is closely related to the structures, such as size, composition, and exposed crystal facet (shape), etc. Although nonsupported metal crystals with well-controlled size and shape can be synthesized easily through various chemical and physical synthetic strategies, most of the graphene-supported metal crystals are sphere in shape, and only a few kinds of graphene-supported nanocrystals with controlled shape have been reported. Therefore, to further improve the catalytic performance, how to synthesize morphology-tunable and graphene-supported nanocatalysts is a critical issue in this field. Second, the catalytic properties of graphene-based nanocatalysts are also strongly dependent on the quality of graphene. From the literature, similar graphene-based electrocatalysts may exhibit different catalytic performance, which is at least partly ascribed to the different quality of the used graphene support. It is anticipated that the electrocatalytic properties of graphene-based catalysts can be further enhanced by improving the quality of graphene nanosheets. Third, the enhancement effect of graphene support for the activity of catalysts and the catalytic mechanism of heteroatom-doped graphene materials need to be elucidated from both experimental and theoretical investigations. Currently, catalytic properties of graphene-based electrocatalysts have been studied extensively, and it has been found that graphene nanosheets can enhance the catalytic activity of the supported nanocatalysts. However, the enhancement mechanism, including the improved stability of nanoparticles on graphene surface and the electronic interactions between graphene and nanocatalysts, is still not clear. On the other hand, a lot of studies have illustrated that the heteroatoms doped in graphene, such as N, S, P, B, can effectively enhance the ORR catalytic activity, and nitrogen types and doping concentration have an obvious effect on the catalytic performance on N-graphene. However, contradictory results were obtained from different research groups about the effects of nitrogen types on their catalytic performance. To design high-performance electrocatalysts, more research on the catalytic mechanism of heteroatom-doped graphene is required. Moreover, the durability of graphene-based catalysts is of crucial importance for their practical application in real fuel cells. Therefore, how to improve the electrochemical stability of graphene-based catalysts is another critical issue. In addition to the intrinsic stability of catalysts, the durability of graphene-supported electrocatalysts is also influenced by the following factors. First, the structure stability of graphene can affect the durability of the graphene-based catalysts.³⁷² Previous studies have shown that the unique graphitic basal plane structure of graphene could guarantee its electrochemical durability.¹⁰⁶ It was proposed that the corrosion of carbon starts from the defects, and carbon materials with more graphitic phase usually exhibit less structure defects.¹⁶⁶ Therefore, the intrinsically high graphitization degree of graphene could improve the durability of metal/graphene composites. Second, the interaction strength between graphene support and composites can also affect the stability of the graphene-based electrocatalysts. For instance, the strong coupling between N-doping sites in graphene nanosheet and metal nanoparticles can lead to enhanced durability of the hybrid catalysts.²⁵³

Overall, graphene-supported electrocatalysts have promising applications in fuel cells, and much progress has been made in recent years on their synthesis, characterization, and property studies. However, there is still a long way to realize their applications into commercial entities. More efforts have to be devoted to the scalable and reproducible synthesis with

controlled composition and morphology, and investigations on properties and catalytic mechanism.

AUTHOR INFORMATION

Corresponding Author

*E-mail: weichen@ciac.ac.cn.

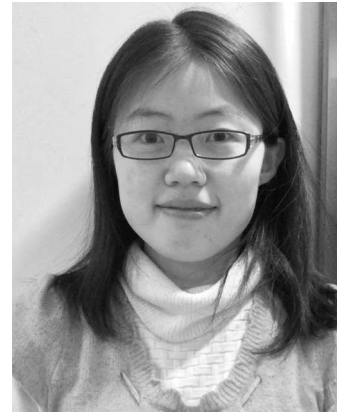
Author Contributions

[§]These authors contributed equally.

Notes

The authors declare no competing financial interest.

Biographies



Minmin Liu was born in Shandong Province, China. She obtained her B.S. degree in chemistry in 2010 from the College of Chemistry and Chemical Engineering, Liao Cheng University. She is currently pursuing a Ph.D. in Electroanalytical Chemistry under the supervision of Prof. Wei Chen at Changchun Institute of Applied Chemistry, Chinese Academy of Sciences. Her current research includes the design and application of graphene-based nanoelectrocatalysts in fuel cells.



Ruizhong Zhang is currently pursuing her Ph.D. under the direction of Professor Wei Chen at Changchun Institute of Applied Chemistry (CIAC), Chinese Academy of Sciences. She received her B.S. in chemistry from Northwest Normal University, China, in 2011. Her current research interests mainly focus on the design and synthesis of carbonous and noble metal-free nanomaterials, as well as their applications in fuel cells and sensors.



Wei Chen received his Ph.D. in electrochemistry from Xiamen University in 2003. Following his graduate studies, he began working as a postdoctoral associate in the area of synthesis and the property studies of metal nanoclusters at the University of California—Santa Cruz. He is currently a full professor at Changchun Institute of Applied Chemistry, Chinese Academy of Sciences. His research interests include electroanalytical chemistry, surface electrochemistry, electrocatalysis, photoelectrocatalysis, and the controlled synthesis, characterization, and application of nanomaterials, especially metal nanoclusters, in fuel cells, solar cells, and optical devices.

ACKNOWLEDGMENTS

This work is supported by grants from the National Natural Science Foundation of China (nos. 21275136, 21043013), the Natural Science Foundation of Jilin Province, China (no. 201215090), the State Key Laboratory of Electroanalytical Chemistry, and the Changchun Institute of Applied Chemistry, Chinese Academy of Sciences.

ABBREVIATIONS

AA	ascorbic acid
AFM	atomic force microscopy
CB	carbon black
CNTs	carbon nanotubes
CoTAPP	cobalt [tetrakis(<i>o</i> -aminophenyl)porphyrin]
CTAB	hexadecyltrimethylammonium bromide
CVD	chemical vapor deposition
DCDA	dicyandiamide
DDS	diphenyldisulfide
DDSe	diphenyldiselenide
DFAFCs	direct formic acid fuel cells
DFT	density functional theory
DMFCs	direct methanol fuel cells
DOE	Department of Energy
ECSA	electrochemical surface area
EDC	N-ethyl- <i>N'</i> -(3-dimethyl aminopropyl)carbodiimide
EDOT	ethylenedioxothiophene
EDS	energy dispersive spectroscopy
EELS	electron energy loss spectroscopy
EG	ethylene glycol
EOR	ethanol oxidation reaction
ESFDA	electrostatic force directed assembly
FAOR	formic acid oxidation reaction
FePc	iron(II) phthalocyanine
FeTsPc	iron tetrasulfophthalocyanine
FTIR	Fourier transform infrared spectroscopy
fwhm	full-width at half-maximum
GNs	graphene nanosheets

GC	glassy carbon
GO	graphene oxide
GQDs	graphene quantum dots
HER	hydrogen evolution reaction
HOMO	highest-occupied molecular orbital
HOPG	highly oriented pyrolytic graphite
HOR	hydrogen oxidation reaction
ITO	indium tin oxide
LUMO	lowest-unoccupied molecular orbital
MEA	membrane-electrode assembly
MOR	methanol oxidation reaction
OCV	open circuit voltage
ODT	1-octadecanethiol
ORR	oxygen reduction reaction
PDAC	poly (diallyldimethylammonium chloride)
PDDA	poly (diallyldimethylammonium chloride)
PEDOT	poly (3,4-ethylenedioxothiophene)
PEMFCs	proton exchange membrane fuel cells
PMAA	poly (methacrylic acid)
PMMA	polymethylmethacrylate
PSS	poly(sodium 4-styrene sulfonate)
PTCA	3,4,9,10-perylene tetracarboxylic acid
PVP	polyvinylpyrrolidone
RDE	rotating disk electrode
rGO	reduced graphene oxide
RRDE	rotation ring-disk electrode
SCE	saturated calomel electrode
SEM	scanning electron microscopy
SSA	specific surface area
STM	scanning tunneling microscopy
STEM	scanning transmission electron microscopy
TAA	thioacetamide
TCPP	5,10,15,20-tetrakis (4-carboxyl)-21H,23H-porphyrin
TDMAC	tridodecylmethylammonium chloride
TEM	transmission electron microscopy
UHV	ultrahigh vacuum
XANES	X-ray absorption near edge structure
XPS	X-ray photoelectron spectroscopic
XRD	X-ray diffraction

REFERENCES

- (1) Armand, M.; Tarascon, J. M. *Nature* **2008**, *451*, 652.
- (2) Potocnik, J. *Science* **2007**, *315*, 810.
- (3) Cook, T. R.; Dogutan, D. K.; Reece, S. Y.; Surendranath, Y.; Teets, T. S.; Nocera, D. G. *Chem. Rev.* **2010**, *110*, 6474.
- (4) Acres, G. J. K. *J. Power Sources* **2001**, *100*, 60.
- (5) Antolini, E. *J. Power Sources* **2007**, *170*, 1.
- (6) Lamy, C.; Lima, A.; LeRhun, V.; Delime, F.; Coutanceau, C.; Leger, J. M. *J. Power Sources* **2002**, *105*, 283.
- (7) Vigier, F.; Rousseau, S.; Coutanceau, C.; Leger, J. M.; Lamy, C. *Top. Catal.* **2006**, *40*, 111.
- (8) James, B. D.; Kalinoski, J. A. Mass Production Cost Estimation for Direct H₂ PEM Fuel Cell System for Automotive Applications: 2008 Update, 2009.
- (9) Steele, B. C. H.; Heinzel, A. *Nature* **2001**, *414*, 345.
- (10) Chen, A. C.; Holt-Hindle, P. *Chem. Rev.* **2010**, *110*, 3767.
- (11) Lu, Y. Z.; Chen, W. *Chem. Commun.* **2011**, *47*, 2541.
- (12) Chen, W.; Xu, L. P.; Chen, S. W. *J. Electroanal. Chem.* **2009**, *631*, 36.
- (13) Chen, W.; Kim, J. M.; Xu, L. P.; Sun, S. H.; Chen, S. W. *J. Phys. Chem. C* **2007**, *111*, 13452.
- (14) Chen, W.; Kim, J. M.; Sun, S. H.; Chen, S. W. *Langmuir* **2007**, *23*, 11303.
- (15) Chen, W.; Kim, J. M.; Sun, S. H.; Chen, S. W. *J. Phys. Chem. C* **2008**, *112*, 3891.

- (16) Chen, W.; Kim, J.; Sun, S. H.; Chen, S. W. *Phys. Chem. Chem. Phys.* **2006**, *8*, 2779.
- (17) Zhang, J.; Yang, H. Z.; Yang, K. K.; Fang, J.; Zou, S. Z.; Luo, Z. P.; Wang, H.; Bae, I. T.; Jung, D. Y. *Adv. Funct. Mater.* **2010**, *20*, 3727.
- (18) Stamenkovic, V. R.; Fowler, B.; Mun, B. S.; Wang, G. F.; Ross, P. N.; Lucas, C. A.; Markovic, N. M. *Science* **2007**, *315*, 493.
- (19) Xia, B. Y.; Wu, H. B.; Wang, X.; Lou, X. W. *J. Am. Chem. Soc.* **2012**, *134*, 13934.
- (20) Yang, H. Z.; Zhang, J.; Sun, K.; Zou, S. Z.; Fang, J. Y. *Angew. Chem., Int. Ed.* **2010**, *49*, 6848.
- (21) Kang, Y. J.; Murray, C. B. *J. Am. Chem. Soc.* **2010**, *132*, 7568.
- (22) Chen, W.; Chen, S. W. *J. Mater. Chem.* **2011**, *21*, 9169.
- (23) Zhang, H.; Jin, M. S.; Xia, Y. N. *Chem. Soc. Rev.* **2012**, *41*, 8035.
- (24) Gasteiger, H. A.; Markovic, N.; Ross, P. N.; Cairns, E. J. *J. Electrochem. Soc.* **1994**, *141*, 1795.
- (25) Goodenough, J. B.; Hamnett, A.; Kennedy, B. J.; Manoharan, R.; Weeks, S. A. *J. Electroanal. Chem.* **1988**, *240*, 133.
- (26) Oetjen, H. F.; Schmidt, V. M.; Stimming, U.; Trila, F. *J. Electrochem. Soc.* **1996**, *143*, 3838.
- (27) Frelink, T.; Visscher, W.; vanVeen, J. A. R. *Langmuir* **1996**, *12*, 3702.
- (28) Dinh, H. N.; Ren, X. M.; Garzon, F. H.; Zelenay, P.; Gottesfeld, S. *J. Electroanal. Chem.* **2000**, *491*, 222.
- (29) Antolini, E. *Energy Environ. Sci.* **2009**, *2*, 915.
- (30) Bianchini, C.; Shen, P. K. *Chem. Rev.* **2009**, *109*, 4183.
- (31) Fernandez, J. L.; Walsh, D. A.; Bard, A. J. *J. Am. Chem. Soc.* **2005**, *127*, 357.
- (32) Schmidt, T. J.; Jusys, Z.; Gasteiger, H. A.; Behm, R. J.; Endruschat, U.; Boennemann, H. *J. Electroanal. Chem.* **2001**, *501*, 132.
- (33) Jiang, L.; Hsu, A.; Chu, D.; Chen, R. *Electrochim. Acta* **2010**, *55*, 4506.
- (34) Shao, M. H.; Sasaki, K.; Adzic, R. R. *J. Am. Chem. Soc.* **2006**, *128*, 3526.
- (35) Jung, C. H.; Sanchez-Sanchez, C. M.; Lin, C. L.; Rodriguez-Lopez, J.; Bard, A. J. *Anal. Chem.* **2009**, *81*, 7003.
- (36) Fernandez, J. L.; Raghuvir, V.; Manthiram, A.; Bard, A. J. *J. Am. Chem. Soc.* **2005**, *127*, 13100.
- (37) Maiyalagan, T.; Scott, K. *J. Power Sources* **2010**, *195*, 5246.
- (38) Koenigsmann, C.; Sutter, E.; Chiesa, T. A.; Adzic, R. R.; Wong, S. S. *Nano Lett.* **2012**, *12*, 2013.
- (39) Xu, C. X.; Zhang, Y.; Wang, L. Q.; Xu, L. Q.; Bian, X. F.; Ma, H. Y.; Ding, Y. *Chem. Mater.* **2009**, *21*, 3110.
- (40) Lu, Y. Z.; Chen, W. *J. Phys. Chem. C* **2010**, *114*, 21190.
- (41) Wang, H.; Xu, C. W.; Cheng, F. L.; Zhang, M.; Wang, S. Y.; Jiang, S. P. *Electrochem. Commun.* **2008**, *10*, 1575.
- (42) Li, W. Z.; Haldar, P. *Electrochem. Commun.* **2009**, *11*, 1195.
- (43) Zhang, Z. Y.; More, K. L.; Sun, K.; Wu, Z. L.; Li, W. Z. *Chem. Mater.* **2011**, *23*, 1570.
- (44) Chen, Z. W.; Waje, M.; Li, W. Z.; Yan, Y. S. *Angew. Chem., Int. Ed.* **2007**, *46*, 4060.
- (45) Lu, Y. Z.; Chen, W. *ACS Catal.* **2012**, *2*, 84.
- (46) Alia, S. M.; Jensen, K. O.; Pivovar, B. S.; Yan, Y. S. *ACS Catal.* **2012**, *2*, 858.
- (47) Wei, W. T.; Chen, W. *J. Power Sources* **2012**, *204*, 85.
- (48) Wei, W. T.; Lu, Y. Z.; Chen, W.; Chen, S. W. *J. Am. Chem. Soc.* **2011**, *133*, 2060.
- (49) Chen, W.; Chen, S. W. *Angew. Chem., Int. Ed.* **2009**, *48*, 4386.
- (50) Yin, H. J.; Tang, H. J.; Wang, D.; Gao, Y.; Tang, Z. Y. *ACS Nano* **2012**, *6*, 8288.
- (51) Lu, Y. Z.; Chen, W. *Chem. Soc. Rev.* **2012**, *41*, 3594.
- (52) Lu, Y. Z.; Chen, W. *J. Power Sources* **2012**, *197*, 107.
- (53) Liu, Y.; Ishihara, A.; Mitsubishi, S.; Kamiya, N.; Ota, K. *J. Electrochem. Soc.* **2007**, *154*, B664.
- (54) Mentus, S. V. *Electrochim. Acta* **2004**, *50*, 27.
- (55) El-Deab, M. S.; Ohsaka, T. *Angew. Chem., Int. Ed.* **2006**, *45*, 5963.
- (56) Liang, Y. Y.; Wang, H. L.; Diao, P.; Chang, W.; Hong, G. S.; Li, Y. G.; Gong, M.; Xie, L. M.; Zhou, J. G.; Wang, J.; Regier, T. Z.; Wei, F.; Dai, H. J. *J. Am. Chem. Soc.* **2012**, *134*, 15849.
- (57) Chen, W.; Ny, D.; Chen, S. W. *J. Power Sources* **2010**, *195*, 412.
- (58) Reeve, R. W.; Christensen, P. A.; Hamnett, A.; Haydock, S. A.; Roy, S. C. *J. Electrochem. Soc.* **1998**, *145*, 3463.
- (59) Liu, H. S.; Song, C. J.; Tang, Y. H.; Zhang, J. L.; Zhang, H. J. *Electrochim. Acta* **2007**, *52*, 4532.
- (60) Zhang, L.; Zhang, J. J.; Wilkinson, D. P.; Wang, H. J. *J. Power Sources* **2006**, *156*, 171.
- (61) Holze, R.; Vogel, I.; Vielstich, W. *J. Electrochem. Soc.* **1986**, *133*, C115.
- (62) Wu, G.; More, K. L.; Johnston, C. M.; Zelenay, P. *Science* **2011**, *332*, 443.
- (63) Lefevre, M.; Proietti, E.; Jaouen, F.; Dodelet, J. P. *Science* **2009**, *324*, 71.
- (64) Wu, H. B.; Chen, W. *J. Am. Chem. Soc.* **2011**, *133*, 15236.
- (65) Gong, K. P.; Du, F.; Xia, Z. H.; Durstock, M.; Dai, L. M. *Science* **2009**, *323*, 760.
- (66) Tang, Y. F.; Allen, B. L.; Kauffman, D. R.; Star, A. *J. Am. Chem. Soc.* **2009**, *131*, 13200.
- (67) Yang, L. J.; Jiang, S. J.; Zhao, Y.; Zhu, L.; Chen, S.; Wang, X. Z.; Wu, Q.; Ma, J.; Ma, Y. W.; Hu, Z. *Angew. Chem., Int. Ed.* **2011**, *50*, 7132.
- (68) Wang, Y. J.; Wilkinson, D. P.; Zhang, J. *J. Chem. Rev.* **2011**, *111*, 7625.
- (69) Novoselov, K. S.; Geim, A. K.; Morozov, S. V.; Jiang, D.; Zhang, Y.; Dubonos, S. V.; Grigorieva, I. V.; Firsov, A. A. *Science* **2004**, *306*, 666.
- (70) Fampiou, I.; Ramasubramaniam, A. *J. Phys. Chem. C* **2012**, *116*, 6543.
- (71) Kou, R.; Shao, Y. Y.; Mei, D. H.; Nie, Z. M.; Wang, D. H.; Wang, C. M.; Viswanathan, V. V.; Park, S.; Aksay, I. A.; Lin, Y. H.; Wang, Y.; Liu, J. *J. Am. Chem. Soc.* **2011**, *133*, 2541.
- (72) Lu, Y. Z.; Jiang, Y. Y.; Wu, H. B.; Chen, W. *J. Phys. Chem. C* **2013**, *117*, 2926.
- (73) Chen, D.; Feng, H. B.; Li, J. H. *Chem. Rev.* **2012**, *112*, 6027.
- (74) Allen, M. J.; Tung, V. C.; Kaner, R. B. *Chem. Rev.* **2010**, *110*, 132.
- (75) Georgakilas, V.; Otyepka, M.; Bourlinos, A. B.; Chandra, V.; Kim, N.; Kemp, K. C.; Hobza, P.; Zboril, R.; Kim, K. S. *Chem. Rev.* **2012**, *112*, 6156.
- (76) Guo, S. J.; Dong, S. *J. Chem. Soc. Rev.* **2011**, *40*, 2644.
- (77) Pumera, M. *Chem. Soc. Rev.* **2010**, *39*, 4146.
- (78) Huang, X.; Qi, X. Y.; Boey, F.; Zhang, H. *Chem. Soc. Rev.* **2012**, *41*, 666.
- (79) Brownson, D. A. C.; Kampouris, D. K.; Banks, C. E. *Chem. Soc. Rev.* **2012**, *41*, 6944.
- (80) Zhu, Y. W.; Murali, S.; Cai, W. W.; Li, X. S.; Suk, J. W.; Potts, J. R.; Ruoff, R. S. *Adv. Mater.* **2010**, *22*, 3906.
- (81) Wang, H. B.; Maiyalagan, T.; Wang, X. *ACS Catal.* **2012**, *2*, 781.
- (82) Vicalis, L. M.; Mack, J. J.; Mayer, O. M.; Hahn, H. T.; Kaner, R. B. *J. Mater. Chem.* **2005**, *15*, 974.
- (83) Si, Y. C.; Samulski, E. T. *Chem. Mater.* **2008**, *20*, 6792.
- (84) Kosynkin, D. V.; Higginbotham, A. L.; Sinit斯基, A.; Lomeda, J. R.; Dimiev, A.; Price, B. K.; Tour, J. M. *Nature* **2009**, *458*, 872.
- (85) Jiao, L. Y.; Zhang, L.; Wang, X. R.; Diankov, G.; Dai, H. J. *Nature* **2009**, *458*, 877.
- (86) Subrahmanyam, K. S.; Panchakarla, L. S.; Govindaraj, A.; Rao, C. N. *R. J. Phys. Chem. C* **2009**, *113*, 4257.
- (87) Panchakarla, L. S.; Subrahmanyam, K. S.; Saha, S. K.; Govindaraj, A.; Krishnamurthy, H. R.; Waghmare, U. V.; Rao, C. N. *R. Adv. Mater.* **2009**, *21*, 4726.
- (88) Wei, D. C.; Liu, Y. Q.; Wang, Y.; Zhang, H. L.; Huang, L. P.; Yu, G. *Nano Lett.* **2009**, *9*, 1752.
- (89) Reina, A.; Jia, X. T.; Ho, J.; Nezich, D.; Son, H. B.; Bulovic, V.; Dresselhaus, M. S.; Kong, J. *Nano Lett.* **2009**, *9*, 30.
- (90) Hass, J.; de Heer, W. A.; Conrad, E. H. *E. H. J. Phys.: Condens. Matter* **2008**, *20*, 323202.
- (91) Li, X. S.; Cai, W. W.; An, J. H.; Kim, S.; Nah, J.; Yang, D. X.; Pineri, R.; Velamakanni, A.; Jung, I.; Tutuc, E.; Banerjee, S. K.; Colombo, L.; Ruoff, R. S. *Science* **2009**, *324*, 1312.

- (92) Gao, T.; Xie, S. B.; Gao, Y. B.; Liu, M. X.; Chen, Y. B.; Zhang, Y. F.; Liu, Z. F. *ACS Nano* **2011**, *5*, 9194.
- (93) Kim, K. S.; Zhao, Y.; Jang, H.; Lee, S. Y.; Kim, J. M.; Kim, K. S.; Ahn, J. H.; Kim, P.; Choi, J. Y.; Hong, B. H. *Nature* **2009**, *457*, 706.
- (94) Qu, L. T.; Liu, Y.; Baek, J. B.; Dai, L. M. *ACS Nano* **2010**, *4*, 1321.
- (95) Reddy, A. L. M.; Srivastava, A.; Gowda, S. R.; Gullapalli, H.; Dubey, M.; Ajayan, P. M. *ACS Nano* **2010**, *4*, 6337.
- (96) Imamura, G.; Saiki, K. *J. Phys. Chem. C* **2011**, *115*, 10000.
- (97) Luo, Z. Q.; Lim, S. H.; Tian, Z. Q.; Shang, J. Z.; Lai, L. F.; MacDonald, B.; Fu, C.; Shen, Z. X.; Yu, T.; Lin, J. Y. *J. Mater. Chem.* **2011**, *21*, 8038.
- (98) Jin, Z.; Yao, J.; Kittrell, C.; Tour, J. M. *ACS Nano* **2011**, *5*, 4112.
- (99) Cattelan, M.; Agnoli, S.; Favaro, M.; Garoli, D.; Romanato, F.; Meneghetti, M.; Barinov, A.; Dudin, P.; Granozzi, G. *Chem. Mater.* **2013**, *25*, 1490.
- (100) Wu, T. R.; Shen, H. L.; Sun, L.; Cheng, B.; Liu, B.; Shen, J. C. *New J. Chem.* **2012**, *36*, 1385.
- (101) Gao, H.; Liu, Z.; Song, L.; Guo, W. H.; Gao, W.; Ci, L. J.; Rao, A.; Quan, W. J.; Vajtai, R.; Ajayan, P. M. *Nanotechnology* **2012**, *23*, 275605.
- (102) Wu, Z. S.; Ren, W. C.; Gao, L. B.; Zhao, J. P.; Chen, Z. P.; Liu, B. L.; Tang, D. M.; Yu, B.; Jiang, C. B.; Cheng, H. M. *ACS Nano* **2009**, *3*, 411.
- (103) Wu, Y. P.; Wang, B.; Ma, Y. F.; Huang, Y.; Li, N.; Zhang, F.; Chen, Y. S. *Nano Res.* **2010**, *3*, 661.
- (104) Volotskova, O.; Levchenko, I.; Shashurin, A.; Raitses, Y.; Ostrikov, K.; Keidar, M. *Nanoscale* **2010**, *2*, 2281.
- (105) Guo, B. D.; Liu, Q. A.; Chen, E. D.; Zhu, H. W.; Fang, L. A.; Gong, J. R. *Nano Lett.* **2010**, *10*, 4975.
- (106) Geng, D. S.; Chen, Y.; Chen, Y. G.; Li, Y. L.; Li, R. Y.; Sun, X. L.; Ye, S. Y.; Knights, S. *Energy Environ. Sci.* **2011**, *4*, 760.
- (107) Geng, D. S.; Yang, S. L.; Zhang, Y.; Yang, J. L.; Liu, J.; Li, R. Y.; Sham, T. K.; Sun, X. L.; Ye, S. Y.; Knights, S. *Appl. Surf. Sci.* **2011**, *257*, 9193.
- (108) Wang, X. R.; Li, X. L.; Zhang, L.; Yoon, Y.; Weber, P. K.; Wang, H. L.; Guo, J.; Dai, H. J. *Science* **2009**, *324*, 768.
- (109) Zhang, L. S.; Liang, X. Q.; Song, W. G.; Wu, Z. Y. *Phys. Chem. Chem. Phys.* **2010**, *12*, 12055.
- (110) Zhang, C.; Fu, L.; Liu, N.; Liu, M.; Wang, Y.; Liu, Z. *Adv. Mater.* **2011**, *23*, 1020.
- (111) Yao, Z.; Nie, H. G.; Yang, Z.; Zhou, X. M.; Liu, Z.; Huang, S. M. *Chem. Commun.* **2012**, *48*, 1027.
- (112) Zhang, C. Z.; Mahmood, N.; Yin, H.; Liu, F.; Hou, Y. L. *Adv. Mater.* **2013**, *25*, 4932.
- (113) Liu, Z. W.; Peng, F.; Wang, H. J.; Yu, H.; Zheng, W. X.; Yang, J. *Angew. Chem., Int. Ed.* **2011**, *50*, 3257.
- (114) Lin, Z. Y.; Waller, G. H.; Liu, Y.; Liu, M. L.; Wong, C. P. *Nano Energy* **2013**, *2*, 241.
- (115) Pan, F. P.; Jin, J. T.; Fu, X. G.; Liu, Q.; Zhang, J. Y. *ACS Appl. Mater. Interfaces* **2013**, *5*, 11108.
- (116) Sheng, Z. H.; Shao, L.; Chen, J. J.; Bao, W. J.; Wang, F. B.; Xia, X. H. *ACS Nano* **2011**, *5*, 4350.
- (117) Sheng, Z. H.; Gao, H. L.; Bao, W. J.; Wang, F. B.; Xia, X. H. *J. Mater. Chem.* **2012**, *22*, 390.
- (118) Kim, Y. A.; Fujisawa, K.; Muramatsu, H.; Hayashi, T.; Endo, M.; Fujimori, T.; Kaneko, K.; Terrones, M.; Behrends, J.; Eckmann, A.; Casiraghi, C.; Novoselov, K. S.; Saito, R.; Dresselhaus, M. S. *ACS Nano* **2012**, *6*, 6293.
- (119) Li, X. L.; Wang, H. L.; Robinson, J. T.; Sanchez, H.; Diankov, G.; Dai, H. J. *J. Am. Chem. Soc.* **2009**, *131*, 15939.
- (120) Yang, Z.; Yao, Z.; Li, G. F.; Fang, G. Y.; Nie, H. G.; Liu, Z.; Zhou, X. M.; Chen, X.; Huang, S. M. *ACS Nano* **2012**, *6*, 205.
- (121) Yang, S. B.; Zhi, L. J.; Tang, K.; Feng, X. L.; Maier, J.; Mullen, K. *Adv. Funct. Mater.* **2012**, *22*, 3634.
- (122) Wang, S. Y.; Zhang, L. P.; Xia, Z. H.; Roy, A.; Chang, D. W.; Baek, J. B.; Dai, L. M. *Angew. Chem., Int. Ed.* **2012**, *51*, 4209.
- (123) Liang, J.; Jiao, Y.; Jaroniec, M.; Qiao, S. Z. *Angew. Chem., Int. Ed.* **2012**, *51*, 11496.
- (124) Su, Y. Z.; Zhang, Y.; Zhuang, X. D.; Li, S.; Wu, D. Q.; Zhang, F.; Feng, X. L. *Carbon* **2013**, *62*, 296.
- (125) Choi, C. H.; Chung, M. W.; Kwon, H. C.; Park, S. H.; Woo, S. I. *J. Mater. Chem. A* **2013**, *1*, 3694.
- (126) Choi, C. H.; Chung, M. W.; Jun, Y. J.; Woo, S. I. *RSC Adv.* **2013**, *3*, 12417.
- (127) Dato, A.; Radmilovic, V.; Lee, Z.; Phillips, J.; Frenklach, M. *Nano Lett.* **2008**, *8*, 2012.
- (128) Hazra, K. S.; Rafiee, J.; Rafiee, M. A.; Mathur, A.; Roy, S. S.; McLauhlin, J.; Koratkar, N.; Misra, D. S. *Nanotechnology* **2011**, *22*, 025704.
- (129) Wang, Y.; Shao, Y. Y.; Matson, D. W.; Li, J. H.; Lin, Y. H. *ACS Nano* **2010**, *4*, 1790.
- (130) Shao, Y. Y.; Zhang, S.; Engelhard, M. H.; Li, G. S.; Shao, G. C.; Wang, Y.; Liu, J.; Aksay, I. A.; Lin, Y. H. *J. Mater. Chem.* **2010**, *20*, 7491.
- (131) Jafri, R. I.; Rajalakshmi, N.; Ramaprabhu, S. *J. Mater. Chem.* **2010**, *20*, 7114.
- (132) Jeong, H. M.; Lee, J. W.; Shin, W. H.; Choi, Y. J.; Shin, H. J.; Kang, J. K.; Choi, J. W. *Nano Lett.* **2011**, *11*, 2472.
- (133) Lin, Y. C.; Lin, C. Y.; Chiu, P. W. *Appl. Phys. Lett.* **2010**, *96*, 133110.
- (134) Kumar, N. A.; Nolan, H.; McEvoy, N.; Rezvani, E.; Doyle, R. L.; Lyons, M.; Duesberg, G. S. *J. Mater. Chem. A* **2013**, *1*, 4431.
- (135) Wang, C. D.; Yuen, M. F.; Ng, T. W.; Jha, S. K.; Lu, Z. Z.; Kwok, S. Y.; Wong, T. L.; Yang, X.; Lee, C. S.; Lee, S. T.; Zhang, W. J. *Appl. Phys. Lett.* **2012**, *100*, 253107.
- (136) Chen, W. F.; Yan, L. F. *Nanoscale* **2010**, *2*, 559.
- (137) Dubin, S.; Gilje, S.; Wang, K.; Tung, V. C.; Cha, K.; Hall, A. S.; Farrar, J.; Varshneya, R.; Yang, Y.; Kaner, R. B. *ACS Nano* **2010**, *4*, 3845.
- (138) Nethravathi, C.; Rajamathi, M. *Carbon* **2008**, *46*, 1994.
- (139) Gao, X. F.; Jang, J.; Nagase, S. *J. Phys. Chem. C* **2010**, *114*, 832.
- (140) Deng, D. H.; Pan, X. L.; Yu, L. A.; Cui, Y.; Jiang, Y. P.; Qi, J.; Li, W. X.; Fu, Q. A.; Ma, X. C.; Xue, Q. K.; Sun, G. Q.; Bao, X. H. *Chem. Mater.* **2011**, *23*, 1188.
- (141) Wang, R. H.; Wang, Y.; Xu, C. H.; Sun, J.; Gao, L. *RSC Adv.* **2013**, *3*, 1194.
- (142) Long, D. H.; Li, W.; Ling, L. C.; Miyawaki, J.; Mochida, I.; Yoon, S. H. *Langmuir* **2010**, *26*, 16096.
- (143) Berger, C.; Song, Z. M.; Li, X. B.; Wu, X. S.; Brown, N.; Naud, C.; Mayou, D.; Li, T. B.; Hass, J.; Marchenkov, A. N.; Conrad, E. H.; First, P. N.; de Heer, W. A. *Science* **2006**, *312*, 1191.
- (144) Shivaraman, S.; Barton, R. A.; Yu, X.; Alden, J.; Herman, L.; Chandrashekhar, M. V. S.; Park, J.; McEuen, P. L.; Parpia, J. M.; Craighead, H. G.; Spencer, M. G. *Nano Lett.* **2009**, *9*, 3100.
- (145) Sutter, P. W.; Flege, J. I.; Sutter, E. A. *Nat. Mater.* **2008**, *7*, 406.
- (146) Lu, X. K.; Yu, M. F.; Huang, H.; Ruoff, R. S. *Nanotechnology* **1999**, *10*, 269.
- (147) Shao, Y. Y.; Wang, J.; Engelhard, M.; Wang, C. M.; Lin, Y. H. *J. Mater. Chem.* **2010**, *20*, 743.
- (148) Guo, H. L.; Wang, X. F.; Qian, Q. Y.; Wang, F. B.; Xia, X. H. *ACS Nano* **2009**, *3*, 2653.
- (149) Murugan, A. V.; Muraliganth, T.; Manthiram, A. *Chem. Mater.* **2009**, *21*, 5004.
- (150) Hirsch, A. *Angew. Chem., Int. Ed.* **2009**, *48*, 6594.
- (151) Wang, G. M.; Qian, F.; Saltikov, C.; Jiao, Y. Q.; Li, Y. *Nano Res.* **2011**, *4*, 563.
- (152) Salas, E. C.; Sun, Z. Z.; Luttge, A.; Tour, J. M. *ACS Nano* **2010**, *4*, 4852.
- (153) Liu, Z. L.; Ling, X. Y.; Su, X. D.; Lee, J. Y. *J. Phys. Chem. B* **2004**, *108*, 8234.
- (154) Rao, C. V.; Cabrera, C. R.; Ishikawa, Y. *J. Phys. Chem. C* **2011**, *115*, 21963.
- (155) Hsieh, C. T.; Chen, W. Y.; Tzou, D. Y.; Roy, A. K.; Hsiao, H. T. *Int. J. Hydrogen Energy* **2012**, *37*, 17837.
- (156) Chen, X. J.; Zang, W. Z.; Vimalanathan, K.; Iyer, K. S.; Raston, C. L. *Chem. Commun.* **2013**, *49*, 1160.

- (157) Gao, L. N.; Yue, W. B.; Tao, S. S.; Fan, L. Z. *Langmuir* **2013**, *29*, 957.
- (158) Jang, B.; Choi, E.; Piao, Y. *Mater. Res. Bull.* **2013**, *48*, 834.
- (159) Qiu, H. J.; Dong, X. C.; Sana, B.; Peng, T.; Paramelle, D.; Chen, P.; Lim, S. *ACS Appl. Mater. Interfaces* **2013**, *5*, 782.
- (160) Huang, C. C.; Li, C.; Shi, G. Q. *Energy Environ. Sci.* **2012**, *5*, 8848.
- (161) Seger, B.; Kamat, P. V. *J. Phys. Chem. C* **2009**, *113*, 7990.
- (162) Jafri, R. I.; Arockiados, T.; Rajalakshmi, N.; Ramaprabhu, S. J. *Electrochim. Soc.* **2010**, *157*, B874.
- (163) Li, Y. M.; Tang, L. H.; Li, J. H. *Electrochim. Commun.* **2009**, *11*, 846.
- (164) Qian, Y.; Wang, C. Y.; Le, Z. G. *Appl. Surf. Sci.* **2011**, *257*, 10758.
- (165) Li, Y. J.; Gao, W.; Ci, L. J.; Wang, C. M.; Ajayan, P. M. *Carbon* **2010**, *48*, 1124.
- (166) Shao, Y. Y.; Zhang, S.; Wang, C. M.; Nie, Z. M.; Liu, J.; Wang, Y.; Lin, Y. H. *J. Power Sources* **2010**, *195*, 4600.
- (167) Huang, H. J.; Chen, H. Q.; Sun, D. P.; Wang, X. J. *Power Sources* **2012**, *204*, 46.
- (168) Grinou, A.; Yun, Y. S.; Cho, S. Y.; Park, H. H.; Jin, H. J. *Materials* **2012**, *S*, 2927.
- (169) Wang, L.; Tian, C. G.; Mu, G.; Zhang, H. X.; Fu, H. G. *Mater. Res. Bull.* **2012**, *47*, 4311.
- (170) Ha, H. W.; Kim, I. Y.; Hwang, S. J.; Ruoff, R. S. *Electrochim. Solid-State Lett.* **2011**, *14*, B70.
- (171) Meng, H.; Wang, C. X.; Shen, P. K.; Wu, G. *Energy Environ. Sci.* **2011**, *4*, 1522.
- (172) Tian, N.; Zhou, Z. Y.; Sun, S. G.; Ding, Y.; Wang, Z. L. *Science* **2007**, *316*, 732.
- (173) Favier, F.; Walter, E. C.; Zach, M. P.; Benter, T.; Penner, R. M. *Science* **2001**, *293*, 2227.
- (174) Zhou, Y. G.; Chen, J. J.; Wang, F. B.; Sheng, Z. H.; Xia, X. H. *Chem. Commun.* **2010**, *46*, 5951.
- (175) Maiyalagan, T.; Dong, X. C.; Chen, P.; Wang, X. J. *Mater. Chem.* **2012**, *22*, 5286.
- (176) Liu, X. W.; Mao, J. J.; Liu, P. D.; Wei, X. W. *Carbon* **2011**, *49*, 477.
- (177) Tu, W. X.; Lin, H. F. *Chem. Mater.* **2000**, *12*, 564.
- (178) Gerbec, J. A.; Magana, D.; Washington, A.; Strouse, G. F. *J. Am. Chem. Soc.* **2005**, *127*, 15791.
- (179) Sharma, S.; Ganguly, A.; Papakonstantinou, P.; Miao, X. P.; Li, M. X.; Hutchison, J. L.; Delichatsios, M.; Ukleja, S. *J. Phys. Chem. C* **2010**, *114*, 19459.
- (180) Kundu, P.; Nethravathi, C.; Deshpande, P. A.; Rajamathi, M.; Madras, G.; Ravishankar, N. *Chem. Mater.* **2011**, *23*, 2772.
- (181) Kou, R.; Shao, Y. Y.; Wang, D. H.; Engelhard, M. H.; Kwak, J. H.; Wang, J.; Viswanathan, V. V.; Wang, C. M.; Lin, Y. H.; Wang, Y.; Aksay, I. A.; Liu, J. *Electrochim. Commun.* **2009**, *11*, 954.
- (182) Giovanni, M.; Poh, H. L.; Ambrosi, A.; Zhao, G. J.; Sofer, Z.; Sanek, F.; Khezri, B.; Webster, R. D.; Pumera, M. *Nanoscale* **2012**, *4*, 5002.
- (183) Zhang, H.; Chen, S.; Quan, X.; Yu, H. T.; Zhao, H. M. *J. Mater. Chem.* **2011**, *21*, 12986.
- (184) Yoo, E.; Okada, T.; Akita, T.; Kohyama, M.; Honma, I.; Nakamura, J. *J. Power Sources* **2011**, *196*, 110.
- (185) Siburian, R.; Nakamura, J. *J. Phys. Chem. C* **2012**, *116*, 22947.
- (186) Guo, S. J.; Wen, D.; Zhai, Y. M.; Dong, S. J.; Wang, E. K. *ACS Nano* **2010**, *4*, 3959.
- (187) Yang, D. Q.; Rochette, J. F.; Sacher, E. *J. Phys. Chem. B* **2005**, *109*, 4481.
- (188) Wang, S. Y.; Wang, X.; Jiang, S. P. *Phys. Chem. Chem. Phys.* **2011**, *13*, 7187.
- (189) Wang, Z. H.; Xia, J. F.; Guo, X. M.; Xia, Y. Z.; Yao, S. Y.; Zhang, F. F.; Li, Y. H.; Xia, L. H. *Anal. Methods* **2013**, *5*, 483.
- (190) Qiu, J. D.; Wang, G. C.; Liang, R. P.; Xia, X. H.; Yu, H. W. *J. Phys. Chem. C* **2011**, *115*, 15639.
- (191) Zhang, S.; Shao, Y. Y.; Liao, H. G.; Engelhard, M. H.; Yin, G. P.; Lin, Y. H. *ACS Nano* **2011**, *5*, 1785.
- (192) Ahmed, M. S.; Kim, D.; Han, H. S.; Jeong, H.; Jeon, S. J. *Nanosci. Nanotechnol.* **2012**, *12*, 8349.
- (193) Mayavan, S.; Jang, H. S.; Lee, M. J.; Choi, S. H.; Choi, S. M. J. *Mater. Chem. A* **2013**, *1*, 3489.
- (194) Nam, K. W.; Song, J.; Oh, K. H.; Choo, M. J.; Park, H. A.; Park, J. K.; Choi, J. W. *J. Solid State Electrochem.* **2013**, *17*, 767.
- (195) Li, Y. J.; Li, Y. J.; Zhu, E. B.; McLouth, T.; Chiu, C. Y.; Huang, X. Q.; Huang, Y. *J. Am. Chem. Soc.* **2012**, *134*, 12326.
- (196) Yuan, Q.; Zhuang, J.; Wang, X. *Chem. Commun.* **2009**, 6613.
- (197) Lim, B.; Jiang, M. J.; Camargo, P. H. C.; Cho, E. C.; Tao, J.; Lu, X. M.; Zhu, Y. M.; Xia, Y. N. *Science* **2009**, *324*, 1302.
- (198) Peng, Z. M.; Yang, H. *J. Am. Chem. Soc.* **2009**, *131*, 7542.
- (199) Lu, Y. Z.; Jiang, Y. Y.; Chen, W. *Nano Energy* **2013**, *2*, 836.
- (200) Guo, S. J.; Dong, S. J.; Wang, E. K. *ACS Nano* **2010**, *4*, 547.
- (201) He, W.; Jiang, H. J.; Zhou, Y.; Yang, S. D.; Xue, X. Z.; Zou, Z. Q.; Zhang, X. G.; Akins, D. L.; Yang, H. *Carbon* **2012**, *50*, 265.
- (202) Ji, H. Q.; Li, M. G.; Wang, Y. L.; Gao, F. *Electrochim. Commun.* **2012**, *24*, 17.
- (203) Yang, X.; Yang, Q. D.; Xu, J.; Lee, C. S. *J. Mater. Chem.* **2012**, *22*, 8057.
- (204) Lu, Y. Z.; Jiang, Y. Y.; Chen, W. *Nanoscale* **2014**, *6*, 3309.
- (205) Zhao, D.; Xu, B. Q. *Angew. Chem., Int. Ed.* **2006**, *45*, 4955.
- (206) Zhang, S.; Shao, Y. Y.; Liao, H. G.; Liu, J.; Aksay, I. A.; Yin, G. P.; Lin, Y. H. *Chem. Mater.* **2011**, *23*, 1079.
- (207) Hu, Y. J.; Zhang, H.; Wu, P.; Zhang, H.; Zhou, B.; Cai, C. X. *Phys. Chem. Chem. Phys.* **2011**, *13*, 4083.
- (208) Yang, G. H.; Li, Y. J.; Rana, R. K.; Zhu, J. *J. Mater. Chem. A* **2013**, *1*, 1754.
- (209) Rolison, D. R.; Hagans, P. L.; Swider, K. E.; Long, J. W. *Langmuir* **1999**, *15*, 774.
- (210) Lu, Y. Z.; Jiang, Y. Y.; Zhang, R. Z.; Chen, W. *Sci. Adv. Mater.* **2013**, *5*, 1718.
- (211) Cong, H. P.; Ren, X. C.; Yu, S. H. *ChemCatChem* **2012**, *4*, 1555.
- (212) Dong, L. F.; Gari, R. R. S.; Li, Z.; Craig, M. M.; Hou, S. F. *Carbon* **2010**, *48*, 781.
- (213) Galal, A.; Atta, N. F.; Hassan, H. K. *Int. J. Electrochem. Sci.* **2012**, *7*, 768.
- (214) Nethravathi, C.; Anumol, E. A.; Rajamathi, M.; Ravishankar, N. *Nanoscale* **2011**, *3*, 569.
- (215) Zhao, J.; Zhang, L.; Xue, H.; Wang, Z. B.; Hu, H. Q. *RSC Adv.* **2012**, *2*, 9651.
- (216) Zhao, J.; Xue, H.; Zhang, L.; Yu, J. H.; Hu, H. Q. *J. Nanopart. Res.* **2012**, *14*.
- (217) Kim, H. J.; Choi, S. M.; Seo, M. H.; Green, S.; Huber, G. W.; Kim, W. B. *Electrochim. Commun.* **2011**, *13*, 890.
- (218) Li, H. Y.; Zhang, X. H.; Pang, H. L.; Huang, C. T.; Chen, J. H. *J. Solid State Electrochem.* **2010**, *14*, 2267.
- (219) Wang, Y. S.; Yang, S. Y.; Li, S. M.; Tien, H. W.; Hsiao, S. T.; Liao, W. H.; Liu, C. H.; Chang, K. H.; Ma, C. C. M.; Hu, C. C. *Electrochim. Acta* **2013**, *87*, 261.
- (220) Lv, R. T.; Cui, T. X.; Jun, M. S.; Zhang, Q.; Cao, A. Y.; Su, D. S.; Zhang, Z. J.; Yoon, S. H.; Miyawaki, J.; Mochida, I.; Kang, F. Y. *Adv. Funct. Mater.* **2011**, *21*, 999.
- (221) Woo, S.; Lee, J.; Park, S. K.; Kim, H.; Chung, T. D.; Piao, Y. J. *Power Sources* **2013**, *222*, 261.
- (222) Huang, H. J.; Sun, D. P.; Wang, X. *Chin. Sci. Bull.* **2012**, *57*, 3071.
- (223) Yang, P.; Jin, S. Y.; Xu, Q. Z.; Yu, S. H. *Small* **2013**, *9*, 199.
- (224) Shi, G. Y.; Wang, Z. H.; Xia, J. F.; Zhang, F. F.; Xia, Y. Z.; Li, Y. H. *Acta Chim. Sin.* **2013**, *71*, 227.
- (225) Yan, Z. H.; Wang, M.; Huang, B. X.; Liu, R. M.; Zhao, J. S. *Int. J. Electrochem. Sci.* **2013**, *8*, 149.
- (226) Ma, Y. W.; Liu, Z. R.; Wang, B. L.; Zhu, L.; Yang, J. P.; Li, X. A. *New Carbon Mater.* **2012**, *27*, 250.
- (227) Shen, J. F.; Yan, B.; Shi, M.; Ma, H. W.; Li, N.; Ye, M. X. *Mater. Res. Bull.* **2012**, *47*, 1486.
- (228) Yue, Q. L.; Zhang, K.; Chen, X. M.; Wang, L.; Zhao, J. S.; Liu, J. F.; Jia, J. B. *Chem. Commun.* **2010**, *46*, 3369.

- (229) Nam, K. W.; Song, J.; Oh, K. H.; Choo, M. J.; Park, H.; Park, J. K.; Choi, J. W. *Carbon* **2012**, *50*, 3739.
- (230) Luo, B. M.; Xu, S.; Yan, X. B.; Xue, Q. *J. Electrochem. Soc.* **2013**, *160*, F262.
- (231) Luo, B. M.; Xu, S.; Yan, X. B.; Xue, Q. *J. Electrochem. Commun.* **2012**, *23*, 72.
- (232) Gao, H. C.; Xiao, F.; Ching, C. B.; Duan, H. W. *ACS Appl. Mater. Interfaces* **2011**, *3*, 3049.
- (233) Zhang, K.; Yue, Q. L.; Chen, G. F.; Zhai, Y. L.; Wang, L.; Wang, H. S.; Zhao, J. S.; Liu, J. F.; Jia, J. B.; Li, H. B. *J. Phys. Chem. C* **2011**, *115*, 379.
- (234) Hu, Y. J.; Wu, P.; Yin, Y. J.; Zhang, H.; Cai, C. X. *Appl. Catal., B* **2012**, *111*, 208.
- (235) Zhang, C.; Lv, W.; Yang, Q. H.; Liu, Y. *Appl. Surf. Sci.* **2012**, *258*, 7795.
- (236) Hu, Y. J.; Wu, P.; Zhang, H.; Cai, C. X. *Electrochim. Acta* **2012**, *85*, 314.
- (237) Guo, S. J.; Sun, S. H. *J. Am. Chem. Soc.* **2012**, *134*, 2492.
- (238) Wei, G.; Zhang, Y.; Steckbeck, S.; Su, Z. Q.; Li, Z. *J. Mater. Chem.* **2012**, *22*, 17190.
- (239) Ji, Z. Y.; Zhu, G. X.; Shen, X. P.; Zhou, H.; Wu, C. M.; Wang, M. *New J. Chem.* **2012**, *36*, 1774.
- (240) Yang, H.; Kwon, Y.; Kwon, T.; Lee, H.; Kim, B. J. *Small* **2012**, *8*, 3161.
- (241) Liu, Y. J.; Huang, Y. Q.; Xie, Y.; Yang, Z. H.; Huang, H. L.; Zhou, Q. Y. *Chem. Eng. J.* **2012**, *197*, 80.
- (242) Anandan, S.; Manivel, A.; Ashokkumar, M. *Fuel Cells* **2012**, *12*, 956.
- (243) Han, F.; Wang, X. M.; Lian, J.; Wang, Y. Z. *Carbon* **2012**, *50*, 5498.
- (244) Rao, C. V.; Reddy, A. L. M.; Ishikawa, Y.; Ajayan, P. M. *Carbon* **2011**, *49*, 931.
- (245) Feng, L. L.; Gao, G.; Huang, P.; Wang, X. S.; Zhang, C. L.; Zhang, J. L.; Guo, S. W.; Cui, D. X. *Nanoscale Res. Lett.* **2011**, *6*, 551.
- (246) Cunci, L.; Rao, C. V.; Velez, C.; Ishikawa, Y.; Cabrera, C. R. *Electrocatalysis* **2013**, *4*, 61.
- (247) Ji, Z. Y.; Shen, X. P.; Zhu, G. X.; Chen, K. M.; Fu, G. H.; Tong, L. *J. Electroanal. Chem.* **2012**, *682*, 95.
- (248) Sun, C. L.; Hsu, Y. K.; Lin, Y. G.; Chen, K. H.; Bock, C.; MacDougall, B.; Wu, X. H.; Chen, L. C. *J. Electrochem. Soc.* **2009**, *156*, B1249.
- (249) Hu, C. G.; Zhao, Y.; Cheng, H. H.; Hu, Y.; Shi, G. Q.; Dai, L. M.; Qu, L. T. *Chem. Commun.* **2012**, *48*, 11865.
- (250) Ye, F.; Cao, X. R.; Yu, L.; Chen, S. Z.; Lin, W. M. *Int. J. Electrochem. Sci.* **2012**, *7*, 1251.
- (251) Zhang, Y. Z.; Gu, Y. E.; Lin, S. X.; Wei, J. P.; Wang, Z. H.; Wang, C. M.; Du, Y. L.; Ye, W. C. *Electrochim. Acta* **2011**, *56*, 8746.
- (252) Hu, C. G.; Cheng, H. H.; Zhao, Y.; Hu, Y.; Liu, Y.; Dai, L. M.; Qu, L. T. *Adv. Mater.* **2012**, *24*, 5493.
- (253) Liang, Y. Y.; Li, Y. G.; Wang, H. L.; Zhou, J. G.; Wang, J.; Regier, T.; Dai, H. J. *J. Nat. Mater.* **2011**, *10*, 780.
- (254) Wu, Z. S.; Yang, S. B.; Sun, Y.; Parvez, K.; Feng, X. L.; Mullen, K. *J. Am. Chem. Soc.* **2012**, *134*, 9082.
- (255) Wang, H. L.; Liang, Y. Y.; Li, Y. G.; Dai, H. J. *Angew. Chem., Int. Ed.* **2011**, *50*, 10969.
- (256) Liang, Y. Y.; Wang, H. L.; Zhou, J. G.; Li, Y. G.; Wang, J.; Regier, T.; Dai, H. J. *J. Am. Chem. Soc.* **2012**, *134*, 3517.
- (257) Awasthi, R.; Singh, R. N. *Carbon* **2013**, *51*, 282.
- (258) Khomyakov, P. A.; Giovannetti, G.; Rusu, P. C.; Brocks, G.; van den Brink, J.; Kelly, P. J. *Phys. Rev. B* **2009**, *79*, 195425.
- (259) Wang, Q. J.; Che, J. G. *Phys. Rev. Lett.* **2009**, *103*, 066802.
- (260) Scheuermann, G. M.; Rumi, L.; Steurer, P.; Bannwarth, W.; Mulhaupt, R. *J. Am. Chem. Soc.* **2009**, *131*, 8262.
- (261) Li, Y.; Fan, X. B.; Qi, J. J.; Ji, J. Y.; Wang, S. L.; Zhang, G. L.; Zhang, F. B. *Nano Res.* **2010**, *3*, 429.
- (262) Chen, X. M.; Wu, G. H.; Chen, J. M.; Chen, X.; Xie, Z. X.; Wang, X. R. *J. Am. Chem. Soc.* **2011**, *133*, 3693.
- (263) Yang, J.; Tian, C. G.; Wang, L.; Fu, H. G. *J. Mater. Chem.* **2011**, *21*, 3384.
- (264) Xi, P. X.; Chen, F. J.; Xie, G. Q.; Ma, C.; Liu, H. Y.; Shao, C. W.; Wang, J.; Xu, Z. H.; Xu, X. M.; Zeng, Z. Z. *Nanoscale* **2012**, *4*, 5597.
- (265) Seo, M. H.; Choi, S. M.; Kim, H. J.; Kim, W. B. *Electrochem. Commun.* **2011**, *13*, 182.
- (266) Zhao, Y. C.; Zhan, L.; Tian, J. N.; Nie, S. L.; Ning, Z. *Electrochim. Acta* **2011**, *56*, 1967.
- (267) Liu, R.; Zhou, H. H.; Liu, J.; Yao, Y.; Huang, Z. Y.; Fu, C. P.; Kuang, Y. F. *Electrochem. Commun.* **2013**, *26*, 63.
- (268) Chen, X. J.; Yasin, F. M.; Eggers, P. K.; Boulos, R. A.; Duan, X. F.; Lamb, R. N.; Iyer, K. S.; Raston, C. L. *RSC Adv.* **2013**, *3*, 3213.
- (269) Yang, J.; Deng, S. Y.; Lei, J. P.; Ju, H. X.; Gunasekaran, S. *Biosens. Bioelectron.* **2011**, *29*, 159.
- (270) Jiang, Y. Y.; Lu, Y. Z.; Li, F. H.; Wu, T. S.; Niu, L.; Chen, W. *Electrochem. Commun.* **2012**, *19*, 21.
- (271) Wang, Y. X.; Balbuena, P. B. *J. Phys. Chem. B* **2005**, *109*, 18902.
- (272) Wang, Y.; Sheng, Z. M.; Yang, H. B.; Jiang, S. P.; Li, C. M. *Int. J. Hydrogen Energy* **2010**, *35*, 10087.
- (273) Awasthi, R.; Singh, R. N. *Int. J. Hydrogen Energy* **2012**, *37*, 2103.
- (274) Wang, J.; Qin, Y. L.; Liu, X.; Zhang, X. B. *J. Mater. Chem.* **2012**, *22*, 12468.
- (275) Chai, J.; Li, F. H.; Hu, Y. W.; Zhang, Q. X.; Han, D. X.; Niu, L. *J. Mater. Chem.* **2011**, *21*, 17922.
- (276) Liu, M. M.; Lu, Y. Z.; Chen, W. *Adv. Funct. Mater.* **2013**, *23*, 1289.
- (277) Awasthi, R.; Singh, R. N. *Catal. Sci. Technol.* **2012**, *2*, 2428.
- (278) Bong, S.; Uhm, S.; Kim, Y. R.; Lee, J.; Kim, H. *Electrocatalysis* **2010**, *1*, 139.
- (279) Choi, S. M.; Seo, M. H.; Kim, H.; Kim, W. B. *Synth. Met.* **2011**, *161*, 2405.
- (280) Li, Y. Z.; Yu, Y.; Wang, J. G.; Song, J.; Li, Q.; Dong, M. D.; Liu, C. J. *Appl. Catal., B* **2012**, *125*, 189.
- (281) Seo, M. H.; Choi, S. M.; Seo, J. K.; Noh, S. H.; Kim, W. B.; Han, B. *Appl. Catal., B* **2013**, *129*, 163.
- (282) Herzing, A. A.; Kiely, C. J.; Carley, A. F.; Landon, P.; Hutchings, G. J. *Science* **2008**, *321*, 1331.
- (283) Wei, W. T.; Chen, W. *Int. J. Smart Nano Mater.* **2013**, *4*, 62.
- (284) Lu, Y. Z.; Wei, W. T.; Chen, W. *Chin. Sci. Bull.* **2012**, *57*, 41.
- (285) Lim, E. J.; Choi, S. M.; Seo, M. H.; Kim, Y.; Lee, S.; Kim, W. B. *Electrochem. Commun.* **2013**, *28*, 100.
- (286) Liu, X.; Wang, X. Y.; He, P. Y.; Yi, L. H.; Liu, Z. L.; Yi, X. *J. Solid State Electrochem.* **2012**, *16*, 3929.
- (287) Xiong, Z. G.; Zhang, L. L.; Ma, J. Z.; Zhao, X. S. *Chem. Commun.* **2010**, *46*, 6099.
- (288) Liu, S.; Tian, J. Q.; Wang, L.; Li, H. L.; Zhang, Y. W.; Sun, X. P. *Macromolecules* **2010**, *43*, 10078.
- (289) Li, Y.; Fan, X. B.; Qi, J. J.; Ji, J. Y.; Wang, S. L.; Zhang, G. L.; Zhang, F. B. *Mater. Res. Bull.* **2010**, *45*, 1413.
- (290) Hu, Y. J.; Jin, J. A.; Wu, P.; Zhang, H.; Cai, C. X. *Electrochim. Acta* **2010**, *56*, 491.
- (291) Zhou, K. F.; Zhu, Y. H.; Yang, X. L.; Li, C. Z. *Electroanalysis* **2010**, *22*, 259.
- (292) Cho, S. J.; Suri, A.; Mei, X. G.; Ouyang, J. Y. *RSC Adv.* **2013**, *3*, 1201.
- (293) Chen, Y.; Shen, Y. Y.; Sun, D.; Zhang, H. Y.; Tian, D. B.; Zhang, J. R.; Zhu, J. J. *Chem. Commun.* **2011**, *47*, 11733.
- (294) Yang, X.; Xu, M. S.; Qiu, W. M.; Chen, X. Q.; Deng, M.; Zhang, J. L.; Iwai, H.; Watanabe, E.; Chen, H. Z. *J. Mater. Chem.* **2011**, *21*, 8096.
- (295) Li, J.; Liu, C. Y. *Eur. J. Inorg. Chem.* **2010**, *1244*.
- (296) Kong, B. S.; Geng, J. X.; Jung, H. T. *Chem. Commun.* **2009**, *2174*.
- (297) Vinodgopal, K.; Neppolian, B.; Lightcap, I. V.; Grieser, F.; Ashokkumar, M.; Kamat, P. V. *J. Phys. Chem. Lett.* **2010**, *1*, 1987.
- (298) Goncalves, G.; Marques, P. A. A. P.; Granadeiro, C. M.; Nogueira, H. I. S.; Singh, M. K.; Gracio, J. *Chem. Mater.* **2009**, *21*, 4796.
- (299) Pasricha, R.; Gupta, S.; Srivastava, A. K. *Small* **2009**, *5*, 2253.

- (300) Shen, J. F.; Shi, M.; Li, N.; Yan, B.; Ma, H. W.; Hu, Y. Z.; Ye, M. X. *Nano Res.* **2010**, *3*, 339.
- (301) Li, J.; Liu, C. Y.; Liu, Y. *J. Mater. Chem.* **2012**, *22*, 8426.
- (302) Le, Z. G.; Liu, Z. R.; Qian, Y.; Wang, C. Y. *Appl. Surf. Sci.* **2012**, *258*, 5348.
- (303) Zhang, Q. X.; Ren, Q. Q.; Miao, Y. Q.; Yuan, J. H.; Wang, K. K.; Li, F. H.; Han, D. X.; Niu, L. *Talanta* **2012**, *89*, 391.
- (304) Lu, Y. Z.; Jiang, Y. Y.; Wei, W. T.; Wu, H. B.; Liu, M. M.; Niu, L.; Chen, W. *J. Mater. Chem.* **2012**, *22*, 2929.
- (305) Zhang, Z.; Xu, F. G.; Yang, W. S.; Guo, M. Y.; Wang, X. D.; Zhang, B. L.; Tang, J. L. *Chem. Commun.* **2011**, *47*, 6440.
- (306) Li, F. H.; Yang, H. F.; Shan, C. S.; Zhang, Q. X.; Han, D. X.; Ivaska, A.; Niu, L. *J. Mater. Chem.* **2009**, *19*, 4022.
- (307) Huang, J.; Zhang, L. M.; Chen, B. A.; Ji, N.; Chen, F. H.; Zhang, Y.; Zhang, Z. *J. Nanoscale* **2010**, *2*, 2733.
- (308) Gong, J. M.; Zhou, T.; Song, D. D.; Zhang, L. Z. *Sens. Actuators, B* **2010**, *150*, 491.
- (309) Lu, G.; Li, H.; Liusman, C.; Yin, Z. Y.; Wu, S. X.; Zhang, H. *Chem. Sci.* **2011**, *2*, 1817.
- (310) Huang, X.; Zhou, X. Z.; Wu, S. X.; Wei, Y. Y.; Qi, X. Y.; Zhang, J.; Boey, F.; Zhang, H. *Small* **2010**, *6*, 513.
- (311) Fu, C. P.; Kuang, Y. F.; Huang, Z. Y.; Wang, X.; Du, N. N.; Chen, J. H.; Zhou, H. H. *Chem. Phys. Lett.* **2010**, *499*, 250.
- (312) Zhao, B.; Liu, Z. R.; Fu, W. Y.; Yang, H. B. *Electrochim. Commun.* **2013**, *27*, 1.
- (313) Zhou, Y. Z.; Yang, J.; Cheng, X. N.; Zhao, N.; Sun, H. B.; Li, D. *RSC Adv.* **2013**, *3*, 3391.
- (314) Lu, G. H.; Mao, S.; Park, S.; Ruoff, R. S.; Chen, J. H. *Nano Res.* **2009**, *2*, 192.
- (315) Lefevre, M.; Dodelet, J. P.; Bertrand, P. *J. Phys. Chem. B* **2002**, *106*, 8705.
- (316) Lee, J. S.; Park, G. S.; Kim, S. T.; Liu, M. L.; Cho, J. *Angew. Chem., Int. Ed.* **2013**, *52*, 1026.
- (317) Wiesener, K. *Electrochim. Acta* **1986**, *31*, 1073.
- (318) Schulenburg, H.; Stankov, S.; Schunemann, V.; Radnik, J.; Dorbandt, I.; Fiechter, S.; Bogdanoff, P.; Tributsch, H. *J. Phys. Chem. B* **2003**, *107*, 9034.
- (319) Gojkovic, S. L.; Gupta, S.; Savinell, R. F. *Electrochim. Acta* **1999**, *45*, 889.
- (320) Sawaguchi, T.; Itabashi, T.; Matsue, T.; Uchida, I. *J. Electroanal. Chem.* **1990**, *279*, 219.
- (321) Hung, T. F.; Tu, M. H.; Tsai, C. W.; Chen, C. J.; Liu, R. S.; Liu, W. R.; Lo, M. Y. *Int. J. Hydrogen Energy* **2013**, *38*, 3956.
- (322) Gupta, S.; Tryk, D.; Bae, I.; Aldred, W.; Yeager, E. *J. Appl. Electrochem.* **1989**, *19*, 19.
- (323) Koslowski, U. I.; Abs-Wurmbach, I.; Fiechter, S.; Bogdanoff, P. *J. Phys. Chem. C* **2008**, *112*, 15356.
- (324) Bae, I. T.; Tryk, D. A.; Scherson, D. A. *J. Phys. Chem. B* **1998**, *102*, 4114.
- (325) Bezerra, C. W. B.; Zhang, L.; Lee, K. C.; Liu, H. S.; Marques, A. L. B.; Marques, E. P.; Wang, H. J.; Zhang, J. *J. Electrochim. Acta* **2008**, *53*, 4937.
- (326) Ye, S. Y.; Vlijh, A. K. *Electrochim. Commun.* **2003**, *5*, 272.
- (327) Choi, J. Y.; Hsu, R. S.; Chen, Z. W. *J. Phys. Chem. C* **2010**, *114*, 8048.
- (328) Wang, H.; Cote, R.; Faubert, G.; Guay, D.; Dodelet, J. P. *J. Phys. Chem. B* **1999**, *103*, 2042.
- (329) Lefevre, M.; Dodelet, J. P.; Bertrand, P. *J. Phys. Chem. B* **2000**, *104*, 11238.
- (330) Chung, H. T.; Johnston, C. M.; Artyushkova, K.; Ferrandon, M.; Myers, D. J.; Zelenay, P. *Electrochim. Commun.* **2010**, *12*, 1792.
- (331) Zhang, Y. Z.; Mo, G. Q.; Li, X. W.; Ye, J. S. *J. Power Sources* **2012**, *197*, 93.
- (332) Parvez, K.; Yang, S. B.; Hernandez, Y.; Winter, A.; Turchanin, A.; Feng, X. L.; Mullen, K. *ACS Nano* **2012**, *6*, 9541.
- (333) Morozan, A.; Campidelli, S.; Filoromo, A.; Jousselme, B.; Palacin, S. *Carbon* **2011**, *49*, 4839.
- (334) Zhang, C. Z.; Hao, R.; Yin, H.; Liu, F.; Hou, Y. L. *Nanoscale* **2012**, *4*, 7326.
- (335) Kamiya, K.; Hashimoto, K.; Nakanishi, S. *Chem. Commun.* **2012**, *48*, 10213.
- (336) Tsai, C. W.; Tu, M. H.; Chen, C. J.; Hung, T. F.; Liu, R. S.; Liu, W. R.; Lo, M. Y.; Peng, Y. M.; Zhang, L.; Zhang, J. J.; Shy, D. S.; Xing, X. K. *RSC Adv.* **2011**, *1*, 1349.
- (337) Byon, H. R.; Suntivich, J.; Shao-Horn, Y. *Chem. Mater.* **2011**, *23*, 3421.
- (338) Li, S. Z.; Hu, Y. Y.; Xu, Q.; Sun, J.; Hou, B.; Zhang, Y. P. *J. Power Sources* **2012**, *213*, 265.
- (339) Choi, J. Y.; Higgins, D.; Chen, Z. W. *J. Electrochem. Soc.* **2012**, *159*, B87.
- (340) Jahan, M.; Bao, Q. L.; Loh, K. P. *J. Am. Chem. Soc.* **2012**, *134*, 6707.
- (341) Guo, S. J.; Zhang, S.; Wu, L. H.; Sun, S. H. *Angew. Chem., Int. Ed.* **2012**, *51*, 11770.
- (342) Tributsch, H.; Koslowski, U. I.; Dorbandt, I. *Electrochim. Acta* **2008**, *53*, 2198.
- (343) Warner, J. H.; Rummeli, M. H.; Bachmatiuk, A.; Wilson, M.; Buchner, B. *ACS Nano* **2010**, *4*, 470.
- (344) Mao, Y.; Yuan, J.; Zhong, J. *J. Phys.: Condens. Matter* **2008**, *20*, 115209.
- (345) Olson, T. S.; Pylypenko, S.; Kattel, S.; Atanassov, P.; Kiefer, B. *J. Phys. Chem. C* **2010**, *114*, 15190.
- (346) Wang, J.; Zhou, J.; Hu, Y. F.; Regier, T. *Energy Environ. Sci.* **2013**, *6*, 926.
- (347) Chen, S.; Zhu, J. W.; Wang, X. *J. Phys. Chem. C* **2010**, *114*, 11829.
- (348) Wu, J. J.; Zhang, D.; Wang, Y.; Wan, Y.; Hou, B. R. *J. Power Sources* **2012**, *198*, 122.
- (349) Yang, S. B.; Cui, G. L.; Pang, S. P.; Cao, Q.; Kolb, U.; Feng, X. L.; Maier, J.; Mullen, K. *ChemSusChem* **2010**, *3*, 236.
- (350) Wang, Z. H.; Du, Y. L.; Zhang, F. Y.; Zheng, Z. X.; Zhang, Y. Z.; Wang, C. M. *J. Solid State Electrochem.* **2013**, *17*, 99.
- (351) Yuasa, M.; Yamaguchi, A.; Itsuki, H.; Tanaka, K.; Yamamoto, M.; Oyaizu, K. *Chem. Mater.* **2005**, *17*, 4278.
- (352) Yuan, X. X.; Zeng, X.; Zhang, H. J.; Ma, Z. F.; Wang, C. Y. *J. Am. Chem. Soc.* **2010**, *132*, 1754.
- (353) Kim, S. K.; Jeon, S. *Electrochim. Commun.* **2012**, *22*, 141.
- (354) Fleischmann, M.; Korinek, K.; Pletcher, D. *J. Electroanal. Chem.* **1971**, *31*, 39.
- (355) Amjad, M.; Pletcher, D.; Smith, C. *J. Electrochim. Soc.* **1977**, *124*, 203.
- (356) Singh, R. N.; Singh, A.; Anindita; Mishra, D. *Int. J. Hydrogen Energy* **2008**, *33*, 6878.
- (357) Tehrani, R. M. A.; Ab Ghani, S. *Fuel Cells* **2009**, *9*, 579.
- (358) Stradiotto, N. R.; Toghill, K. E.; Xiao, L.; Moshar, A.; Compton, R. G. *Electroanalysis* **2009**, *21*, 2627.
- (359) Martinez-Huerta, M. V.; Rojas, S.; de la Fuente, J. L. G.; Terreros, P.; Pena, M. A.; Fierro, J. L. G. *Appl. Catal., B* **2006**, *69*, 75.
- (360) Zhao, X. H.; Fuji, M.; Shirai, T.; Watanabe, H.; Takahashi, M. *J. Am. Ceram. Soc.* **2011**, *94*, 1167.
- (361) Danaee, I.; Jafarian, M.; Forouzandeh, F.; Gobal, F.; Mahjani, M. G. *Int. J. Hydrogen Energy* **2008**, *33*, 4367.
- (362) Lv, X. Y.; Xu, Z. H.; Yan, Z. X.; Li, X. H. *Electrocatalysis* **2011**, *2*, 82.
- (363) Liu, Q.; Jin, J. T.; Zhang, J. Y. *ACS Appl. Mater. Interfaces* **2013**, *5*, 5002.
- (364) Yang, J. H.; Tan, J.; Yang, F.; Li, X. Y.; Liu, X. H.; Ma, D. *Electrochim. Commun.* **2012**, *23*, 13.
- (365) Jafarian, M.; Mahjani, M. G.; Heli, H.; Gobal, F.; Heydarpoor, M. *Electrochim. Commun.* **2003**, *5*, 184.
- (366) Zhang, L. R.; Zhao, J.; Li, M.; Ni, H. T.; Zhang, J. L.; Feng, X. M.; Ma, Y. W.; Fan, Q. L.; Wang, X. Z.; Hu, Z.; Huang, W. *New J. Chem.* **2012**, *36*, 1108.
- (367) Elzatahyry, A. A.; Abdulla, A. M.; El-Din, T. A. S.; Al-Enizi, A. M.; Maarouf, A. A.; Galal, A.; Hassan, H. K.; El-Ads, E. H.; Al-Theyab, S. S.; Al-Ghamdi, A. A. *Int. J. Electrochim. Sci.* **2012**, *7*, 3115.

- (368) Lambert, T. N.; Davis, D. J.; Lu, W.; Limmer, S. J.; Kotula, P. G.; Thuli, A.; Hungate, M.; Ruan, G. D.; Jin, Z.; Tour, J. M. *Chem. Commun.* **2012**, *48*, 7931.
- (369) Tian, X. K.; Zhao, X. Y.; Zhang, L. D.; Yang, C.; Pi, Z. B.; Zhang, S. X. *Nanotechnology* **2008**, *19*, 215711.
- (370) Tehrani, R. M. A.; Ab Ghani, S. J. *Electrochim. Soc.* **2008**, *155*, K199.
- (371) Zhou, R. F.; Zheng, Y.; Hulicova-Jurcakova, D.; Qiao, S. Z. J. *Mater. Chem. A* **2013**, *1*, 13179.
- (372) Liang, Y. Y.; Li, Y. G.; Wang, H. L.; Dai, H. J. *J. Am. Chem. Soc.* **2013**, *135*, 2013.
- (373) Yan, X. Y.; Tong, X. L.; Zhang, Y. F.; Han, X. D.; Wang, Y. Y.; Jin, G. Q.; Qin, Y.; Guo, X. Y. *Chem. Commun.* **2012**, *48*, 1892.
- (374) Cheng, F. Y.; Zhang, T. R.; Zhang, Y.; Du, J.; Han, X. P.; Chen, J. *Angew. Chem., Int. Ed.* **2013**, *52*, 2474.
- (375) Yang, C. C.; Hsu, S. T.; Chien, W. C.; Shih, M. C.; Chiu, S. J.; Lee, K. T.; Wang, C. L. *Int. J. Hydrogen Energy* **2006**, *31*, 2076.
- (376) Roche, I.; Chainet, E.; Chatenet, M.; Vondrak, J. *J. Phys. Chem. C* **2007**, *111*, 1434.
- (377) Cheng, F. Y.; Su, Y.; Liang, J.; Tao, Z. L.; Chen, J. *Chem. Mater.* **2010**, *22*, 898.
- (378) Qian, Y.; Lu, S. B.; Gao, F. L. *Mater. Lett.* **2011**, *65*, 56.
- (379) Lee, J. S.; Lee, T.; Song, H. K.; Cho, J.; Kim, B. S. *Energy Environ. Sci.* **2011**, *4*, 4148.
- (380) Wu, J. J.; Zhang, D.; Wang, Y.; Wan, Y. *Electrochim. Acta* **2012**, *75*, 305.
- (381) Zhang, R. Z.; Chen, W. J. *Mater. Chem. A* **2013**, *1*, 11457.
- (382) Paraknowitsch, J. P.; Thomas, A. *Energy Environ. Sci.* **2013**, *6*, 2839.
- (383) Liu, Y.; Wu, P. Y. *ACS Appl. Mater. Interfaces* **2013**, *5*, 3362.
- (384) Lai, L. F.; Potts, J. R.; Zhan, D.; Wang, L.; Poh, C. K.; Tang, C. H.; Gong, H.; Shen, Z. X.; Jianyi, L. Y.; Ruoff, R. S. *Energy Environ. Sci.* **2012**, *5*, 7936.
- (385) Lu, Z. J.; Bao, S. J.; Gou, Y. T.; Cai, C. J.; Ji, C. C.; Xu, M. W.; Song, J.; Wang, R. Y. *RSC Adv.* **2013**, *3*, 3990.
- (386) Park, J. E.; Jang, Y. J.; Kim, Y. J.; Song, M. S.; Yoon, S.; Kim, D. H.; Kim, S. J. *Phys. Chem. Chem. Phys.* **2014**, *16*, 103.
- (387) Seredych, M.; Bandosz, T. J. *Carbon* **2014**, *66*, 227.
- (388) Seredych, M.; Idrobo, J. C.; Bandosz, T. J. *J. Mater. Chem. A* **2013**, *1*, 7059.
- (389) Ma, Y. W.; Sun, L. Y.; Huang, W.; Zhang, L. R.; Zhao, J.; Fan, Q. L.; Huang, W. *J. Phys. Chem. C* **2011**, *115*, 24592.
- (390) Lee, J. S.; Jo, K.; Lee, T.; Yun, T.; Cho, J.; Kim, B. S. *J. Mater. Chem. A* **2013**, *1*, 9603.
- (391) Chen, P.; Xiao, T. Y.; Qian, Y. H.; Li, S. S.; Yu, S. H. *Adv. Mater.* **2013**, *25*, 3192.
- (392) Jin, Z. P.; Nie, H. G.; Yang, Z.; Zhang, J.; Liu, Z.; Xu, X. J.; Huang, S. M. *Nanoscale* **2012**, *4*, 6455.
- (393) Lyth, S. M.; Nabae, Y.; Islam, N. M.; Kuroki, S.; Kakimoto, M.; Miyata, S. J. *Nanosci. Nanotechnol.* **2012**, *12*, 4887.
- (394) Lyth, S. M.; Nabae, Y.; Islam, N. M.; Kuroki, S.; Kakimoto, M.; Miyata, S. J. *Electrochim. Soc.* **2011**, *158*, B194.
- (395) Lyth, S. M.; Nabae, Y.; Moriya, S.; Kuroki, S.; Kakimoto, M.; Ozaki, J.; Miyata, S. J. *Phys. Chem. C* **2009**, *113*, 20148.
- (396) Zhai, H. S.; Cao, L.; Xia, X. H. *Chin. Chem. Lett.* **2013**, *24*, 103.
- (397) Feng, Y. X.; Yao, X. L.; Wang, M.; Hu, Z. P.; Luo, X. G.; Wang, H. T.; Zhang, L. X. *J. Chem. Phys.* **2013**, *138*, 164706.
- (398) Ma, Y. W.; Zhang, L. R.; Li, J. J.; Ni, H. T.; Li, M.; Zhang, J. L.; Feng, X. M.; Fan, Q. L.; Hu, Z.; Huang, W. *Chin. Sci. Bull.* **2011**, *56*, 3583.
- (399) Yang, S. B.; Feng, X. L.; Wang, X. C.; Mullen, K. *Angew. Chem., Int. Ed.* **2011**, *50*, 5339.
- (400) Zhou, Y. F.; Zhang, G. Q.; Chen, J.; Yuan, G. E.; Xu, L.; Liu, L. F.; Yang, F. L. *Electrochim. Commun.* **2012**, *22*, 69.
- (401) Unni, S. M.; Bhange, S. N.; Anothumakkool, B.; Kurungot, S. *ChemPlusChem* **2013**, *78*, 1296.
- (402) Unni, S. M.; Devulapally, S.; Karjule, N.; Kurungot, S. J. *Mater. Chem.* **2012**, *22*, 23506.
- (403) Jeon, I. Y.; Choi, H. J.; Jung, S. M.; Seo, J. M.; Kim, M. J.; Dai, L. M.; Baek, J. B. *J. Am. Chem. Soc.* **2013**, *135*, 1386.
- (404) Ahmed, M. S.; Jeon, S. J. *Power Sources* **2012**, *218*, 168.
- (405) Wang, L.; Ambrosi, A.; Pumera, M. *Angew. Chem., Int. Ed.* **2013**, *52*, 13818.
- (406) Huang, J. Y.; Ding, F.; Yakobson, B. I.; Lu, P.; Qi, L.; Li, J. *Proc. Natl. Acad. Sci. U.S.A.* **2009**, *106*, 10103.
- (407) Gass, M. H.; Bangert, U.; Bleloch, A. L.; Wang, P.; Nair, R. R.; Geim, A. K. *Nat. Nanotechnol.* **2008**, *3*, 676.
- (408) Gomez-Navarro, C.; Meyer, J. C.; Sundaram, R. S.; Chuvalin, A.; Kurasch, S.; Burghard, M.; Kern, K.; Kaiser, U. *Nano Lett.* **2010**, *10*, 1144.
- (409) Meyer, J. C.; Geim, A. K.; Katsnelson, M. I.; Novoselov, K. S.; Booth, T. J.; Roth, S. *Nature* **2007**, *446*, 60.
- (410) Mkhoyan, K. A.; Contryman, A. W.; Silcox, J.; Stewart, D. A.; Eda, G.; Mattevi, C.; Miller, S.; Chhowalla, M. *Nano Lett.* **2009**, *9*, 1058.
- (411) Jung, I.; Vaupel, M.; Pelton, M.; Piner, R.; Dikin, D. A.; Stankovich, S.; An, J.; Ruoff, R. S. *J. Phys. Chem. C* **2008**, *112*, 8499.
- (412) Gunther, S.; Danhardt, S.; Ehrenspurger, M.; Zeller, P.; Schmitt, S.; Wintterlin, J. *ACS Nano* **2013**, *7*, 154.
- (413) Gunther, S.; Danhardt, S.; Wang, B.; Bocquet, M. L.; Schmitt, S.; Wintterlin, J. *Nano Lett.* **2011**, *11*, 1895.
- (414) Ferrari, A. C.; Meyer, J. C.; Scardaci, V.; Casiraghi, C.; Lazzeri, M.; Mauri, F.; Piscanec, S.; Jiang, D.; Novoselov, K. S.; Roth, S.; Geim, A. K. *Phys. Rev. Lett.* **2006**, *97*, 187401.
- (415) Cancado, L. G.; Jorio, A.; Ferreira, E. H. M.; Stavale, F.; Achete, C. A.; Capaz, R. B.; Moutinho, M. V. O.; Lombardo, A.; Kulmala, T. S.; Ferrari, A. C. *Nano Lett.* **2011**, *11*, 3190.
- (416) Dresselhaus, M. S.; Jorio, A.; Hofmann, M.; Dresselhaus, G.; Saito, R. *Nano Lett.* **2010**, *10*, 751.
- (417) Ferrari, A. C. *Solid State Commun.* **2007**, *143*, 47.
- (418) Obraztsov, A. N.; Tyurnina, A. V.; Obraztsova, E. A.; Zolotukhin, A. A.; Liu, B. H.; Chin, K. C.; Wee, A. T. S. *Carbon* **2008**, *46*, 963.
- (419) Casiraghi, C. *Phys. Status Solidi RRL* **2009**, *3*, 175.
- (420) Das, A.; Pisana, S.; Chakraborty, B.; Piscanec, S.; Saha, S. K.; Waghmare, U. V.; Novoselov, K. S.; Krishnamurthy, H. R.; Geim, A. K.; Ferrari, A. C.; Sood, A. K. *Nat. Nanotechnol.* **2008**, *3*, 210.
- (421) Hassan, H. M. A.; Abdelsayed, V.; Khder, A. E. R. S.; AbouZeid, K. M.; Terner, J.; El-Shall, M. S.; Al-Resayes, S. I.; El-Azhary, A. A. *J. Mater. Chem.* **2009**, *19*, 3832.
- (422) Shin, H. J.; Kim, K. K.; Benayad, A.; Yoon, S. M.; Park, H. K.; Jung, I. S.; Jin, M. H.; Jeong, H. K.; Kim, J. M.; Choi, J. Y.; Lee, Y. H. *Adv. Funct. Mater.* **2009**, *19*, 1987.
- (423) Sun, Z. Z.; Yan, Z.; Yao, J.; Beitler, E.; Zhu, Y.; Tour, J. M. *Nature* **2010**, *468*, 549.
- (424) Liu, M. M.; Liu, R.; Chen, W. *Biosens. Bioelectron.* **2013**, *45*, 206.
- (425) Liu, M. M.; Chen, W. *Biosens. Bioelectron.* **2013**, *46*, 68.
- (426) Schultz, B. J.; Patridge, C. J.; Lee, V.; Jaye, C.; Lysaght, P. S.; Smith, C.; Barnett, J.; Fischer, D. A.; Prendergast, D.; Banerjee, S. *Nat. Commun.* **2011**, *2*, 372.
- (427) Dennis, R. V.; Schultz, B. J.; Jaye, C.; Wang, X.; Fischer, D. A.; Cartwright, A. N.; Banerjee, S. *J. Vac. Sci. Technol., B* **2013**, *31*, 041204.
- (428) Zhao, L. Y.; He, R.; Rim, K. T.; Schiros, T.; Kim, K. S.; Zhou, H.; Gutierrez, C.; Chockalingam, S. P.; Arguello, C. J.; Palova, L.; Nordlund, D.; Hybertsen, M. S.; Reichman, D. R.; Heinz, T. F.; Kim, P.; Pinczuk, A.; Flynn, G. W.; Pasupathy, A. N. *Science* **2011**, *333*, 999.
- (429) Shang, N. G.; Papakonstantinou, P.; McMullan, M.; Chu, M.; Stamboulis, A.; Potenza, A.; Dhesi, S. S.; Marchetto, H. *Adv. Funct. Mater.* **2008**, *18*, 3506.
- (430) Zhou, X. H.; Chen, Z. X.; Yan, D. H.; Lu, H. B. *J. Mater. Chem.* **2012**, *22*, 13506.
- (431) Jiang, Y. Y.; Lu, Y. Z.; Lv, X. Y.; Han, D. X.; Zhang, Q. X.; Niu, L.; Chen, W. *ACS Catal.* **2013**, *3*, 1263.
- (432) Xu, Y. X.; Bai, H.; Lu, G. W.; Li, C.; Shi, G. Q. *J. Am. Chem. Soc.* **2008**, *130*, 5856.
- (433) Sun, Y. Q.; Li, C.; Shi, G. Q. *J. Mater. Chem.* **2012**, *22*, 12810.

- (434) Li, Q. Q.; Zhang, S.; Dai, L. M.; Li, L. S. *J. Am. Chem. Soc.* **2012**, *134*, 18932.
- (435) Yang, Z.; Nie, H. G.; Chen, X.; Chen, X. H.; Huang, S. M. *J. Power Sources* **2013**, *236*, 238.
- (436) Park, M.; Lee, T.; Kim, B. S. *Nanoscale* **2013**, *5*, 12255.
- (437) Zheng, Y.; Jiao, Y.; Ge, L.; Jaroniec, M.; Qiao, S. Z. *Angew. Chem., Int. Ed.* **2013**, *52*, 3110.
- (438) Zhang, L. P.; Xia, Z. H. *J. Phys. Chem. C* **2011**, *115*, 11170.
- (439) Zhang, L. P.; Niu, J. B.; Dai, L.; Xia, Z. H. *Langmuir* **2012**, *28*, 7542.
- (440) Boukhvalov, D. W.; Son, Y. W. *Nanoscale* **2012**, *4*, 417.
- (441) Kong, X. K.; Chen, Q. W.; Sun, Z. Y. *ChemPhysChem* **2013**, *14*, 514.
- (442) Johll, H.; Wu, J.; Ong, S. W.; Kang, H. C.; Tok, E. S. *Phys. Rev. B* **2011**, *83*, 205408.
- (443) Li, Y. G.; Wang, H. L.; Xie, L. M.; Liang, Y. Y.; Hong, G. S.; Dai, H. J. *J. Am. Chem. Soc.* **2011**, *133*, 7296.
- (444) Okamoto, Y. *Chem. Phys. Lett.* **2006**, *420*, 382.
- (445) Zhou, M.; Zhang, A. H.; Dai, Z. X.; Zhang, C.; Feng, Y. P. *J. Chem. Phys.* **2010**, *132*, 194704.
- (446) Groves, M. N.; Chan, A. S. W.; Malardier-Jugroot, C.; Jugroot, M. *Chem. Phys. Lett.* **2009**, *481*, 214.
- (447) Akturk, O. U.; Tomak, M. *Phys. Rev. B* **2009**, *80*, 085417.
- (448) Liu, X.; Meng, C. G.; Han, Y. *J. Phys. Chem. C* **2013**, *117*, 1350.
- (449) Frank, I. W.; Tanenbaum, D. M.; Van der Zande, A. M.; McEuen, P. L. *J. Vac. Sci. Technol., B* **2007**, *25*, 2558.
- (450) Lee, C.; Wei, X. D.; Kysar, J. W.; Hone, J. *Science* **2008**, *321*, 385.
- (451) Bolotin, K. I.; Sikes, K. J.; Jiang, Z.; Klima, M.; Fudenberg, G.; Hone, J.; Kim, P.; Stormer, H. L. *Solid State Commun.* **2008**, *146*, 351.
- (452) Kuila, T.; Bose, S.; Khanra, P.; Mishra, A. K.; Kim, N. H.; Lee, J. H. *Biosens. Bioelectron.* **2011**, *26*, 4637.
- (453) Liu, Y. X.; Dong, X. C.; Chen, P. *Chem. Soc. Rev.* **2012**, *41*, 2283.
- (454) Zhu, S. J.; Zhang, J. H.; Tang, S. J.; Qiao, C. Y.; Wang, L.; Wang, H. Y.; Liu, X.; Li, B.; Li, Y. F.; Yu, W. L.; Wang, X. F.; Sun, H. C.; Yang, B. *Adv. Funct. Mater.* **2012**, *22*, 4732.
- (455) Pan, D. Y.; Guo, L.; Zhang, J. C.; Xi, C.; Xue, Q.; Huang, H.; Li, J. H.; Zhang, Z. W.; Yu, W. J.; Chen, Z. W.; Li, Z.; Wu, M. H. *J. Mater. Chem.* **2012**, *22*, 3314.
- (456) Wu, Z. S.; Zhou, G. M.; Yin, L. C.; Ren, W.; Li, F.; Cheng, H. M. *Nano Energy* **2012**, *1*, 107.
- (457) Leger, J. M. *J. Appl. Electrochem.* **2001**, *31*, 767.
- (458) Yoo, E.; Okata, T.; Akita, T.; Kohyama, M.; Nakamura, J.; Honma, I. *Nano Lett.* **2009**, *9*, 2255.
- (459) Xin, Y. C.; Liu, J. G.; Zhou, Y.; Liu, W. M.; Gao, J. A.; Xie, Y.; Yin, Y.; Zou, Z. G. *J. Power Sources* **2011**, *196*, 1012.
- (460) Kakaei, K.; Zhiani, M. *J. Power Sources* **2013**, *225*, 356.
- (461) Bong, S.; Kim, Y. R.; Kim, I.; Woo, S.; Uhm, S.; Lee, J.; Kim, H. *Electrochim. Commun.* **2010**, *12*, 129.
- (462) Wang, S. Y.; Jiang, S. P.; Wang, X. *Electrochim. Acta* **2011**, *56*, 3338.
- (463) Jha, N.; Jafri, R. I.; Rajalakshmi, N.; Ramaprabhu, S. *Int. J. Hydrogen Energy* **2011**, *36*, 7284.
- (464) Yu, X. W.; Pickup, P. G. *J. Power Sources* **2008**, *182*, 124.
- (465) Yang, S. D.; Shen, C. M.; Lu, X. J.; Tong, H.; Zhu, J. J.; Zhang, X. G.; Gao, H. J. *Electrochim. Acta* **2012**, *62*, 242.
- (466) Huang, H. J.; Wang, X. *J. Mater. Chem.* **2012**, *22*, 22533.
- (467) Wang, Y.; Liu, H. L.; Wang, L.; Wang, H. B.; Du, X.; Wang, F.; Qi, T.; Lee, J. M.; Wang, X. *J. Mater. Chem. A* **2013**, *1*, 6839.
- (468) Jin, T.; Guo, S. J.; Zuo, J. L.; Sun, S. H. *Nanoscale* **2013**, *5*, 160.
- (469) Pandey, R. K.; Lakshminarayanan, V. *J. Phys. Chem. C* **2009**, *113*, 21596.
- (470) Wang, S. Y.; Manthiram, A. *Electrochim. Acta* **2013**, *88*, 565.
- (471) Zhao, H.; Yang, J.; Wang, L.; Tian, C. G.; Jiang, B. J.; Fu, H. G. *Chem. Commun.* **2011**, *47*, 2014.
- (472) Lamy, C.; Rousseau, S.; Belgsir, E. M.; Coutanceau, C.; Leger, J. M. *Electrochim. Acta* **2004**, *49*, 3901.
- (473) Simoes, F. C.; dos Anjos, D. M.; Vigier, F.; Leger, J. M.; Hahn, F.; Coutanceau, C.; Gonzalez, E. R.; Tremiliosi, G.; de Andrade, A. R.; Olivi, P.; Kokoh, K. B. *J. Power Sources* **2007**, *167*, 1.
- (474) Fang, X.; Wang, L. Q.; Shen, P. K.; Cui, G. F.; Bianchini, C. *J. Power Sources* **2010**, *195*, 1375.
- (475) Jiang, F. X.; Yao, Z. Q.; Yue, R. R.; Du, Y. K.; Xu, J. K.; Yang, P.; Wang, C. Y. *Int. J. Hydrogen Energy* **2012**, *37*, 14085.
- (476) Singh, R. N.; Awasthi, R. *Catal. Sci. Technol.* **2011**, *1*, 778.
- (477) Sheng, W. C.; Gasteiger, H. A.; Shao-Horn, Y. *J. Electrochem. Soc.* **2010**, *157*, B1529.
- (478) Neyerlin, K. C.; Gu, W. B.; Jorne, J.; Gasteiger, H. A. *J. Electrochem. Soc.* **2007**, *154*, B631.
- (479) Carmo, M.; Paganin, V. A.; Rosolen, J. M.; Gonzalez, E. R. *J. Power Sources* **2005**, *142*, 169.
- (480) Genorio, B.; Strmcnik, D.; Subbaraman, R.; Tripkovic, D.; Karapetrov, G.; Stamenkovic, V. R.; Pejovnik, S.; Markovic, N. M. *Nat. Mater.* **2010**, *9*, 998.
- (481) Izhar, S.; Nagai, M. *Catal. Today* **2009**, *146*, 172.
- (482) Elezovic, N. R.; Babic, B. M.; Vracar, L. M.; Radmilovic, V. R.; Krstajic, N. V. *Phys. Chem. Chem. Phys.* **2009**, *11*, 5192.
- (483) Uchida, H.; Izumi, K.; Aoki, K.; Watanabe, M. *Phys. Chem. Chem. Phys.* **2009**, *11*, 1771.
- (484) Gotz, M.; Wendt, H. *Electrochim. Acta* **1998**, *43*, 3637.
- (485) Yeager, E. *Electrochim. Acta* **1984**, *29*, 1527.
- (486) Coutanceau, C.; Crouigneau, P.; Leger, J. M.; Lamy, C. *J. Electroanal. Chem.* **1994**, *379*, 389.
- (487) Sato, J.; Higurashi, K.; Fukuda, K.; Sugimoto, W. *Electrochemistry* **2011**, *79*, 337.
- (488) Wang, D. L.; Xin, H. L.; Wang, H. S.; Yu, Y. C.; Rus, E.; Muller, D. A.; DiSalvo, F. J.; Abruna, H. D. *Chem. Mater.* **2012**, *24*, 2274.
- (489) Gotoh, K.; Kinumoto, T.; Fujii, E.; Yamamoto, A.; Hashimoto, H.; Ohkubo, T.; Itadani, A.; Kuroda, Y.; Ishida, H. *Carbon* **2011**, *49*, 1118.
- (490) Toh, R. J.; Poh, H. L.; Sofer, Z.; Pumera, M. *Chem.-Asian J.* **2013**, *8*, 1295.
- (491) Bashyam, R.; Zelenay, P. *Nature* **2006**, *443*, 63.
- (492) Wang, S. Y.; Yu, D. S.; Dai, L. M.; Chang, D. W.; Baek, J. B. *ACS Nano* **2011**, *5*, 6202.
- (493) Zhang, C. Z.; Hao, R.; Liao, H. B.; Hou, Y. L. *Nano Energy* **2013**, *2*, 88.
- (494) He, C. Y.; Li, Z. S.; Cai, M. L.; Cai, M.; Wang, J. Q.; Tian, Z. Q.; Zhang, X.; Shen, P. K. *J. Mater. Chem. A* **2013**, *1*, 1401.
- (495) Zhao, Y.; Hu, C. G.; Hu, Y.; Cheng, H. H.; Shi, G. Q.; Qu, L. T. *Angew. Chem., Int. Ed.* **2012**, *51*, 11371.
- (496) Wu, J. J.; Zhang, D.; Wang, Y.; Hou, B. R. *J. Power Sources* **2013**, *227*, 185.
- (497) Lee, K. R.; Lee, K. U.; Lee, J. W.; Ahn, B. T.; Woo, S. I. *Electrochim. Commun.* **2010**, *12*, 1052.
- (498) Lin, Z. Y.; Waller, G.; Liu, Y.; Liu, M. L.; Wong, C. P. *Adv. Energy Mater.* **2012**, *2*, 884.



Synthesis of hydrothermally stable MCM-48 mesoporous molecular sieve at low cost of CTAB surfactant

Lingzhi Wang, Jinlong Zhang*, Feng Chen

Lab for Advanced Materials and Institute of Fine Chemicals, East China University of Science and Technology, 130 Meilong Road, Shanghai 200237, People's Republic of China

ARTICLE INFO

Article history:

Received 16 January 2009

Received in revised form 2 March 2009

Accepted 3 March 2009

Available online 11 March 2009

Keywords:

MCM-48

CTAB/Si

Crystallization temperature

Fluoride

Hydrothermal stability

ABSTRACT

The hydrothermally stable MCM-48 mesoporous molecular sieve was successfully prepared at extremely low cost of cetyltrimethylammonium bromide (CTAB) by carefully adjusting the synthesis conditions. The increasing of the crystallization temperature from 373 K to 423 K can dramatically reduce the CTAB surfactant amount for the preparation of MCM-48 from 0.65 to 0.1 of the CTAB/Si ratio. The effect of increasing crystallization temperature on the formation process of MCM-48 at low CTAB cost was carefully studied. The influences of OH⁻/Si ratio and fluoride addition to the structure stability of the MCM-48 material synthesized at CTAB/Si = 0.1 and 423 K were systematically studied by XRD patterns. Moreover, the combination of increasing crystallization temperature and adding small amount of fluoride ions can considerably improve the structure stability of MCM-48 when reducing the CTAB cost.

© 2009 Elsevier Inc. All rights reserved.

1. Introduction

MCM-48 has got high attentions mainly due to its attractive three-dimensional interwoven channel structure; however, its requirement for the high template surfactant cost such as CTAB and sensitivity to the crystallization conditions have seriously restricted its developments in the fields of catalysis, drug loading and separation. Most of the current researches about the application of mesoporous materials have focused on MCM-41 and SBA-15 [1–10]. In consideration of the excellent pore structure and to accelerate the application of MCM-48, many researchers have devoted their attentions on optimizing the synthesis conditions for MCM-48 by adjusting the crystallization temperature, crystallization time and adding assistants such as salts or cosurfactant [11–14]. Among those challenges for the synthesis of MCM-48, reducing the high CTAB surfactant cost is the most attractive and important one in consideration of the environmental protection. It is reported that adding cosurfactant such as OP-10 can reduce the CTAB amount [15–20]. Moreover, using self-prepared GEMINI surfactant instead of CTAB can also prepare MCM-48 at low cost of surfactant [21–25]. These methods are all effective; however, it sounds better and is more economic if MCM-48 can be synthesized only by using cheap CTAB as the template instead of adding expensive cosurfactant or using self-made surfactant.

In this paper, we reported the results about the specific influence of crystallization temperature to the CTAB amount for the synthesis of MCM-48. It was found the CTAB amount gradually reduced with the increasing crystallization temperature. The combination of increasing the crystallization temperature and adding NaF can form hydrothermally stable MCM-48 at extremely low CTAB/Si ratio. The formation mechanism and the optimum conditions for the formation of hydrothermally stable MCM-48 with low CTAB cost was carefully studied by XRD patterns.

2. Experimental section

2.1. Synthesis of MCM-48 mesoporous molecular sieve

The typical synthesis procedure for MCM-48 was as follows: 10 mL tetraethyl orthosilicate (TEOS) and 56 mL H₂O were mixed and stirred for about 30 min, and then solid NaOH was directly added to the solution. After that, solid NaF powder was introduced to the mixture and stirred until the appearance of white silicates gel. Subsequently, solid cetyltrimethylammonium bromide powder (CTAB) was added under vigorous stirring. The mixture was stirred for 1 h at room temperature. Finally, it was transferred to an autoclave and crystallized at various temperatures. The molar composition for the reactants is as follows: 1SiO₂:xNaOH:yCTAB:70H₂O:zNaF, where x = 0.45–0.55, y = 0–0.65 and z = 0–0.4. The solid product (as-synthesized sample) was collected by filtration, dried in air at 353 K and calcined at 823 K for 6 h to remove the template.

* Corresponding author. Tel./fax: +86 21 64252062.
E-mail address: jlzhang@ecust.edu.cn (J. Zhang).

2.2. Characterization

X-ray powder diffraction (XRD) patterns of all samples were recorded on Rigaku D/MAX-2550 diffractometer using Cu K α radiation of wavelength 1.541 Å. Transmission electron micrographs (TEM) were taken on a 2000 JEOL electron microscope operating at 200 kV. The samples for TEM were prepared by dispersing a large number of particles in alcohol, and depositing onto a holey carbon film on a Cu grid. Magic-angle spinning (MAS) ^{29}Si NMR spectra were measured using a Bruker DMX 400 instrument. Data were obtained at 79.45 MHz with 90° pulses and 100 s recycle delays using zirconia rotors 4 mm in diameter spun at 5 kHz. The chemical shifts are given in ppm from external tetramethylsilane (TMS).

3. Results and discussion

3.1. Reduction of the CTAB amount for MCM-48

The CTAB amount can be gradually reduced by increasing the crystallization temperature. Fig. 1 shows the relationship between CTAB/Si ratio and the crystallization temperature for the synthesis of MCM-48. The crystallization time fixes for 24 h. From Fig. 1 we can find that a well-ordered MCM-48 can be formed at CTAB/Si = 0.65 and 373 K, which is in accordance with the previous report by Monnier et al. [26]. This result indicates that the formation of MCM-48 generally needs high concentration of CTAB. The CTAB/Si ratio decreases to 0.3 when the crystallization temperature increases from 373 K to 403 K, and further decreases to 0.1 when the crystallization temperature increases to 423 K. These results clearly indicate that the increasing of the crystallization temperature is actually favorable for the formation of MCM-48 at low CTAB cost.

To study the formation mechanism and determine the optimum conditions for the formation of MCM-48 at low CTAB cost, we investigated the phase transformation processes of MCM-48 samples synthesized at CTAB/Si = 0.1 and 423 K by XRD patterns. The sample synthesized at 423 K experiences the phase transformation process of H(hexagonal phase) → C(cubic phase) → C + L(lamellar phase) → L within 72 h as seen from Fig. 2. The hexagonal phase

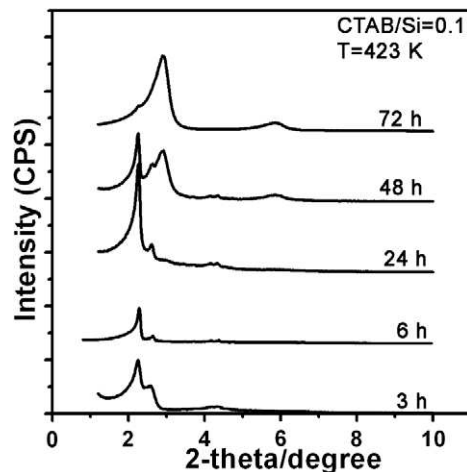


Fig. 2. XRD patterns of the sample synthesized at 423 K for various crystallization time.

is formed before the crystallization treatment (not shown) and the cubic phase is predominant only after crystallized for 3 h, which turns to the pure cubic phase after another 3 h. The cubic phase is still preserved and the pore structure ordering is greatly improved after totally crystallization for 24 h. However, the cubic phase is not the ultimate phase and is still flexible, which turns to the mixture of the cubic and lamellar phases when the crystallization time is prolonged to 48 h. It finally becomes the pure lamellar phase after crystallization for 72 h. We previously reported that the appropriate addition of fluoride ions can also play the role of CTAB-reduction [27]. Different with the sample synthesized at 423 K, the sample synthesized at the same CTAB/Si ratio with the aid of fluoride ions ($\text{F}/\text{Si} = 1.0$) experiences the phase transformation process of $\text{H} \rightarrow \text{C} \rightarrow \text{C} + \text{L} \rightarrow \text{C}$ within 72 h (Fig. 3), where the cubic phase formed within 6 h gradually change towards the lamellar phase and the mixture of cubic and lamellar phase is formed after 24 h, but the pure lamellar phase does not appear, even by finely varying the crystallization time (see the insert). The mixture phase finally transforms to the pure cubic phase after crystallization for 48 h and preserves to 72 h. The above result indicates that for the formation of MCM-48 with low CTAB cost by adding fluoride ions, the longer crystallization time is favorable to the formation of cubic phase.

The above phase transformation processes for the formation of cubic MCM-48 by increasing the crystallization temperature and adding fluoride ions can be explained by their influences to the surfactant packing parameter, g ($g = V/(a_0)L$, where V is the total volume of the surfactant chain plus any cosolvent organic molecules between the chains, a_0 is the effective headgroup area at the organic-inorganic interface, and L is the kinetic surfactant chain length). The higher crystallization temperature or the addition of fluoride ions can both accelerate the hydrolysis of TEOS and the subsequent formation of EtOH. The EtOH tends to locate in the outer shell of the surfactant due to their polarity and hydrogen bonding to water [28,29], leading to the increase of the g value. Smaller g favors the formation of MCM-41 ($1/3 < g < 1/2$) and larger g favors the formation of MCM-48 ($1/2 < g < 2/3$). As seen from Figs. 2 and 3, the hexagonal phase formed in the initial period transforms to the cubic $Ia3d$ phase only within 6 h either by crystallizing at 423 K or adding fluoride ions. Unlike the migration process of EtOH to the outer shell of a surfactant micelle, the silicates polymerization process causes the decrease of the negative charge density of the silicate network, which leads to the increase of the surfactant headgroup area and the subsequent decrease of the g value. With more and more Si-OH groups formed by TEOS hydro-

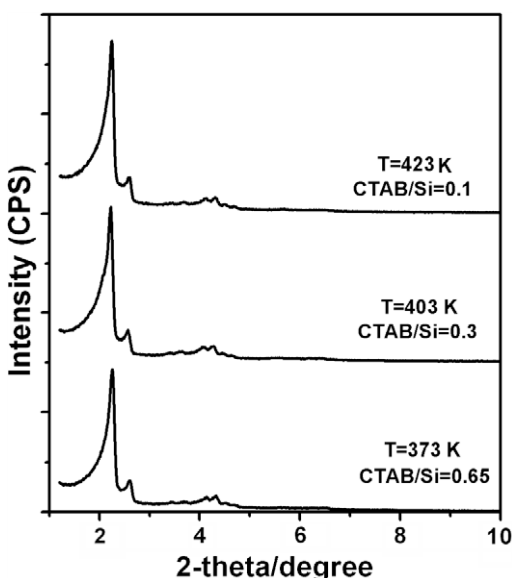


Fig. 1. The relationship between CTAB/Si ratio and the crystallization temperature for the synthesis of MCM-48.

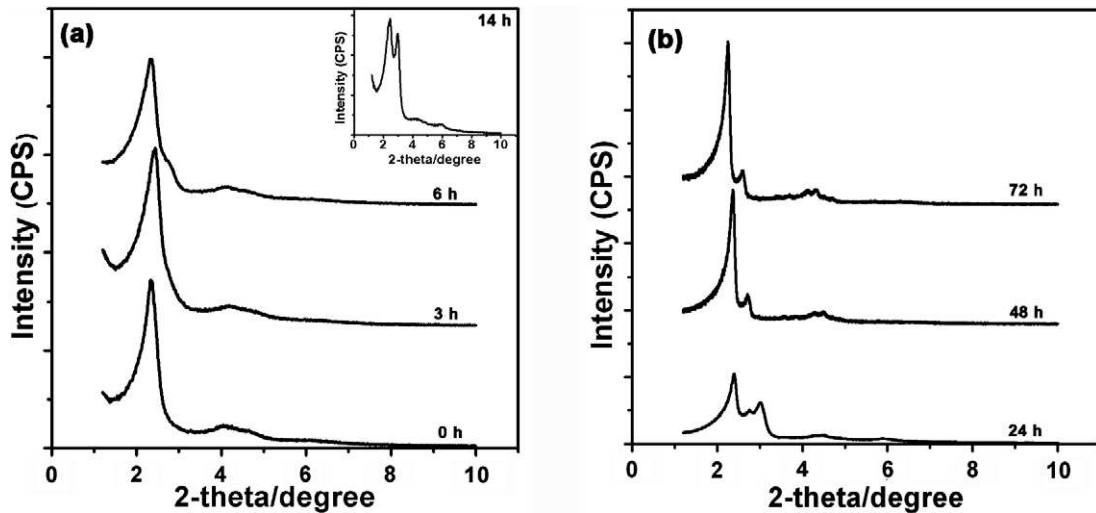


Fig. 3. XRD patterns of samples synthesized at 373 K after various crystallization time. The CTAB/Si and F/Si ratio are 0.1 and 1.0, respectively.

lysis, the Si-OH polymerization degree and its effect on the product phase are improved. The competition between the effects of EtOH migration and the silicates polymerization on the *g* value determines the phase transformation process. The reaction in the presence of fluoride ion produces the mixture phase of cubic and lamellar after crystallization for 24 h as seen from Fig. 3, indicating the EtOH migration further enlarges the micelle volume with the increasing time. However, the reaction carried at 423 K for 24 h does not show the appearance of the lamellar phase, which indicates the silicates polymerization speed is more accelerated at 423 K than that in the presence of fluoride ions within 24 h and the effect of EtOH migration on the *g* value is negligible. Fig. 4 shows the Si MAS NMR spectra of the sample synthesized at 423 K without fluoride ions for 12 h and 373 K with F/Si = 1.0 for 24 h. The silicates polymerization speed of the sample synthesized at 423 K is actually more accelerated than that with fluoride ions since the sample synthesized at 423 K only for 12 h has similar silicates polymerization degree to the sample synthesized at 373 K for 24 h with fluoride ions. However, the silica polymerization in basic condition will gradually increase the system pH as the reaction further proceeds [30], which prevents the complete silica polymerization and leads to the reversed silicates hydrolysis. As seen from Fig. 2, the reaction at 423 K for 72 h finally leads to

the formation of the lamellar phase, which is the joint effect of the silicates hydrolysis at higher pH and the EtOH migration. Contrarily, the reaction in the presence of fluoride ions does not lead to the formation of lamellar phase after 72 h. This can be attributed to the strong hydration tendency of fluoride ions, which can effectively dehydrate the hydration layer around silicates network with the reaction proceeding. The silicates polymerization reaches to a more sufficient degree without the hydration buffering and prevents the *g* increase caused by EtOH migration.

3.2. The influence of OH⁻/Si ratio and fluoride addition on the structure stability of MCM-48 synthesized at the low CTAB cost

The above results indicate that increasing the crystallization temperature can quickly form MCM-48 with low cost of CTAB surfactant. However, our further studies indicate that the structure stability of MCM-48 material becomes weaker with the decreasing CTAB amount. The sample synthesized at CTAB/Si = 0.1 and 423 K becomes amorphous after the removal of CTAB template by calcination at 823 K for 6 h. This result indicates that although increasing the crystallization temperature can effectively reduce the CTAB

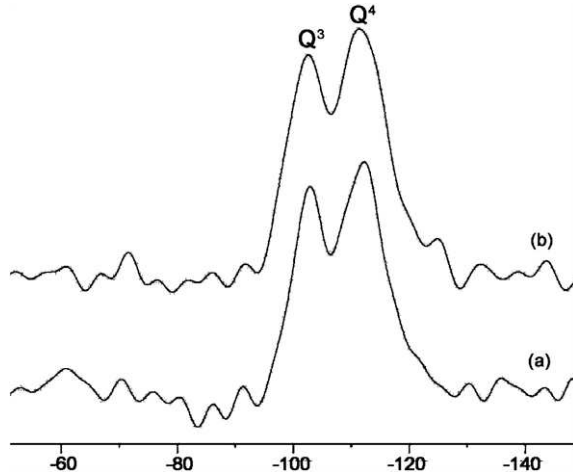


Fig. 4. ²⁹Si MAS NMR of samples synthesized at (a): CTAB/Si = 0.1 and F⁻/Si = 1.0 at 373 K for 24 h; (b): CTAB/Si = 0.1 at 423 K for 12 h.

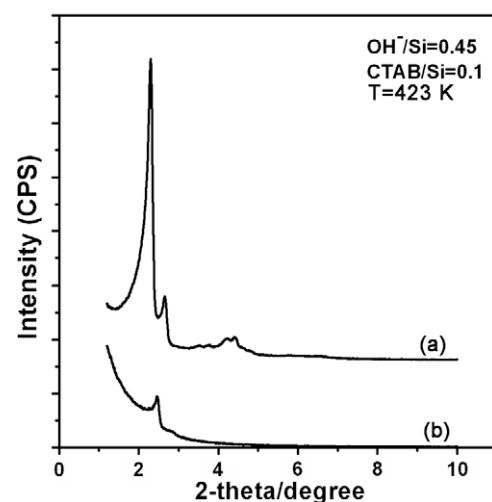


Fig. 5. XRD patterns of MCM-48 synthesized at OH⁻/Si = 0.45 and CTAB/Si = 0.1 before (a) and after (b) calcination treatment. The crystallization temperature is 423 K.

cost, the framework of the MCM-48 sample synthesized at low CTAB concentration is greatly weakened. In consideration that adjusting the initial OH^-/Si ratio can change the silicates condensation degree, we investigated the influence of the OH^-/Si ratio to the product phase and the framework stability by fixing the other reaction factors. Since the above sample is synthesized at $\text{OH}^-/\text{Si} = 0.5$, we further studied the product synthesized at $\text{OH}^-/\text{Si} = 0.45$ and 0.55, respectively. Fig. 5 shows that when the OH^-/Si ratio is set at 0.45, the product is also the cubic phase after crystallization for 24 h, but the calcination treatment proves that the framework stability does not get improved (not shown). Interestingly, when the OH^-/Si ratio is 0.55, the product transforms to the lamellar phase as shown in Fig. 6. So, the variation of OH^-/Si ratio cannot lead to the formation of structurally stable MCM-48 sample.

The silicates condensation and hydrolysis is a base catalyzed process. When the OH^-/Si ratio is 0.45, the silicates condensation degrees of the framework are comparatively low, leading to the poor structure stability. Although increasing the OH^-/Si ratio is advantageous to accelerate the silicates condensation, the structure stability of the sample synthesized at $\text{OH}^-/\text{Si} = 0.5$ is not much improved. The sample changes to lamellar phase when the OH^-/Si ratio further increases to 0.55. This is because MCM-48 is the intermediate phase of hexagonal MCM-41 and lamellar MCM-50, which may easily change to another phase. The formation of MCM-48 and the phase transformation to the other phase are influenced by the electronic interaction between silicates and CTAB template, the sil-

icates condensation and the EtOH distribution. In the conditions of $\text{OH}^-/\text{Si} = 0.55$, the TEOS hydrolysis is accelerated but the subsequent silicates condensation is weakened since the much higher OH^-/Si ratio leads to the hydrolysis of silicates. The EtOH produced from the hydrolysis of TEOS may distribute between the chains of the CTAB, and the less polymerized silicates leads to the improvement of the g value, thus leading to the final formation of lamellar MCM-50. Therefore, the simple adjusting of the OH^-/Si ratio cannot form the structurally stable MCM-48.

Our previous study showed that the appropriate addition of fluoride ions with $\text{F}/\text{Si} = 1.0$ can form MCM-48 at $\text{CTAB}/\text{Si} = 0.1$ with hydrothermal stability for 12 h in boiling water [27]. This result motivated us to investigate whether the addition of fluoride ions can improve the structure stability of the sample synthesized at $\text{CTAB}/\text{Si} = 0.1$ and 423 K. As seen from Fig. 7, when the fluoride ions with $\text{F}/\text{Si} = 0.1$ was added to the synthesis system at $\text{OH}^-/\text{Si} = 0.45$, the pore ordering of the sample is greatly deteriorated after calcination treatment. The structure stability is not considerably improved until the F/Si ratio increases to 0.4. When the OH^-/Si ratio increases to 0.5, the addition of fluoride ions with $\text{F}/\text{Si} = 0.1$ can dramatically improve the structure stability of the sample synthesized at $\text{CTAB}/\text{Si} = 0.1$ and 423 K, which preserves the cubic

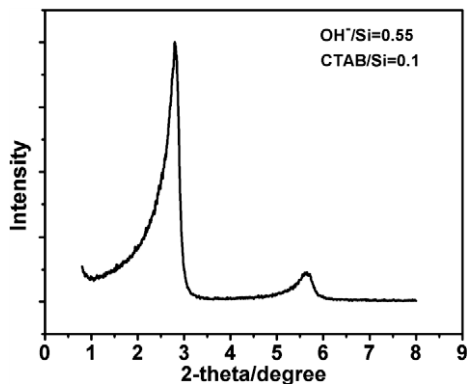


Fig. 6. XRD pattern of the sample synthesized at $\text{OH}^-/\text{Si} = 0.55$ and $\text{CTAB}/\text{Si} = 0.1$. The crystallization temperature is 423 K.

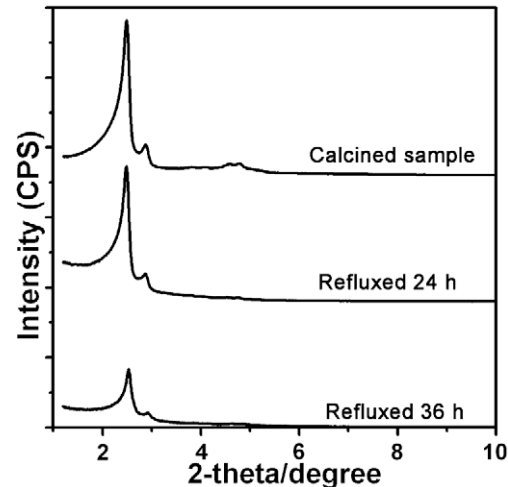


Fig. 8. XRD patterns of MCM-48 samples before and after hydrothermal stability, which is synthesized at 423 K, $\text{CTAB}/\text{Si} = 0.1$ and $\text{F}/\text{Si} = 0.1$.

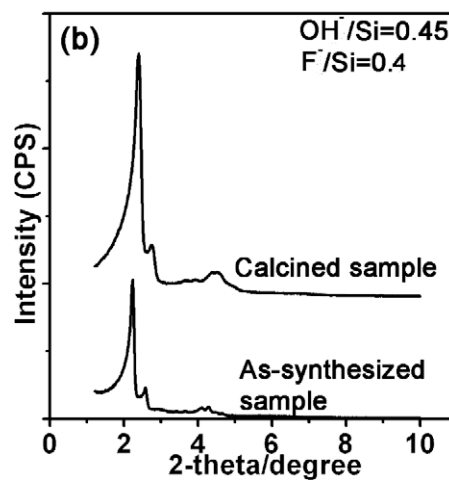
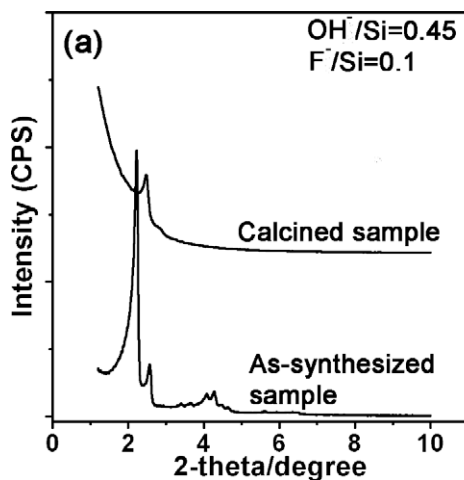


Fig. 7. XRD patterns of MCM-48 samples synthesized at 423 K in the presence of fluoride ions: (a) $\text{OH}^-/\text{Si} = 0.45$ and $\text{F}/\text{Si} = 0.1$; (b) $\text{OH}^-/\text{Si} = 0.45$ and $\text{F}/\text{Si} = 0.4$. The CTAB/Si is 0.1.

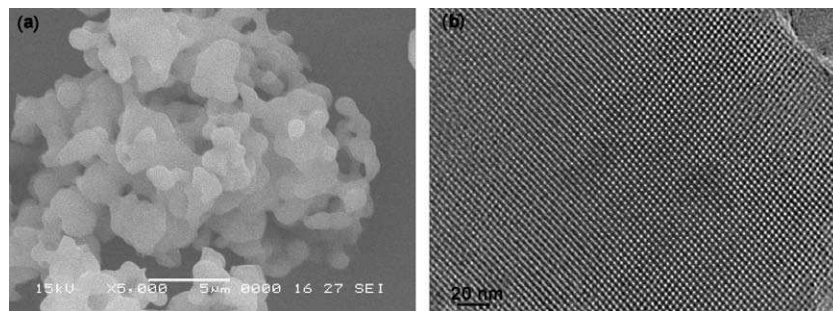


Fig. 9. SEM (a) and HRTEM (b) of the MCM-48 sample synthesized at CTAB/Si = 0.1, F⁻/Si = 0.1 and 423 K.

structure after calcination at 823 K. This sample even can endure the hydrothermal stability in boiling water for 24 h and the pore structure does not considerably decrease until 36 h as seen from Fig. 8. The above results indicate the structure stability of the MCM-48 sample synthesized at CTAB/Si = 0.1 and 423 K can be greatly improved by adding small amount of fluoride ions. Therefore, the combination of increasing the crystallization temperature and adding fluoride ions can lead to the formation of more hydrothermally stable MCM-48 sample.

Fig. 9 shows the particle morphology and the pore ordering of MCM-48 material by SEM and HRTEM. The samples are synthesized at CTAB/Si = 0.1, F/Si = 0.1 and 423 K (a and b). From the figures, we can find that the particles of the above sample have irregular shape and are agglomerated, which is similar to the sample synthesized in the general conditions [30] and indicates the fluoride addition and temperature increase have little influence on the particle morphology. Moreover, the pore is highly ordered as observed along the [001] (b) direction, which is in accordance with the results from XRD pattern. Therefore, the TEM result further confirms that the combination of increasing crystallization temperature and adding small amount of fluoride ions can synthesize high-quality MCM-48 materials with the low cost of CTAB template.

4. Conclusion

This paper shows the result that increasing the crystallization temperature can effectively reduce the CTAB amount for the synthesis of cubic MCM-48. Studies on the formation process for the MCM-48 T 423 K indicate the best crystallization time is 24 h. Further prolonging the crystallization time leads to the formation of lamellar phase. However, the sample obtained is not strong enough to endure the calcination treatment, and the structure stability cannot be improved by changing the OH⁻/Si ratio. The addition of fluoride ions is an effective way to improve the structure stability, and the addition amount decreases with the increasing OH⁻/Si ratio of the synthesis system. The sample obtained by both increasing the crystallization temperature and adding fluoride ions has higher stability than that synthesized by simply adding fluoride ions.

Acknowledgment

This work has been supported by Morning Light Plan of Shanghai Education Development Foundation (2007CG040); Shanghai

Natural Science Foundation (08ZR1406100); Science and Technology Commission of Shanghai Municipality (07JC14015); National Basic Research Program of China (973 Program, 2007CB613306, 2004CB719500), the Research Fund for the Doctoral Program of Higher Education (20070251006) and the Ministry of Science and Technology of China (2006AA06Z379, 2007AA05Z303, 2006DFA52710).

References

- [1] T.D. Conesa, R. Mokaya, Z. Yang, *J. Catal.* 252 (2007) 1–10.
- [2] M.Z. Cai, J.C. Sha, *Catal. Commun.* 8 (2007) 1691–1696.
- [3] R.Y. Zhang, W. Ding, B. Tu, D.Y. Zhao, *Chem. Mater.* 19 (2007) 4379–4381.
- [4] Y.S. Chi, H.P. Lin, C.P. Mou, *Appl. Catal. A: Gen.* 284 (2005) 199.
- [5] D.R. Radu, C.Y. Lai, K. Jeftinija, E.W. Rowe, S. Jeftinija, V.S.-Y. Lin, *J. Am. Chem. Soc.* 126 (2004) 13216–13217.
- [6] J. Andersson, J. Rosenholm, S. Areva, M. Lindén, *Chem. Mater.* 16 (2004) 4160–4167.
- [7] M. Vallet-Regi, F. Balas, D. Arcos, *Angew. Chem. Int. Ed.* 46 (2007) 7548–7558.
- [8] A. Gabashvili, D.D. Medina, A. Gedanken, *J. Phys. Chem. B* 111 (2007) 11105–11110.
- [9] K.F. Lam, K.L. Yeung, G. McKay, *Environ. Sci. Technol.* 41 (2007) 3329–3334.
- [10] Y. Sakamoto, K. Nagata, K. Yogo, *Micropor. Mesopor. Mater.* 101 (2007) 303–311.
- [11] M.L. Pena, Q. Kan, A. Corma, *Micropor. Mesopor. Mater.* 44 (2001) 9–16.
- [12] W. Zhao, L. Kong, Y.F. Luo, Q.Z. Li, *Micropor. Mesopor. Mater.* 100 (2007) 111–117.
- [13] L.Z. Wang, Y.F. Shao, J.L. Zhang, *Micropor. Mesopor. Mater.* 100 (2007) 111–117.
- [14] L.Z. Wang, Y.F. Shao, J.L. Zhang, *Chem. Lett.* 35 (2006) 70–71.
- [15] F.X. Chen, L.M. Huang, Q.Z. Li, *Chem. Mater.* 9 (1997) 2685–2686.
- [16] F.X. Chen, F.B. Song, Q.Z. Li, *Micropor. Mesopor. Mater.* 29 (1999) 305–310.
- [17] L.D. Kong, S. Liu, X.W. Yan, Q.Z. Li, H.Y. He, *Micropor. Mesopor. Mater.* 81 (2005) 251–257.
- [18] R. Ryoo, S.H. Joo, J.M. Kim, *J. Phys. Chem. B* 103 (1999) 7435–7440.
- [19] S.R. Zhai, J.L. Zheng, J.A. Zou, D. Wu, Y.H. Sun, *J. Sol-Gel Sci. Technol.* 30 (2004) 149–155.
- [20] M. Kruck, M. Jaroniec, R. Ryoo, S.H. Joo, *Chem. Mater.* 12 (2000) 1414–1421.
- [21] P. Van Der Voort, F. Mathieu, F. Mees, E.F. Vansant, *J. Phys. Chem. B* 102 (1998) 8847–8851.
- [22] K. Czechura, A. Sayari, *Chem. Mater.* 18 (2006) 4147–4150.
- [23] S.H. Han, J. Xu, W.G. Hou, *J. Phys. Chem. B* 108 (2004) 15043–15048.
- [24] O. Collart, P. Van Der Voort, E.F. Vansant, D. Desplantier, A. Galarneau, F. Di Renzo, F. Fajula, *J. Phys. Chem. B* 105 (2001) 12771–12777.
- [25] M. Widemann, R. Anwander, *Chem. Mater.* 14 (2002) 1827–1831.
- [26] A. Monnier, F. Schüth, Q. Huo, D. Kumar, D. Margolese, R.S. Maxwell, G.D. Stucky, M. Krishnamurti, P. Petroff, A. Firouzi, M. Janicke, B.F. Chmelka, *Science* 261 (1993) 1299.
- [27] L.Z. Wang, J.L. Zhang, F. Chen, *J. Phys. Chem. C* 111 (2007) 13648–13651.
- [28] Q. Huo, R. Leon, P.M. Petroff, G.D. Stucky, *Science* 268 (1995) 1324.
- [29] Q. Huo, D.I. Margolese, G.D. Stucky, *Chem. Mater.* 8 (1996) 1147.
- [30] J. Xu, Z. Luan, H. He, W. Zhou, L. Kevan, *Chem. Mater.* 10 (1998) 3690.

Chemical Vapor Deposition Methods for the Controlled Preparation of Supported Catalytic Materials

Philippe Serp and Philippe Kalck*

*Laboratoire de Catalyse Chimie Fine et Polymères, Ecole Nationale Supérieure d'Ingénieurs en Arts Chimiques Et Technologiques,
118 Route de Narbone Toulouse 31077, France*

Roselyne Feurer

*CIRIMAT-UMR-CNRS/INPT/UPS, Ecole Nationale Supérieure d'Ingénieurs en Arts Chimiques Et Technologiques,
118 Route de Narbone Toulouse 31077, France*

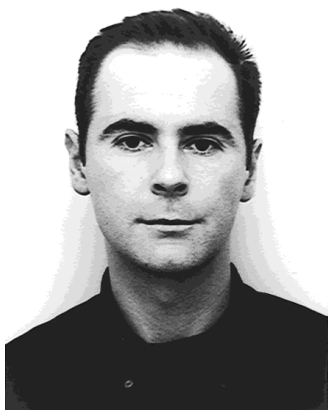
Received April 10, 2002

Contents

I. Introduction	3085	C. Noble Metals	3108
II. Studies on the Mechanisms of Adsorption and Reaction of Transition Metal Compounds on a Surface	3087	1. Gold	3108
A. Description of the Supports	3087	2. Palladium	3108
1. Silica	3087	3. Platinum	3109
2. Alumina	3089	4. Rhodium, Iridium, Ruthenium, and Osmium	3111
3. Titania	3090	5. Bimetallics	3111
4. Magnesia	3090	D. Miscellaneous	3113
5. Zeolites	3090	E. Conclusion	3116
6. New Mesoporous Molecular Sieves Supports	3090	IV. Overlayers, Thin Films, and Surface Modifications	3116
7. Carbons	3091	A. Introduction	3116
8. Conclusion	3091	B. Gas-Phase Deposition of SiO ₂ , GeO ₂ , Carbon, ZrO ₂ , and TiO ₂	3116
B. Interactions between a Zerovalent Organometallic Complex and the Support	3091	1. Gas-Phase Deposition of SiO ₂ on Al ₂ O ₃	3116
1. Zerovalent Carbonyl Metal Complexes of Molybdenum, Chromium, and Tungsten	3091	2. Gas-Phase Deposition of SiO ₂ on Other Oxides	3117
2. Other Zerovalent Metal Carbonyl Complexes	3094	3. Gas-Phase Deposition of GeO ₂ and Carbon	3118
3. Conclusion	3096	4. Gas-Phase Deposition of SiO ₂ on Zeolites	3118
C. Interactions between Rhodium(I) and (III) Precursors and a Support	3096	5. Gas-Phase Deposition of GeO ₂ or ZrO ₂ on Zeolites	3120
D. Miscellaneous Metal Precursors	3098	6. TiO ₂ Deposition from the Gas Phase	3120
E. Conclusion	3100	C. Gas-Phase Preparation of Catalytic Membranes	3122
III. Preparation and Surface Properties of CVD Catalysts	3100	D. Conclusion	3123
A. Zerovalent Metal Precursors	3100	V. Conclusions and Perspectives	3123
1. Chromium, Molybdenum, and Tungsten	3100	VI. Acknowledgments	3124
2. Nickel, Iron, Cobalt, Ruthenium, and Rhenium	3101	VII. References	3124
3. Miscellaneous	3103		
4. Conclusion	3103		
B. Other Non-Noble Metal Precursors	3103		
1. Iron	3103		
2. Nickel	3104		
3. Cobalt	3105		
4. Molybdenum	3105		
5. Vanadium	3106		
6. Chromium	3107		

I. Introduction

The controlled preparation of heterogeneous catalysts is a gentle art, and various procedures are at the disposal of chemists to elaborate efficiently supported catalysts.¹ However, perfectly designed catalysts still remain a challenge: indeed, an heterogeneous catalyst consists of a solid support and an active phase each presenting their own physical and chemical properties, which can evolve during the preparation. Many studies have been devoted to liquid-phase methods to prepare supported catalysts,



Philippe Serp was born in Montauban, France, in 1966. After receiving his Ph.D. from the Université Paul Sabatier de Toulouse in 1994 where he worked on CVD catalysts with Professor Philippe Kalck, he moved to Universidade de Porto (Portugal) to carry out postdoctoral research with Professor José-Luis Figueiredo on catalytic CVD to prepare carbon fibers. Since 1998, he has been Associate Professor in the Laboratoire de Catalyse, Chimie Fine et Polymères of ENSIACET. His current research interests include CVD and catalytic CVD preparation of nanostructured materials as nanoparticles or nanotubes, and the understanding of homogeneous carbonylation catalytic reactions.



Philippe Kalck was born near Besançon, France, in 1944. He studied in Toulouse, and received his Diplôme d'Ingénieur Chimiste from the Ecole Nationale Supérieure de Chimie de Toulouse (ENSCT) in 1967. He remained in Toulouse for his doctoral research under the supervision of Professor René Poilblanc, completing his Doctorat d'Etat in 1975. Up until 1980, he combined research at the Laboratoire de Chimie de Coordination (CNRS) with teaching at the ENSCT. At that point, he was appointed Professor at the Institut National Polytechnique de Toulouse (of which the ENSCT forms part), and started a research group devoted to the catalysis of carbonylation reactions that has now become the Laboratoire de Catalyse, Chimie Fine et Polymères in the Ecole Nationale Supérieure des Ingénieurs en Arts Chimiques et Technologiques. He is particularly attached to promoting links between industry and academia, and spent two years on secondment to Rhône-Poulenc Chimie between 1986 and 1988. His research interests include the design of highly selective catalysts and the molecular understanding of catalytic processes, fields in which he has published over 145 papers and supervised 45 Ph.D. students.

and so, according to our own experience and to their promising development, we have focused our attention on gas-phase procedures, i.e., chemical vapor deposition (CVD) and related techniques.

One review directly concerns the preparation of supported catalysts by CVD and related techniques and covers the literature until 1995.² Three other papers treat partially the subject,^{3–5} and several chapters in the book *Advanced Catalysts and Nanostructured Materials* published in 1996 are relevant



Roselyne Feurer is Associate Professor of solid-state chemistry in the Chemistry and Chemical Engineering School (ENSIACET), in Toulouse. She received her "Diplôme d'Ingénieur Chimiste" degree from this school, a M.Sc. from the University of Bordeaux, and a Ph.D. from the National Polytechnic Institute, Toulouse, in 1983. Her current research interests in CIRIMAT focus on the investigation of the fluidized bed MOCVD process for the preparation of noble metals supported catalysts.

to this topic.⁶ Our bibliography covers the period 1990–2001 and includes most of the former literature.

Investigations on the reactions between transition metal carbonyl complexes and solid surfaces to produce surface organometallic complexes and subsequent catalysts have been initiated in the early 80s.^{7–10} Then, similar studies on surface organometallic chemistry have been extended to other coordination compounds, some of them volatile.^{11–15} These detailed studies, including very recent sophisticated investigations, are analyzed in the first part of this review. Such an approach allows a good knowledge of the first step of the CVD process.

The second part is devoted to the catalysts reported in the literature that have been prepared by a gas-phase method. Among the various methods called CVD in the literature, we have introduced a classification to make a clear distinction between the one-step and the two- or more generally multistep processes. When possible, we have reported the relationship between the structure and the catalytic activity of these materials, and compared their performance to that of catalysts prepared by liquid-phase impregnation.

In a third part, we have taken into consideration the surface modifications of the support either to adjust the morphology, i.e., the pore opening size, or to control its acid base properties. The preparation of TiO₂ deposits on various silica or alumina supports is considered separately, since supported TiO₂ can present its own catalytic activity, or become a new support. Finally, preparations of catalytic membranes are also described. In this part of the review, the deposits do not involve nanoparticles, but can go from submonolayers, to thin films, including overlayers. This field is certainly the more recent one, the first review on the subject having appeared in 1996,¹⁶ and extended studies are missing, so that a complete rationalization is still difficult.

The present review shows that the study of the surface reactions between a catalyst precursor and

a support is a key point in the design of a supported catalyst. Our analysis has been focused on catalytic materials, but we had in our hands numerous papers from different fields in which this approach has been followed, for instance, for the elaboration of micro-electronic devices or for metallurgical coatings by CVD. Thus, this review can provide valuable information for researchers coming from different disciplines.

We believed that, as the CVD method allows the production of deposits in a controlled manner and on a large scale, it could be applied to the preparation of supported catalysts. Such a unified view has prompted us to review the literature with the point of view of the physicochemical processes that occur at a gas–solid interface in the course of the elaboration.

II. Studies on the Mechanisms of Adsorption and Reaction of Transition Metal Compounds on a Surface

Historically, Mond has demonstrated in 1890¹⁷ that $[\text{Ni}(\text{CO})_4]$ is a very convenient precursor for the preparation of pure nickel films by CVD at low temperature. Later on, it has been shown that these films are active hydrogenation catalysts.¹⁸ The progressive availability of various transition metal carbonyls has led to many studies on the preparation of supported catalysts from these precursors. Indeed, all homoleptic carbonyl complexes decompose at relatively low temperatures (<773 K) yielding zero-valent supported metals. Moreover, as the CO ligand is very sensitive to the electronic variations in the coordination sphere of a given metal, many studies from the 70s to the present day have been devoted to infrared measurements to follow the progressive transformation of a carbonyl complex when it is adsorbed on a surface.

The tremendous progress in the analytical techniques that occurred in the mid-80s allowed further investigations of the chemical and physical properties of surfaces down to the nanoscale level.¹⁹ Such investigative tools, as well as the great strides made in the synthesis of coordination compounds, have opened the new field of surface chemistry, and more particularly of surface organometallic chemistry. Studies on the early steps of film growth by organometallic chemical vapor deposition (OMCVD), and on the deposition of nanomaterials have appeared. Indeed, the OMCVD technique has moved toward systems in which the ratio between the substrate area and the gas-phase volume becomes larger (porous and/or finely divided supports, ultrathin films, small particles) so that the surface reactions become a crucial parameter. Thus, the interactions between the metallic species and the surface take such a great importance that it is necessary to have a deep knowledge of the surface itself.

For this reason, after a brief description of the main supports used in catalysis (metal oxides, activated carbons, zeolites), the first part of this review will deal with the interactions that have been clearly established between an organometallic complex and

a surface. Although our present objective is to focus on the gas-phase deposition methods, we will, when necessary, take into account the surface chemistry of organometallic complexes dissolved in an inert solvent to impregnate a support. A comprehensive table that covers the supports used, the precursors, the experimental conditions, and the characterization of the final material is given below (Table 1).

A. Description of the Supports

The supports usually used in catalysis, i.e., metal oxides, activated carbons, or zeolites are characterized by large specific areas and by the presence of anchoring sites on their surface. Among the most studied metal oxides, we find silica, alumina under different allotropic forms, magnesia, and titania. The specific area and the porosity vary greatly from one support to the other. According to IUPAC, three types of pores can be distinguished for a given support according to their size: micropores, less than 2 nm; mesopores, ranging from 2 to 50 nm; and macropores, greater than 50 nm. The types, as well as the concentration, of the anchoring groups have been investigated by thermogravimetric analysis, infrared spectroscopy, nuclear magnetic resonance spectrometry, or more occasionally, extended X-ray adsorption fine structure. The acid–base properties of the surfaces have also been characterized by infrared spectral studies of adsorbed molecules.²⁰

1. Silica

Micro-, meso- and macroporous silica can be prepared selectively. Thus, very high specific areas can be reached, until $800 \text{ m}^2 \text{ g}^{-1}$, but it is possible to obtain silica with low specific areas. The bulk of this solid consists of SiO_4 tetrahedra sharing their oxygen atoms. There exist several forms of amorphous and crystallized silica, among them α -quartz has been used as model support, most often the 0001 plane.^{21,22} It can be mentioned that spherical and flat nonporous supports can be also used, especially for specific studies.¹⁹ The fully hydrated surface of silica contains hydroxyl groups terminating the bulk with a concentration ranging from 4 to 6.5 OH nm^{-2} .^{19,23} They are isolated or bonded to vicinal OH groups through hydrogen bonds, and constitute a monolayer. This hydrophilic surface is covered by several layers of physisorbed water. Such a surface, with pK_a value of 4 to 7, depending on the methods of measurements, shows a weakly acidic behavior.

Physisorbed water can be rather easily removed by heating at 473 K, whereas silanol group elimination requires higher thermal treatments (Figure 1). Although there are some discrepancies between the temperature values published in the literature (presumably due to the pressure at which the experiments have been performed), the first step of dehydroxylation leads to isolated and geminal hydroxyl groups. Above 1073 K, only isolated OH groups still subsist, ca. 1 OH nm^{-2} , with the simultaneous formation of siloxane hydrophobic groups which preclude rehydration. Above 1100 K, complete dehydroxylation can be reached giving rise to more or less

Table 1. Selected Studies of Reactions of Transition Metal Compounds with the Surface of a Support

precursor	support	conditions	main identified species	ref
[Mo(CO) ₆]	Al ₂ O ₃ thin film <i>FH</i> ^a	295 K, 6.6 × 10 ⁻⁵ Pa	[Mo(CO) ₆] weakly adsorbed	46
	γ-Al ₂ O ₃ pellets <i>FH</i>	295 K, time dependence	[Mo(CO) ₆] _{ads} + [Mo(CO) ₅] _{Surf^b}	45
	γ-Al ₂ O ₃ pellets <i>PD</i>	295 K, outgassing	[Mo(CO) ₆] _{ads} → [Mo(CO) ₅] _{ads} → [Mo(CO) ₃] _{ads}	45
	γ-Al ₂ O ₃ wafer <i>FH</i>	373 K and heating	[Mo(CO) ₃] _{ads} → [Mo(CO) _{3-n}] _{ads}	49
	γ-Al ₂ O ₃ wafer <i>PD</i>	373 K	[Mo(CO) ₃] _{ads} more stable	49
	Al ₂ O ₃ film <i>FH</i>	80–175 K, UHV	[Mo(CO) ₅] _{ads} and [Mo(CO) ₃] _{ads}	50
	Al ₂ O ₃ film <i>FH</i>	205–450 K, UHV	[MoO ₂ (CO) _n] + (oxalates) _{ads}	50
	γ-Al ₂ O ₃ <i>PD</i>	373 K	[Mo(CO) ₅] _{ads}	58
	γ-Al ₂ O ₃ <i>PD</i>	773 K	Mo ⁶⁺ , Mo ⁰	58
	γ-Al ₂ O ₃ <i>PD</i>	573 K	Mo ⁴⁺ and Mo ⁰ or Mo ²⁺	59
	γ-Al ₂ O ₃ <i>HD</i>	573 K	Mo ⁰	59
	SiO ₂ <i>FH</i>	>283 K, vacuum	[Mo(CO) ₆] _{ads} , no stable subcarbonyl species	47
	SiO ₂ <i>PD</i>	326 K → 373 K, N ₂	partially decarbonylated Mo species	64
	TiO ₂ single crystal ^c	150 K	[Mo(CO) ₆] _{ads}	70
	TiO ₂ single crystal	400–700 K	no subcarbonyls, Mo ⁰ + C(graphitic or carbidic)	70
	NaY zeolite (673 K, vacuum)	295 K	[Mo(CO) ₆] _{ads} → [Mo(CO) ₅] _{ads}	73
	NaY zeolite (673 K, vacuum)	370 K	[Mo(CO) ₃] _{ads}	73
	NaY zeolite (673 K, vacuum)	373 K → 473 K	[Mo(CO) ₃] _{ads}	78
	NaY zeolite (623 K, vacuum)	298 K	[Mo(CO) ₆] _{ads} , 2 per cage	80
	NaY zeolite (623 K, vacuum)	623 K	Mo ⁰	80
	NaY zeolite (dehydrated)	673 K, vacuum	Mo ⁰	86
	HY zeolite (623 K)	673 K	Mo ⁵⁺	83
[Mo(<i>η</i> ³ -C ₃ H ₅) ₄]	HY zeolite	673 K	Mo ⁵⁺	165
[Cr(CO) ₆]	γ-Al ₂ O ₃ <i>FH</i>	283 K	[Cr(CO) ₆] _{ads}	47
	γ-Al ₂ O ₃ <i>FH</i>	>283 K, vacuum	decarbonylation, no stable subcarbonyl species	47
	γ-Al ₂ O ₃ <i>PD</i>	328 K	[Cr(CO) ₆] _{ads} , [CrCO] ₅] _{ads} – [Cr(CO) ₄] _{ads}	55
	γ-Al ₂ O ₃ <i>PD</i>	473 K	complete decarbonylation	55
	γ-Al ₂ O ₃ <i>HD</i>	298 K	[Cr(CO) ₆] _{ads}	60
	γ-Al ₂ O ₃ <i>HD</i>	298 K, outgassing	desorption of [Cr(CO) ₆] _{ads} + [Cr(CO) ₅] _{ads}	60
	SiO ₂ <i>PD</i> ^c	473 K, atm. pressure	Cr ⁿ⁺ , evolution of H ₂ , CH ₄ , CO, and CO ₂	67
	SiO ₂ <i>PD</i>	298 K	[Cr(CO) ₆] _{ads}	68
	SiO ₂ <i>PD</i>	423 K, static vacuum	complete decarbonylation	68
	NaX zeolite (673 K)	298 K	[Cr(CO) ₆] _{encapsulated}	76
	NaX zeolite (673 K)	373 K, outgassing	[Cr(CO) ₄] _{ads} and [Cr(CO) ₃] _{ads}	76
	NaX zeolite (673 K)	423 K	[Cr(CO) ₃] _{ads}	76
[Cr(neopentyl) ₄]	SiO ₂ <i>PD</i> (473 K)	298 K	-SiO–Cr(neopentyl) ₂	151
	SiO ₂ <i>PD</i> (473 K)	333 K	Cr ⁴⁺	151
	SiO ₂ <i>PD</i> (773 K)	298 K	-SiO–Cr(neopentyl) ₃	151
[Cr(acac) ₃]	SiO ₂ <i>PD</i>	473–553 K	-SiO–Cr(acac) ₂	160
	SiO ₂ <i>PD</i>	673 K, H ₂ O	Cr ³⁺	160
	SiO ₂ <i>PD</i>	673 K, O ₂	Cr ⁶⁺	160
[Cr(<i>η</i> ⁵ -C ₅ H ₅) ₂]	SiO ₂ <i>HD</i>	298 K	-SiO–Cr(<i>η</i> ⁵ -C ₅ H ₅)	161
[Cr(CO) ₃ (<i>η</i> ⁶ -C ₆ H ₆)]	γ-Al ₂ O ₃ <i>HD</i>	298 K	[Cr(CO) ₃ (<i>η</i> ⁶ -C ₆ H ₆)] _{ads}	162
	γ-Al ₂ O ₃ <i>HD</i>	333 K, outgassing	subcarbonyl species	162
	SiO ₂ <i>HD</i>	298 K	[Cr(CO) ₃ (<i>η</i> ⁶ -C ₆ H ₆)] _{ads}	163
	SiO ₂ <i>HD</i>	358 K	desorption of [Cr(CO) ₃ (<i>η</i> ⁶ -C ₆ H ₆)] _{ads}	163
[W(CO) ₆]	γ-Al ₂ O ₃ <i>PD</i>	473 K	[W(CO) ₃] _{ads}	54, 57
	γ-Al ₂ O ₃ <i>PD</i>	723 K	complete decarbonylation	54, 57
	NaY zeolite (623 K)	>473 K	W ⁰	89
	HY zeolite (623 K)	>473 K	W ⁵⁺	89
[Fe(CO) ₅]	SiO ₂ <i>PD</i>	298 K	[Fe(CO) ₅] weakly adsorbed	91
	SiO ₂ <i>PD</i>	298 K, outgassing	easy desorption of [Fe(CO) ₅]	91
	MgO <i>HD</i>	298 K	[CO] ₄ Fe(CO ₂) ²⁻ Mg ²⁺	95
	MgO <i>HD</i>	>350 K	Fe ⁰	95
	C (graphite)	298–300 K	[Fe(CO) ₅] physisorbed	97
	C (graphite)	>378 K	decarbonylation, Fe ⁰	97
	HY zeolite (623 K, vacuum)	298 K	[Fe(CO) ₅] physisorbed	98
	HY zeolite (623 K, vacuum)	333 K, outgassing	[Fe(CO) ₄]-zeolite	98
	HY zeolite (623 K, vacuum)	523 K, outgassing	Fe ²⁺	98
	Na zeolite (720 K, vacuum)	450 K	Fe ⁰	103
	γ-Al ₂ O ₃ <i>PD</i>	<423 K	zerovalent subcarbonyl	102
	γ-Al ₂ O ₃ <i>PD</i>	>573 K	Fe ²⁺	102

Table 1 (Continued)

precursor	support	conditions	main identified species	ref
[Fe ₃ (CO) ₁₂]	γ -Al ₂ O ₃ PD	313 K, vacuum	[HFe ₃ (CO) ₁₀](OAl \equiv)	96
	SiO ₂ PD	317 K, vacuum	[Fe ₃ (CO) ₁₂] weakly adsorbed	96
	HY (623 K, vacuum)	333 K, outgassing	[Fe ₃ (CO) ₁₂] _{ads}	98
	HY (623 K, vacuum)	523 K, outgassing	Fe ²⁺	98
[Co ₂ (CO) ₈]	SiO ₂ HD	298 K	[Co(CO) ₈] _{ads}	105, 106
	SiO ₂ HD	outgassing	[Co ₄ (CO) ₁₂] _{ads}	105, 106
	MgO HD	298 K	higher nuclearity clusters neutral and anionic	105, 106
	γ -Al ₂ O ₃ PD	sublimation, vacuum	[Co ₂ (CO) ₈], [Co ₄ (CO) ₁₂] and [Co(CO) ₄] ⁻ adsorbed	107
	γ -Al ₂ O ₃ PD	313 K	[Co ₄ (CO) ₁₂] _{ads}	108–111
	γ -Al ₂ O ₃ PD	520 K, outgassing	various oxides	108–111
	γ -Al ₂ O ₃ PD	293 K, O ₂	[Co ^{II}] ₄ moieties	108–111
	γ -Al ₂ O ₃ PD	773 K, O ₂	[Co ₃ O ₄] _n spinel-like particles	108–111
[Re ₂ (CO) ₁₀]	MgO film (111) HD	320 K	[Re(CO) ₄ (OMg \equiv) ₂]	118
	MgO film (111) HD	>400 K	Re(CO) ₃ (OMg \equiv) ₃	118
	MgO film (111) HD	>600 K	Re metal cluster	118
[RhCl(CO) ₂] ₂	SiO ₂ wafers, FH, PD or HD	298 K	[RhCl(CO) ₂] ₂ weakly adsorbed	122, 123
	γ -Al ₂ O ₃ wafers, PD	298 K	[Rh ^I (CO) ₂], [Rh ^I (CO)] + remaining Cl	123
	γ -Al ₂ O ₃ (100), –OH free	108 K	multilayer adsorption	127
	γ -Al ₂ O ₃ (100), –OH free	231 K	outer multilayer desorption	127
	γ -Al ₂ O ₃ (100), –OH free	270–573 K	only one monolayer left	127
	γ -Al ₂ O ₃ (100), –OH free	>623 K	Rh ⁰ and Cl (atomic ratio Cl/Rh=3)	127
	TiO ₂ [110]	300 K	[Rh ^I (CO) ₂] coordinate to 2 O _{surf} + remaining Cl	128–137
	TiO ₂ [110]	500 K	Rh ⁰ particles (+ Cl until 800 K)	128–137
	NaY, HY FH	353 K	[Rh ^I (CO) ₂]	138
[Rh(η^3 -C ₃ H ₅) ₃]	SiO ₂ ^d PD	298 K	[Rh (η^3 -C ₃ H ₅) ₂] grafted	142
	SiO ₂ ^d PD	623 K	Rh ⁰ particles	142
	TiO ₂ PD	293 K, H ₂	grafted Rh–H species	144, 145
[Cu(hfacac) ₂]	SiO ₂ FH, PD or HD	143 K	physisorption	154
	SiO ₂ FH, PD or HD	298 K	[Cu(hfacac) ₂] H bonded (–OH groups) + interaction with siloxane bridges	154
			hfacacH evolution + ill defined products and/or desorption	154
	SiO ₂ FH, PD or HD	673 K		

^a FH: fully hydroxylated; PD: partially dehydroxylated; HD: highly dehydroxylated. ^b Surf: –OH of the support. ^c The same studies has been performed for [Mo(CO)₆], [Cr(CO)₆], and [W(CO)₆]. ^d A similar study has been performed on Al₂O₃, TiO₂, and MgO. The order of reactivity for the grafting is TiO₂ > SiO₂ ≫ Al₂O₃ > MgO.

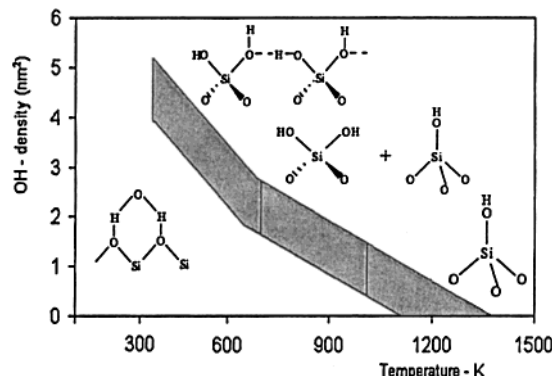


Figure 1. OH group density as a function of temperature pretreatment (adapted from ref 19).

strained Si–O–Si frameworks which present a weak Lewis acidity.

Preparation, physical and chemical characterization, as well as surface modification of silica have been described in detail by Vansant et al.²³

2. Alumina

The structural chemistry of alumina is richer and somewhat more complicated than that of silica because, according to the elaboration temperature and

the porosity, the crystalline forms are different. Generally, the specific areas of these supports are comparable to those of silica. Among the various allotropic forms, η -Al₂O₃ and in a lesser extent γ -Al₂O₃, whose lattices are close to a spinel structure, are the most commonly used supports in catalysis. The η -alumina presents a more acidic character. Knözinger and co-workers²⁴ have demonstrated (by infrared spectroscopy) five types of OH groups depending on the environment of the aluminum atoms in the defect spinel structure (Figure 2). A recent review dealing with the historical attempts to resolve the controversial structure of γ -alumina and including recent computational results has been published by Sohlberg and co-workers.²⁵

The total concentration of the OH groups on alumina ranges from 10 to 15 OH nm⁻² for a fully hydroxylated support (i.e., roughly three times the concentration on a silica). Half of these OH groups can be removed by heating at 650 K, and one-third more at 800 K. But even in the range 1173–1273 K, OH groups still remain on the surface.

Varying the temperature treatments can modify the acid–base properties of these supports. Indeed, at room temperature η - and γ -Al₂O₃ present a weak Brönsted acidity (OH groups) as well as Lewis basic

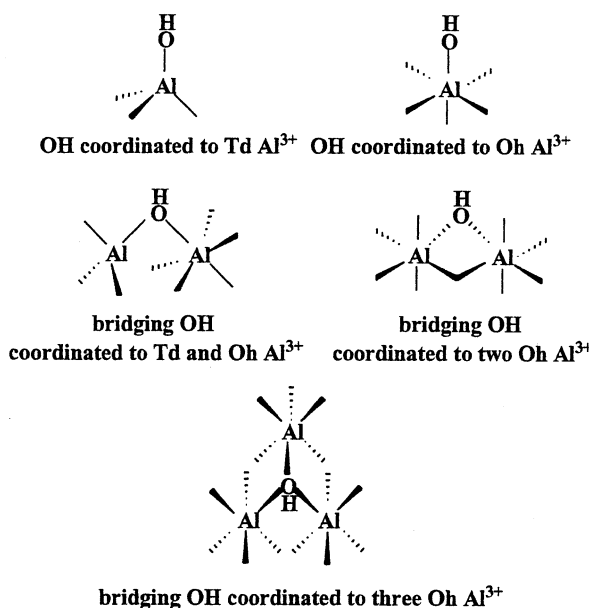


Figure 2. Different types of OH groups on the alumina surface (adapted from ref 24).

sites due to the presence of OH or O^{2-} , and Al^{3+} .²⁶ When physisorbed water is eliminated at 473 K, the Brönsted acidity is increased by elimination of the hydrogen interactions of water with the hydroxyl groups. Further heating until 900 K decreases this acidity (removal of OH groups) and causes the simultaneous presence of Lewis acidic (Al^{3+}) and basic (O^{2-}) sites. It is worth noting that heating alumina also induces significant modifications in the structure, which thus change the acid–base properties.

3. Titania

Generally, the specific areas of titania are somewhat lower than those of the two previous supports. Two allotropic forms are encountered: anatase at low temperatures and rutile at high temperatures. The most common commercial support contains 80% anatase and 20% rutile with a specific area of $50\text{ m}^2\text{ g}^{-1}$. A fully hydroxylated titania can reach 10 OH nm^{-2} ; dehydroxylation at 473 K induces a dramatic decrease in OH population (2 OH nm^{-2}). A complete dehydroxylation requires temperature of 1000 K. Moreover, the techniques of preparation of single crystals often used as models for adsorption studies need high temperatures, so that partially hydroxylated model surfaces are obtained. Due to the ionic character of this support, both Brönsted acidic and basic OH groups have been evidenced. This support is much more acidic than alumina but largely less basic than magnesia. However, the problem of the precise interpretation of the different hydroxyl groups of anatase has not been solved, as concluded in a recent review about surface chemistry of TiO_2 .²⁷

4. Magnesia

Magnesium oxide presents the simplest structure, i.e., rock-salt, and has been largely used as model support (100 face). It can also be prepared as large surface area powders ($>100\text{ m}^2\text{ g}^{-1}$) with hydroxyl

concentrations around 10 OH nm^{-2} . Dehydroxylation by heating leads to an OH concentration of 4 OH nm^{-2} at 850 K and 1 OH nm^{-2} remains even at 1073 K. Among the different oxide supports, MgO is the most basic and presents two types of sites: Mg–O–Mg and -OH groups, these latter groups being very weakly acidic in character.

Other oxides have been used, but less extensively studied, for instance, CaO , ZrO_2 , La_2O_3 , and CeO_2 , and will not be presented here.

5. Zeolites

Zeolites are built from SiO_4 and AlO_4 edge-sharing tetrahedra, and involve cations to neutralize the negative charge due to the presence of aluminum. The cations can be exchanged either by protons or transition metals, and their properties are thus modified. The arrangement of the various tetrahedra leads to a great variety of frameworks, which define channels and cages. Such low-density microporous materials show different thermal stability, depending on structural and compositional factors. A great number of zeolites can be synthesized by varying the SiO_2/Al_2O_3 ratio. The first generation of synthetic zeolites presents low silica-to-alumina ratios (<10): typical zeolites are A, X, Y, mordenite... The second generation, among which ZSM-5 is the most well-known, contains SiO_2/Al_2O_3 building blocks ratios >20.

This class of supports presents high specific surface areas (300 to $1000\text{ m}^2\text{ g}^{-1}$) with a controlled porosity, which stems from the presence of channels (0.4 to 0.7 nm) and supercages, the size of which being in the 1.14–1.4 nm range. Thus, they offer the possibility of restricting the particle size distribution of the metal particles and, at the same time, of imposing a steric influence on catalytic reactions. Their pores contain physisorbed water, which can be easily and reversibly removed by heating, without affecting the structure of the material. The concentration of OH groups in internal and external surface is usually around 2 mmol g^{-1} .

Among the great variety of zeolites, few of them are used in catalysis as supports, each of them having its own specificity, so that no more general description will be attempted in this review.

6. New Mesoporous Molecular Sieves Supports

Since 1992, the family of materials generically called M-41S has attracted the attention of many scientists working in the field of catalysis.^{28,29} Their synthesis, characterization, and catalytic properties have been recently reviewed.^{30,31} They present a uniform mesoporous structure (silicate or aluminosilicate) ordered in a hexagonal (MCM-41), cubic (MCM-48), or laminar (MCM-50) array. Their pore size may be tuned from ca. 2 to 10 nm by using different synthetic strategies. The surface area of these materials is usually higher than $700\text{ m}^2\text{ g}^{-1}$.

In the case of aluminosilicates, the Si/Al ratio governs the specific surface area, the pore volume, and the acidic properties of these materials. As in the case of zeolites, cation exchange can be performed to tune the acid–base properties. The high surface

area of MCM-41 together with the presence of silanol groups able to be functionalized have been of great use to support organometallic compounds, achieving high dispersion of the metallic phase.

Very recently, different groups of researchers have independently synthesized samples of a new class of hybrid porous material that incorporate organic components within a silica framework.^{32–34}

7. Carbons

The increasing importance of carbon materials in catalytic processes has been recently analyzed.³⁵ Carbon supports are generally graphitic materials, which can vary from highly oriented pyrolytic graphite (HOPG as model support) to quasi amorphous activated carbons. This latter kind of support, whose activation results from various oxidizing treatments, is by far the most used. They present a large surface area, near to $1000 \text{ m}^2 \text{ g}^{-1}$ essentially due to the presence of micropores. Although the chemistry of the carbon surfaces still needs a better understanding, in addition to the “graphene” sheets which provide aromatic CH groups, several acidic and basic groups have been evidenced.^{36,37} Carboxylic acid, anhydride, lactone, lactol, and hydroxyl groups have been characterized as weak acidic sites. About the basic properties, although less understood, quinone, cyclic ketone, and ether groups are reported, as well as the π electrons of the aromatic rings.

The concentrations and the nature of these surface functional groups can be modified by suitable thermal or chemical post-treatments.³⁸ Temperature programmed desorption (TPD) measurements allow one

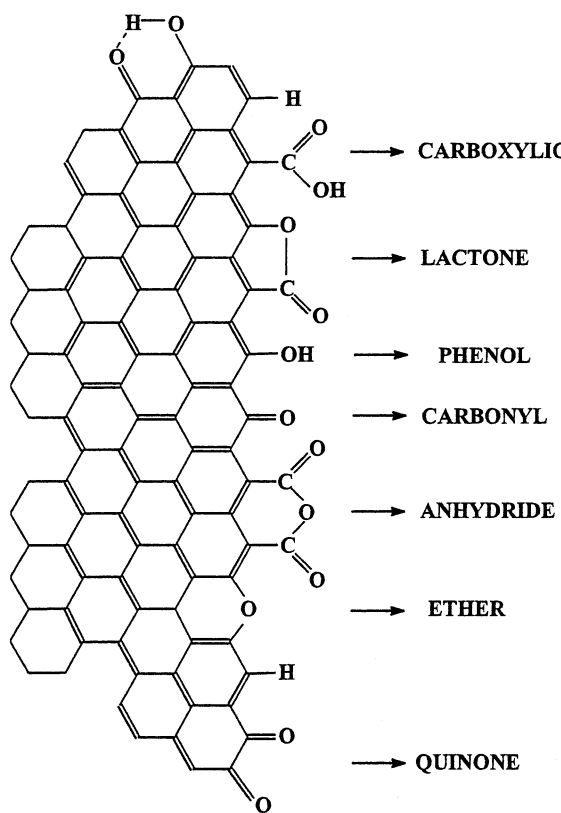


Figure 3. Surface containing oxygen groups on activated carbon (adapted from ref 38).

to follow the CO and CO_2 gas evolution arising from the decomposition of the surface groups and to show that all of them have disappeared at 1300 K. From this CO/ CO_2 evolution, the concentration of these groups can be estimated to $2\text{--}3.5 \text{ mmol g}^{-1}$. A schematic representation of these functions is shown in Figure 3.

Finally, it is worth mentioning that new forms of carbon such as fullerenes or carbon nanotubes have also been used recently as supports for heterogeneous catalysts.³⁹

8. Conclusion

It can be seen that the surface of any support contains various kinds of grafting sites. It is interesting to refer to the seminal view of Basset and Choplin⁴⁰ who consider these sites as rigid ligands as in molecular coordination chemistry. These surface ligands can bind to the metal, donating one electron (X ligand), or two (L ligand). Table 2 summarizes the various types of ligands, assuming the 18-electron rule is obeyed for the metal center.

Table 2. Types of Surface Ligands and Counting of Electrons^a

Type of surface ligand	Number of electrons given by this ligand to M	Examples
Z	0	$\text{Al}^{3+}, \text{Mg}^{2+}, \text{Ti}^{4+}, \dots$
X	1	$-\text{O}^- \text{M}$
L	2	$-\text{O} \rightarrow \text{M}$ $-\text{O} \begin{matrix} \nearrow \text{M} \\ \searrow \text{H} \end{matrix}$
X_2	2	$-\text{O} \begin{matrix} \nearrow \text{M} \\ \searrow \text{O} \end{matrix}$ $\text{M}=\text{O}$
XL	3	$-\text{O} \begin{matrix} \nearrow \text{M} \\ \searrow \text{M} \end{matrix}$
2X_2	4	$\text{M} \begin{matrix} \nearrow \text{O} \\ \searrow \text{O} \end{matrix}$

^a Adapted from ref 40.

B. Interactions between a Zerovalent Organometallic Complex and the Support

1. Zerovalent Carbonyl Metal Complexes of Molybdenum, Chromium, and Tungsten

Although these interactions have been largely described,^{41–44} we will focus our attention on the possible correlations, that we can deduce from the literature, between the gas-phase adsorption studies, the decarbonylation steps, and the nature of the final deposits, when available.

a. Alumina Support. Due to the high catalytic activity of deposits prepared from $[\text{Cr}(\text{CO})_6]$, $[\text{Mo}(\text{CO})_6]$, or $[\text{W}(\text{CO})_6]$ (mainly in polymerization or metathesis reactions) as well as to the importance of these precursors for the elaboration of coatings for metallurgic applications, a great number of studies

have been carried out on these three carbonyl complexes, especially by infrared and temperature programmed desorption (TPD). The early steps of adsorption and reactions on the surface of alumina have been studied in detail.

First of all, it appears clearly that the hydroxylation level of the surface influences the nature of the adsorbed species and of the resulting deposit. When vapors of $[\text{Mo}(\text{CO})_6]$ come in contact with a fully hydroxylated γ -alumina, physisorbed $[\text{Mo}(\text{CO})_6]$ species have been detected in the early stages. Indeed, the infrared spectra are consistent with a perturbation of the O_h symmetry, presumably due to an interaction between the oxygen atom of a surface OH group and the carbon atom of one CO ligand.⁴⁵ A study by inelastic electron tunneling spectroscopy⁴⁶ has allowed the proposal of an additional interaction between the oxygen atom of a CO ligand and an aluminum atom. The $\text{OC}\cdots\text{OH}$ surface interaction provides the labilization of the CO ligand in *cis*-position, so that the loss of one CO gives $\text{Mo}(\text{CO})_5(\text{L})$ where the sixth ligand is now an oxygen atom from a surface OH group.⁴⁵ Further CO loss occurs slowly to provide ill-defined $\text{Mo}(\text{CO})_x$ species, also called lower subcarbonyl species. If, still at room temperature, the system is placed for hours under reduced pressure, these subcarbonyl species are the only one present on the surface.

For chromium and tungsten, the physisorbed $[\text{M}(\text{CO})_6]$ species are the only one observed at room temperature, and, as in the case of $[\text{Mo}(\text{CO})_6]$ on silica, no subcarbonyls have been observed.⁴⁷

Heating at 373 K produces $\text{Mo}(\text{CO})_3$ fragments grafted onto the surface⁴⁸ by two different types of sites, which have not been clearly identified. A progressive decarbonylation occurs with further heating, and at 473 K complete decarbonylation occurs. EPR spectra have shown that molybdenum has been oxidized, mostly to Mo^{5+} . This oxidation is accompanied by a stoichiometric release of H_2 (from the hydroxyl protons), as shown by TPD experiments.⁴⁹ A more recent paper related to the synthesis of model catalysts under UHV from $[\text{Mo}(\text{CO})_6]$ on planar hydroxylated alumina films grown on molybdenum substrates has allowed the study of low loading catalysts.⁵⁰ Under these conditions, $[\text{Mo}(\text{CO})_6]$ adsorbs at 80 K and desorbs almost completely at 200 K, with only 2% of a monolayer reacting with the surface. The decarbonylation of the adsorbed carbonyl occurs between 80 and 175 K, and adsorbed $\text{Mo}(\text{CO})_5$ and $\text{Mo}(\text{CO})_3$ species are identified. On the basis of IR and XPS analysis, oxalate and $\text{Mo}^{\text{IV}}\text{O}_2(\text{CO})_x$ species are proposed to be formed when heating upon 205 K. TPD experiments have shown that the Mo^{4+} species is thermally stable up to 450 K, whereas the oxalate species decomposes at 300 K to form a bidentate carbonate species. Then, above 560 K, this latter carbonate species reacts to evolve CO, and molybdenum carbide is formed. It has been observed that, on partially dehydroxylated (50%) alumina films, the extent of decarbonylation and thus the oxalate coverage is decreased by 50%.

On a partially hydroxylated support (573–773 K, under vacuum) $[\text{Mo}(\text{CO})_6]$ is adsorbed in a first step

at room temperature. However, as acidic sites have appeared during the dehydroxylation process, the system evolves rapidly and an interaction between a CO ligand and two types of Lewis acidic sites takes place. As previously noted for the fully hydroxylated alumina, $\text{Mo}(\text{CO})_5$ is slowly obtained at room temperature, and an additional interaction between a CO ligand and an Al^{3+} surface ion is proposed.⁴⁵ Nevertheless, CPMAS solid state ^{13}C NMR measurements have shown that the $\text{Mo}(\text{CO})_5$ surface species can rotate around the surface–molybdenum bond, so that this $\text{CO}\cdots\text{Al}^{3+}$ interaction is certainly weak. Evidence is also provided that this $\text{Mo}(\text{CO})_5$ species presents some restricted mobility.⁵¹ Similarly, $\text{W}(\text{CO})_5$ and $\text{Cr}(\text{CO})_5$ surface species have been suggested in several papers.^{52,53} Recent thorough infrared studies carried out by Pakkanen and his group have allowed the assignment of the interactions of $\text{W}(\text{CO})_5$ with three types of sites: tetrahedral-, octahedral-, and defective surface Al^{3+} .⁵⁴ For $\text{Cr}(\text{CO})_5$, only one ν_{CO} band has been detected, together with a ν_{CO} band which has been assigned to $\text{Cr}(\text{CO})_4$.⁵⁵ For molybdenum, further decarbonylation, obtained by heating at 373 K under a stream of helium or overnight pumping, provides $\text{Mo}(\text{CO})_3$ bound to the surface which is stable until 473 K. A convincing scheme shows an octahedral environment for this species in which three coordination positions are occupied by three oxygen atoms from the support, and an oxygen atom of one CO ligand interacting with a surface Al^{3+} (Figure 4). However, some controversy exists in the literature concerning the existence of dimeric $\text{Mo}_2(\text{CO})_6$ species.^{45,51} The corresponding $\text{W}(\text{CO})_3$ species^{56,57} is quoted but not $\text{Cr}(\text{CO})_3$.^{52,55} The $\text{W}(\text{CO})_3$ moieties appears to be relatively stable, since it is observed, from $[\text{W}(\text{CO})_6]$, by TPD under a helium flow at 408 K. The decarbonylation reaction is reversible,⁵⁶ and $\text{W}(\text{CO})_3$ species decomposed above 623 K.⁵⁷ It is worth noting that these $\text{M}(\text{CO})_3$ species are to be considered as molybdenum(0), or tungsten(0) tricarbonyl complexes as the three other coordination positions are occupied by three oxygen donating ligands from the surface. TPD observations have shown that, when the temperature is increased, a redox reaction that depends on the OH concentration occurs between the metal center and the hydroxyl surface groups giving rise to H_2 and CO as well as some CO_2 and CH_4 evolution.^{56,58} The oxidation state of Mo or W varies largely, as evaluated from the H_2 evolution in TPD, and has been shown by XPS to be Mo^{4+} , Mo^{2+} , in addition to Mo^0 .⁵⁹ Chromium has been less studied, but a similar oxidation reaction pathway occurring above 373 K has been proposed.⁵²

The interactions between $[\text{Cr}(\text{CO})_6]$, $[\text{Mo}(\text{CO})_6]$, or $[\text{W}(\text{CO})_6]$ and a highly dehydroxylated alumina (heated at 1073 K under dynamic vacuum for 20 min) have been studied by Zecchina et al. by infrared spectroscopy.⁶⁰ In addition to a $[\text{M}(\text{CO})_6]$ species physically adsorbed, three species of C_{4v} symmetry have been clearly identified: they are assigned to $[\text{M}(\text{CO})_6]$ in interaction with defective aluminum sites, tetrahedral sites, and octahedral sites in the decreasing order of interaction. The ν_{CO} band for the O-bound CO to the surface is found near 1800 cm^{-1} .

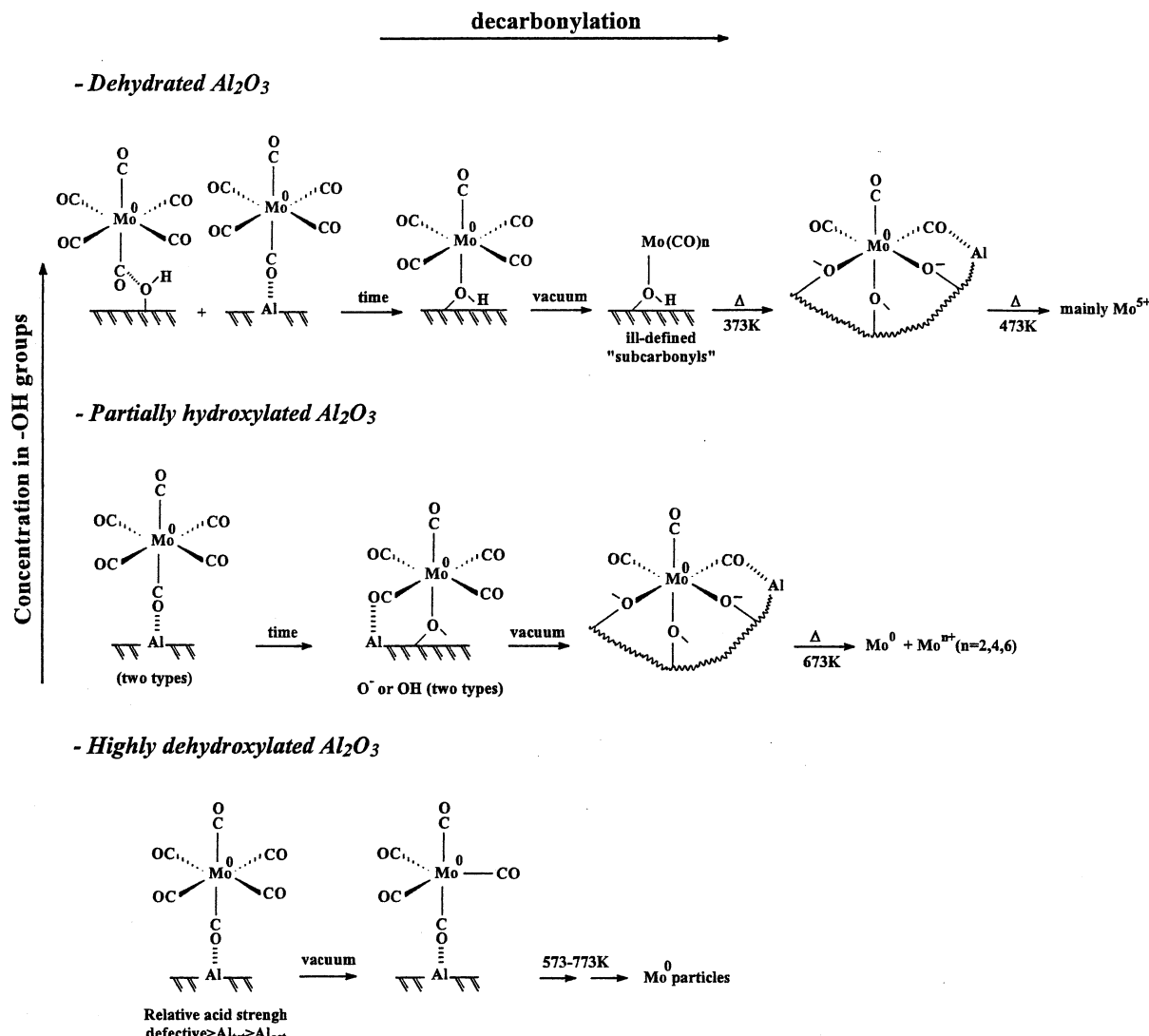


Figure 4. Surface organometallic chemistry of $[\text{Mo}(\text{CO})_6]$ on alumina.

and the stronger the interaction, the lower this CO stretching frequency. Prolonged outgassing at room temperature gives rise to some desorption and to the loss of a CO ligand to afford a $\text{M}(\text{CO})_5$ species, more likely monomeric than dimeric, attached by O bonding to a Lewis acid Al^{3+} site. From the infrared analysis, a bipyramidal geometry has been assigned to $\text{Mo}(\text{CO})_5$ and $\text{Cr}(\text{CO})_5$, the situation being more confused for $[\text{W}(\text{CO})_6]$. Further outgassing under heating allows more CO ligands to be evolved but no assignment has been done for the remaining species; then, as almost no hydroxyl group remains on the surface, complete decomposition affords molybdenum(0) on alumina.^{58,59,61,62} The same situation should prevail for chromium and tungsten. Figure 4 displays the various molybdenum species observed on an alumina support, depending on the degree of dehydroxylation.

Very recently, DFT calculations have been performed to modelize the interactions between $[\text{M}(\text{CO})_6]$ ($\text{M} = \text{Cr}, \text{Mo}, \text{W}$) and alumina.⁶³ The acidic and basic surface sites of alumina have been first modeled as tetrahedral or octahedral clusters. Two kinds of interactions are possible: (i) a weak interaction

between an Al^{3+} Lewis acid site and a CO ligand of the complex, and (ii) a stronger interaction between AlO^- basic site and a vacant site created when the complex loses one of the CO ligand; in this case, a metal–oxygen bond is formed. For Lewis basic sites models, the strength of the M–O bond increases in the order: $[\text{Cr}(\text{CO})_6] \leq [\text{Mo}(\text{CO})_6] \leq [\text{W}(\text{CO})_6]$, whereas the nature of the metal has no effect on the interaction with a Lewis acid site. The stronger interaction between $[\text{W}(\text{CO})_6]$ and alumina could explain the peculiar behavior of alumina-supported tungsten catalyst. Briefly, the hydroxylation degree of alumina controls the temperature of complete decarbonylation of the $[\text{M}(\text{CO})_6]$ species but also the oxidation state of the final deposit.

b. Silica, Titania, and Magnesia. On a fully hydroxylated silica, and under mild conditions (298–318 K), the physically adsorbed $[\text{M}(\text{CO})_6]$ species have been clearly identified by infrared spectroscopy with a weak interaction between the oxygen atom of a carbonyl ligand and the surface. Whereas the experimental conditions differ markedly from one paper to the other one, no subcarbonyl species have been observed⁴⁷ except by Pakkanen et al. who adsorb

$[\text{Mo}(\text{CO})_6]$ in the 326–373 K temperature range on high surface area silica in a fluidized bed reactor.⁶⁴ Nevertheless, the subcarbonyl molybdenum species have not been definitely characterized. On partially dehydroxylated support, the same situation prevails. The adsorption at room temperature of $[\text{Cr}(\text{CO})_6]$ on SiO_2 (treated under vacuum at 773 and 1073 K) has been studied by Hunter et al.⁶⁵ Beside the unperturbed physically adsorbed molecule, three different interactions, through O-bond, with Lewis acid sites have been observed. The strength of these interactions depends on the Lewis acidity of the electron deficient silicon sites resulting from the thermal treatment. The same authors⁶⁶ have demonstrated that, on silica–alumina supports (13% alumina) the adsorption process is quite similar to the one observed on partially dehydroxylated alumina.

Complete decarbonylation of $[\text{M}(\text{CO})_6]$ requires temperatures around 473 K (atmospheric pressure)^{67,68} and produces metal oxides with simultaneous loss of H_2 , CH_4 , and CO_2 with heating until 873 K.

Thus, it appears that the interactions between metal hexacarbonyls and silica are weaker than those observed for alumina and that they concern mainly physically adsorbed species. The absence of strong Lewis acid cationic sites presumably explains the poor stabilization, not only of the hexacarbonyls themselves but also of the subcarbonyl species. This phenomenon is probably connected to the total decarbonylation temperature, which is lower for partially dehydroxylated silica than for the corresponding alumina. Stronger interactions have been obtained when $[\text{Cr}(\text{CO})_6]$ or $[\text{Mo}(\text{CO})_6]$ are adsorbed on pre-existing Cr/SiO_2 or Mo/SiO_2 which are due to the presence of cationic chromium or molybdenum surface sites; in this case physisorbed and chemisorbed species are simultaneously observed.^{68,69}

Titania has been mainly used as model support in single crystalline form (110 plane). The adsorption at 150 K of $[\text{Mo}(\text{CO})_6]$ on OH free sample has been studied by FT-RAIRS and XPS.⁷⁰ The only phenomenon is physisorption of multilayers that desorbs at 220 K without formation of subcarbonyl species. Addition of OH groups on the TiO_2 surface prior to $[\text{Mo}(\text{CO})_6]$ adsorption, under the same conditions, does not modify this behavior. Chemical vapor deposition from $[\text{Mo}(\text{CO})_6]$ on (110) dehydroxylated TiO_2 , in UHV chamber, has been reported by the same author at 400 K. No subcarbonyl is observed and the deposits consist of metallic molybdenum and significant amounts of graphitic carbon.

A different behavior is reported in the case of magnesia, a highly basic support.⁷¹ Adsorption of $[\text{M}(\text{CO})_6]$ ($\text{M} = \text{Cr}$, Mo , or W) on highly dehydroxylated MgO , at room temperature, results in the formation of chemisorbed species, in addition to small amounts of physisorbed species. An adsorption mechanism of the metal carbonyls is proposed, by analogy with homogeneous phase reaction between $[\text{M}(\text{CO})_6]$ and Li^+R^- , leading to the formation of $[(\text{CO})_5\text{M}-(\text{COO})]\text{L}^-\text{Mg}^{2+}$ species. By outgassing in the 293–350 K range, a stepwise decarbonylation occurs. After infrared studies, the authors propose the formation

of clusters of different nuclearity. At 523 K, they report a complete decarbonylation and the formation of metallic particles.

c. Zeolites. Most of the studies of adsorption and decomposition of metal carbonyls have been carried out with Na and HY zeolites. Prior to the adsorption, the supports are dehydrated by outgassing at around 650 K. Many workers have investigated the interaction of $[\text{Mo}(\text{CO})_6]$ with these supports. Room temperature adsorption of $[\text{Mo}(\text{CO})_6]$ vapors on HY or NaY zeolites results in the formation of two adsorbed species presenting a slightly distorted octahedral symmetry.^{72,73} In the case of $[\text{Cr}(\text{CO})_6]$ on HY support, Zecchina et al. have observed physisorbed $[\text{Cr}(\text{CO})_6]$ and hydrogen bonded $\text{M}-\text{CO}\cdots\text{H}_{\text{surface}}$ species.⁷⁴ On NaX^{74} or NaY^{75} zeolites, $[\text{Cr}(\text{CO})_6]$ can be encapsulated at room temperature into the zeolite and interacts strongly with the surface, probably through the extraframework cations. An infrared study shows that progressive heating and evacuating induces the formation of $\text{Cr}(\text{CO})_4$ and then $\text{Cr}(\text{CO})_3$ encapsulated species. This latter surface– $\text{Cr}(\text{CO})_3$ species remains stable until 423 K under vacuum.⁷⁶

In an extensive structural and spectroscopic study of $[\text{M}(\text{CO})_6]$ on MY, Özkar et al. propose an interaction between extraframework cations of the zeolite and CO ligands.⁷⁷ Saturation adsorption at room temperature give around two $[\text{Mo}(\text{CO})_6]$ per HY or NaY supercage.^{77–81} Stepwise decarbonylation occurs by heating under vacuum and the temperatures of CO evolution depend on the electronegativity of the cation or of the proton and on the Si/Al ratio.^{78,79} Different interpretations have been proposed in the early studies,^{81–83} based on the formation of different mono- or dimeric subcarbonyl species. It appears now that the more stable species consists of $\text{Mo}(\text{CO})_3$ formed at 373 K.^{73,77,82,84,85} Indeed, EXAFS structural data indicate a monomeric *fac*- $\text{Mo}(\text{CO})_3(\text{O-zeolite})_3$ structure,^{77,84} characterized by a shortening of the Mo–C bond compared to that observed in $[\text{Mo}(\text{CO})_6]$ and by a high oxygen sensitivity producing Mo^{6+} species.⁸⁵ A complete decarbonylation has been observed by all the authors at around 500 K under vacuum. In these conditions, the decomposition leads to zerovalent molybdenum species.^{77,83,86,87} On NaY supports, EXAFS, XPS, and ^{129}Xe NMR spectroscopy have shown that, after decomposition at 473 K in vacuo, Mo_2 species are uniformly dispersed in the zeolite supercages.⁸⁷ If the decomposition is performed under molecular oxygen, molybdenum(VI) oxide dimeric species (Mo–Mo distance: 0.321 nm) were produced.⁸⁸ However, in the case of HY support, molybdenum becomes oxidized by zeolite protons,^{72,82,83} and the presence of Mo^{5+} species have been proposed from EPR studies.⁷² Similar results have been reported in the case of the decomposition of $[\text{W}(\text{CO})_6]$ on Y zeolites.⁸⁹ From XPS results, $[\text{Mo}(\text{CO})_6]$ decomposition on HNaY leads to Mo^0 and Mo^{2+} species,⁹⁰ and to Mo^{6+} species after air oxidation at 523 K.

2. Other Zerovalent Metal Carbonyl Complexes

Besides these numerous studies on chromium, molybdenum, and tungsten carbonyls and their interactions with various supports which justify the

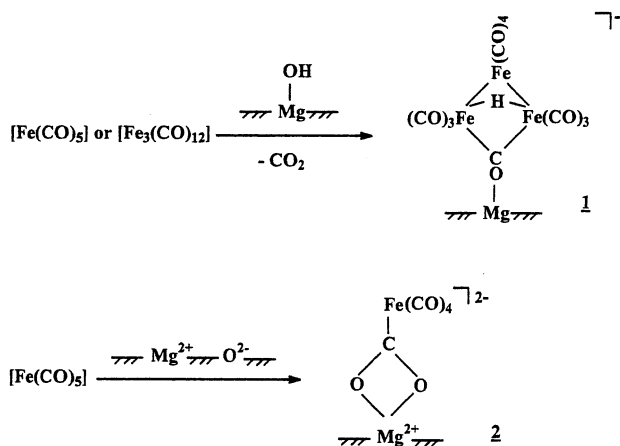


Figure 5. Surface organometallic chemistry of $[Fe(CO)_5]$ on magnesia.

separate analysis of each support, some work has been carried out on the reactivity of $[Fe(CO)_5]$, $[Fe_2(CO)_9]$, $[Fe_3(CO)_{12}]$, $[Re_2(CO)_{10}]$, and $[Co_2(CO)_8]$, with surfaces of silica, alumina, magnesia, zinc oxide, and zeolites.

a. Iron Precursors. Concerning the three iron complexes, their interactions with the supports have been examined, mainly by infrared spectroscopy. Partially dehydroxylated silica has been shown to lead to physisorption,^{91–93} so that, for instance, $[Fe(CO)_5]$ can be easily removed from the support, due to the weak interactions that exist between the iron complex and the silanol groups. Photochemical irradiation of this physisorbed $[Fe(CO)_5]$ produces mainly $[Fe_3(CO)_{12}]$ presumably through an $Fe(CO)_4(SiO_2)$ intermediate species.⁹³

A thorough study on the nature of the species formed at 298 K by reacting $[Fe(CO)_5]$ and $[Fe_3(CO)_{12}]$ with the surface has shown that, for alumina, magnesia, and zinc oxide a heterogenized $[HFe_3(CO)_{11}]^-$ species is obtained.⁹¹ Indeed, a surface hydroxyl group reacts with the iron carbonyl to provide the hydride complex with simultaneous elimination of one equivalent of CO_2 . This complex has been shown to be grafted to the support through a direct bond between the bridging carbonyl group and an acidic center of the surface (Al^{3+} , Mg^{2+} ...).^{91,92} Once more, the presence of surface OH groups determines the reactivity and thus the nature of the chemisorbed species: whereas fully hydroxylated and hydrated magnesia gives rise to grafted $[HFe_3(CO)_{11}]^-$,⁹⁴ a total dehydroxylation of magnesia allows one to obtain the anchoring through an $[(CO)_4Fe(CO_2)]^{2-}Mg^{2+}$ interaction,⁹⁵ as summarized in Figure 5.

EXAFS studies carried out on the chemisorption at 313 K of $[Fe_3(CO)_{12}]$ on $\gamma-Al_2O_3$ activated at 573 K in dry air revealed the presence of $[HFe_3(CO)_{10-(OAl\equiv)}]$, where the bridging CO of 1 has been replaced by an oxygen atom directly bound to a surface aluminum atom.⁹⁶ The small differences in the experimental conditions could explain that, in this case, a loss of two CO ligands has been observed.

With graphite as the support, $[Fe(CO)_5]$ is physisorbed as with silica.⁹⁷ Similarly, iron carbonyls are mainly physisorbed on various zeolites,^{98–100} although it has been suggested that small amounts of a

$[Fe(CO)_4\text{-zeolite}]$ species can be produced at 298 K from $[Fe(CO)_5]$ on HY-zeolite.⁹⁸

It is tempting to rationalize these results by considering that provided a polarized bond is present between the main metal of the support and the oxygen atom of a hydroxyl group, a chemisorbed iron carbonyl can be obtained. The first step is a nucleophilic attack of one CO ligand by an oxygen atom, like in the water gas shift reaction; then the hydroxycarbonyl species loses CO_2 to provide the hydrido species 1, the Lewis acid site on the surface giving a strong interaction with the bridging CO ligand.

Starting from these adsorption measurements, several studies have been done on the decomposition of the surface carbonyl. Hence, fully or partially hydrated MgO supports have been studied by Bassett and his group. In the first case, complete decarbonylation of $[Fe_3(CO)_{12}]$ occurs at 383 K, whereas a partially hydrated magnesia requires 403 K: CO , CO_2 , and H_2 have been identified in the gas phase. For the fully hydrated magnesia, Fe^0 dispersed particles and Fe^{2+} sites have been identified by Mössbauer and ESR spectroscopies. Moreover, on partially hydrated magnesia, Fe^0 particles are not oxidized.⁹⁴ On completely dehydroxylated MgO supports, metallic iron is obtained upon decarbonylation of $[Fe(CO)_5]$ at around 350 K.⁹⁵ On γ -alumina (calcined at 773 K), decomposition of $[Fe(CO)_5]$ or $[Fe_3(CO)_{12}]$ leads to zerovalent subcarbonyl species at temperatures below 423 K, and to oxidized iron Fe^{2+} at higher temperatures (≈ 573 K). In this case, in addition to CO , CO_2 and H_2 , methane was detected as a decomposition product.^{101,102} On synthetic graphite supports, $[Fe(CO)_5]$ decomposition produces metallic iron at temperature as low as 378 K.⁹⁷ Similarly, low temperatures of decarbonylation (ca. 343 K) were reported by Derouane and co-workers during their NMR investigations on HY-zeolite, where highly dispersed pyrophoric iron particles are produced.¹⁰⁰ Infrared and thermogravimetric studies performed on adsorption and decomposition of $[Fe(CO)_5]$,¹⁰³ $[Fe_2(CO)_9]$, and $[Fe_3(CO)_{12}]^{98,104}$ have shown that, contrary to alkali metal containing zeolites, a HY-zeolite promotes the formation of Fe^{2+} species at ca. 550 K.

b. Cobalt Precursor. Many studies have been carried out by infrared spectroscopy on cobalt carbonyls to elucidate their interaction with different supports. For all the studied supports, in the absence of a partial CO pressure, the first reaction is mainly the transformation of $[Co_2(CO)_8]$ into the cluster $[Co_4(CO)_{12}]$. Whatever the degree of dehydroxylation of silica, there exists a weak interaction between the cluster and the surface through a direct interaction between a bridging carbonyl group and a hydrogen atom of an OH group.^{105–112} Decarbonylation can be achieved more or less rapidly at 373 K in vacuo ,¹⁰⁷ or eventually under nitrogen,¹¹² and a subcarbonyl species with a ν_{CO} band at ca. 2000 cm^{-1} has been detected. Cobalt should be in the zero oxidation state since CO uptake, at room temperature, is facile and provides $[Co_4(CO)_{12}]$ with small amounts of $[Co_2(CO)_8]$.¹⁰⁷ Nevertheless, Pakkanen and his group¹¹³

have estimated possible charged or radical species by computational methods. The geometry of $\text{Co}(\text{CO})_4$ and $\text{Co}(\text{CO})_3$ interacting with SiO_2 via $\text{Si}-\text{Co}$, $\text{Si}-\text{O}-\text{Co}$, and $\text{Si}-\text{O}-\text{C}-\text{Co}$ bonds have been optimized and the interaction energies were calculated. All bond distances between a cobalt atom and its nearest neighbors are shorter when the number of CO ligand decreased. The interaction energies of charged species ($[\text{Co}(\text{CO})_4]^-$, $[\text{Co}(\text{CO})_3]^-$, $[\text{Co}(\text{CO})_4]^+$, $[\text{Co}(\text{CO})_3]^+$) are much stronger than the interaction energies of radical species ${}^{\bullet}\text{Co}(\text{CO})_4$ and ${}^{\bullet}\text{Co}(\text{CO})_3$, and depend on the surface site ($\equiv\text{SiO}^- > \equiv\text{Si}^+ > \equiv\text{SiO} > \equiv\text{Si}$). The strongest interaction has been found for the negatively charged $[\text{Co}(\text{CO})_4]^-$ and $[\text{Co}(\text{CO})_3]^-$ species bonded to the silica surface via $\text{Si}-\text{O}-\text{Co}$ bonds.

Introduction of oxygen at 293 K favors the removal of CO ligands and provides a surface species that approximatively contains one CO ligand and an oxygen atom per cobalt.¹¹² Further heating at 473 K under vacuum results in a total decarbonylation and the formation of cobalt(II) species.¹⁰⁸

With the more basic Al_2O_3 ^{107–111,114} and MgO ^{105,106} supports, the situation is somewhat more complex. Indeed, as soon as $[\text{Co}_2(\text{CO})_8]$ and/or $[\text{Co}_4(\text{CO})_{12}]$ are gas-phase adsorbed or impregnated they react with the surface. In addition to the transformation of $[\text{Co}_2(\text{CO})_8]$ into $[\text{Co}_4(\text{CO})_{12}]$ and small amounts of $[\text{Co}_6(\text{CO})_{16}]$, basic O^{2-} sites assist the disproportionation of the cobalt carbonyls to provide $[\text{Co}(\text{CO})_4]^-$ and cobalt(II) species of the type $[\text{Co}(\text{CO})_x\text{B}_y]^{2+}$ where B represents a Lewis base. Moreover, $[\text{Co}_2(\text{CO})_8]$ can react on the surface with $[\text{Co}(\text{CO})_4]^-$ to form $[\text{Co}_6(\text{CO})_{16}]^{2-}$, which has been detected by infrared spectroscopy. Simultaneously, carbonate and bicarbonate species have been detected, which result mainly from CO_2 formed through oxidation of the cobalt carbonyls by the oxide surface, followed by adsorption of the resulting species. EXAFS studies carried out on the species adsorbed on Al_2O_3 have allowed Iwasawa and co-workers to propose the structure of the initially adsorbed complex $[\text{Co}_4(\text{CO})_{12}]$.¹⁰⁸ Various thermal treatments induce decarbonylation reactions and the formation of several forms of cobalt oxides by reaction with the OH groups or additional oxygen. Worth noting is the $[\text{Co}^{II}]_4$ moiety produced after treatment in O_2 at 293 K,^{109,110} and the small spinel-like particles $[\text{Co}_3\text{O}_4]_n$ obtained after treatment in O_2 at 773 K,¹¹¹ that have been both identified by EXAFS.

Concerning the sublimation of $[\text{Co}_2(\text{CO})_8]$ and $[\text{Co}_4(\text{CO})_{12}]$ on X, and Y zeolites (pretreated at 673 K) the situation is, to some extent, similar to alumina.¹¹⁵ $[\text{Co}_4(\text{CO})_{12}]$ and the anionic species $[\text{Co}(\text{CO})_4]^-$ appear rapidly under vacuum with other unidentified carbonyl species revealed by additional CO bands. Heating above 423 K results in the complete and irreversible decarbonylation whatever the zeolites.

c. Rhenium Precursor. As rhenium catalysts play an important role in reforming, alkenes metathesis, and hydrogenation reactions, the interaction of $[\text{Re}_2(\text{CO})_{10}]$ with various supports has been investigated by several groups. Sublimation of this dimeric carbonyl at 330–350 K onto highly dehydroxylated alumina (1073 K under vacuum) results in the O-bonding of an axial CO ligand with an aluminum

surface atom either in a tetrahedral or an octahedral environment.¹¹⁶ Due to the presence of strong Lewis acid centers which induce the loss of the initial symmetry of $[\text{Re}_2(\text{CO})_{10}]$ to reach a C_{4v} symmetry with the appearance of a new ν_{CO} band near 1800 cm^{-1} , the authors propose a CO-aluminum bond instead of a CO weak interaction as previously noted for partially (400 K) dehydrated alumina.¹¹⁷ The decomposition of this surface complex has not been reported.

In the same temperature range (320 K), $[\text{Re}_2(\text{CO})_{10}]$ vapors react with a model MgO (111) surface to afford $[\text{Re}(\text{CO})_4(\text{OMg})_{\text{surf}2}]$. Further heating above 400 K provides a tricarbonyl species in which the rhenium center is bound to three oxygen surface atoms. Total decarbonylation occurs at 700 K leading to metallic rhenium.¹¹⁸ On MgO powders, the $[\text{Re}(\text{CO})_3(\text{OMg})_{\text{surf}3}]$ species is also present on highly dehydroxylated supports, whereas on fully hydroxylated MgO a shift in the ν_{CO} bands has been correlated to the formation of $[\text{Re}(\text{CO})_3(\text{HOMg})_{\text{surf}3}]$.¹¹⁹ On a support treated at 673 K, a mixed species has been proposed with two types of oxygen rhenium bonds $[\text{Re}(\text{CO})_3(\text{HOMg})_{\text{surf}2}(\text{OMg})_{\text{surf}1}]$. Density functional calculations carried out on these species were used to modelize the surface phenomena and have shown that the rhenium–oxygen bonds of $[\text{Re}(\text{CO})_3(\text{OMg})_3]$ are as strong as those found in coordination chemistry.¹²⁰ The concept of surface sites acting as polydentate ligands is thus strengthened. Tricarbonyl rhenium species grafted on silica or alumina under UV irradiation, or on a NaHY zeolite have also been reported.^{117,121}

3. Conclusion

For a given support, the level of dehydroxylation plays a central role on the anchoring mode of the zerovalent carbonyl complex. Usually, there are strong interactions with the most Lewis acidic sites obtained after high-temperature treatment: the absence of OH groups precludes the oxidation of the metal during the final stages of decomposition and allows the formation of metallic deposits. Many studies have shown that the decarbonylation occurs step by step giving rise to intermediate subcarbonyl species.

However, in some cases, it is necessary to have hydroxyl groups to anchor a certain carbonylmetal complex: that means that the first stage of the interaction is related to a nucleophilic reaction of the support on the complex.

C. Interactions between Rhodium(I) and (III) Precursors and a Support

Because of its activity in the NO reduction reaction resulting in a large use in automotive catalytic converters, rhodium has been the subject of numerous catalytic studies, including model systems. Two precursors have been particularly investigated for gas-phase deposition, $[\text{Rh}^{\text{I}}\text{Cl}(\text{CO})_2]_2$ and $[\text{Rh}^{\text{III}}(\eta^3\text{C}_3\text{H}_5)_3]$.

The $[\text{RhCl}(\text{CO})_2]_2$ complex adsorbs on silica powder pressed into wafers (pretreated between 373 and 1073 K under vacuum) without decomposition and

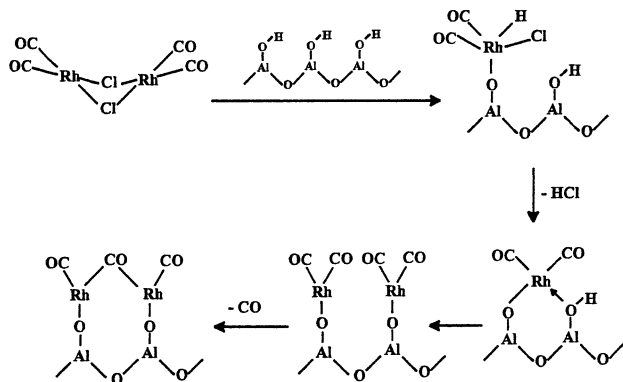


Figure 6. Postulated surface organometallic chemistry of $[\text{RhCl}(\text{CO})_2]_2$ on alumina (adapted from ref 125).

can be extracted by solvent treatment.^{122,123} When exposed to 600 Torr of CO at 800 K $[\text{RhCl}(\text{CO})_2]_2/\text{SiO}_2$ reacts to give a $[\text{RhCl}(\text{CO})_3]/\text{SiO}_2$ species.

Under the same conditions, the same authors have reported a different behavior on alumina support.¹²³ Two rhodium(I) carbonyl species, namely, $\text{Rh}^{\text{I}}(\text{CO})_2$ and $\text{Rh}^{\text{I}}(\text{CO})$, have been proposed from IR observations. Chemical analysis shows that all the chlorine is retained in the samples. Similar $\text{Rh}(\text{CO})_2$ species have been obtained from zerovalent $[\text{Rh}_4(\text{CO})_{12}]$ and $[\text{Rh}_6(\text{CO})_{16}]$ cluster precursors on alumina¹²⁴ under UHV conditions; XPS measurements display a Rh 3d_{5/2} binding energy of 310.2 eV comparable to that for Rh^{3+} compounds.

Model studies concerning the $[\text{RhCl}(\text{CO})_2]_2$ interaction with alumina surfaces have been carried out using inelastic electron-tunneling spectroscopy,¹²⁵ high-resolution electron energy loss spectroscopy,¹²⁶ or XPS-AES.¹²⁷ The first observation is that only one monolayer strongly adsorbs to the surface, while the outer physically adsorbed layers is desorbed upon warming below 273 K. At room temperature, different rhodium carbonyl species have been proposed including bridging carbonyls. A postulated adsorption mechanism is depicted in Figure 6. On the basis of the absence of Rh–Cl vibrations, the authors proposed an oxidative addition of an hydroxyl group followed by reductive elimination of HCl.

On a hydroxyl free substrate,¹²⁷ a TPD study of multilayer adsorbed $[\text{RhCl}(\text{CO})_2]_2$ at 108 K shows the

desorption of the outer multilayer at 231 K and, from 270 to 573 K, further CO evolution from thermal decomposition of the monolayer left on the surface. Above 623 K, AES data indicate about 3 Cl per Rh atom on the surface, and XPS measurements reveal zerovalent rhodium. Effective chlorine removal is achieved by temperature cycling between 108 and 623 K under 6.5×10^{-6} Pa of H_2O . After CO chemisorption, a mean particle size of 12 nm has been measured.

Several surface science techniques have been used by Evans and Hayden to follow the reactions occurring during the interaction of $[\text{RhCl}(\text{CO})_2]_2$ with a TiO_2 (110) surface.^{128–137} A general behavior similar to the one observed on Al_2O_3 model substrate has been observed. At 300 K, a rhodium(I) geminal dicarbonyl is formed by the dissociative adsorption of the precursor, and chlorine is coadsorbed on the TiO_2 (110) surface. The rhodium gem-dicarbonyls coordinate to two oxygen atoms of the surface adopting either a square planar or a tetrahedral geometry (Figure 7).¹³⁴ Very recently, the same authors have evidenced by scanning tunneling microscopy that, besides these rhodium(I) gem-dicarbonyl adlayers, some discrete particles are formed, preferentially at step edges of the support.^{135,136} The $\text{Rh}^{\text{I}}(\text{CO})_2$ species decompose at 500 K to produce metallic rhodium particles Rh^0 , while chlorine remains on the surface even after heating until 800 K. Partial regeneration of the parent $\text{Rh}^{\text{I}}(\text{CO})_2$ is observed by subsequent CO exposure. Reaction of H_2 with $\text{Rh}^{\text{I}}(\text{CO})_2/\text{TiO}_2$ at 300 K produces an absorbed monocarbonyl intermediate, presumably $\text{Rh}(\text{H})\text{CO}$ together with a slight decrease of the amount of adsorbed chlorine. Further heating at 425 K under H_2 is accompanied by a reduction of the carbon and of the rhodium. The $\text{Rh}(\text{CO})_2/\text{TiO}_2$ (110) is converted by exposure to NO at 300 K into highly dispersed $\text{Rh}(\text{NO})^+$ species, that are thermally more stable than the geminal dicarbonyl species.¹³⁷ This $\text{Rh}(\text{NO})^+$ species produced $\text{Rh}^0\text{-TiO}_2$ by heating at 600–650 K. The different reactions occurring on TiO_2 surface are depicted in Figure 7.

The rhodium(I) species containing two geminal-carbonyls has also been observed on NaY or HY dehydrated zeolites (773 K in vacuo) starting from

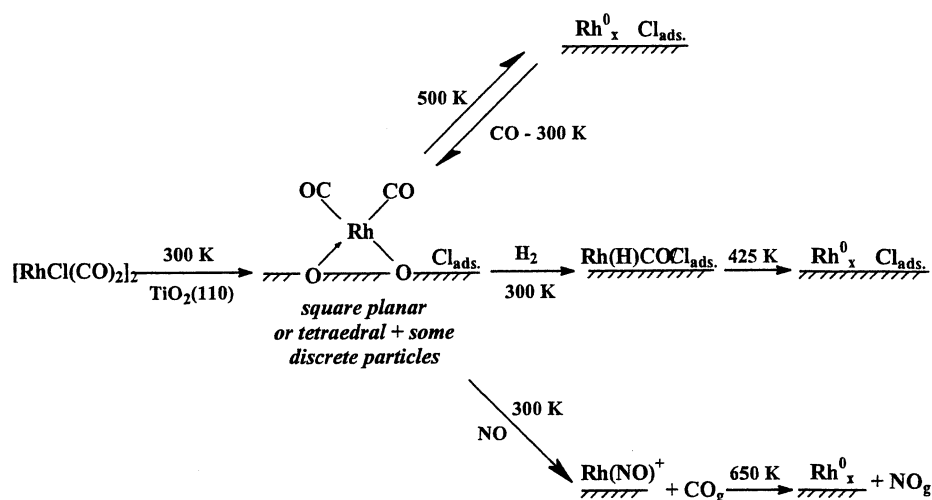


Figure 7. Surface organometallic chemistry of $[\text{RhCl}(\text{CO})_2]_2$ on titania.

$[\text{RhCl}(\text{CO})_2]_2$ or $[\text{Rh}_6(\text{CO})_{16}]$ in the presence of di-oxygen,¹³⁸ as well as on TiO_2 (110) starting from $[\text{Rh}(\text{CO})_2(\text{acac})]$.¹³⁹

The $[\text{Rh}(\eta^3\text{-C}_3\text{H}_5)_3]$ precursor has been largely used to prepare supported rhodium on various substrates, and thus, its chemistry during the deposition and decomposition steps has been investigated. However, controversial conclusions have been reported, so that a clear description of this chemistry is not possible. Whatever is the nature of the support (silica, titania, alumina, or magnesia), the hydroxyl groups play a major role during the first step of interaction. Most of the authors propose a $\equiv\text{M}-\text{O}_{\text{surf}}-\text{Rh}(\text{C}_3\text{H}_5)_2$ rhodium(III) species, which is grafted to the surface through an oxygen–rhodium bond and which contains two allyl ligands.^{140–143} On the contrary, Iwasawa has proposed the direct formation of a mono allyl rhodium(III) species on TiO_2 previously treated at 473 K.^{144,145} Basset and co-workers have noted that the more acidic the support, the faster the grafting. The order of reactivity is $\text{TiO}_2 > \text{SiO}_2 \gg \text{Al}_2\text{O}_3 > \text{MgO}$, the two first supports being activated between 298 and 523 K, and Al_2O_3 or MgO between 473 and 673 K. Due to the loss of physisorbed water an alumina activated in these latter conditions is more reactive than one activated in the 298–573 K temperature range. In a further step, the authors use dihydrogen as a reactive gas to promote the decomposition of the remaining allyl ligand(s). Immediate displacement of the allyl group is observed on titania support when dihydrogen is introduced at room temperature, and a band is detected at 2048 cm^{-1} .^{144–147} This band has been assigned to a Rh–H vibration by Iwasawa et al.,^{144,145} whereas Basset et al.^{146,147} have assigned this band to a CO ligand arising from allylic alcohol formed by coupling of the allyl ligand with a surface OH group. Under similar conditions, Schwarz et al. have proposed the formation of rhodium-hydride species.^{140,141} Finally, heating under dihydrogen in the temperature range 623–773 K affords metallic rhodium particles.^{141,142,145}

D. Miscellaneous Metal Precursors

Several papers have appeared recently that deal with the first step(s) of anchoring of various elaborated precursors presenting, of course, a significant vapor pressure. Moreover, highly sophisticated analytical tools have been used to obtain very precise information, e.g., CP-MAS ^{13}C NMR, EXAFS, polarized total-reflection fluorescence extended X-ray absorption fine structure (PTRF-XAFS),^{21,22} and sometimes theoretical calculations. In many cases, an approach of the grafting at the molecular level can be reached.

Thus, Basset and his group, have studied by IR, ^{13}C , and ^{119}Sn MAS NMR the reaction of tetraalkyl tin complexes with the surface of silica.¹⁴⁸ On partially dehydroxylated support (573–873 K) and below 373 K, the complexes are physisorbed via hydrogen-type bonding between the hydrogen of the terminal methyl group of the alkyl ligand and the oxygen of the surface silanol group. Above 373 K, a reaction occurs leading to the formation of essentially one type

of surface complex $[\equiv\text{Si}-\text{O}-\text{Sn}(\text{R})_3]$ and evolution of one mole of the corresponding alkane per mole of tin surface. Using the same analytical techniques as well as deuteration experiments, they have shown that $[\text{Zr}(\text{neopentyl})_4]$ ¹⁴⁹ or $[\text{Ti}(\text{neopentyl})_4]$ ¹⁵⁰ react at 333 K with the surface of a partially dehydroxylated silica (773 K) to afford $[\equiv\text{Si}-\text{O}-\text{Zr}(\text{neopentyl})_3]$ or $[\equiv\text{Ti}-\text{O}-\text{Zr}(\text{neopentyl})_3]$ and loss of neopentane.¹⁰⁶ Similarly, $[\text{Cr}(\text{neopentyl})_4]$ reacts with the surface of a partially dehydroxylated silica activated at 473 or 773 K containing a reduced number of surface OH groups. In the latter case, only one neopentane molecule is formed per chromium atom (0.92 measured) by reaction with an OH group providing the $[\equiv\text{Si}-\text{O}-\text{Cr}(\text{neopentyl})_3]$ surface species. For the silica activated at 473 K, the species $[\equiv\text{Si}-\text{O}-\text{Cr}(\text{neopentyl})_2]$ is mainly formed (1.87 neopentyl equivalents measured).¹⁵¹ Further thermolysis under mild conditions (333 K) liberates one more alkyl ligand, eliminated as neopentane, to give a Cr^{IV} species which is formulated either as an $[(\equiv\text{SiO})_2\text{Cr}=\text{CH}(\text{tBu})]$ alkylidene species or a $[(\equiv\text{SiO})_2\text{CrCH}_2\text{C}(\text{CH}_3)_2\text{CH}_2]$ metalla-cyclobutane species. The presence of the alkylidene species seems more consistent with the deuteration experiments,¹⁵¹ and kinetic studies.¹⁵² Vanadium(IV) species have been similarly generated.¹⁵² The direct introduction by sublimation of an alkylidene complex, e.g., $[\text{Ta}(\text{=CH}^{\text{tBu}})(\text{neopentyl})_3]$, on a silica activated at 773 K, affords a surface species where the alkylidene moiety remains coordinated to the metal, whereas an alkyl group is removed as neopentane. From isotopic labeling experiments, the authors propose that an OH surface group is primarily added on the metal–carbene bond and that a α -hydrogen elimination occurs on one of the alkyl ligands to regenerate the alkylidene ligand.¹⁵³ The same mechanism is proposed for the second loss of an alkyl group, giving rise to $[(\equiv\text{SiO})_2\text{Ta}(\text{=CH}^{\text{tBu}})(\text{neopentyl})]$.¹⁵³

Due to their high volatility the β -diketonato complexes have been largely studied. Moreover, by trapping a hydrogen atom the ligand can be more or less easily eliminated as a volatile β -diketone molecule. Interaction of $[\text{Cu}(\text{hfacac})_2]$, in which hfacac is a hexafluoroacetylacetone ligand, with high surface area silica has been investigated by infrared in the frame of CVD deposit studies.¹⁵⁴ The supports have been more or less dehydroxylated with activation temperatures of 298, 673, and 1123 K. In any case, the authors observed a physisorption at 143 K. At 298 K, on silica treated at 1123 K an interaction with siloxane groups has been noticed, whereas on supports activated at 298 and 673 K, chemisorption is proposed to occur by the interaction between the copper atom and a silanol group.

The complex $[\text{Cu}(\text{dpm})_2]$, in which the acetyl-acetonato ligand contains four *tert*-butyl substituents, i.e., 2,2,6,6-tetramethyl-3,5-heptanedionato, reacts at 323 K with the surface silanol groups of a silica treated at 733 K. Infrared measurements show that the OH groups disappear with the simultaneous appearance of CH_2 stretching frequencies due to ligand hydrogenation.¹⁵⁵ XPS¹⁵⁶ and EXAFS¹⁵⁷ measurements indicate that the oxidation state and the

oxygen distribution around the metal remain unchanged after chemisorption. Similar observations have been made with $[\text{Ca}(\text{dpm})_2]$.^{156–158} Further reaction with water vapor at 673 K restores the silanol groups, allows the ligands to be removed, and produces copper(I) deposits. The same copper complex has been used by Iwasawa and co-workers to deposit submonolayers of copper oxide on α -quartz (0001).¹⁵⁹ EXAFS reveals that the copper atoms are dispersed on the 3-fold sites of the quartz surface.

The chemisorption of $[\text{Cr}(\text{acac})_3]$ on porous high surface area silica has been shown to occur at 473–553 K and involves one silanol group, giving rise to the loss of one equivalent of acetylacetone and to the formation of a chromium–oxygen bond between the complex and the surface. The isolated OH groups present a higher activity than the strongly H-bonded OH groups as shown by varying the pretreatment of silica. The two other acac ligands can be removed at 673 K in air to produce Cr^{4+} species, or in the presence of water vapor to maintain the +III oxidation state of chromium.¹⁶⁰

Chromocene has been used as chromium precursor and its grafting has been studied because it produces an active polymerization catalyst.¹⁶¹ On highly dehydroxylated silica (973 K), sublimation of $[\text{Cr}(\eta^5\text{-C}_5\text{H}_5)_2]$ at room temperature gives, in a first step, a reaction with the silanol groups of the surface. One equivalent of cyclopentadiene is evolved and the surface species $[\equiv\text{Si}-\text{O}-\text{CrCp}]$ is formed, as shown by infrared spectroscopy. The authors show that further addition of chromocene can occur; it is weakly bonded through one cyclopentadienyl ligand to the first chromium atom and can be relatively easily removed under vacuum (this dinuclear species is supposed to be inactive in ethene polymerization).

The reaction of benzene tricarbonyl chromium, another catalyst precursor for ethene polymerization, with alumina, silica–alumina, or silica surfaces has also been studied,^{162–164} and the resulting species are presented in Figure 8. Depending on the temperature pretreatment of the alumina support, two kinds of interactions have been indicated. On alumina pretreated at 773 K, the main adsorption involves H interactions between a hydroxyl group and a benzene ligand (Figure 8a). If the number of OH surface groups is decreased ($T = 1073$ K) then a direct bond is formed between an oxygen atom of a carbonyl ligand and an Al^{3+} surface cation (Figure 8b). Further treatments under mild conditions (333 K for instance, outgassing...) induce the loss of benzene and of carbonyl ligands to produce subcarbonyl species. On silica support,¹⁶³ pretreatment and coverage ratios play a major role on the adsorption process at 298 K. Silanol groups interact with one of the CO ligands when vicinal silanol groups are available (hydroxylated surface), and additionally via H-bonding with the benzene ligand for highly dehydroxylated surface (Figure 8c,d). Furthermore, for high temperatures treatments of the support (1073 K), electron-deficient silicon atoms are created, and constitute Lewis acid sites able to interact with a CO ligand via an oxygen atom. On the contrary to alumina supports, raising the temperature of the impregnated sample to 358

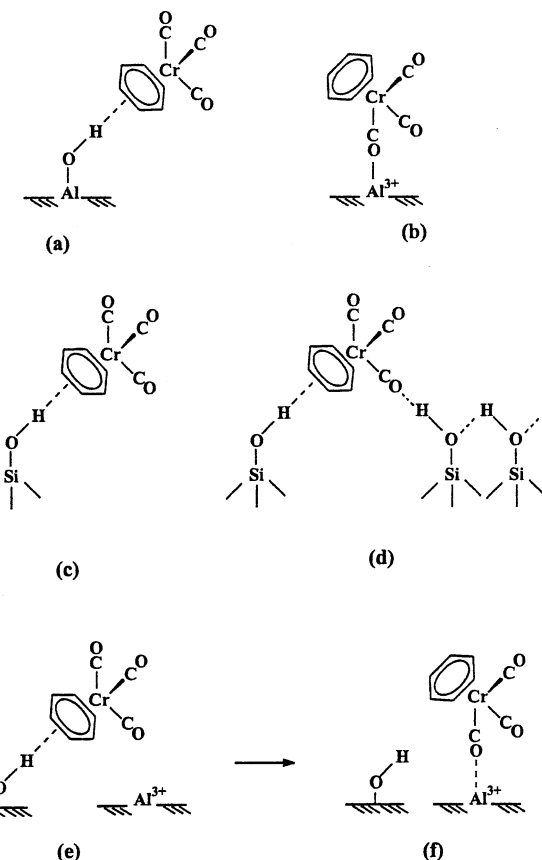


Figure 8. Adsorption of $[\text{Cr}(\text{CO})_3(\eta^6\text{-C}_6\text{H}_6)]$ on alumina (a) and (b), silica (c) and (d), or silica–alumina supports (e) and (f).

K results in desorption rather than decomposition of the precursor. Finally, on silica–alumina support, (pretreated at 773 K), $[\text{Cr}(\text{CO})_3(\text{C}_6\text{H}_6)]$ is first adsorbed (298 K) via $\equiv\text{Si}-\text{OH}\cdots\text{benzene}$ ligand interaction and is rapidly transformed giving a $[\equiv\text{Al}^{3+}\cdots\text{OCCr}(\text{CO})_2(\text{C}_6\text{H}_6)]$ species (Figure 8e,f).¹⁶⁴ In this case, ligand loss occurs upon evacuation at 298 K or on thermal treatment (353 K), producing subcarbonyl species.

In addition to the hexacarbonylmolybdenum precursor (vide supra), the lability of the allyl ligands has also been used to anchor a molybdenum fragment on a surface.¹⁶⁵ At 318 K, $[\text{Mo}(\eta^3\text{-C}_3\text{H}_5)_4]$ reacts with silica (pretreated at 823 K under O_2) to yield an anchored species with a Mo/C ratio of 1/6. This result is in agreement with the bis-allyl molybdenum(IV) $[(\equiv\text{SiO})_2\text{Mo}(\eta^3\text{-C}_3\text{H}_5)_2]$ species observed by Iwasawa in pentane solutions.¹⁶⁶ ESCA measurements performed after samples reduction at 823 K indicate the presence of Mo^{2+} surface species.

Ozin and co-workers have examined the vapor-phase impregnation of $[(\eta^5\text{-C}_5\text{H}_5)\text{Ir}(\text{CO})(\text{H})_2]$ onto various $M_{56}\text{Y}$ zeolites where M is an alkaline metal present in the framework as cation.¹⁶⁷ This study shows that for the small Li^+ and Na^+ cations, the bonding involves the simultaneous interaction of the CO and the cyclopentadienyl ligands with two cations. However, with the larger K^+ , Rb^+ , and Cs^+ cations, the interaction occurs only between a cation and the two hydrides. At saturation, two iridium molecules can be incorporated in the α -cage of the zeolite.

E. Conclusion

It appears from this analysis of the literature that the fate of a metal complex approaching a solid surface obviously depends on the nature of that surface. The most recent physicochemical investigations on oxide supports, show clearly the main role of the surface hydroxyl groups and the presence of Lewis acidic sites in coordinating the metal precursor and then stabilizing any subcarbonyl species. These intermediate complexes, in which the support acts as a ligand, have in certain cases been fully characterized. Further removal of the primary ligand requires heating and, in some cases, the presence of a reactive gas.

When, in the first step, molecular or quasi-molecular species are obtained, the resulting material consists mainly either in an oxide or in zerovalent metallic aggregates. Here also the noninnocent nature of the support needs to be underlined. Unfortunately, the second step of decomposition has been poorly investigated, particularly the nucleation step.

Besides zerovalent carbonyl complexes which have been mainly studied, a few complexes containing other ligands than CO, such as allyl or acetylacetato, that show good volatility properties deserve more investigation, not only to understand more deeply all the steps of a surface-organometallic chemistry but also to have at one's disposal a large range of metallic precursors.

III. Preparation and Surface Properties of CVD Catalysts

After the first part of this review devoted to the interactions between the surface of the support and a precursor, we examine the various gas-phase methods that can be used to elaborate heterogeneous catalysts. We have focused on the various strategies that have been adopted to prepare catalysts with a controlled morphology. The structural and physicochemical characterization of the resulting materials will be emphasized. Finally, their catalytic performance will be analyzed and compared with those of the corresponding catalysts prepared by conventional impregnation methods.

In this section, we will distinguish between two kinds of gas-phase methods: (i) the two-step process that consists of the gas-phase adsorption of the precursor on the support followed by the thermal treatments required to obtain the active catalyst, and (ii) the one-step process in which the sublimated precursor is simultaneously adsorbed and decomposed on the heated support. This latter process which is similar to the chemical vapor deposition one used for film elaboration in microelectronics will be specifically called CVD. As the two-steps process is often named in the literature CVD, atomic layer epitaxy (ALE), grafting or anchoring, we will call it here for clarity reasons "gas-phase impregnation-decomposition" (GPI-D). Additionally, a dry-mix method has also been reported in which the precursor is physically mixed with the support, heated for gas-phase impregnation and then decomposed.

While most of the studies deal with the fixed bed technique, the use of a fluidized bed has proved its efficiency to obtain a narrow distribution of the particle size on the surface of the grains together with a homogeneous dispersion on the whole surface of the porous support. Omata et al.¹⁶⁸ were the first to report the use of a fluidized bed reactor to decompose nickel tetracarbonyl in a two-step reaction. Due to the high vapor pressure of $[Ni(CO)_4]$, a low-temperature gas-phase impregnation is followed by a decomposition stage under a nitrogen atmosphere. The same two-step procedure was used by Dossi et al. to prepare, in a U-shaped tube, Pd and Pt particles supported on zeolites.¹⁶⁹ We have reported the design of a CVD reactor that allows the vapor of a precursor to come into contact with the support in a fluidized bed under reduced pressure, as well the small sizes obtained for highly dispersed noble metal aggregates, easily produced at relatively low temperatures of decomposition.¹⁷⁰ Generalization of this method has appeared and we can mention the work of Pakkanen and his group,¹⁷¹ who describes the use of a fluidized bed to obtain structurally well-defined catalysts by a controlled gas-phase deposition which involves successive GPI-D cycles, similar to the ALE process described by Lakomaa et al.¹⁷² A similar approach has been used by Baerns et al. who prefer to define their method as "CVD and decomposition".¹⁷³

For reasons of clarity, we have chosen to classify the different catalysts prepared by gas-phase techniques according to the metal precursor that has been used. The choice of the metal precursor for catalyst preparation is mainly governed by some well-known general criteria, which can be summarized as follows: good volatility and thermal stability under transport conditions, simple preparation, high purity, easy and clean decomposition, reduced-toxicity, and stability under storage conditions over a long period.

A. Zerovalent Metal Precursors

1. Chromium, Molybdenum, and Tungsten

Several zerovalent carbonyl precursors especially $[Cr(CO)_6]$, $[Mo(CO)_6]$, and $[W(CO)_6]$ have been used by Brenner et al. to prepare γ -Al₂O₃ or TiO₂-supported catalysts.^{174–178} These catalysts have been prepared by GPI-D and the influence of various pretreatments of the support on the catalytic activity in the hydrogenation of ethylene has been studied.^{174–176} Low-temperature decomposition (473–573 K under He) leads to the formation of well-dispersed subcarbonyl species more active than catalyst activated at 873 K. The decrease of activity is explained as resulting from the oxidation of the metal by the remaining surface hydroxyl groups at high temperature. When a dehydroxylated alumina (1223 K) is used, the metal oxidation is less pronounced and a much more active catalyst is produced. On titania support, the oxidation degrees of Cr, Mo, and W deposited by GPI-D from the hexacarbonyl precursors depends also on the dehydroxylation level of the support.¹⁷⁹ From TPD experiments performed until

1073 K, it appears that dehydroxylated titania at 773 K provokes less oxidation than the same support dehydroxylated at 523 K. All these latter catalysts are active for ethylene hydrogenation and the reactivity increases in the order Cr < W < Mo as in the case of alumina-supported catalysts.

[Mo(CO)₆]-based catalysts supported on TiO₂, Al₂O₃, ZrO₂, or MgO after dehydration at 773 K have been characterized by TPD, XPS, and the catalytic activities evaluated for various reactions, as propene metathesis and 1,3-butadiene hydrogenation.¹⁸⁰ Molybdenum catalysts supported on TiO₂ show the highest catalytic activity, and the oxidation degree of molybdenum is lower on this support than on the others. It is worth noting that the GPI-D method does not allow grafting of molybdenum on a silica support.

When [Mo(CO)₆] is encaged at room temperature in MY zeolites, a very active catalyst for hydrogenation of butadiene (423 K) is produced, the grafting of the complex being accompanied by CO evolution. Treatment at 473 K, corresponding to a complete decarbonylation, has a negative effect on the activity of this catalyst.¹⁸¹

Recently, molybdenum dimer oxycarbides entrapped in NaY supercages and prepared by GPI-D cycles from [Mo(CO)₆] have shown a specific activity for the methanol decomposition reaction to produce CH₄, CO₂, and H₂.¹⁸² After exposure to [Mo(CO)₆] vapors at room temperature, the supercages are filled with two [Mo(CO)₆] molecules. Decarbonylation at 573 K under vacuum results in the evolution of 5.5 equiv of carbon per molybdenum atom and in the formation of Mo₂(C)O_x dimers as shown by TPD, EXAFS, XPS, and XRF analyses. Oxidation at 623 K induces Mo–Mo bond breaking and formation of tetrahedral monomeric MoO₄ species with evolution of the remaining carbon atoms. Further reduction at 723 K under H₂ produces clusters, which contain both Mo–O and Mo–Mo bonds. The catalysts have been tested in the methanol decomposition reaction at each step of their preparation; the oxycarbide dimer species is the only one to produce CH₄, CO₂, and H₂, whereas the oxidized and reduced samples produce only dimethyl ether.

Although less common than the gas-phase impregnation process, the dry-mix method is described here since it would seem to involve the diffusion of the precursor in the gaseous state. For instance, [Mo(CO)₆] has been mixed in the solid state with alumina, treated under vacuum at low temperature, and then heated slowly until 573 K to achieve a complete decarbonylation. Dispersions obtained by this way are significantly lower than those observed for the catalysts prepared by impregnation of [Mo(CO)₆] in hexane solution.¹⁸³

Finally, photoactivation of [Mo(CO)₆] or [W(CO)₆] has been reported as an effective method for the preparation of active catalysts for but-1-ene metathesis.¹⁸⁴ Sublimation of the metal carbonyl at 333 K followed by irradiation at room-temperature induces the formation of subcarbonyl species that could be active catalyst precursors. Alumina-supported subcarbonyl tungsten species prepared by GPI from [W(CO)₆] or [W(CO)₅L] (L = PPh₃, P(OPh)₃, or PBu₃)

are active catalyst precursors in the *cis*-2-pentene metathesis.¹⁸⁵

2. Nickel, Iron, Cobalt, Ruthenium, and Rhenium

a. Nickel. Due to its high toxicity, [Ni(CO)₄] has been relatively rarely employed as precursor for catalyst preparation. Gas-phase impregnation at 298 K of [Ni(CO)₄] on γ -Al₂O₃, alumina fibers (Saffil), or HY and NaY-zeolites has been performed by Derouane et al.¹⁸⁶ On alumina fibers, decomposition of the impregnated material at 473 K affords Ni metal crystallites (5–15 μ m) consisting of 50–200 nm Ni particles. Active Ni/C* catalysts for methanol carbonylation can also be prepared by GPI-D from [Ni(CO)₄.¹⁶⁸ The GPI step is performed either at 325 K or at 423 K in a fluidized bed reactor, and the decomposition occurs at 523 K under N₂ in the same reactor. Although the nickel particles are much larger for the GPI-D catalyst (7% Ni w/w) than for a wet impregnated catalyst (10% Ni w/w from aqueous solution of nickel acetate), both exhibit very similar catalytic activities for methanol carbonylation. Furthermore, no activation step, such as H₂ reduction, is needed in the case of the GPI-D catalyst.

b. Iron. Iron-based catalysts supported on γ -alumina, dehydrated at 473 K, have been prepared from [Fe(CO)₅] vapor, followed by decomposition under vacuum at 673 K.¹⁸⁷ They present a poor activity in the hydrogenation of ethylene. However, when KOH-doped γ -alumina is used as a support, this method of preparation leads to higher activities than a classical promoted-iron ammonia catalyst.

c. Cobalt. Suvanto and Pakkanen have studied the preparation of cobalt particles dispersed on silica support by the GPI-D method starting from [Co₂(CO)₈] in a fluidized bed reactor.¹⁷¹ Prior to impregnation, silica having a 320 m² g⁻¹ surface area has been sieved to 200–500 μ m to ensure an easy fluidization (elimination of fine particles); then, the support has been dehydrated at 573 K under vacuum for 10 h. Cobalt carbonyl, which has a high volatility even at low temperature (80 Pa at 323 K), has been reacted with silica powder in the fluidized bed, either under a CO atmosphere providing orange brown silica particles, or under nitrogen, giving rise to black or black-brown powders. In a second step, heating at 373 K under nitrogen assists the decarbonylation. After 25 h of contact, a loading of 2.5% w/w of cobalt is obtained. The authors show also that on a MCM-41 support much larger amounts of [Co₂(CO)₈] are adsorbed compared to SiO₂.¹⁸⁸ After one GPI-D cycle, the monolayer coverage is ca. 20% Co w/w, the metal loading increases up to 41% Co w/w by using a sequential pulse GPI-D technique. Further comparison of SiO₂ and MCM-41 supports and of two GPI methods (direct or pulsed) on the ease of reduction of the supported cobalt is also reported.¹⁸⁹ The results reveal that samples in which [Co₂(CO)₈] has been deposited on MCM-41 via the pulsed method are more easily reduced or oxidized.

By the same process, tungsten and bimetallic tungsten–cobalt particles have been prepared on γ -alumina supports.^{190,191} Loading of tungsten has been realized through successive pulses of [W(CO)₆];

typical sequences are 2 h of sublimation at 363 K, 10 h of decarbonylation at 473 K, and then a second pulse under the same conditions followed by a final reduction step at 723 K under hydrogen for 5 h. To prepare the bimetallic catalysts $[\text{Co}_2(\text{CO})_8]$ has been added by a similar pulse sequence to the tungsten-supported catalyst. The preparation has been monitored by infrared spectroscopy in parallel to TPD measurements, mainly to measure the efficiency of the decarbonylation: $[\text{Co}_2(\text{CO})_8]$, $[\text{Co}_4(\text{CO})_{12}]$, as well as $[\text{Co}(\text{CO})_4]$ have been identified as surface-adsorbed complexes. The particle size, their dispersion, and the potential presence of carbonaceous deposits are not indicated. However, these bimetallic catalysts show higher activity than a commercial Co/Mo catalyst for the hydrodesulfurization reaction (HDS) of thiophene. As shown by temperature programmed reduction experiments, after an oxidation pulse at 523 K tungsten catalysts present reduction peaks at temperatures significantly lower than traditional tungsten oxide catalysts. These results are consistent with a good dispersion of the particles on the surface of the alumina supports. $\text{CoMo}/\text{Al}_2\text{O}_3$ ¹⁹² and $\text{CrCo}/\text{Al}_2\text{O}_3$ ¹⁹³ have been also prepared by a similar GPI-D method and tested in thiophene HDS. In the case of $\text{CoMo}/\text{Al}_2\text{O}_3$ samples, the order of metal deposition has been found to moderately affect the catalytic activities, the better results being obtained when cobalt is deposited before molybdenum. For $\text{CrCo}/\text{Al}_2\text{O}_3$, a pronounced promoting effect of Co has been noticed for thiophene conversion: 51.1% with Cr/ Al_2O_3 and 86.6% with $\text{CrCo}/\text{Al}_2\text{O}_3$.

The catalytic performances of the well-characterized $[\text{Co}^{\text{II}}]_4/\text{Al}_2\text{O}_3$ catalytic species (see part II of this review) prepared from $[\text{Co}_2(\text{CO})_8]$ by Iwasawa et al. have been studied.¹⁹⁴ This catalyst presents a much higher catalytic activity than a conventionally prepared impregnated catalyst in the NO–CO reaction.

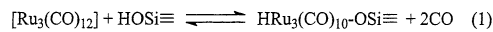
A dry-mix method has been used to prepare Co/ SiO_2 from $[\text{Co}_2(\text{CO})_8]$: contrary to other preparation methods as liquid-phase impregnation or physical mixtures, it allows one to obtain a very small metallic particle size (<2 nm).¹⁹⁵

Finally, the preparation of cobalt containing zeolites catalysts via a microwave discharge method has also been reported.^{196,197} The compound $[\text{Co}_2(\text{CO})_8]$ has been sublimed onto a dehydrated NaX zeolite and the argon plasma (1–3 W) ignited to decompose $[\text{Co}_2(\text{CO})_8]$. The highly dispersed metal clusters located both on the surface and in the bulk of the zeolite are active catalysts in the Fischer Tropsch reaction.

d. Ruthenium. The volatile cluster $[\text{Ru}_3(\text{CO})_{12}]$ can be used to deposit ruthenium on various supports. Ichikawa et al.^{198,199} use a dry-mix method to incorporate $[\text{Ru}_3(\text{CO})_{12}]$ in the α -cages of a NaY zeolite at 333 K under vacuum. A binding site model is proposed¹⁹⁸ that involves the interaction of the oxygen atoms of two cis-carbonyl ligands with a single extraframework Na^+ α -cage cation. The reaction of this $[\text{Ru}_3(\text{CO})_{12}]/\text{NaY}$ material with dihydrogen at 363 K produces the single hydride species $[\text{H}_4\text{Ru}_4(\text{CO})_{12}]/\text{NaY}$.

When dry mixing is carried out at 403 K under argon at atmospheric pressure with NaY or FSM-16 (amorphous silicate) supports, a black material is obtained²⁰⁰ indicative of $[\text{Ru}_3(\text{CO})_{12}]$ decomposition. After reduction under hydrogen at 723 K, small Ru particle sizes are measured by TEM and H_2 chemisorption (Ru/NaY: 2.4 nm and Ru/FSM-16: 3.6 nm), which can be compared to those of Ru/Y prepared by ion exchange (2.6 nm) but are smaller than those of Ru/NaY prepared from $[\text{Ru}(\text{NH}_3)_6]\text{Cl}_3$ aqueous solutions. The catalytic activity of these dry-mix catalysts has been compared to that of impregnated and ion-exchanged samples in the CO_2 hydrogenation reaction at 423 K and 3 MPa total pressure ($\text{CO}_2/\text{H}_2 = 1:3$). On NaY support, no significant difference in activity has been measured whatever the catalyst; however, the ion-exchanged sample shows a higher selectivity for methanol production. It is concluded that the preparation method rather than the metal particle size influences the reactivity.

Pakkanen et al. have used a GPI-fluidized bed method to prepare ruthenium-bipyridine catalysts supported on SiO_2 , silica gel, or alumina, starting from $[\text{Ru}_3(\text{CO})_{12}]$.²⁰¹ Sublimation of the ruthenium precursor has been performed between 408 and 418 K and the vapors carried out to the fluidized bed maintained at lower or higher temperatures. At 373 K, $[\text{Ru}_3(\text{CO})_{12}]$ is mainly physisorbed on the silica support. At higher temperatures, infrared analyses of the fluidized bed, allow to propose the following surface reaction:



Further reaction of this species with bipyridine at 373 K results in the formation of an unknown surface species whose infrared bands indicate a compound containing two carbonyl groups. These as-prepared catalysts have been shown to be active in hex-1-ene hydroformylation and water gas shift reactions. In this latter reaction, the GPI-D catalysts are 2–2.5 times more active than the corresponding impregnated catalysts.²⁰¹

On planar model TiO_2 (110) surfaces, $[\text{Ru}_3(\text{CO})_{12}]$ can be used for depositing nanosized metallic ruthenium particles under UHV conditions.²⁰² The precursor decomposition proceeds through some intermediate subcarbonyl species which are completely decomposed at 573 K; however, the metal particles show some residual carbon contamination.

Finally, a series of ruthenium, molybdenum, and ruthenium–molybdenum catalysts supported on Al_2O_3 have been prepared from $[\text{Ru}_3(\text{CO})_{12}]$ and $[\text{Mo}(\text{CO})_6]$ by GPI-D or wet impregnation (hexane solutions) and tested for thiophene HDS.²⁰³ In HDS tests, the mono- and bimetallic GPI-D catalysts give better thiophene conversion than the corresponding catalysts produced by liquid-phase impregnation. These results clearly demonstrate the benefits of the absence of solvent during supported catalyst preparation.

e. Rhodium. The $[\text{Re}_2(\text{CO})_{10}]$ complex has been used to prepare Re/NaY and RePt/NaY catalysts by GPI-D.^{204,121} The precursor can be easily deposited by sublimation in flowing He at 363 K onto the zeolite or on a Pt/NaY prerduced support. This behavior

contrasts with that observed on dehydrated SiO_2 , on which no deposition takes place as in the case of $[\text{Mo}(\text{CO})_6]$.¹⁸⁰ Reductive decomposition of $[\text{Re}_2(\text{CO})_{10}]$ is assisted by the presence of platinum particles and complete decarbonylation has been achieved at 723 K, whereas, in the absence of platinum, the required temperature is 773 K. Furthermore, when pre-reduced Pt particles are present on NaY, the decomposition pathway of $[\text{Re}_2(\text{CO})_{10}]$ changes, and complete decarbonylation and aggregation to bimetallic PtRe particles occur in one step. On NaHY support,¹²¹ $\text{Re}(\text{CO})_x$ subcarbonyl species are formed that interact with acidic Brønsted sites, so that diffusion inside the zeolite is slow. In this case, a two-step decomposition of $[\text{Re}_2(\text{CO})_{10}]$ is observed to obtain PtRe bimetallic particles. The high activity shown by these PtRe/NaY catalysts in the cyclopentane hydrogenolysis reaction is characteristic of a large concentration of platinum–rhenium bimetallic particles.²⁰⁴

Active Re/ $\gamma\text{-Al}_2\text{O}_3$ catalysts for thiophene HDS have been prepared through GPI-D cycles in a fluidized bed reactor.^{205,206} The gas-phase impregnation has been performed at 388 K and the metal loading (1–11% Re w/w) controlled by adjusting the exposure time (4–17 h) or by doing successive GPI-D cycles of 6 h. TPD experiments for different rhenium loadings have shown that a complete decarbonylation occurs between 773 and 873 K, and that whatever the metal content the first step of the decarbonylation corresponds to the formation of $\text{Re}(\text{CO})_3$ species. Temperature programmed oxidation and reduction profiles allow to conclude that, for a given metal loading, the dispersion of the resulting particles is better when successive deposition/decarbonylation cycles are performed: a 43% dispersion is obtained for a 11% Re w/w catalyst in one cycle, whereas a 68% dispersion characterizes a 11% w/w Re catalyst prepared by GPI-D cycles.

3. Miscellaneous

Chemical vapor deposition of MnO nanoparticles from $[\text{Mn}_2(\text{CO})_{10}]$ has been carried out on platinum(111) surfaces.²⁰⁷ At 473 K, in the presence of water vapor under UHV conditions, pure ultrathin films of MnO are obtained in a first stage. XPS reveals the presence of MnO , and the absence of any carbon incorporation, presumably due to a catalytic role of the platinum substrate. Careful deconvolution of the XPS spectra for the deposits obtained in the early stages shows the presence of MnO and zero-valent manganese. Longer contact time produces three-dimensional nanoclusters, which grow epitaxially. MnO is known to present a first-order phase transition at 118 K from para- to anti-ferromagnetism; however, performances of this material in catalysis have not been reported.²⁰⁷ Such a catalytic effect of the metallic support has clearly been observed in recent studies on GPI-D of $[\text{Cr}(\text{CO})_6]$ on Pd(100) under UHV conditions. Indeed, infrared measurements have shown that $[\text{Cr}(\text{CO})_6]$ can be decomposed on the palladium surface after physisorption and then chemisorption, whereas on a copper (100) surface $[\text{Cr}(\text{CO})_6]$ is physisorbed and desorbs without any decomposition.²⁰⁸

Finally, it is worth mentioning a recent study on the homogeneous gas-phase decomposition of $[\text{Mo}(\text{CO})_6]$ for the preparation of unsupported catalysts.²⁰⁹ The homogeneous gas-phase decomposition between 773 and 1373 K of $[\text{Mo}(\text{CO})_6]/\text{H}_2\text{S}$ mixtures produces bulk catalysts of molybdenum sulfides characterized by high surface area ($16\text{--}120 \text{ m}^2 \text{ g}^{-1}$). This method has been extended to $[\text{Mo}(\text{CO})_6]/\text{NH}_3$, $[\text{Mo}(\text{CO})_6]/[\text{Fe}(\text{CO})_5]/\text{NH}_3$ mixtures.

4. Conclusion

It appears from these reports that whereas zero-valent carbonyls are convenient precursors for metallic catalyst preparation, some questions remain unanswered concerning the characterization of the resulting materials, especially the chemical purity, the morphology of the deposits, and the particle size distribution. In addition, films deposited by MOCVD starting from carbonyl precursors, in other scientific fields than catalysis, have been reported to be contaminated by substantial amounts of carbon and oxygen.²¹⁰

B. Other Non-Noble Metal Precursors

1. Iron

Two catalytic materials have been extensively studied in the literature due to their high catalytic performances: FeMo heterobimetallic systems and Fe/ZSM5 materials.

Iron–molybdenum bimetallic catalysts supported on borosilicate molecular sieves have been prepared by GPI-D through sublimation of the corresponding chlorides, and their catalytic activities have been evaluated for the oxidation of alkyl aromatics.^{211–217}

The supports used in these studies are previously treated to adjust the silanol content on the sieve surface. Iron chloride and the support, separated by quartz wool plugs, are placed in an horizontal quartz reactor. The chloride is sublimed and transported onto the support with N_2 carrier gas at 733 K for approximately 1 h, until the powder becomes uniformly yellow. The anchoring proceeds through the elimination of 1 equiv of HCl per Fe atom, and presumably a $[\text{Si}-\text{O}-\text{FeCl}_2]$ surface species is formed.²¹¹ The resulting material is washed with deionized water, oven dried at 393 K, and heated under N_2 at 673 K. A similar subsequent procedure has been used for molybdenum deposition starting from MoO_2Cl_2 , MoOCl_4 , or MoCl_5 . The active catalyst is obtained after air calcination in the 923–963 K temperature range in such a way that the ratio Mo/Fe = 1.6–2.0 is reached. The reaction proceeds through the transient $\text{MoO}_3\cdot 3\text{H}_2\text{O}$ species, which can sublime under the reaction conditions.²¹²

This active catalyst has been characterized by X-ray diffraction, X-ray photoelectron spectroscopy, electron microscopy, Raman spectroscopy, and in situ synchrotron radiation studies.²¹³ In addition, the effect of iron and molybdenum deposition on the surface area has been examined. The two main phases on DBH, i.e., deboronated borosilicate molecular sieves, are $\text{Fe}_2(\text{MoO}_4)_3$ and MoO_3 . High-resolution electron microscopy has revealed that molybde-

num and iron are deposited as rodlike small particles inside the two microporous channel systems characteristic of the support.²¹³ Concerning the surface area, deposition of ca. 2% of iron has no effect, whereas after addition of 5% more molybdenum a small but definite decrease in both surface area and pore volume is noticed.²¹²

The activity of these catalysts in the gas-phase (oxygen^{214–217} or N₂O²¹⁵) oxidation of alkyl aromatics has been investigated. For the oxidation of benzene by N₂O to produce phenol,²¹⁵ the GPI-D Fe/Mo/DBH catalysts exhibit a significantly higher catalytic activity than their impregnated counterparts prepared from aqueous solutions of iron nitrate and ammonium paramolybdate. TEM observations show clearly a uniform and well-dispersed deposit for the GPI-D catalysts, whereas large aggregates are deposited nonuniformly and mostly on the external surface for the impregnated samples.

For the oxidation of alkyl aromatics by oxygen, the effect of the para-substituents in toluene derivatives has been studied²¹⁷ to understand the para-selective oxidation properties of the GPI-D catalysts. For the selective synthesis of terephthaldehyde from *para*-xylene, the authors show that further deposition of SiO₂ from [Si(OMe)₄] vapors on the previous catalysts (1.4% Si w/w) has a positive effect.²¹⁶ The use of other supports than DBH, such as a ZSM-5 zeolite or a silicalite, for the GPI-D preparation of the Fe/Mo catalysts has been reported.²¹⁴ On a silicate support, the limited number of silanol groups restricts the possible metal loading: 0.58% Mo w/w and 0.13% Fe w/w, vs 7% Mo w/w and 1.3% Fe w/w for the DBH support. Furthermore, a partial destruction of the silicalite and the ZMS-5 structure occurs during the catalyst preparation as observed on TEM micrographs.⁴⁷

For the selective oxidation of *para*-fluorotoluene to produce *para*-fluorobenzaldehyde, an FeMo/Boralite catalyst, prepared by a GPI-D method similar to that described by Yoo et al., shows a higher selectivity at low conversion, than bulk Fe₂(MoO₄)₃.²¹⁸ This reactivity is correlated to the presence of nanosized iron-molybdate particles inside the zeolite channels.

As reported by Sachtler et al.,^{219–224} an iron-containing zeolite, Fe/ZSM-5 prepared by GPI-D from FeCl₃, catalyzes very efficiently the reduction of NO by hydrocarbons, in the presence of high concentrations of water at temperatures as low as 623 K. The catalyst is prepared by sublimation of FeCl₃ into the cavities of a H/ZSM-5 zeolite under an argon flow at 593 K in a U-shaped reactor. The reactions between FeCl₃, or Fe₂Cl₆, that prevail in the gas phase and the Brönsted acidic sites of the zeolite result in the formation of one HCl molecule per iron atom. The samples are then washed with water and further calcinated in flowing O₂ at 773–873 K, resulting in the removal of most of the remaining chlorine. XRD measurements and HREM observations demonstrate that the GPI-D process does not cause any damage to the zeolite structure. Furthermore, only few particles have been observed and identified as iron oxides, while most of the iron is located inside the cavities and molecularly dispersed.²¹⁹ Even if a

structural identification of the active species has not been performed, the cross-checking of various experimental results provided by H₂ and CO TPR, oxygen TPD, and catalytic activity for different Si/Al ratios have allowed the proposal of the formation of a binuclear iron complex [(HO)Fe—O—Fe(OH)]²⁺.^{219,220} The presence of binuclear ionic species with a bridging oxygen ligand is also indicated by ESR spectroscopy.²²³

A similar method has been used by Centi et al. to prepare, without any calcination step, iron supported onto NaZSM-5.^{218,225,226} The comparison with an ion-exchanged catalyst, calcinated at 873 K, in the N₂O reduction reaction with the simultaneous presence of propane and oxygen has been done. The activity for N₂O reduction to N₂ is higher for the GPI-D catalyst even at lower loading (GPI-D: 1% Fe w/w, impregnation: 5% Fe w/w), but lower for propane oxidation. Both catalysts present isolated Fe³⁺ ions or small clusters. Besides these species, diffuse reflectance spectra indicate that the impregnated sample contains highly clustered Fe³⁺ and Fe₂O₃ particles. In our opinion, the high-temperature calcination step performed for the impregnated catalyst should be at the origin of the differences in reactivity.

Additional studies concerning Sachtler catalyst have confirmed the excellent performances of this GPI-D materials for selective catalytic reduction of NO_x.^{227–229} Particularly, the wide temperature range (600–800 K) of catalytic activity and stability has been demonstrated.²²⁷ Compared with a commercial vanadia catalyst, the Fe/ZSM-5 catalyst is five times more active at 673 K and produced only N₂ and H₂O in the selective reduction of NO with ammonia.²²⁸ ESR analyses have shown that the GPI-D catalyst contain mainly Fe³⁺ ions in tetrahedral and distorted tetrahedral sites.²²⁹

2. Nickel

The deposition of nickel on alumina spheres by CVD from nickel chloride vapors at 1073 K followed by a reduction step has been investigated.²³⁰ The use of a fixed bed reactor induces inhomogeneities in the deposit between the upper and the lower part of the bed. Moreover, the intraparticle nickel concentration profile shows a limited diffusion of the metal in the case of the 3.5-mm diameter alumina spheres, despite a modal pore diameter of 9 nm. TEM observations show a mean particle size ranging from 500 to 650 nm. This catalyst has been tested after a reduction step in the acetylene hydrogenation reaction and is more active than an impregnated one.

A mathematical modeling of NiCl₂ chemical vapor infiltration into a porous catalyst support has been developed by Moulijn et al.²³¹ This model shows that the intraparticle metal profile depends on (i) the associative or dissociative adsorption mode of the precursor and (ii) the decomposition rate of the adsorbed metal precursor.

The growth mechanism and reactivity of nickel particles has been studied in the sequential preparation of Ni/Al₂O₃ catalyst via GPI-D (the authors use the term of atomic layer epitaxy) by bringing [Ni(acac)₂] vapors into contact with a stationary bed

of alumina.^{232,233} During the first impregnation cycle (3–4% Ni w/w), at 473 K and 10 kPa under nitrogen, the grafted nickel species retain acetylacetone ligands with the ring structure intact. However, the C/Ni atomic ratios were 5 and 8 for alumina supports preheated at 473 and 1073 K, respectively. An atomic dispersion of nickel is obtained after the first impregnation cycle. Such dispersion is maintained after oxidation at 673 K and reduction at 773 K; however, this catalyst shows no activity for toluene hydrogenation. During the 2 to 4 cycles to prepare 5–10% Ni w/w, low-energy ion scattering (LETS) and XPS analyses reveal a growth of nickel that occurs preferentially on the nucleation centers. The best catalytic activity is obtained for 10% w/w of Ni and further increase of the amount of nickel by additional cycles does not improve the performance of the catalyst.

3. Cobalt

An extensive study of Co/SiO₂ catalysts prepared by a similar sequential GPI-D technique (once again called atomic layer epitaxy) has been performed by Backman et al. (see Figure 9).^{234–236} The organo-

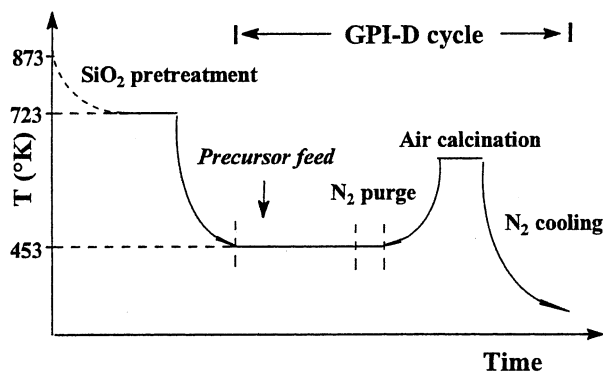


Figure 9. Catalysts preparation using GPI-D cycles (adapted from ref 234).

metallic complex [Co(acac)₃] is adsorbed at 453 K and 6–10 kPa under nitrogen on a fixed bed of silica, preheated at 873 K. The first impregnation cycle allows the deposition of around 5% Co w/w, and after seven cycles metal loading as high as 20% can be reached. The reducibility of these catalysts is low (max 30%) when compared to a classically cobalt nitrate impregnated catalyst (85–90%).²³⁴ However, if the calcination step after the last sequence is omitted, the reducibility increased up to 60%. The authors explain this phenomenon by the presence of more easily reduced cobalt species that enhance, by spillover, the easier reducibility of silicate CoO_x·SiO₂ species, which are more abundant on GPI-D catalysts than on a impregnated catalyst. The existence of higher quantities of silicates on the former catalyst is related to a higher dispersion compared to impregnated catalysts. The presence of these silicate species has been confirmed by XRD and XPS analyses.²³⁵

The resulting catalysts have been characterized and a slight decrease of the surface area and pore size has been observed when increasing the metal loading from 6 to 20% Co w/w. In parallel, the particle

size increases from 5 to 25 nm, but the catalytic activity in toluene hydrogenation is not very sensitive to these variations.²³⁵

These Co/SiO₂ catalysts have been compared to Co/Al₂O₃ samples prepared in a similar way starting from [Co(acac)₂]²³⁶ to investigate the effect of the support on the properties of the final material. Smaller quantities of metal are deposited after the first cycle on alumina support: 3 and 5% Co w/w for Al₂O₃ and SiO₂ respectively, and, for each cycle, the cobalt loading increases more slowly on alumina than on silica. In all cases, highly reducible silicates or aluminates are formed, essentially during the first cycle of the preparation. After reduction between 773 and 873 K (41 to 78% of reduction), better dispersions have been observed on alumina support for a comparable metal loading. However, no significant differences have been noticed in the toluene hydrogenation reaction. The Co/SiO₂ catalyst is three times more active than a classically impregnated catalyst (prepared from Co(NO₃)₂·6H₂O) in the ethylene hydroformylation reaction.²³⁷ This result has to be directly connected to the smaller particle size obtained with the gas-phase process: 4.3 nm for a 5% w/w Co/SiO₂ GPI-D catalyst and 11.3 nm for a 4% w/w Co/SiO₂-impregnated catalyst.

4. Molybdenum

Supported molybdenum catalysts are used in a wide variety of reactions and have been prepared by using different gas-phase methods and precursors.

The early works of Sonnemans and Mars²³⁸ have shown that a monolayered Al₂O₃·MoO₃ catalyst can be obtained by adsorbing MoO₂(OH)₂ from the gas phase on alumina. In this process, the volatile precursor is formed by flowing water/air mixtures at 868 K through a fixed bed of MoO₃ particles. The MoO₂(OH)₂ vapors react with the alumina in another fixed bed at 873 K to produce an aluminum molybdate layer Al₂O₃·MoO₃. Metal oxide loadings as high as 20% w/w have been reached for reaction times of several days. At high coverage, MoO₃ is also present on the catalyst. This material shows similar catalytic activity in the dehydrogenation of cyclohexane reaction than a catalyst prepared from the liquid phase from ammonium molybdate.

The chemically well-defined Mo²⁺/SiO₂ catalyst prepared by GPI-D from the alkyl molybdenum precursor [Mo₂(η-C₃H₅)₄]^{239,240} (Figure 10) is four

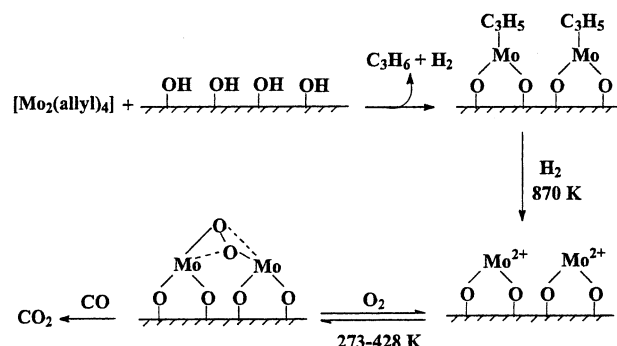


Figure 10. Surface organometallic chemistry of [Mo₂(allyl)₄] on silica.

times more active in ethene hydrogenation at 293 K than a classically impregnated catalyst.²³⁹ It has also been shown that the same Mo²⁺/SiO₂ catalyst can reversibly fix oxygen in the temperature range 273–428 K. The oxidation of CO to CO₂ by this Mo₂·O₂/SiO₂ catalyst has also been reported.²⁴⁰

Che and co-workers have extensively studied Mo/SiO₂ catalysts prepared from MoCl₅ vapor on dehydrated silica by a GPI-D method called “grafting”.^{241–243} The photoluminescence behavior of this catalyst has been investigated to get information about the structure of the surface species and their reactivity, and to compare them to impregnated catalysts.^{241,242} Dynamic photoluminescence spectroscopy studies revealed that the GPI-D catalyst contains only one type of Mo emitting site, whereas the impregnated one, obtained from the same precursor in cyclohexane solutions, contains at least two kinds of sites. The presence of isolated tetrahedral Mo species for the GPI-D catalyst and the additional presence of aggregated Mo and/or polymolybdate species on the impregnated one could be an explanation of this result.²⁴¹ The GPI-D catalyst has been tested in the photoinduced methatesis of propylene and compared with an impregnated catalyst prepared from aqueous solutions of ammonium heptamolybdate. The GPI-D catalyst presents a greater activity than its impregnated counterpart. These good performances result from the higher dispersion and the same environment for all the Mo ions (tetrahedral) on the GPI-D catalyst.²⁴² In the structure sensitive methanol oxidation reaction, good activities and selectivities have been obtained with the GPI-D catalyst. However, contrasting results have been obtained when using the impregnated catalyst, probably due to the lack of reproducibility of its preparation and to its lower metal dispersion.²⁴³

Silica-supported molybdenum oxide catalysts have also been prepared from the acetylacetato precursor [MoO₂(acac)₂] by a similar procedure.^{244,245} The gas-phase impregnation has been carried out under vacuum, between 393 and 433 K on a dehydroxylated silica (973 K) and is followed by a calcination step at 773 K. A comparison of the dispersion and of the anchoring of the complex with a conventionally prepared catalyst (aqueous impregnation of ammonium heptamolybdate) has been presented.²⁴⁵ The use of the organometallic precursor allows the formation of Si—O—Mo bonds via ligand loss and leads to larger molybdenum network (Mo—O—Mo bonds) than the impregnated catalyst. XRD shows the presence of orthorombic MoO₃ crystals for both catalysts.

Molybdenum carbide catalysts²⁴⁶ have been prepared on alumina by using a vapor mixture of MoCl₅, benzene, and H₂ under a total pressure of 0.12 kPa. The activity of this catalyst in the reduction of CO₂ has been compared to that of a molybdenum carbide catalyst prepared by impregnation. After a reduction step at 923 K in flowing hydrogen, the catalytic activity of the GPI-D catalyst is 20 times higher than that of its impregnated counterpart. XPS measurements reveal that the valency of molybdenum changes from II for the GPI-D carbide to IV for the impregnated one.

Finally, steam-deposited MoO₃/SiO₂ catalysts have been prepared from MoO₃ and water at high temperature (around 973 K).²⁴⁷ The presence of water allows the formation of volatile molybdenum hydroxyoxides and the transient formation of Si—OH groups that permit the attachment of molybdenum species.

5. Vanadium

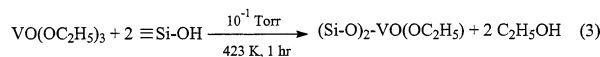
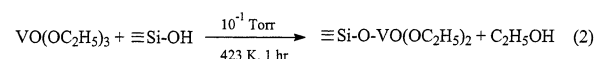
First, the reactivity of VCl₄ vapors with different oxide surfaces (Al₂O₃, SiO₂) has been used to get insight on the hydroxyl groups distribution on these surfaces.²⁴⁸ Then, vanadium-supported catalysts have been studied because of their activity and selectivity in oxidation reactions of organic compounds.^{249,250}

The reaction at room temperature of VOCl₃ vapors with hydroxylated anatase followed by a calcination step at 670 K allows a loading of V₂O₅ substantially lower than the value expected for a complete monolayer. Four additional GPI-D cycles are necessary to obtain a catalyst corresponding to one monolayer, which gave a very high selectivity to phthalic anhydride in the *o*-xylene oxidation reaction. Such selectivity is noticeable for a low loading V₂O₅ catalyst and without the aid of any promoter.²⁴⁹ However, it is worth noting that a similar catalyst can be prepared by a standard procedure that consists of wet impregnation of VOCl₃ in different organic solvents.²⁵⁰

More recently, it has been shown that VOCl₃ can be introduced in the channels of MCM-41 by a GPI-D process.²⁵¹ Gas-phase impregnation of VOCl₃ at 375 K under nitrogen, followed by purging in N₂ to remove physisorbed VOCl₃, affords chemically bonded vanadium species. Previous studies on silica support have allowed proposing Si—O—VOCl₂ species.²⁵² Hydrolysis at 375 K and calcination in dry oxygen at 675 K produces predominantly mononuclear V⁵⁺ oxide in tetrahedral coordination VO₄³⁻ together with easily reducible polynuclear V⁵⁺ oxide species.

Photoassisted (300–450 nm) chemical vapor deposition of VOCl₃ at 273 K on porous Vycor glass allows one to obtain the chemically anchored Si—O—VOCl₂ species via reaction with hydroxyl groups and HCl elimination.²⁵³ Further hydrolysis and calcination steps give a tetrahedral V⁵⁺ mononuclear species that presents photoluminescent properties. These anchored vanadium oxide catalysts show a much higher activity for the photocatalytic isomerization of 2-butene than that of oxides prepared by conventional impregnation.

Vanadyl alkoxides precursors have also been used with success to prepare supported V₂O₅ catalysts.^{254–258} The [VO(OC₂H₅)₃] vapors react at 423 K under a pressure of 13 Pa with the OH groups of a high surface area silica to produce two surface species:



as suggested by ethanol evolution measurements and changes in the OH region of the IR spectra during GPI-D cycles. Further treatments at 623 or

723 K under vacuum produce highly dispersed V₂O₅ overlayers (thin film or small sized nanoparticles) as indicated by XPS from semiquantitative measurements of the V to Si ratio (I_V/I_{Si}).^{254,255} After seven GPI-D cycles, V₂O₅ loading as high as 18% w/w are reached with a high I_V/I_{Si} ratio (0.7) compared to a conventional prepared impregnated catalyst ($I_V/I_{Si} = 0.2$). The as-prepared GPI-D catalyst is 3–4 times more active than the impregnated one in the oxidative dehydrogenation of ethanol reaction at 493 K.²⁵⁴

The same authors have studied by EXAFS the influence of the preparation method (GPI-D or impregnation) and of the nature of the support on the structure of the overlayers.²⁵⁶ The GPI-D method leads to thin films of V₂O₅ (5–10% w/w) on SiO₂ (2 OH nm⁻²) and on Al₂O₃ (10 OH nm⁻²), whereas liquid-phase impregnation produces crystallites, defined by the authors as entities, detectable by XRD on silica and thin films on alumina. In the same oxidative dehydrogenation of ethanol reaction the catalytic activity decreases in the order V₂O₅/Al₂O₃- (GPI-D) > V₂O₅/Al₂O₃(imp) > V₂O₅/SiO₂(GPI-D) > V₂O₅/SiO₂(imp). The conclusion is that the activity of the thin films is greater than that of crystallites.

Vanadyl triisopropoxide [VO(*i*-C₃H₇)₃] (VOTIP) has been used to prepare vanadia catalysts on different supports.^{257,258,245,173} On titania, a support that presents low surface area and low OH concentrations, low loadings of metal are obtained by a cyclic GPI-D process. After three cycles (GPI at 300 K and calcination under O₂ or decomposition under N₂ at 573 K), a V₂O₅ loading of 3.5% w/w is obtained, whereas for an impregnated catalyst (immersion of the support in VOTIP) 5% w/w is obtained in one operation. Raman spectroscopy and ⁵¹V NMR spectrometry have been used to characterize the structure of the vanadia species as a function of the dehydroxylation degree of the support. Tetrahedral coordinated vanadia species predominate on highly dehydroxylated surfaces, whereas octahedral coordinated vanadia ions are present on fully hydroxylated supports.²⁵⁷ Silica, alumina, and zirconia supports have also been investigated,²⁵⁸ and the catalytic properties of the final material have been reported for the reduction of NO by NH₃. The intrinsic activity decreases following the sequence: V₂O₅/TiO₂ > V₂O₅/ZrO₂ > V₂O₅/Al₂O₃ > V₂O₅/SiO₂ and is correlated to the various distributions of the Lewis- and Brönsted-bound ammonia sites on the supported vanadia catalysts.

The preparation of vanadium oxide on different supports from the vanadium acetylacetones [V(acac)₃]¹⁷³ and [VO(acac)₂]²⁴⁵ has been reported. The complex [V(acac)₃] is adsorbed on dehydrated silica or alumina at 400 K under N₂ in a fluidized bed reactor.¹⁷³ On silica, the chemisorption involves a partial precursor decomposition via acetylacetone evolution, which is more complete on the alumina support. Further decomposition of the surface species in air produces V₂O₅ at 470 K on SiO₂ support and at 570 K on Al₂O₃ support. The [VO(acac)₂] precursor has been adsorbed on silica gel by GPI (called “molecular designed dispersion”) and by impregnation in toluene.^{245,259} In the liquid-phase impregnation at room temperature, hydrogen bonding occurs

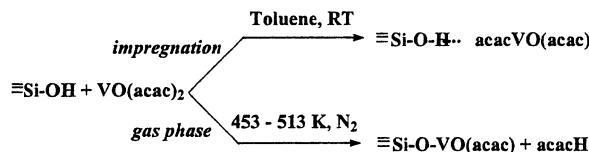


Figure 11. Surface reaction of [VO(acac)₂] with silica.

through an hydroxyl group of the support and an acetylacetato ligand (Figure 11).

For the gas-phase impregnation at 453–513 K and under nitrogen a ligand exchange mechanism prevails (Figure 11), whereas at 403–443 K under vacuum both hydrogen bonding and exchange mechanism coexist. On alumina, a more reactive support, the reaction of [VO(acac)₂] proceeds exclusively by a ligand exchange mechanism. It has been demonstrated from infrared investigations that the environment of the vanadium atoms changes slightly according to the preparation method and to the supports: it is essentially tetrahedral with some fraction of octahedral sites in the case of GPI-D of [VO(acac)₂] on silica support. These catalysts present a significant activity for the oxidation of methanol.²⁵⁹ To obtain the vanadium oxide catalyst; the precursors are thermally converted by oxidation in air at 773 K.

On new mesoporous MCM-48 silica support, the same GPI-D procedure has been applied and after calcination of the grafted complex the supported vanadium species are present in a tetrahedral configuration, mainly as linked tetrahedra and not as isolated species. The final catalyst, 8.7% V w/w, still presents a narrow pore size distribution and a high surface area ($S_{BET} = 800 \text{ m}^2 \text{ g}^{-1}$) compared to the original support ($S_{BET} = 1000 \text{ m}^2 \text{ g}^{-1}$).²⁶⁰ Modified MCM-48 supports have also been used to obtain larger amounts of anchoring sites and a better anchoring of the vanadium species.²⁶¹ An extremely stable catalytic material (under hydrothermal conditions) is produced in which isolated tetrahedral V⁵⁺ species are dominant.

6. Chromium

The preparation of CrO_x/Al₂O₃ catalysts has been studied by several authors, mainly because of their catalytic activity in dehydrogenation reactions.^{173,262–264} The [Cr(acac)₃] precursor has been employed for gas-phase impregnation under N₂, and decomposition has been performed under air between 673 and 873 K. The metal loading is adjusted either by using a repeated pulse technique^{262,263} (1.3 to 12.5% Cr w/w), or by adjusting the gas-phase impregnation duration (1.2 to 16.9% Cr w/w).²⁶² Adsorption of [Cr(acac)₃] on alumina between 400 and 473 K seems to proceed via a dissociative pathway as reported by Baerns et al.¹⁷³ and Kytkivi et al.,^{262,263} however, Vansant et al.²⁶⁴ report that adsorption proceeds in a molecularly dispersed form without acac ligand elimination. Air oxidation of the impregnated samples produces both Cr³⁺ and Cr⁶⁺ amorphous species.^{262,263} The CrO_x dispersion decreased from 77 to 22% when increasing CrO_x loading from 0.9% w/w to 11.8% w/w.⁶ The activity and selectivity of the GPI-D catalysts for

isobutane dehydrogenation to butene is very similar to those of impregnated catalysts.²⁶³

C. Noble Metals

Due to the wide use of mono- or bimetallic supported noble metals catalysts, their preparation by gas methods will retain particularly our attention. In this group of elements, many complexes have been prepared and characterized, so that organometallic chemistry affords a large variety of potential precursors. However, in the platinum group metal, no zerovalent carbonyl complexes are stable enough to be used in a gas-phase preparation process.

1. Gold

Although it is well established that the surface of gold is intrinsically inert, it has been shown that the control of a high metal dispersion (particle size around 2–5 nm) through a strong interaction between the gold particles and the support can give highly active catalysts for a large variety of reactions.^{265–269}

Haruta et al. have compared different methods for the preparation of gold catalysts on various oxide supports (TiO_2 , Al_2O_3 , SiO_2 , MgO , ZnO , or Fe_2O_3): three different liquid-phase methods using HAuCl_4 as starting reagent and one GPI-D method using $[\text{Au}(\text{CH}_3)_2(\text{acac})]$ as volatile precursor.^{265–267} It results from these studies that, only the GPI-D technique allows the deposition of active gold nanoparticles with relatively high dispersion whatever the investigated supports (2–6 nm gold nanoparticles), even on acidic ones.²⁶⁶ The main drawbacks of the liquid-phase methods are interpreted by the authors as being due to (i) a weak interaction between the HAuCl_4 precursor and acidic supports giving rise to large gold particles and/or (ii) the partial embedding of gold nanoparticles in the bulk of Al_2O_3 in the coprecipitation preparation methods.

The GPI-D method consists of (i) contacting overnight $[\text{Au}(\text{CH}_3)_2(\text{acac})]$ vapors at 306 K with the pretreated support (dehydration for hours at 473 K and oxidation under 2.6 kPa O_2 at 473 K), and (ii) a calcination step in air in the temperature range 473–773 K to decompose the precursor into metallic gold particles. The highly dispersed gold nanoparticles deposited on SiO_2 are particularly active for CO oxidation at low temperatures.²⁶⁹

2. Palladium

In 1991, Sachtler and Faly²⁷⁰ have shown that chlorine treatments at 623 K of Pd/NaY or Pd/HY impregnated catalysts lead to a redispersion of the palladium. The redispersed species are palladium(II) halides that sublime and transport the metal from the external surface to the interior of the zeolite support. Further H_2 reduction produces HCl and highly dispersed (<12 Å) Pd^0 particles. Although this study would suggest the potentiality of PdCl_2 as a volatile precursor, later studies report only the use of organometallic palladium precursors.

The palladium complex $[\text{Pd}^{\text{II}}(\eta^3\text{-C}_3\text{H}_5)(\eta^5\text{-C}_5\text{H}_5)]$ has been used by Dossi et al. to prepare Pd/NaY or Pd/NaHY catalysts by GPI-D.^{169,271–273} These studies

highlight some advantages of gas-phase processes compared to wet impregnation. The gas-phase impregnation of the support is carried out in a U-shaped tube under argon at 298 K and atmospheric pressure. After impregnation, the organometallic precursor is decomposed into metal by heating under a 95% He/5% H_2 atmosphere. The thermal decomposition has been monitored until 773 K by temperature programmed reductive decomposition technique (TPRD) for both NaY and NaHY supports.²⁷² On both supports, the authors observe the formation of propane and cyclopentane resulting from the hydrogenation of the two allyl and cyclopentadienyl ligands on the metal. However, the evolution of cyclopentane is significantly lower and spread out over a much larger temperature range on NaHY than on NaY support. The authors explain this phenomenon by the presence of intrazeolite protons, probably favoring cationic polymerization of the cyclopentadienyl ligand prior to its hydrogenation.

On NaY support, a clean decomposition to metallic palladium is assumed to be achieved at 473 K. This catalyst presents a bimodal particle size distribution²⁷³ with maxima corresponding to the supercage diameters: 1.3 and 2.5 nm. Thus, the GPI-D technique allows the reduction of the surface migration of metal clusters to the surface of the zeolite by using mild reduction conditions. Pd/NaY catalysts produced by GPI-D or conventional wet impregnation methods have also been studied at 573 K in the methylcyclopentane reforming reaction, leading to ring opening products, ring enlargement products, and coke deposition. The GPI-D catalysts are characterized by a lower deactivation rate compared to the conventional ones. Another advantage of GPI-D is the absence of solvent that prevents the precursor molecule from entering inside the zeolite cages. Similarly, the authors have shown that, on a MgO support, GPI-D catalysts prepared from $[\text{Pd}(\eta^3\text{-C}_3\text{H}_5)(\eta^5\text{-C}_5\text{H}_5)]$ are more active and selective than the impregnated one for methylcyclopentene aromatization.²⁷⁴

The same precursor has been used by Ying et al.^{275,276} to graft palladium on mesoporous molecular sieves by GPI-D. The precursor has been contacted under reduced pressure at 358–393 K with MCM-41 ($997 \text{ m}^2 \text{ g}^{-1}$, pore size 27.4 Å) and in a second step reduced under a hydrogen stream at 573–623 K. The resulting black material consists of 15–25% Pd w/w, with dispersions around 30%. The authors have also reported the use of a fluidized bed to scale-up the preparation of the catalyst and to ensure a uniform exposure of the large amounts of support with the precursor during the gas-phase process. Impregnated catalysts have also been prepared starting from different precursors, including $[\text{Pd}(\eta^3\text{-C}_3\text{H}_5)(\eta^5\text{-C}_5\text{H}_5)]$ in hexane solutions; all of them present lower dispersions, and lower activities in the Heck carbon–carbon coupling reaction.

A one-step CVD process has been reported to prepare Pd/SiO₂ catalysts in a fluidized bed reactor.^{277–279} Preliminary CVD experiments have been performed on model planar supports in an horizontal hot-wall reactor. The CVD process consists of carrying the vapor of the palladium precursor toward the support

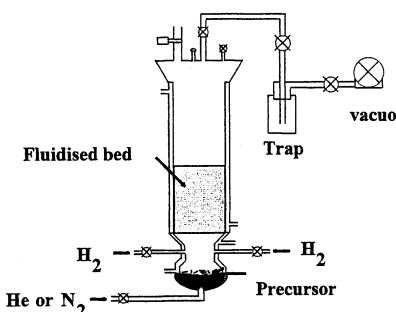


Figure 12. Fluidized bed CVD reactor for the preparation of supported catalysts.

that is heated to a temperature able to ensure metal deposition and ligand removal. A reactive gas such as hydrogen can be introduced to activate this reaction via ligand hydrogenation.

The two complexes $[\text{Pd}(\eta^3\text{-C}_3\text{H}_5)(\eta^5\text{-C}_5\text{H}_5)]$ (**1**) and $[\text{Pd}(\eta^3\text{-C}_3\text{H}_5)\text{(hfa)}]$ (**2**) (hfa = $\text{CF}_3\text{COCHCOCF}_3$) have been heated between 303 and 323 K and carried by a helium stream toward the support under a total pressure of 6.6 kPa. In these conditions, precursor **1** decomposed at 533 K and precursor **2** at 683 K. The addition of controlled amounts of hydrogen as reactive gas in the precursor and helium mixtures allows one to decrease dramatically the decomposition temperatures to 333 K for **1** and **2** and to produce pure metallic films as evidenced by X-ray diffraction and XPS analyses.²⁷⁷ On-line MS analyses of the gas phase at the exit of the reactor confirm the role of hydrogen and show the autocatalytic behavior of the reaction. The decomposition products are cyclopentane and propane as already reported by Dossi et al.²⁷⁸ plus cyclopentene and cyclopentadiene resulting from a partial hydrogenation due to the low partial pressure of hydrogen introduced in the gas phase. The same tuned conditions have been applied to the preparation of Pd/SiO₂ catalysts in a fluidized bed reactor (Figure 12) from $[\text{Pd}(\eta^3\text{-C}_3\text{H}_5)(\eta^5\text{-C}_5\text{H}_5)]$.²⁷⁷ Homogeneous deposits of pure palladium have been observed by TEM that consist in 2–4 nm nanoparticles for metal leading ranging between 1 and 4% Pd w/w. These catalysts show high activities in cyclohexane dehydrogenation²⁷⁸ and octene hydrogenation²⁷⁹ reactions.

Palladium acetylacetonate $[\text{Pd}(\text{acac})_2]$ has been used to prepare Pd/MgO catalysts by the dry-mix method²⁸⁰ or Pd catalytic monoliths by CVD.²⁸¹

In the first case, the support consists of ultrafine single crystals (100 nm and $S_{\text{BET}} = 144 \text{ m}^2 \text{ g}^{-1}$) that are uniformly mixed by ultrasonic vibrations with $[\text{Pd}(\text{acac})_2]$ and heated at a temperature higher than the melting point of the precursor, i.e., around 473 K. Then, the acetylacetonate ligand is decomposed at 523 K and finally the catalysts are calcinated from 1023 to 1773 K to test their thermal stability. The catalysts present surface area as large as $60 \text{ m}^2 \text{ g}^{-1}$ after calcination and show a high activity for methane combustion. Similar results have been obtained for Pt/MgO and Ru/MgO starting from $[\text{Pt}(\text{acac})_2]$ and $[\text{Ru}(\text{acac})_3]$ respectively.

In the second case, palladium catalytic monolith with a nonuniform distribution of the active metal is produced by CVD. The sublimation temperature

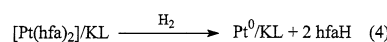
(373–393 K) and the decomposition temperature (403–423 K) are ensured by the temperature profile of the furnace. The reaction takes place under atmospheric pressure for 2–4 h and leads to non-uniformly distributed nanoparticles (0.01–0.03% Pd w/w). The particle size in the entry region of the monolith is centered at 4–5 nm. A nonuniform distribution has been shown theoretically to offer good performance in automotive catalysis.²⁸¹

3. Platinum

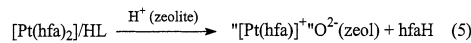
Platinum acetylacetones $[\text{Pt}(\text{acac})_2]$ and $[\text{Pt}(\text{hfa})_2]$ have been extensively used to prepare platinum-based catalysts.

A dry-mix method has been developed by Davis et al. to load $[\text{Pt}(\text{acac})_2]$ into aluminosilicate and aluminophosphate supports.²⁸² A dry mixture of the precursor and the molecular sieve is kept under vacuum in a sealed tube at 418 K for 16–34 h. The resulting material is analyzed by ¹³C-MAS NMR and TEM and compared to an $[\text{Pt}(\text{acac})_2]$ /acetone impregnated catalyst. For the dry-mix method, the ¹³C-MAS NMR spectra are similar to those of the free complex, suggesting that it remains located on the outer surface of the support. For Pt/AlPO₄₋₅ catalysts, the TEM observations confirm the localization of the particles (well dispersed over the support) with a mean particle size of 2–3 nm for the dry-mix catalyst, and 20 nm for the impregnated catalysts with most of the particles being located on the outer surface. The authors propose that, in the liquid phase, the metal complex can be solvated by acetone and, with such a solvation sphere, may be too large to enter the pores of the supports.

Using the same apparatus as for the GPI-D preparation of palladium-based catalysts (see above), Dossi et al. have prepared 1% w/w Pt/KL or Pt/HL zeolites catalysts.^{271,272,283–285} The precursor is sublimed at 343 K under argon and decomposed to metal by heating in flowing H₂ at 523 K. Once the precursor has been encaged in the zeolite, TPRD (H₂) studies revealed different behaviors for $[\text{Pt}(\text{hfa})_2]$ /KL and $[\text{Pt}(\text{hfa})_2]$ /HL. One peak ($m/z = 69$, hfaH) is observed at 559 K for $[\text{Pt}(\text{hfa})_2]$ /KL, whereas two peaks at 433 and 553 K are present for $[\text{Pt}(\text{hfa})_2]$ /HL. On KL support, the decomposition follows the pathway:



On HL zeolites, the presence of protons induces the intermediate step:



From EXAFS experiments, the authors propose that the precursor molecule is entrapped within the channels of the KL support, and that, after decomposition, the size of the metal particles is not influenced by the zeolite protons and do not exceed 0.7–0.8 nm in size.^{283,284} The activity of these two catalysts in the reaction of conversion of methyl cyclopentane (MCP) to benzene at 773 K has been reported. The Pt/KL catalyst is characterized by unique properties, i.e., activity and selectivity to benzene formation,

Table 3. Atom Number of Platinum in the Cluster Formed on HMOR and KLTL

preparation procedure of 2% (w/w) Pt/support	average number of Pt atoms per cluster	
	HMOR	KLTL
dry-mix: $[\text{Pt}(\text{acac})_2]$ + support (318 K, vacuum, 2 h)	45	10
wet impregnation: $[\text{Pt}(\text{acac})_2]$ + support (acetone, 300 K, + drying overnight 383 K)	230	15
ion-exchange: $[\text{Pt}(\text{NH}_3)_4]\text{Cl}_2$ + sup. (water + NH_3 ($\text{pH} = 11$), 353 K, + drying overnight 383 K)	45	< 10

Table 4. Effect of the Addition of Hydrogen to the Carrier Gas for the Decomposition of Platinum Precursors

precursor/ H_2	$T_{\text{sublim}}/T_{\text{decomp.}}$ (K)	impurities (XPS and EDX)	metal loading % (w/w)/ mean particle size (nm) ^a
$[\text{PtMe}_2(\text{COD})]$	343–353/513	C (high amounts)	
$[\text{PtMe}_2(\text{COD})]/\text{H}_2$	343–353/363–393	C (1%)	2.3/3
$[\text{Pt}(\text{hfa})_2]$	328–348/673	F, C (10%), O	
$[\text{Pt}(\text{hfa})_2]/\text{H}_2$	328–348/413–423	C (10%), O (1%)	1.7–5.7/10–100

^a On SiO_2 powders.

while Pt/HL activity drops rapidly to 10% after 30 min and continuously decreases. It is assumed that this deactivation is due to a preferential deposition of carbonaceous residues onto acidic sites.

Similar Pt/KL catalysts have been prepared by the dry-mix method starting from $[\text{Pt}(\text{acac})_2]$ and compared to impregnated catalysts in the reaction of conversion of MCP.²⁸⁶ The solid mixture of zeolite and $[\text{Pt}(\text{acac})_2]$ is heated under vacuum between 333 and 403 K to ensure a complete and homogeneous re-partition by sublimation of the precursor, and then calcinated under air at 623 K to decompose the precursor. TEM and EXAFS show that the dry-mix catalysts results in smaller particles than the catalyst prepared by impregnation with an aqueous solution of tetraamine platinum(II) nitrate. Such morphology induces an improvement of the performance of the dry-mix catalyst under clean and sulfur-poisoned conditions, enhancing the catalyst resistance to coke formation and decreasing the sintering.

On unidimensional molecular sieves (MOR, KLTL), the influence of the preparation procedures has been confirmed by EXAFS and XANES.²⁸⁷ The number of atoms per cluster of platinum after calcination and reduction is reported in Table 3 according to the preparation procedure.

On neutral molecular sieves, the authors note that larger clusters are obtained, but the dry-mix method still gives better results than wet impregnation.

A fluidized bed GPI-D process has been used by Baerns et al. to deposit platinum on SiO_2 and Al_2O_3 from $[\text{Pt}(\text{acac})_2]$.¹⁷³ After adsorption on the support at 400 K under N_2 at atmospheric pressure, DRIFT spectra of the adsorbed precursor show that (i) on SiO_2 , the adsorbate consists of the entire $[\text{Pt}(\text{acac})_2]$ molecule, H-bridges between silanol groups and the delocalized π -electrons of an oxygen of the acac ligand and (ii) on Al_2O_3 , a partial decomposition of $[\text{Pt}(\text{acac})_2]$ occurs leading to acetylacetone adsorbed as an enolate and to surface carbonate formation. Upon decomposition under N_2 between 420 and 570 K, CO is the main gaseous decomposition product whatever the support, as well as some acetylacetone and acetone on silica support. Carbonates and carboxylate species are present on the alumina support after complete decomposition of the platinum precur-

sor. It is reported that, on silica supports, the dispersion of the final catalyst can be affected by the atmosphere used to perform the decomposition (N_2 or air).

A one-step CVD process in fluidized bed reactor has been used by Kalck et al. to prepare Pt/SiO_2 ,^{278,279} Pt/C^* ,^{288,289} and $\text{Pt-Pd}/\text{SiO}_2$ catalysts.²⁹⁰ In the case of Pt/SiO_2 , $[\text{Pt}(\text{hfa})_2]$ and $[\text{Pt}(\text{CH}_3)_2(\text{COD})]$ have been investigated as potential precursors. A preliminary study on planar SiO_2 substrates in a classical horizontal CVD reactor as well as TGA analyses have allowed the determination of the temperatures of decomposition and to demonstrate their significant decrease when a partial pressure of hydrogen is added to the gas phase. XPS and EDX analyses have demonstrated that H_2 also improves the purity of the final deposit (Table 4).

The disappointing results obtained starting from $[\text{Pt}(\text{hfa})_2]$ have to be interpreted as resulting directly from the stability of the complex and from the difficulty of decomposition, even in the presence of hydrogen. In the case of $[\text{Pt}(\text{CH}_3)_2(\text{COD})]$, a clean decomposition is observed under H_2 , giving rise to methane, cyclooctane, cyclooctene, and cyclooctadiene as organic products.

Furthermore, the authors have demonstrated the crucial role of a high supersaturation regime to obtain a high nucleation rate with regard to the growth rate. Indeed, for a high supersaturation of the $[\text{Pt}(\text{CH}_3)_2(\text{COD})]$ precursor ($T_{\text{sublimation}} = 468$ K, vapor pressure = 4.6 Pa) a mean particle size of 2–6 nm is obtained, whereas for a low supersaturation ($T_{\text{sublimation}} = 402$ K, vapor pressure = 0.48 Pa) the mean particle size is around 60 nm.

On activated carbon or carbon nanospheres,^{288,289} the platinum dispersion, starting from $[\text{Pt}(\text{CH}_3)_2(\text{COD})]$, depends strongly on the amount of anchoring sites. On commercial activated carbon, a mean particle size of 10–15 nm has been measured. Oxidative treatments (HNO_3 or O_2) of the supports lead to a dramatic increase of surface oxygen containing groups that result in a better dispersion of the platinum with a mean particle size of 4–5 nm. On carbon nanospheres, a support that does not present anchoring sites, no deposition is observed in the absence of oxidative treatment. After oxidation, a mean particle

Table 5. Main Characteristics of the Rh/SiO₂ (1% w/w) Catalysts Starting from Various Complexes

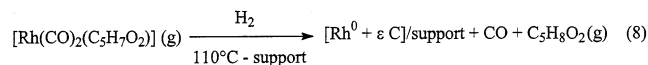
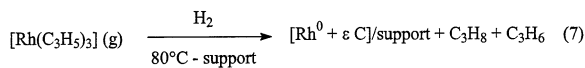
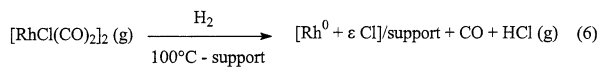
precursor/H ₂	T _{sublim/} T _{decomp} (K)	impurities (XPS) w/w	mean particle size (nm)
[RCl(CO) ₂] ₂	326/398	Cl (23%)	
[RCl(CO) ₂] ₂ /H ₂	326/348	Cl (1.5%)	1.8
[Rh(allyl) ₃]	313/373	C (19%)	
[Rh(allyl) ₃]/H ₂	313/333	C (7%)	1.5
[Rh(CO) ₂ (acac)]	328/408	C (32%)	
[Rh(CO) ₂ (acac)]/H ₂	328/358	C (14%)	1.7

size of 5 nm is measured on this support of low surface area ($10 \text{ m}^2 \text{ g}^{-1}$).

Bimetallic Pt/Pd nanoparticles have also been produced on silica support in a fluidized bed reactor by two successive CVD runs starting from [Pt(CH₃)₂(COD)] at 393 K and then [Pd(η^3 -C₃H₅)(hfa)] at 333 K in the presence of a low partial pressure of H₂.²⁹⁰ The selective deposition of palladium on preformed platinum nanoparticles is observed that leads to a layered, pure bimetallic structure (mean particle size 5–15 nm). Catalytic dehydrogenation of cyclohexane tests have shown the high activity and stability of these bimetallic catalysts.

4. Rhodium, Iridium, Ruthenium, and Osmium

Although the surface chemistry of [RhCl(CO)₂]₂ and [Rh(η^3 -C₃H₅)₃] on oxide supports has been deeply investigated (see part II), the direct preparation of metallic rhodium catalysts by CVD has only been reported by Kalck et al.^{291–295} Three rhodium complexes [Rh(η^3 -C₃H₅)₃], [RhCl(CO)₂]₂, and [Rh(CO)₂(acac)] have been identified as convenient precursors for the one-step preparation of rhodium-supported catalysts on SiO₂ or activated carbon (C*) in the fluidized bed reactor already described.¹¹² To control the molar ratio and the metal loading of the catalysts, the vapor pressure laws have been determined.²⁹⁴ A precursor/helium molar ratio of around 10^{-3} has been used under a total pressure of 13 kPa, corresponding to temperatures of sublimation ranging between 307 and 338 K according to the complex. The temperatures of decomposition decrease significantly upon addition of hydrogen (~10%) in the gas phase and ligand hydrogenation allows a decrease in the amount of impurities in the final deposit (Table 5). The results of ligand removal on silica supports can be summarized as:



It is worth mentioning that, contrary to the GPI-D process, in this one-step CVD process, the fast kinetics of the reactions does not allow the identification of the intermediate rhodium surface species. Furthermore, gas-phase reactions could occur, but in the case of the [RhCl(CO)₂]₂ precursor all attempts to identify gaseous intermediate species have been

unsuccessful.²⁹⁶ The presence of metallic rhodium in all the samples has been evidenced by XRD and XPS analyses.

In the case of [RhCl(CO)₂]₂, the mean particle size increases from 1.2 nm for 0.5% Rh/SiO₂ w/w to 3.0 nm for 5% Rh/SiO₂ w/w. On activated carbon, a larger mean particle size of 4–5 nm is measured for a 2% Rh/C* w/w. These CVD Rh/C* catalysts are efficient for the hydrocarbonylation of acetic acid into higher acids (mainly propionic) at 20 MPa and 493 K.²⁹⁵

Basset and co-workers have studied the GPI-D and the wet impregnation and decomposition processes of [Ir(acac)₃] on silica supports by infrared spectroscopy.²⁹⁷ In a first step, at room temperature, both methods produce physisorbed [Ir(acac)₃] on the surface. Upon oxidation under oxygen at 573 K, it seems that the decomposition of the physisorbed complex occurs by complete oxidation of the acetylacetone groups into CO, CO₂, and carbonates. Upon reduction under hydrogen, CO, CO₂, acetylacetone, and hydrocarbon have been detected. The mean particle size has been found in the case of the wet impregnation, to be 0.7–4 nm after the reduction step.

Due to its high volatility, ruthenocene has been used by Miura et al. to prepare Ru/SiO₂ catalysts or Ru/Pt wire gauze materials.^{298,299} On silica support, a GPI-D process has been used: ruthenocene is sublimed under hydrogen at 360 K and is further reduced at 500 K in flowing H₂. The Ru dispersion in the final catalyst has been found to be very low (2–3%), presumably due to a weak interaction between the precursor and the silanol groups that induces the ruthenium atoms migration across the support during the reduction step. On platinum wire gauze, chemical vapor deposition is optimal at 450 K under hydrogen and leads to selective deposition on the platinum substrate, while at higher temperatures deposition occurs also on the Pyrex walls of the reactor.

Finally, osmium carbonyl clusters have been entrapped in Y zeolite by exposure of the support to [H₂O₂Os(CO)₄] vapors at room temperature.³⁰⁰ This material has been found to be a selective and stable catalyst for CO hydrogenation at 573 K and 2 MPa to give C₂–C₄ hydrocarbons.

5. Bimetallics

As the catalytic performances, and particularly the selectivity, of supported metal catalysts can be substantially modified by tin addition, the deposition of tin has been used for the production of Rh/Sn, Pt/Sn, and Ni/Sn bimetallic catalysts. Alkyl tin precursors have been particularly investigated.

Iwasawa et al. have prepared highly active Rh–Sn/SiO₂ catalysts for NO/H₂ and ketone hydrogenation reactions.^{301–306} The Rh/SiO₂ catalyst has been prepared by classical wet impregnation of RhCl₃, followed by a reduction step. The mean particle size of this Rh/SiO₂ catalyst is 2.5 nm. Then, GPI of [Sn(CH₃)₄] has been performed in a closed circulating system at low pressure and 423 K. The vapors of [Sn(CH₃)₄] react exclusively with the rhodium nanoparticles and two molecules of methane per tin atom evolve, probably via OH groups activation. By further

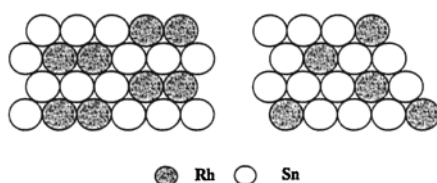


Figure 13. Bimetallic Rh–Sn structure model of Rh–Sn/SiO₂.

reduction at 573 K under hydrogen, two more molecules of methane are formed, leading to complete elimination of carbon on the surface. The rhodium loading has been fixed at 14% w/w, while the Sn/Rh ratio ranges from 0 to 1. A mean particle size of 2.5 nm has been measured for Rh–Sn/SiO₂ (Sn/Rh = 0.45) and of 3 nm for Rh–Sn/SiO₂ (Sn/Rh = 0.9). The structure of these catalysts has also been studied by EXAFS as a function of the Sn/Rh ratio. The Sn atoms in the bimetallic particles remain located in the first layer as long as Sn/Rh < 0.4, whereas above this value Sn atoms intrude into Rh metal particles. Bimetallic ensemble models have been proposed for Sn/Rh = 0.2³⁰⁶ and Sn/Rh = 0.4³⁰² (Figure 13). For a surface composition of Sn_{surf}/Rh_{surf} = 1.5 (Sn/Rh = 0.2 at.), two atoms of Rh are surrounded by 8 atoms of Sn. For a surface composition of Sn_{surf}/Rh_{surf} = 3 (Sn/Rh = 0.4), one rhodium atom is surrounded by six tin atoms. These two different environments confer different reactivity to the catalysts. For example, in the NO/H₂ reaction the best activity has been obtained for Sn/Rh = 0.4,³⁰¹ and for the ketone hydrogenation,³⁰⁶ the best results have been obtained for Sn/Rh = 0.2. In the case of coimpregnated catalysts, the particular Rh–Sn bimetallic surface structure (Sn/Rh = 0.4) is not present, and these catalysts are six times less active in the NO/H₂ reaction than the one obtained by GPI-D.³⁰¹

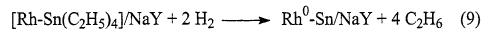
A PtSn/SiO₂ catalyst has been prepared by the same group in a similar way³⁰⁷ by reacting [Sn(CH₃)₄] vapors at 423 K with a Pt/SiO₂ catalyst prepared by the usual impregnation method using H₂PtCl₆ solutions. For a Sn/Pt ratio of 0.2 (Sn_{surf}/Pt_{surf} = 1.5) the same surface structure model than for rhodium has been proposed from EXAFS analyses. These PtSn/SiO₂ catalysts are active in the synthesis of unsaturated nitriles from NO and alkanes or alkenes.

The surface reaction of [Sn(i-C₄H₉)₄] with Rh/SiO₂³⁰⁸ or Ni/SiO₂³⁰⁹ catalysts has been studied and the deposits characterized by different analytical methods. The Rh/SiO₂ and Ni/SiO₂ catalysts have been prepared by a cationic exchange between [RhCl-(NH₃)₅]²⁺ or [Ni(NH₃)₆]²⁺ and \equiv SiO–NH₄⁺ groups, followed by oxidation and reduction. In the absence of Rh or Ni, the tin precursor does not interact with the silica surface, even upon heating at 573 K. When the tin precursor reacts with the metallic surface under an hydrogen atmosphere (30 kPa), a controlled hydrogenolysis of [Sn(i-C₄H₉)₄] on M/SiO₂ has been evidenced. This reaction, which produces butane and ethene on Rh catalysts or butane and butene on Ni catalysts, is controlled both by the Sn_{surf}/M_{surf} ratio and by the temperature. At a given temperature (<373 K) and for a high surface coverage, there is incomplete hydrogenolysis and surface organometal-

lic fragments are stable. At low coverage, the organometallic fragments are fully dealkylated. An MSn/SiO₂ catalyst is obtained at 473 K on Rh or 373 K on Ni. The particle size varies slightly before and after tin deposition: 1–2 nm for Rh/SiO₂ and 2–3 nm for RhSn/SiO₂ as well as 3–4 nm for Ni/SiO₂ and 4–5 nm for NiSn/SiO₂.

Miura and Itoh have also studied the selective deposition of tin on Pt/ZnAl₂O₄.³¹⁰ The Pt/ZnAl₂O₄ catalyst (0.6% w/w) has been prepared by liquid-phase impregnation from H₂PtCl₆ and tin introduced either by a CVD technique or by a liquid-phase impregnation. The two volatile precursors, [Sn(CH₃)₄] and [Sn(i-C₄H₉)₄], have been dissolved in cyclohexane and vaporized at temperature ranging between 423 and 523 K, to deposit selectively Sn on Pt in a flow of dihydrogen. The two nonvolatile precursors [SnCl(acac)₂] and [Sn(C₆H₅)₄] have been used to deposit tin nonselectively by acetone impregnation, followed by a reduction step under H₂ at 673 K. On the ZnAl₂O₄ support, the CVD process does not allow the deposition of tin, whatever the temperature. On Pt/ZnAl₂O₄, the amounts of deposited tin have been fixed between 0.5 and 0.6% w/w in the 423–473 K temperature range. At deposition temperature beyond the melting point of tin (523 K), the amount of deposited tin increases sharply, and it entirely covers the catalyst. The selective deposition of tin on platinum particles achieved by the CVD technique has been evidenced by CO chemisorption measurements, whereas liquid-phase impregnation leads to a distribution of tin both on the support and on the metal. The addition of tin to platinum improves the activity of the catalyst in the isobutane dehydrogenation reaction whatever the preparation method. However, higher amounts of tin are needed for the impregnated catalyst than for the CVD catalyst, e.g., 3–4% w/w instead of 0.1% w/w.

Rhodium–tin bimetallic particles entrapped in NaY zeolites have been obtained by Psaro et al. by GPI-D of SnR₄ (R = C₂H₅ or C₆H₅) onto Rh/NaY catalysts that have been prepared either by GPI-D from [Rh(CO)₂(acac)] or by ion-exchange from [RhCl-(NH₃)₅]²⁺.³¹¹ The main difference between the two Rh/NaY catalysts (1% w/w Rh) is the presence (ion-exchange preparation) or not (GPI-D preparation) of significant amounts of protons. The gas-phase impregnation of tin has been performed at 328 K for [Sn(C₂H₅)₄] or 508 K for [Sn(C₆H₅)₄], and the decomposition performed under H₂ at 773 K. The selective deposition of tin on the rhodium particles as shown by TPRD profiles occurs only if the monolayer capacity is not overcome. The mechanism of decomposition is influenced by the presence of protons and by the nature of the tin precursor. On GPI-D Rh/NaY catalysts, the reaction is as follows:



On impregnated catalysts, methane formation has also been demonstrated, and a relevant mechanism for its formation involving the presence of protons on the Rh/NaY support has been proposed. In the case of [Sn(C₆H₅)₄]/RhNaY, whatever the Rh/NaY catalyst used, the only product of decomposition is methane (573–673 K). In the case of the GPI-D

catalyst, DRIFT spectra of adsorbed CO clearly evidence a bimetallic Rh–Sn interaction. The selective hydrogenation of citral (3,7-dimethyl-2,6-octadienal) to the corresponding unsaturated alcohol has been observed only for RhSn/NaY catalysts entirely prepared by GPI-D.

Finally, the selective deposition of tin by GPI-D on Ni/SiO₂ has been reported by Komatsu et al.³¹² Ni₃Sn particles have been obtained by GPI of [Sn(CH₃)₄] on Ni/SiO₂ (5% w/w, prepared by impregnation of a Ni(NO₃)₂ solution) at temperatures ranging from 373 to 523 K, followed by a decomposition in hydrogen at 873–1173 K. The amounts of deposited tin on Ni/SiO₂ are much more important than on SiO₂. In particular, no appreciable deposition of tin is observed on SiO₂ below 423 K. The mean particle size of Ni₃Sn/SiO₂ is about 18 nm as shown by TEM and XRD. These GPI-D Ni₃Sn/SiO₂ catalysts are 500 times more active than nonsupported ones.

Besides these bimetallic catalysts, SnO₂ nanoparticles encapsulated in zeolites have also been prepared by GPI-D to study their properties as sensors of reducible gases.³¹³ The SnO₂/NaY material has been prepared from SnCl₄ previously adsorbed on NaY that has been hydrolyzed and then oxidized. The loading of the support leads to very small SnO₂ particles, not detectable by TEM (<1.5 nm) that are too small for applications as sensor materials. Attempts to increase the Sn loading up to 3% w/w induces the zeolite framework to be destroyed due to the formation of HCl that reacts with aluminum atoms.

D. Miscellaneous

A dry-mix method has been used by Kwak and Sachtler^{314,315} to produce Ga/HZSM-5 catalysts. The preparation method includes the dry mixing of GaCl₃ with the zeolite and further heating in a quartz tube up to 773 K. The Brönsted acidity of the HZSM-5 support is markedly lowered after this treatment and HCl is released without destruction of the zeolite framework. At high Ga loading (3–4% w/w), the formation of GaO⁺ cations that replace zeolitic protons prevails, whereas at low loading (\approx 1% w/w) significant amounts of highly dispersed Ga₂O₃ (mean particle size < 0.5 nm by high-resolution analytical electron microscopy) are also formed. As protons are replaced by gallium cationic species, this Ga/HZSM-5 material acts as a bifunctional catalyst for C₃ conversion to aromatics. A similar preparation method has been used to produce Zn/ZSM-5,²²³ where isolated Zn²⁺ cations are present. The Zn ions are stabilized in this state and cannot be reduced below 1073 K.

Deposition of B₂O₃ on alumina or silica by CVD produces highly active catalysts for the Beckmann rearrangement of cyclohexanone oxime into ϵ -caprolactam.^{316–318} Vapors of [B(OC₂H₅)₃] are contacted in air between 523 and 673 K with SiO₂ or γ -Al₂O₃, and directly deposited as B₂O₃ (2–34% w/w). The higher catalytic activity and selectivity of these catalysts, when compared to impregnated ones obtained from aqueous solutions of H₃BO₃ and calcination at 623 K, should be attributed to a larger amount of effective acid sites in addition to more uniform acid strength.

Such characteristics should result from a more uniform deposition of B₂O₃ by CVD; in particular, large crystals of B₂O₃ (50 μ m) have been observed by SEM on impregnated catalysts.³¹⁸ An amorphous, highly dispersed silica-supported boron phosphate catalyst has been prepared by CVD using mixtures of boron triethoxide and phosphoryl trimethoxide.³¹⁹ The choice of convenient CVD conditions taking into account the temperature and the P/B molar ratio allows the production of more active catalysts for the isomerization of 1-butene and simultaneous oligomerization of 1-butane than conventional ones.

Niobia (6–8% w/w) has been deposited on γ -Al₂O₃ powders by GPI-D from niobium pentachloride at 423 K under vacuum in a closed vessel followed by hydrolysis at 423 K and a 723 K thermal treatment with steam.³²⁰ To remove chlorine contamination, further hydrothermal treatments are required. Specific surface area of the material decreases slightly depending on the treatments (from 246 to 170 m² g⁻¹), but no details are given concerning the morphology of the deposits (particles or film). Deposition of niobia on alumina up to a level of 6.5% w/w results in a slight increase both in the ammonium adsorption capacity and in the catalytic activity for cumene dealkylation.

Chemical vapor deposition has been employed to prepare films of tungsten or niobium nitride on γ -Al₂O₃ pellets that have been used as catalysts for thiophene hydrodesulfurization.^{321,322} Metal chlorides (WCl₆ or NbCl₅) vapors are carried in an argon flow together with NH₃ and H₂ at reduced pressure and decomposes on γ -Al₂O₃ at temperatures ranging between 773 and 973 K. Nitride films of several micrometers characterized by high surface area (150–180 m² g⁻¹) are obtained. These metal nitride films deposited on γ -Al₂O₃ are active catalysts in the thiophene HDS reaction at 673 K at atmospheric pressure. However, for NbN/Al₂O₃ a deactivation of the catalyst occurs due to replacement of N by S atoms.

Copper(II) acetylacetone has been employed to deposit, under oxygen, copper oxides onto fiber glass in a classical horizontal hot-wall CVD reactor; producing a novel catalyst for oxidation reactions.³²³ The decomposition temperature 588–613 K has a strong effect on both the crystallinity and the composition of the film. The authors have shown that the films deposited between 593 and 613 K consist in a mixture of Cu₂O and CuO, and present remarkable properties for the oxidation of ethanol at temperatures below 473 K.

Mn/MCM-41 catalysts have been prepared by a dry-mix method and compared to impregnated catalysts.³²⁴ Four different volatile manganese precursors have been used: [Mn₂(CO)₁₀], [MnBr(CO)₅], [Mn(CO)₃(η ⁵-C₅H₅)], and [Mn(η ⁵-C₅H₅)₂]. Each precursor is dry-mixed in a Schlenk tube with the support, and then the tube is evacuated, sealed, and heated between 393 and 423 K for 2 days. After removal of the excess of precursor, no more than one monolayer remains attached to the support, and surface species have been analyzed by FTIR and EXAFS.³²⁵ After calcination in flowing air at 573 K,

Table 6. Selected Catalytic Studies Using GPI-D and CVD Catalysts

catalytic system	metal loading (%)	particle size (nm) ^a	reaction	catalytic activity	ref
Fe/Al ₂ O ₃ (KOH doped) GPI-D ([Fe(CO) ₅])	7		ethylene hydroformylation	GPI-D > commercial	20
commercial catalyst	10	(iron oxide)			58
Fe/ZSM5					
GPI-D (FeCl ₃)	1.1	(Fe ³⁺ nanoclusters)	NO _x reduction	GPI-D > ion ex.	
ion exchange (Fe ³⁺ aqueous sol.)	2.5 and 5	(Fe ³⁺ highly clustered + Fe ₂ O ₃)			
FeMo/DBH					48
GPI-D (FeCl ₃ + MoO ₂ Cl ₂) impregnation (Fe(NO ₃) ₃ ·xH ₂ O + (NH ₄) ₂ (MoO ₄))	Fe 1.4 – Mo 4.6 Fe 1.5 – Mo 4.5	(well dispersed) (large aggregates)	benzene oxidation	GPI-D > imp. (x2)	
Co/Al ₂ O ₃					
GPI-D ([Co ₂ (CO) ₈])	2.2	-	NO–CO reaction	GPI-D > imp. (x23)	27
impregnation (-)	3				
Co/SiO ₂					70
GPI-D ([Co(acac) ₃])	5	4.3 (23%)	ethylene	GPI-D > imp. (x2)	
impregnation (Co(NO ₃) ₂ ·6H ₂ O)	4	11.3 (8.5%)	hydroformylation		
Ni/C*					1
GPI-D ([Ni(CO) ₄])	7	(GPI-D > imp.)	methanol carbonylation	GPI-D = imp.	
impregnation ([Ni(OAc) ₂])	10				
Mo/Al ₂ O ₃					36
GPI-D ([Mo(CO) ₆])	2.7		hydrodesulfurization	GPI-D > imp.	
impregnation ([Mo(CO) ₆])	0.9				
Mo/SiO ₂					75
GPI-D (MoCl ₅)	0.01–0.37	(isolated Td Mo species)	propene metathesis		
impregnation ((NH ₄) ₆ (Mo ₇ O ₂₄))	0.01–0.1	(idem + aggregates of Mo and polymolybdate)		GPI-D > imp.	
MoO ₃ /Al ₂ O ₃					71
CVD (MoO ₂ (OH) ₂)	15	-			
impregnation ((NH ₄) ₂ (MoO ₄))	22	-	cyclohexane dehydrogenation	CVD = imp.	
Mocarbide/Al ₂ O ₃					79
CVD (MoCl ₅ + C ₆ H ₆)	1–6	1.4 (Mo ^{II})	CO ₂ reduction	CVD > imp. (x 20)	
impregnation ((NH ₄) ₂ (MoO ₄) + CH ₄)		Mo ^{IV}			
Ru/NaY					33
dry mix ([Ru ₃ (CO) ₁₂])	2	2.2–2.4	CO ₂ hydrogenation	dry mix = imp. = i.e.	
impregnation ([Ru(NH ₃) ₆]Cl ₃)	3	4.7–13			
ion exchange (Ru/Y)	3	2.6			
Ru/FSM16					33
dry mix ([Ru ₃ (CO) ₁₂])	2	3.3	CO ₂ hydrogenation	dry mix > imp. (x2)	
impregnation ([Ru(NH ₃) ₆]Cl ₃)	3	8			
Ru/Al ₂ O ₃					36
GPI-D ([Ru ₃ (CO) ₁₂])	1.1	-	hydrodesulfurization	GPI-D > imp.	
impregnation ([Ru ₃ (CO) ₁₂])	1.6	-			
RuMo/Al ₂ O ₃					36
GPI-D ([Ru ₃ (CO) ₁₂] + [Mo(CO) ₆])	Ru 2 Mo 2.7	-	hydrodesulfurization	GPI-D > imp.	
impregnation ([Ru ₃ (CO) ₁₂] + [Mo(CO) ₆])	Ru 1.8 Mo 0.7	-			
Mn/MCM41					157
dry mix ([Mn ₂ (CO) ₁₀])	8.2	(lower particle size)	trans-stilbene oxidation	dry mix > imp.	
impregnation ([Mn(acac) ₃])	8.6				
B ₂ O ₃ /SiO ₂					151
CVD (B(OEt) ₃ + air)	25	(uniform deposition)	Beckmann rearrangement of cyclohexanone oxime	CVD > imp.	

Table 6 (Continued)

catalytic system	metal loading (%)	particle size (nm) ^a	reaction	catalytic activity	ref
impregnation (H ₃ BO ₃ + water)	19	(large B ₂ O ₃ crystallites)			
V ₂ O ₅ /SiO ₂					87
GPI-D cycles [(VO(OC ₂ H ₅) ₃)]	19.4	(overlayer or nanoparticles)	oxidative ethanol dehydration	GPI-D > imp. (x4)	
impregnation (-)	19.4				
Pd/MgO					107
GPI-D Pd(η^3 -C ₃ H ₅)(η^5 -C ₅ H ₅)	2	-	methylcyclopentene aromatization	GPI-D > imp.	
impregnation (Pd(NO ₂) ₂ (NH ₃) ₂)	2	-			
Pd/MCM41					108, 109
GPI-D Pd(η^3 -C ₃ H ₅)(η^5 -C ₅ H ₅)	22.3	(32%)	Heck reaction	GPI-D > imp.	
impregnation Pd(η^3 -C ₃ H ₅)(η^5 -C ₅ H ₅)	4.4	(17%)			
Pt/KL					119
dry mix ([Pt(acac) ₂])	0.5–2.5	(better dispersion)	hexane aromatization	dry mix > imp.	
impregnation (NH ₃) ₄ Pt(NO ₃) ₂)	0.5–2.5				
Rh/C*					128
CVD ([RhCl(CO) ₂] ₂)	2	4–5 (chlorine free)	acetic acid hydrocarbonylation	CVD > imp.	
impregnation (RhCl ₃ ·3H ₂ O)	2	4–5 (remaining chlorine)			
Rh–Sn/SiO ₂					134–138
GPI-D ([Sn(CH ₃) ₄])	Rh 1 – Sn/Rh 0.45	2.5	NO/H ₂	GPI-D > coimp. (x6)	
coimpregnation (RhCl ₃ ·3H ₂ O–SnCl ₂)	Rh 1 – Sn/Rh 0.45	-			

^a Between parentheses are given either the dispersion (%) either available information concerning the catalytic material.

the surface area of the calcinated samples does not significantly decrease contrary to the case of calcinated wet impregnated samples: MCM41, 1236 m² g⁻¹; dry-mix samples, 1050–1200 m² g⁻¹; impregnated samples, 550–950 m² g⁻¹. These results show that the gas-phase method generates small particles that anchor onto the channel walls without blocking the pores. TPR experiments performed on all the calcinated samples suggest that dry-mix samples contain more reactive Mn-oxygen species than the impregnated catalysts. Moreover, some differences in the TPR profiles of the dry-mix samples have been noted according to the nature of the volatile precursor. Finally, the dry-mix catalysts show different, but in any case higher, activity than the impregnated samples in the oxidation of trans-stilbene to trans-stilbene oxide reaction.

Manganese-promoted rhodium/NaY catalysts³²⁶ have been prepared by successive GPI-D from [Rh(CO)₂(acac)] (sublimation at 353 K – decomposition at 673 K under H₂) and [Mn₂(CO)₁₀] (sublimation at 378 K – decomposition at 673 K under H₂). A detailed FTIR study indicates that no discrete monometallic Mn aggregates are present upon decomposition of [Mn₂(CO)₁₀] on the prereduced rhodium particles, consistent with the formation of bimetallic particles.

Surface reactions between vapors of [ZrCl₂(η^5 -C₅H₅)₂] (temperature of sublimation = 503 K) and SiO₂ (300–340 m² g⁻¹) have been studied by preparing different samples by GPI (ALE method) at 573 K, to synthesize heterogeneous metallocene catalysts.³²⁷ The [ZrCl₂(η^5 -C₅H₅)₂] complex reacts mainly with the isolated silanol groups. The effect of dehydroxylation of silica on [ZrCl₂(η^5 -C₅H₅)₂] reactivity has been followed by NMR and FTIR analyses. On partially dehydroxylated SiO₂ (573 K – 2.6 isolated

OH nm⁻²), ¹³C NMR spectra reveal the presence of triply, doubly, and singly bonded Zr species on the silica, while on highly dehydroxylated SiO₂ (873 K – 0.2 isolated OH nm⁻²), Zr is mainly monofunctionally bonded to the surface. Due to the surface saturation through chemisorption, the controlled deposition is an attractive method for fabrication of metallocene catalysts.

The Se(CH₃)₂ precursor has been used to dope impregnated Rh-supported catalysts for ethene hydroformylation reaction.^{328–330} On zirconia support,³²⁸ adsorption of vapors of Se(CH₃)₂ has been performed at 373 K. The reactivity of Se(CH₃)₂ with ZrO₂ or Rh/ZrO₂ has been studied by TPD, and the results show that Se(CH₃)₂ preferentially reacts with the hydrogen atoms adsorbed on the Rh metal surface to form CH₄ rather than with the surface OH groups of ZrO₂. From TEM observations, the mean particle size is not altered after Se deposition (around 4 nm), and similar observations have been made for silica-supported catalysts.³²⁹ Whatever the support used, ZrO₂,³²⁸ SiO₂,³²⁹ or MgO,³³⁰ the addition of Se promotes the hydroformylation of ethene. On zirconia, the activity enhancement is more pronounced for the GPI-D catalyst than for a coimpregnated one. EXAFS experiments performed for all the GPI-D-supported catalysts show that Se is selectively bound to Rh with bond distances of 2.41 Å on SiO₂ or ZrO₂ and 2.43 Å on MgO.

Pt–Ge intermetallic compounds supported on HZSM-5 have been prepared by CVD of [Ge(acac)₂Cl₂] at 493 K on impregnated Pt/HZSM-5 and subsequent hydrogen reduction at 823 K.³³¹ XRD measurements have shown that, according to the Pt/Ge molar ratio, Ge reacts with Pt particles (34 nm) to form different Pt–Ge intermetallic phases. The particles are located

on the external surface of the zeolite whose structure, and specific surface areas are not affected by the deposit. These intermetallic compounds show higher selectivity toward aromatic hydrocarbons than HZSM-5 or Pt/HZSM-5 in the aromatization reaction of butane.

E. Conclusion

As shown in Table 6 the results reported in the literature are rather spread out. However, from the great variety of metal or metal oxides deposits that have been described, it is possible to draw general trends about the potentialities of such methods.

Generally speaking, two main gas-phase methods for the preparation of supported catalysts have to be distinguished.

Most of the studies concern the GPI-D two-step process, and very often the authors carry out several cycles to increase the loading of the deposited metal. The growth of the aggregates becomes the dominant phenomenon after the first GPI-D cycle is completed. Preferential deposition on the metallic phase rather than on the support has been systematically observed during the preparation of heterobimetallic catalysts. Such a method allows control of the metal loading, and produces well-dispersed catalysts.

The one-step process has been less widely used, maybe because it is necessary to fine-tune the operating conditions, especially the vapor pressure of the precursor, the reactor temperature, and the presence of an additional reactive gas to the carrier gas. The main advantage of this method lies in the possibility to control the particle size for a given metal loading by adjusting the precursor supersaturation, which governs the nucleation rate.

In both cases, the fluidized bed technology allows the easy preparation of homogeneous deposits.

Compared to the conventional wet impregnation methods, the absence of any solvent favors the diffusion of the precursor inside the pores and precludes the drying step during which redistribution of the active phase can occur. In addition, for the impregnation methods, when water is used as solvent, the possibility to adjust the concentration of the OH surface groups no longer exists. Compared to the coprecipitation method, the partial embedding of nanoparticles in the bulk of the support does not occur.

It should be underlined that the use of organometallics complexes as metal precursors provides an efficient way to produce deposits at relatively low temperatures. However, in many papers that have been examined in this review, analyses to determine the chemical purity of the deposits are lacking. Additionally, the problems of weak interactions between an acidic precursor and an acidic surface (or basic precursor/basic surface), which often give rise to large particles in the wet impregnation technique, do not occur.

Most of the time, catalytic materials resulting from gas-phase methods preparation show good dispersion and high catalytic activities.

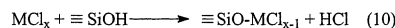
IV. Overlays, Thin Films, and Surface Modifications

A. Introduction

In heterogeneous catalysis, the nature and the morphology of the support contribute greatly to the performances of the catalyst. Modifications of the surface of the support can be carried out to adjust the acid-base characteristics and/or the pore opening size. For such a purpose, the gas-phase methods proved to be efficient. Therefore, the resulting material can either be used directly as a catalyst—this is, for instance, the case of zeolites—or as a support that will require further treatments to deposit the catalytic phase. We have to point out that the deposits reported in this part do not present the same morphology than the supported catalysts described in the previous parts of this review. Thus, layered deposits as well as thin films are frequently described. Moreover, we will include in this part the incorporation of noble metals on membranes to design catalytic membrane reactors.

B. Gas-Phase Deposition of SiO₂, GeO₂, Carbon, ZrO₂, and TiO₂

First, we will mention that gaseous-phase interactions between different molecules and a silica surface have been widely investigated by infrared and Raman spectroscopy in attempts to elucidate the molecular nature of the silica surface.^{332–338} Thus, silanes, diboranes, or boron, titanium, and germanium halides have been frequently used as probes to study the number and the nature of the surface hydroxyl groups. Some of these molecules seem to be hydroxyl specific, and a distinction between free and bridged hydroxyl groups is achievable. For example, Vansant et al.^{337,338} have shown that trichlorosilane reacts differently with bridged and free (or terminal) hydroxyl groups, whereas diborane does not allow one to distinguish between these two kinds of groups because it reacts easily with siloxane bridges. When metal chlorides are used as probe molecules, the main reaction is



that is, in some cases, accompanied by a direct concurrent chlorination of the surface³³⁴ by formation of $\equiv \text{Si}-\text{Cl}$ bonds.

1. Gas-Phase Deposition of SiO₂ on Al₂O₃

To obtain a novel and alternative catalyst and to compare it to the usual silica–alumina oxides, chemical vapor deposition of tetraalkoxysilane has been applied to prepare thin layers of silica on alumina.

Starting from Si(OMe)₄ (~2 Torr at 273 K), Niwa and co-workers have prepared a silica monolayer by repeated CVD cycles at 593 K followed by hydrolysis with water vapor^{339,340} or oxygen calcination.^{341–343} A monolayer of silica that fully covers the alumina support (~165 m² g⁻¹) is obtained with 20% w/w SiO₂/Al₂O₃. From chemical titration,³⁴⁴ it has been shown that this monolayer presents concentrations of 12 Si

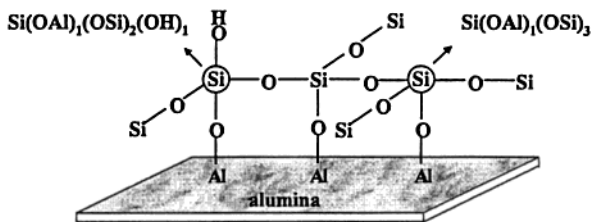


Figure 14. Monolayered structure of a Si–O–Si network covering the surface of alumina.

nm^{-2} and 1.5 OH nm^{-2} that remain quite stable upon heating to 1100 K. These observations as well as NMR studies are consistent with the predominance of $\text{Si(OAl)}_1(\text{OSi})_3$ species with regard to $\text{Si(OAl)}_1-(\text{OSi})_2(\text{OH})_1$ species.³⁴³ On the basis of IR, gravimetry, and products analyses, a mechanism of decomposition has been proposed:³⁴² Si(OMe)_4 is deposited quickly on alumina until the silicon alkoxide and a fraction of methanol would cover the surface; at high temperature, water contaminating the support hydrolyses the silicon alkoxide into silanol, which reacts with another Si(OMe)_4 . The successive deposition processes create a monolayer with a network of Si–O–Si covering the surface almost completely (Figure 14).

The silicon atoms bonded to alumina behave as weak Brønsted acid sites compared to silica–alumina commercial catalysts prepared by co-gelation or kneading method. The Lewis acidic sites of alumina are completely converted into strong Brønsted acid sites. The final material presents a sharp distribution of acidic sites with a homogeneous strength of the acidity.³⁴⁰ These SiO_2 monolayered CVD catalysts present a remarkable thermal stability and a high resistance to sintering compared to conventional mixed oxides catalysts.³⁴¹ They are active for cumene cracking, but-1-ene and cyclopropane isomerization and alcohol dehydration.^{340,341,345–347} The maximum conversion for these various reactions is attained at different SiO_2 loadings, corresponding to one or less than one monolayer. The catalytic activities are comparable to those of a commercial $\text{SiO}_2/\text{Al}_2\text{O}_3$ catalyst.

Deposition of silica from Si(OEt)_4 onto an amorphous silica alumina support has also been reported to give active cumene cracking catalyst.³⁴⁸ It has been demonstrated by TPD that, in this case also, the strong Lewis acid sites of the original support are converted into strong Brønsted acid sites.

$\text{SiO}_2/\text{Al}_2\text{O}_3$ materials³⁴⁰ have also been used as supports to prepare active palladium-based catalysts for complete oxidation of methane.^{349,350} The Al_2O_3 surface is not fully covered by silica, and the palladium is preferentially deposited (PdCl_2 , liquid impregnation) on the remaining part of the alumina. With 5% w/w SiO_2 on Al_2O_3 a strong influence on the sintering behavior is noted, the deposited SiO_2 preventing the palladium metal from sintering.

2. Gas-Phase Deposition of SiO_2 on Other Oxides

Similar deposition of silica from $\text{Si(OCH}_3)_4$ on TiO_2 and ZrO_2 have been reported by the same authors.³⁵¹ The highest loadings of silica on titania or on zirconia were 8.81% w/w (surface concentration 17.5 Si nm^{-2})

and 8.77% w/w (13.2 Si nm^{-2}), respectively, and correspond to a coverage of around 90%. The authors suggest that the silica overlayers present a structure similar to the support surface up to these concentrations, with however a little alteration in the case of titania. The formation of weak Brønsted acidic sites is evidenced by the IR spectra of adsorbed gases on this monolayers. The catalytic activity for the dehydration of ethanol into ethene decreases with the silicon content, while isomerization of but-1-ene and dehydration of *tert*-butyl alcohol are both enhanced, reaching a maximum rate for Si surface concentrations around 14% w/w on TiO_2 and 9% w/w on ZrO_2 , respectively.

The deposition under UHV conditions of SiO_2 by CVD from $\text{Si(OCH}_2\text{CH}_3)_4$ onto ZrO_2 , TiO_2 , MgO , SiO_2 , and Al_2O_3 has been studied by TPD and Auger electron spectroscopy.³⁵² The precursor adsorbs at 300 K and decomposes during TPD to give ethene and H_2O on every support except SiO_2 , where it adsorbs physically and then desorbs by evacuation at 300 K. On ZrO_2 , a uniform SiO_2 film free from carbon contamination is obtained, with a thickness of about 10 Å (four monolayers), while carbon contamination occurs on the other supports. On TiO_2 ,³⁵³ the formation of small clusters of SiO_2 and/or a mixed metal oxide layer has been proposed.

Yamaguchi and al.³⁵⁴ have tested several methods to prepare acid–base hybrid catalysts by the combination of typical solid-base and solid-acid materials or by deposition of SiO_2 overlayers on MgO from $\text{Si(OCH}_3)_4$. Gaseous $\text{Si(OCH}_3)_4$ is adsorbed on MgO (preheated at 773 K) at room temperature, and the adsorption is followed by oxidation and evacuation at 773 K, this cycle being repeated 4 or 8 times. This GPI-D method allows the preparation of a SiO_x/MgO catalyst that is twice more active for the decomposition reaction of $(\text{C}_2\text{H}_5)_3\text{N}$ to produce acetonitrile than a conventionally prepared $\text{SiO}_2-\text{Al}_2\text{O}_3/\text{MgO}$ catalyst. This result indicates clearly the generation of acidic sites on the MgO surface.

Si-modified Pd/ SiO_2 or Pd/ Al_2O_3 have been prepared by CVD of SiH_4/H_2 mixtures at 523 K followed by exposure to O_2 at room temperature.³⁵⁵ The Si/Pd atomic ratio is fixed between 0.1 and 0.2 and, due to Pd-catalyzed silane decomposition, the Si deposits selectively on Pd as Si or SiO_2 patches. The deposition does not affect the pore size distribution and XPS and CO chemisorption measurements have shown that it modifies the palladium surface geometrically but not electronically. The geometric modifications improve the performance of the catalyst that presents higher ethene selectivity and longer catalytic lifetimes in the selective hydrogenation of acetylene.

Iwasawa et al. have used a surface silica modification reaction to prepare a new supported iron carbonyl cluster $[\text{Fe}_3(\text{CO})_6]$.³⁵⁶ The surface modification has been carried out by GPI-D of SiCl_2R_2 ($\text{R} = \text{CH}_3$, C_6H_5) or SiCl_3R at 343 K followed by heating to 473 K in a vacuum, exposure to water at 273–373 K and evacuation at 473 K to convert the SiCl into SiOH groups. The gas-phase impregnation of $[\text{Fe}_3(\text{CO})_{12}]$ (room temperature, evacuation at 393 K) on this modified hydrophobic $\text{SiR}_x/\text{SiO}_2$ surface leads to the

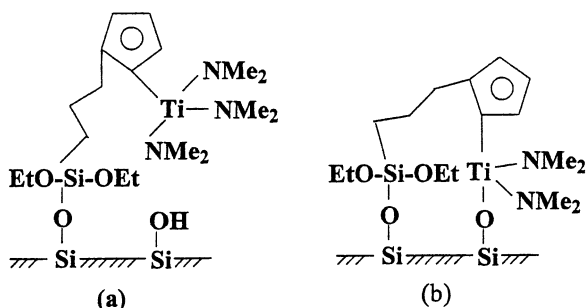
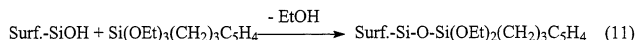


Figure 15. Surface reaction of $[\text{Ti}(\text{NMe}_2)_4]$ with a modified silica.

supported $[\text{Fe}_3(\text{CO})_6]$ cluster that presents an unusual Fe–Fe bond length as shown by EXAFS studies. The iron clusters on $\text{SiMe}_2/\text{SiO}_2$ showed a higher activity for propene hydrogenation (by a factor of 200) than $[\text{Fe}_3(\text{CO})_{12}]$.

Such a strategy to modify a silica surface has been extended by Pakkanen and co-workers³⁵⁷⁻³⁵⁹ to the grafting of a cyclopentadienyl ligand through a spacer bond to a siloxane surface group as shown in eq 11:



Surface Si—O—Si termini react similarly to provide the same functional group and a surface Si—O(C₂H₅) function. Further reaction in the liquid phase with butyllithium and then with [(η⁵-C₅H₅)ZrCl₃] allows the grafting of the zirconium complex onto the support through a surface Si—O—Si(OEt)₂CH₂CH₂—CH₂(η⁵-C₅H₄) bond.³⁵⁷ Such an anchored complex is an active precursor in the presence of the methylating methylaluminoxane agent for the polymerization of ethene. Its catalytic activity is twice that of [(η⁵-C₅H₅)ZrCl₃] in purely homogeneous conditions.

The same authors have grafted titanium by using $[\text{Ti}(\text{NMe}_2)_4]$ in hexane solutions onto a silica, chemically modified by $\text{C}_5\text{H}_4(\text{CH}_2)_3\text{Si}(\text{OEt})_3$.³⁵⁸ The metal center is either bonded to the surface through the spacer or attached directly onto the surface (Figure 15).

The surface can be methylated after functionalization of silica to reduce the Si—OH surface group concentrations. These catalysts present the same activity for the polymerization of ethene as the homogeneous counterpart [$(\eta^5\text{-C}_5\text{H}_4\text{SiMe}_3)\text{Ti}(\text{NMe}_2)_3$]. Analogous zirconium systems have been prepared and tested in ethene polymerization.³⁵⁹

3. Gas-Phase Deposition of GeO_2 and Carbon

GeO₂-modified silica prepared by GPI-D has been used to prepare new rhodium-supported catalysts.³⁶⁰⁻³⁶⁴ The reaction in a closed circulating system of gaseous Ge(OMe)₄ with isolated OH groups of SiO₂ at 393 K, followed by calcination at 693 K induces the deposition of monolayered GeO₂.³⁶⁰ The characterization of this material has been performed by FTIR, XRD, and EXAFS. After one cycle of impregnation, the coverage of GeO₂ at saturation, which corresponds to the disappearance of the Si-OH groups as monitored by FTIR, is estimated to be 1/5 monolayer (7.4% Ge w/w). After calcination, isolated GeO₂ and SiOH groups are formed, and those

permit further GeO_2 deposition. The local structure of germanium in $\text{GeO}_2/\text{SiO}_2$ has been characterized by EXAFS and is similar to that of hexagonal GeO_2 . Neither Brönsted nor Lewis acidic sites have been detected on $\text{GeO}_2/\text{SiO}_2$. A 2% w/w Rh/ $\text{GeO}_2-\text{SiO}_2$ catalyst has been prepared by impregnating at room temperature CHCl_3 solutions of $[\text{Rh}_6(\text{CO})_{16}]$ on 7.4% w/w $\text{GeO}_2/\text{SiO}_2$ followed by a reduction step.³⁶¹⁻³⁶⁴ Before reduction, EXAFS experiments have shown that the supported $[\text{Rh}_6(\text{CO})_{16}]$ cluster interacts preferentially with the Ge-OH groups and remains unchanged. Upon reduction at 423–523 K, the carbonyl ligands partially desorb and metallic rhodium particles (2.6 nm) are formed. RhGe alloys are also produced when starting from the rhodium complex $[\text{Rh}(\mu\text{-CH}_2)(\text{CH}_3)(\eta^5\text{-C}_5\text{Me}_5)]_2$ and by using a similar procedure.³⁶⁴ By further reduction at 623–723 K RhGe alloy particles (2.8 nm) are formed. The catalyst that has been reduced at 423–523 K shows high activity and selectivity for hydrogenation of ethyl acetate to ethanol, while Rh/ GeO_2 and Rh/ SiO_2 are inactive for this reaction. These studies demonstrate the significance of the use of support surface modifications on the metal activity for catalytic reactions.

Finally, thick (20–50 nm) porous diamond coatings have been deposited on silica–alumina pellets by using voltage-based, hot filament CVD from CH_4/H_2 mixtures.³⁶⁵ The resulting material presents the same BET surface, the same pore size distribution and the same catalytic activity for methanol dehydration reaction than uncoated pellets. However, the diamond coating measurably enhanced the thermal conductivity, and the temperature gradient for a fixed bed reactor could be reduced.

4. Gas-Phase Deposition of SiO_2 on Zeolites

Acidity and pore size are the main characteristics of zeolites as catalysts. Generally speaking, the acidity is dependent on the components or impurities that they contain; on the other hand, the size of the channels is determined by the zeolite structure. Chemical vapor deposition of SiO_2 from different precursors as silicon alkoxydes, silanes, or disilanes has been used to control the pore-opening size or/and the physicochemical properties of zeolites.

a. Gas-Phase Deposition of SiO₂ on Mordenite.

at Gas Phase Deposition of SiO_2 on Mordenite. Niwa and his group have used $\text{Si}(\text{OMe})_4$ as a precursor to deposit SiO_2 to control the pore-opening size of mordenite (H form) without affecting the acid sites. Indeed, the molecular size of this silicon alkoxide is too large to enter the pores of the mordenite; thus, it interacts only with the external surface.³⁶⁶⁻³⁶⁸ $\text{Si}(\text{OMe})_4$ has been deposited at 598 K on dehydrated HM zeolite followed by calcination at 673 K in flowing oxygen to remove carbon contamination.³⁶⁷ TPD experiments with ammonia show no change in the acidity whatever the temperature and the amount of deposition, and adsorption of water indicates the conservation of the internal surface. Thus, it is proposed that $\text{Si}(\text{OMe})_4$ does not interact with the inside surface of the pores but is deposited only on the external surface of the zeolite. The pore-opening size of the zeolite is effectively reduced by 0.1 and 0.2 nm upon formation of 1-2 and 3 molecular layers

of SiO_2 respectively. The mechanisms of CVD from $\text{Si}(\text{OMe})_4$ on HM has also been investigated;³⁶⁸ it involves first the reaction of $\text{Si}(\text{OMe})_4$ with the hydroxyl groups of the external surface to yield an anchored trimethoxide and methanol. Second, the trimethoxide is hydrolyzed by remaining water to form hydroxide groups, which further react with the gaseous alkoxide or with vicinal trimethoxide. The products of the reaction are methanol and dimethyl ether produced by methanol dehydration. Si–HM yields better results than HM for the selective disproportionation of toluene to *p*-xylene.³⁶⁶

On NaM, that does not present strong acid sites that could catalyze the dehydration of methanol, deposition of SiO_2 from $\text{Si}(\text{OMe})_4$ is possible by performing repeated cycles of deposition and hydrolysis;³⁶⁹ indeed, deposition at 593 K was possible, but readily saturated at low surface concentration. Therefore, water vapor has been admitted at 593 K into the zeolite that is saturated with methoxide deposit residue. The deposit is converted into hydroxide, and thus, further deposition can occur. On the basis of the competitive cracking of octane isomers as test reaction, it has been found that adjusting the extent of the deposition controlled the pore-opening size of the zeolite.

On Ba-dealuminated mordenite Ba(DM), a low coverage of SiO_2 has also been obtained from $\text{Si}(\text{OMe})_4$ at 593 K.³⁷⁰ In the conversion of methanol to gasoline reaction, differences in selectivity toward heavy aromatics have been noticed between Si–Ba(DM) and Ba(DM) catalysts. The deposition of SiO_2 results in a decrease of the yield of heavy aromatics and a complementary increase of the yield of small molecules ($\text{C}_1\text{--C}_4$), indicating a decrease of the pore opening size.

Silane, disilane, and diborane have been used with success to modified H-mordenite zeolites.^{371,372} In the case of Si_2H_6 , the disilane reacts with OH groups, either at high temperature (373–473 K) on the zeolite external surface or at low temperature (253–303 K) throughout the zeolite (both internal and external surface). The authors have developed a method for fine-tuning of the pore size without affecting the internal acid sites and volume. Introduction of small amounts of Si_2H_6 at around 423 K followed by hydrolysis at 473 K and dehydration at 733 K results in a narrowing of the pore diameter as evidenced by a study of sorption rate of different gas mixtures and their separation. The cracking reaction of hexanes has also been investigated to confirm the fine control of the pore-opening size without affecting the catalytic active sites. The remarkable increase in propane productivity compared to isobutane indicates the shape selectivity of the catalyst.⁴¹

b. Gas-Phase Deposition of SiO_2 on ZSM-5 and other Zeolites. On ZSM-5 support, Niwa and his group have used different precursors^{373–375} to modify both the external pore opening and the acidity. By deposition of $\text{Si}(\text{OMe})_4$ ^{373,374} at 593 K followed by calcination in flowing oxygen at 673 K, SiO_2 is formed on the external surface. Repeated cycles allow depositing between 4.5 and 12% w/w of SiO_2 . As $\text{Si}(\text{OMe})_4$ is too large (0.89 nm) to enter the pore of

the zeolite (0.54–0.56 nm), SiO_2 is depleted as about six monolayers (12% w/w SiHZSM-5) on the external surface, reducing significantly the pore-opening size. TPD of ammonia has shown no significant modifications of the strength and amount of acidity of the SiO_2 modified zeolite.³⁷³ However, it gives information on the acidity of the whole material, and further catalytic reaction studies³⁷⁴ have shown that the number of active sites on the external surface can be reduced. The authors have also shown that the nature of the silicon compound precursor $\text{Si}(\text{OCH}_3)_2(\text{CH}_3)_3$, $\text{Si}(\text{OCH}_3)_2(\text{CH}_3)_2$, $\text{Si}(\text{OCH}_3)_3\text{CH}_3$, or $\text{Si}(\text{OCH}_3)_-(\text{C}_3\text{H}_7)_3$ affects the extent of inactivation of the external acid sites of HZSM-5.³⁷⁵ Among the various silicon compounds used, the $\text{Si}(\text{OCH}_3)_-(\text{C}_3\text{H}_7)_3$ is particularly effective for the selective inactivation of acid sites on the external surface of HZSM-5, without affecting its void space. In the case of the reaction of methylation of toluene with methanol, the enhancement of para-selectivity is connected to the control of the pore-opening size rather than to acid site modification. By using $\text{Si}(\text{OCH}_3)_4$ or $\text{Si}(\text{OCH}_3)_2(\text{CH}_3)_2$ to deposit SiO_2 or HY zeolite,³⁷⁶ Niwa et al. have indicated that the pore-opening size, which is controlled by the deposition, is affected by the aluminum concentration of the zeolite. Pore-openings in HY are completely closed at high aluminum concentration, while pore-opening size could be controlled with low aluminum concentration.

The $\text{Si}(\text{OC}_2\text{H}_5)_4$ precursor has been used by different groups to modify HZSM-5 zeolites.^{377–381} The modified zeolites have been used for different catalytic reactions and compared to zeolites modified by liquid-phase impregnation.^{377–379} The influence of preparation parameters importance on the external acidity of the modified zeolites is noticeable.³⁷⁷ The deposition of $\text{Si}(\text{OC}_2\text{H}_5)_4$ has been performed either by static vapor phase or flow systems followed by calcination, or by liquid phase mixing of the zeolite with solutions containing ethanol or hexane, water, and $\text{Si}(\text{OC}_2\text{H}_5)_4$. In the case of the static vapor-phase system, it has been shown that physisorbed species must be removed by evacuation or calcination to reexpose active sites to obtain an almost complete (97%) passivation of the external surface activity. In the vapor flow system, continuous $\text{Si}(\text{OC}_2\text{H}_5)_4$ deposition is observed if water is added at relatively high temperature. For liquid impregnation, the presence of a diluent is necessarily to obtain 86% passivation. In any case, a more uniform coverage is obtained by gradual deposition process. Si/HZSM5 modified catalysts have been prepared from $\text{Si}(\text{OC}_2\text{H}_5)_4$ by the vapor phase flow method (373 K deposition temperature – calcination in air at 773 K), and the Si loading has been controlled by adjusting the number of deposition cycles.³⁷⁸ The isomerization, disproportionation, and cracking of various molecules have been used to probe the effects of SiO_2 deposition on the external surface acidity and the pore-opening size.

A reactive CVD method has been used to deposit SiO_2 on H-ZSM5 from 50% toluene–45% MeOH–5% $\text{Si}(\text{OC}_2\text{H}_5)_4$ ^{379,380} mixture vapors at 473–483 K. During the reaction, methanol converts to dimethyl ether

and water on acidic sites of the support, leading to hydrolysis of the $\text{Si}(\text{OC}_2\text{H}_5)_4$ precursor. FT-IR, MAS NMR, and catalytic test reactions have shown that this treatment passivates the external surface of the zeolite and that the concentration of Brønsted acid sites increases at the cost of Lewis sites.³⁷⁹ By using the same preparation procedure, Wang et al.³⁸⁰ have prepared a Si-modified ZSM-5 catalyst that shows better activity and better durability in various reactions of preparation of para-alkylbenzenes than a catalyst modified by the conventional impregnation method. It has also been shown that an additional coking of the modified catalyst is a good technique for achieving para-selectivity for extended time on stream.³⁸¹

Si-modified zeolites have also been used as support for metal-supported catalyst preparation.^{382,383} The synthesis of pyridine-bases on Pb, Tl, or Ca/Si-ZSM5 catalysts has been investigated by Abe et al.,³⁸² and it has been shown that repeated CVD cycles induce a decrease in activity because the entrance pore size becomes smaller. SiO_2 has been deposited on a nonacidic KL zeolite by GPI from $\text{Si}(\text{OC}_2\text{H}_5)_4$ or $(\text{Me})_3\text{Si}-\text{O}-\text{Si}(\text{Me})_3$ vapors at room temperature followed by a calcination step under O_2 at 673 K.³⁸³ Contrary to H-type zeolites, the framework oxygen ion is the deposition site. Due to the appearance of new basic sites, the interaction between platinum and the Si-modified zeolite is strengthened, and electron-rich platinum particles are obtained after dry impregnation with *cis*-[Pt(NH₃)₂Cl₂].

Finally, some authors have also deposited SiO_2 on zeolite-supported metal catalysts to modify their properties.^{384–390} Chemical vapor depositon of $\text{Si}(\text{OC}_2\text{H}_5)_4$ on Cu/HZSM-5 catalyst has been used to modify its pore-opening size to allow a selective combustion of hydrogen in a gas mixture containing isobutene.³⁸⁴ Silicon tetraethoxide is deposited on Mg/ZSM-22 at 423 K and then calcined at 723 K.³⁸⁵ The deposition of SiO_2 leads to a decrease in the amount of external acid sites (TPD of NH₃ and trimethyl pyridine) and also reduces the pore-opening size (*n*-hexane chemisorption). The increase of selectivity in the isomerization of 1-butene to iso-butene appears to be the result of passivation of strong acidic sites and narrowing of the pore-opening.

Silica modified Pt-supported zeolites have been prepared from $\text{Si}(\text{OC}_2\text{H}_5)_4$ ³⁸⁶ or $\text{Si}(\text{C}_6\text{H}_5)_2(\text{OC}_2\text{H}_5)_2$.³⁸⁷ It has been demonstrated that a high regioselective hydrogenation of unsaturated hydrocarbons can be achieved with this catalytic system. Similarly, treatment of a Ga-MFI zeolite with $\text{Si}(\text{OC}_2\text{H}_5)_4$ enhances the para-selectivity during toluene alkylation.³⁸⁸

On Pt-loaded mordenite catalysts,³⁸⁹ silica has been selectively deposited on the external surface of the zeolite without affecting the internal acidic sites. This narrowing of the zeolite pores can be tuned by controlling the extent of surface modification; it induces a shape selectivity for the hydrocracking of paraffins.

An interesting effect of deposited silica on Pd/HZSM-5 is the recovery of the activity for the reaction of NO-methane-oxygen that is suppressed by water vapor.³⁹⁰ Indeed, without SiO_2 deposition, palladium

migrates from the inside pores to the surface and sinters into large particles. This phenomenon, accelerated by the presence of water vapor, may be suppressed by SiO_2 deposition from $\text{Si}(\text{OCH}_3)_4$ and heating at 773 K under He. Water adsorption experiments have shown that the equilibrium amount of adsorbed water is reduced by SiO_2 deposition on the external surface.

5. Gas-Phase Deposition of GeO_2 or ZrO_2 on Zeolites

The deposition of germanium dioxide on different zeolites (H-mordenite, Z-HM10 or ZSM-5) from $\text{Ge}(\text{OCH}_3)_4$ or $\text{Ge}(\text{OC}_2\text{H}_5)_4$ affords similar results than for SiO_2 deposition.^{391,392} The GeO_2 thin film is located mainly on the external surface of the support; it is unstable to moisture and reconstructs by heating at 773 K to give GeO_2 particles with size above 5 nm, leading to heterogeneous narrowing of the pore-opening size.³⁹¹ On ZSM-5 zeolite,³⁹³ the reduction of pore-opening and the passivation of the outer surface acidity is less drastic with GeO_2 than with SiO_2 .

An one-atomic layer $\text{ZrO}_2/\text{ZSM-5}$ catalyst has been prepared by reaction of $[\text{Zr}(\text{OC}_2\text{H}_5)_4]$ vapors at 473 K with surface OH groups of the zeolite, followed by heating at 503 K to complete the reaction, exposure to H_2O vapor at room temperature, and calcination at 773 K in air.³⁹⁴ This GPI-D cycle allows the preparation of 1.7% w/w Zr/ZSM-5 that corresponds to 1/3 atomic layer and can be repeated to obtain a full monolayer coverage. The reduction of the pore size and volume of the ZSM-5 is not observed, indicating that $[\text{Zr}(\text{OC}_2\text{H}_5)_4]$ reacts only with the external OH groups of the support. EXAFS measurements show that this one-atomic layer of ZrO_2 grows epitaxially in a [111] direction of tetragonal ZrO_2 . This particular structure could explain the unique behavior of this catalyst for methanol conversion reactions during which isopentane is obtained selectively, and CO hydrogenation where C_4H_8 hydrocarbons are obtained selectively (mainly isobutene).

6. TiO_2 Deposition from the Gas Phase

The gas-phase reactions between TiCl_4 or $[\text{Ti}(\text{OR})_4]$ precursors and high surface area oxides supports have been studied extensively over the last two decades.^{395,396} First, TiCl_4 , like SiCl_4 , has been used as a probe molecule to study the surface chemistry (OH groups) of silica. Then, catalytic applications have merged: TiO_2 -supported overlayers have been shown to exhibit special surfaces properties as metal catalyst support; titania-silica materials have been used as acidic catalysts and supported TiO_2 is known to be an effective photocatalyst.

The gas-phase reaction of TiCl_4 with the surface of silica has been studied by several groups^{332–334,397–401} by infrared, NMR, and chemical analysis. The possible reactions of TiCl_4 with the surface of the silica surface are presented in Figure 16. The results of these different studies show that monofunctional, bifunctional, or siloxane-based reaction become more or less important according to the pretreatment temperature of the silica, or to the reaction temperature.

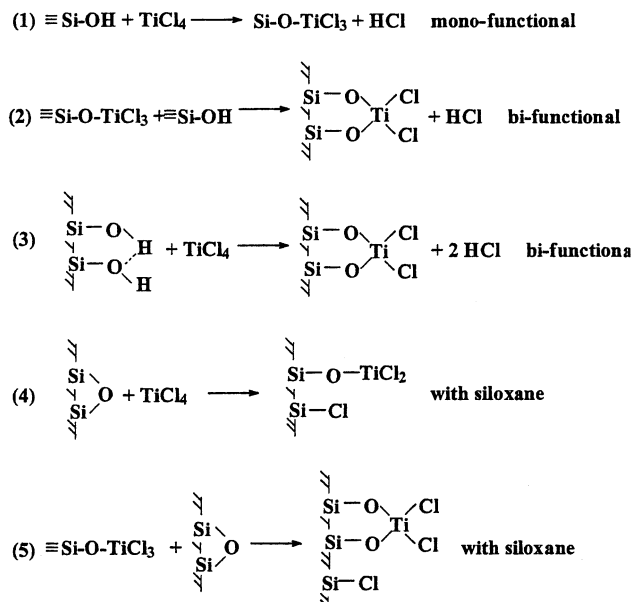


Figure 16. Possible surface reaction between TiCl_4 and a silica surface.

a. Preparation of Supported TiO_2 Photocatalysts. Kinney and Staley have shown by using Fourier transform infrared photoacoustic spectroscopy that, on dehydrated (673 K) SiO_2 , TiCl_4 reacts first (at room temperature) with siloxane bridges (reaction 4 in Figure 16) and then with silanol groups.³⁹⁷ Other authors have completely excluded this reaction pathway⁴⁰⁰ or have proposed only a certain contribution for high-temperature treatment of the silica (>873 K).³⁹⁸ The amount of bidentate species grafted on the surface increases with increasing concentration of hydroxyl groups and with reaction temperature. The maximum number of grafted groups is sterically limited for low-temperature pretreatment (high OH concentration) and decreases by high-temperature treatment.

Deposition of TiO_2 on silica can be performed by water vapor treatment of the above grafted titanium species at high temperature.^{399–401} If the reaction with water is performed at 373 K, no crystalline phase is detected by XRD whatever the titanium content (up to 21% w/w). Raman spectra performed after three GPI-D cycles indicate the presence of a TiO_2 anatase-like structure. After calcination of the sample at 773 K, a reorganization of the layer occurs and XRD indicates that anatase is present.³⁹⁹ If the reaction with water is carried out at 448 K, both ^1H MAS NMR and FTIR analyses show that anatase-like $\text{Ti}-\text{OH}$ groups are formed.⁴⁰⁰ After reaction with water above 723 K, XRD has revealed a mixture of rutile and anatase crystalline phase.⁴⁰¹

Li et al. have also observed different titanium species during the preparation of Ti/SiO_2 catalysts for the styrene epoxidation reaction.^{402,403} From UV-Raman spectra and XRD experiments, they have demonstrated that the temperatures of both the silica pretreatment and the TiCl_4 gas-phase impregnation influence the titanium loading and the nature and structure of the supported species.

Deposition of titanium oxide species on zeolites has been reported.⁴⁰⁴ TiCl_4 chemisorption, followed by

hydrolysis at 373 or 773 K, affords either TiO_x mononuclear species at low temperature, or bulk anatase at 773 K.

The use of supported titanium oxide as photocatalysts for degradation of different toxic organic compounds in water or air is of current interest to solve environmental problems. A TiO_2 /Vycor glass catalyst has been prepared from TiCl_4 , followed by a hydrolysis and a calcination step in O_2 . Due to the presence of well-dispersed titanium ions, it presents photoluminescent properties, distinct from bulk or impregnated TiO_2 catalysts.⁴⁰⁵ This catalyst is active for the photocatalytic reduction of CO_2 with H_2O in CH_4 .

Supported anatase TiO_2 particles on hollow glass micro-beads have been prepared by reacting TiCl_4 vapors between 573 and 773 K with the support, followed by hydrolysis at the same temperature.⁴⁰⁶ The final material has been tested in the photo-assisted oxidation of ethanol to acetaldehyde and compared to TiO_2 -supported catalyst prepared by different methods. Anpo and Che have prepared by a similar method highly dispersed TiO_2 anchored on a porous Vycor glass to investigate photocatalytic reaction mechanisms.^{407,408} This preparation method allows the control of the deposit homogeneity and the degree of coordinative unsaturation on the surface. The photocatalytic activity of the GPI-D catalyst in the photohydrogenation reaction of $\text{CH}_3-\text{C}\equiv\text{CH}$ with H_2O is much higher than that of the bulk TiO_2 , by about 2 or 3 orders of magnitude. This catalyst has also been used for the photoformation of N_2 from N_2O .

A silica gel supported TiO_2 photocatalyst has been prepared by a CVD method from titanium tetraisopropoxide. This precursor is characterized by a high vapor pressure and a high reactivity with water adsorbed on the support.⁴⁰⁹ An anatase form of TiO_2 is produced at 573 K, but a further calcination in air is necessary to obtain better results. TiO_2 loadings around 6% w/w have been reached, and the deposit is located mainly on the external surface of the support with a minor alteration of the total surface area. The photocatalytic activity of this material for phenol aqueous solution oxidation has been evaluated and compared to a commercial TiO_2 catalyst (Degussa P25). Its activity is lower than that of P25, but it can be easily separated from the reaction medium and recycled without loss of activity.

Fine TiO_2 particles have been prepared by homogeneous phase CVD, starting from $[\text{Ti}(\text{OC}_3\text{H}_7)]$.⁴¹⁰ The tuning of some parameters as the temperature of the process, the precursor concentration, and the residence time allows the control of properties such as surface area, particle diameter, crystallinity, and porosity. Surface area as large as $270 \text{ m}^2 \text{ g}^{-1}$ can be reached, and the particles are amorphous up to 673 K and crystallized in the anatase form above this temperature.

b. Preparation of Modified Supports. Development of new catalysts for deep hydrodesulfurization (HDS) of gas oil is possible by using a CVD method to create new composite supports for metal deposition that associate the advantageous properties of both alumina and titania.^{411–414} Surface modification of a porous $\gamma\text{-Al}_2\text{O}_3$ support ($186 \text{ m}^2 \text{ g}^{-1}$) has been realized

by depositing TiCl_4 at 473 K on the dehydroxylated support (773 K), then hydrolyzed at the same temperature, and finally calcinated under O_2 at 773 K. From IR measurements, it has been shown that almost all the bands of Al–OH groups disappear for 11% w/w of TiO_2 , indicating a high dispersion of Ti-species on alumina. TiO_2 deposition allows one to obtain a material in which Al_2O_3 is almost completely covered by TiO_2 (14% w/w) without significant modification of the specific surface area and of the pore volume. After preparation of Mo-supported or Ni–Mo-supported catalyst by liquid-phase impregnation, it has been shown by XPS that the state of molybdenum on $\text{Mo/TiO}_2\text{--Al}_2\text{O}_3$ catalyst is closer to the state of molybdenum on Mo/TiO_2 than to the molybdenum-supported on Al_2O_3 . After sulfurization ($\text{H}_2\text{S}/\text{H}_2$), similar results are obtained. The conversion rates for dibenzothiophene derivatives HDS obtained over $\text{Mo/TiO}_2\text{--Al}_2\text{O}_3$ are much higher than that obtained over $\text{Mo/Al}_2\text{O}_3$, and in some cases higher than that obtained over Mo/TiO_2 . When a composite type $\text{TiO}_2\text{--Al}_2\text{O}_3$ support prepared by classical impregnation method is used, the catalytic activity for HDS is lower than with the GPI-D prepared support.

TiO_2 deposition on highly porous supports such as alumina⁴¹⁵ or silica⁴¹⁶ has been investigated to prepare high surface area supports that could present strong metal support interaction (SMSI) properties. Anderson and Fogar⁴¹⁵ have prepared titania surface layer on $\gamma\text{-Al}_2\text{O}_3$ by using the same method as Segawa et al.^{411–414} with very similar results. A significant difference between samples prepared by this method and samples prepared by liquid (hexane)-phase impregnation is the presence of TiO_2 monolayer. Then, highly dispersed (~1 nm) iridium particles have been deposited by liquid-phase impregnation.⁴¹⁵ These catalysts are active for *n*-butane and 2,2-dimethylpropane conversion, and it has been shown that, for GPI-D catalysts, a SMSI phenomenon occurs and is more pronounced when increasing the amount of deposited TiO_2 (1–3 layers).

Iwasawa et al. have studied by EXAFS the structure of one atomic layer TiO_2 on SiO_2 ⁴¹⁶ as well as its restructuration through the reduction mediated by Pd and Pt deposition. The modified $\text{TiO}_2\text{--SiO}_2$ support has been prepared by the gas-phase deposition of $[\text{Ti}(\text{OC}_3\text{H}_7)_4]$ at 353 K followed by hydrolysis at room temperature and calcination at 773 K. Two cycles are necessarily to prepare a TiO_2 monolayer. No X-ray diffraction pattern has been observed indicating no TiO_2 crystallite formation on SiO_2 . The EXAFS and XANES results indicate that TiO_2 is present as anatase on the SiO_2 support. Thus, one atomic layer TiO_2 is much less reducible (H_2 – 773 K) than when dispersed or than bulk TiO_2 , possibly because of a direct TiO_2 bonding. The deposition by liquid-phase impregnation of Pd or Pt followed by calcination and reduction at 773 K affects the structure of the TiO_2 layer in a different way. The Pt-one atomic layer TiO_2 (Pt mean particle size 2 nm) retains the anatase structure, whereas this structure is transformed to rutile in the Pd-one atomic layer TiO_2 (Pd mean particle size 5 nm). It has been proposed that the larger size of the Pd particles plays a role

in this structural change. These two catalysts do not present SMSI, probably because of the presence of Ti–O–Si bonds.

C. Gas-Phase Preparation of Catalytic Membranes

The application of porous ceramic membranes in catalytic reactors has started in the 1980s with some studies in the engineering of reactors. Two classes of catalytic reactors based on ceramic membranes have to be distinguished: (i) inert membranes reactors where the role of the membrane is to allow the specific introduction of compounds and the catalyst is located apart from the membrane, and (ii) catalytic membrane reactors where the membrane itself is catalytic, or becomes catalytic.⁴¹⁷

Porous ceramic membranes are made of alumina, silica, titania, zirconia, zeolites, etc., and composite membranes can be obtained by depositing a metal or an oxide on the surface or in the porosity of the ceramic.

Beside recent advances in chemical vapor deposition of thin ceramic films (SiO_2 , Al_2O_3 , TiO_2 , or B_2O_3) on porous alumina membranes to develop hydrogen-permselective membranes,^{418–422} noble metal deposits have been investigated, especially palladium deposits which are particularly efficient to sorb hydrogen.

Palladium(II) acetate has been used as precursor by Morooka et al.^{423,424} to deposit metallic palladium by a low-pressure CVD process between 573 and 773 K on a porous α -alumina membrane, which presents an average pore size of 150 nm. Palladium films of 2 μm consisting of 80 nm crystallites have been deposited on the alumina membrane surface at 573 K, and the palladium deposit layer extends as far as 8 μm from the top surface to the inside of the support. At 773 K, the penetration is only of 2 μm due to the fast decomposition of the precursor at this temperature. In all cases, the top 2 μm layer is defective and does not separate the gas. The best H_2 permeability is observed with the palladium membrane prepared at 573 K.

Palladium(II) chloride has been deposited at around 723 K by CVD on $\alpha\text{-Al}_2\text{O}_3$ (pore size 200 nm) and $\gamma\text{-Al}_2\text{O}_3$ coated $\alpha\text{-Al}_2\text{O}_3$ (pore size 3–6 nm) in the presence of hydrogen.⁴²⁵ On $\alpha\text{-Al}_2\text{O}_3$, thick (50 μm) and defective Pd films (grain size: 15–20 nm) are obtained on the surface, and the major part of palladium is supposed to lie inside the $\gamma\text{-Al}_2\text{O}_3$ pores. An explanation of this result could be given either by differences in Knudsen diffusivity of H_2 and PdCl_2 vapors, or by a different reaction rates in the α - and γ -pores. The $\text{Pd}/\gamma\text{-Al}_2\text{O}_3/\alpha\text{-Al}_2\text{O}_3$ membranes present a substantial H_2 permeation rate. The same authors have also studied the deposition of palladium from $[\text{Pd}(\text{acac})_2]$ on a $\gamma\text{-Al}_2\text{O}_3$ membrane under low pressure, and in the presence or not of hydrogen.⁴²⁶ In the absence of H_2 , the deposit obtained at 623 K is poorly crystallized (grain size < 5 nm) and is present inside the $\gamma\text{-Al}_2\text{O}_3$ layer (until 6 μm depth) with a maximum concentration near the $\gamma\text{-Al}_2\text{O}_3$ surface. The presence of hydrogen allows a clean decomposition of the palladium precursor, and a well-crystallized pure palladium film is obtained (0.8 μm thick-

ness – grain size 30–50 nm), but the fast reaction rate prevents a deep penetration. This latter Pd-modified membrane exhibits substantial selective permeability for H₂.

Palladium, as well as ruthenium, rhodium, iridium, and platinum acetylacetones have been used as CVD precursors to prepare asymmetric membranes by coating a tubular γ -Al₂O₃. This membrane consists of a 10 μm γ -Al₂O₃ layer with a mean pore size of 200 nm supported on the outer surface of a matrix having a pore size of 10 μm .^{427,428} The CVD conditions leading to the optimal membrane efficiency in hydrogen permeation have been determined. Metal deposition occurs in the outer thin γ -Al₂O₃ layer, and the effective thickness of this deposit ranges between 3 and 10 μm . These membranes are thermally stable up to 773 K. The palladium membrane gives the best results and shows a H₂ flux around 1.6 times higher than that of a dense palladium membrane prepared by electroless-plating and having a thickness of 4.5 μm . These CVD membranes have also been used for steam reforming of methane at 773 K in a membrane reactor and compared to 8 μm palladium electroless-plating membranes.⁴²⁹ In this case, the CVD platinum and Pd electroless-plating membranes give excellent performances. However, the advantages of the CVD Pt membrane are (i) a lower metal loading and thus a lower cost, and (ii) a lower tendency toward hydrogen embrittlement.

Catalytic membranes have also been prepared by CVD techniques for other applications. Thus, a CVD Ni/Al₂O₃ membrane catalyst is active for methanol reforming.⁴³⁰ The preparation of this material consists of depositing NiO at 1023 K and at atmospheric pressure in the pores of an alumina filter of mean pore diameter 1 μm from NiCl₂ and oxygen. The deposition must operate by a reaction limited regime to allow a suitable mass transfer of the reactant and to fill deeply (along 1 mm), and homogeneously the Al₂O₃ pores. After reduction by hydrogen at 623 K, this Ni/Al₂O₃ catalyst has been employed for methanol decomposition.

A bimetallic Pd–Sn/ α -Al₂O₃ catalytic membrane has been prepared by CVD and used for the hydrogenation of nitrates in water.⁴³¹ The preferred sequence for precursor deposition is to deposit first tin, from [Sn(hfa)₂] under H₂, and then palladium from [Pd(hfa)₂] at 523 K under reduced pressure. Typical palladium concentration profiles across the asymmetric membrane, as determined by EPMA/WDX, indicate that Pd is located mainly in the first 50 μm depth, and that the Pd/Sn atomic ratio remains constant over the whole depth. XRD patterns show that metallic palladium is deposited and Auger electron spectroscopy reveals high carbon contamination presumably due to the absence of hydrogen during the palladium deposition. TEM observations show that the deposit consists of particles with diameter around 8–10 nm. Pore size distribution of the catalytic top layer decreases from 64 to 48 nm. These catalytic membranes offer a high activity and fair selectivity to nitrogen for selective hydrogenation of nitrates and are thus an interesting material for nitrates removal from drinking water. The influence

of the preparation method on the distribution of Pd and Sn in the deposit has also been reported.^{432,433} The palladium-to-tin ratio on the surface, as measured by XPS, is significantly higher when the material is prepared by CVD than when impregnation is used. It has been proposed that the high temperatures for calcination (773 K)-reduction (623 K) steps performed during the impregnation procedure are responsible for tin enrichment on the surface. These two membranes exhibit a similar activity for nitrate reduction, but their selectivity differs markedly. Indeed, N₂ is produced selectively (91%) on the CVD membrane, whereas NH₄⁺ is obtained (68%) on the impregnated Pd-Sn membrane.

Pt-based catalytic membranes are of interest for the removal of volatile organic compounds contained in air, and waste streams. Some attempts to prepare Pt/ γ -Al₂O₃ membranes by GPI-D from [Pt(η^3 -C₃H₅)-(η^5 -C₅H₅)] have been reported.⁴³⁴ The gas-phase impregnation is performed at room temperature by introducing the organometallic precursor inside the tubular membrane and maintaining the outer side under high vacuum. Further calcination to remove the organic ligands follows. Comparison with impregnated membranes for the combustion of toluene and methylethylketone shows that both catalytic membranes present similar performances.

D. Conclusion

Surface modifications and/or thin films deposition constitute new topics in the field of catalyst preparation. The promising results described in this review open new perspectives for the application of gas-phase methods to elaborate catalytic materials. However, it is worth mentioning that, for layered deposits, most of the time the structure has not been fully determined. The terms submonolayer, monolayer, overlayers do not give any information on the structural characteristics of the deposit but are rather an indication of the coverage of the surface by the deposited material. As far as the catalytic membranes are concerned, the use of gas-phase methods allows a good control of the diffusion of the precursor inside the pores and thus of the deposit depth from the surface to the inside of the support. Additional studies devoted to this subject will be necessary. These preliminary positive results should promote additional studies.

V. Conclusions and Perspectives

This review shows that a wide variety of information on gas-phase deposition methods is available, starting from a large series of precursors to prepare supported catalysts. However, this domain suffers from the dispersion of available data that would permit the clear identification of the fundamentals trends and thus to achieve the complete coverage of the subject. This is certainly because specialists of the molecular approach of catalyst preparation, of CVD, and of chemical engineering have too often carried out independent investigations. Indeed, the first stage of the preparation related to the interaction of the gaseous precursor and the surface has

been deeply studied for a limited number of carbon-yls; the chemical role of the surface has been clearly explained. Unfortunately, the parameters that govern either the germination, or the growth of the aggregates have been rather neglected. In many cases, the composition and the morphology of the deposits have not been systematically determined. The studies of nucleation/growth phenomena, and of solid characterization classically carried out in CVD on planar substrates, need to be applied to catalytic material elaboration. Chemical engineering is also involved in the design of specific reactors, either for the preparation or for the use of the catalysts.

In our opinion, future studies should combine the skills of researcher of these three specialities.

Since most often the performances of these materials are already higher than those of the corresponding catalysts prepared by wet impregnation, such a unified approach will be fruitful for the comprehension of all the phenomena and will promote the development of gas-phase methods of catalyst preparation.

Finally, the easy and reproducible conditions to prepare more active catalysts than by the classical impregnation method should attract the attention of industry. The patent literature seems to give the same indication, as well as a recent paper of K. P. de Jong.⁴³⁵

VI. Acknowledgments

At the beginning of our studies on the preparation of metal deposits by CVD in fluidized bed reactors, a Brite Euram European Program allowed us to collaborate with several other scientists from various specialities and to promote the quality of our investigations: Prof. J.-P. Couderc (CVD, chemical engineering, ENSIACET, Toulouse), Prof. R. Morancho (CVD and materials, ENSIACET, Toulouse), Prof. A. Kiennemann (heterogeneous catalysis, ECPM, Strasbourg), Prof. C. Mazzocchia (heterogeneous catalysis and industrial chemistry, Politecnico di Milano, Milano, Italy), and Dr. J.-P. Guerlet and Dr. N. Petit (chemistry of precious metals, Engelhard-CLAL, Paris). We are grateful to them for the quality of our collaboration. This subject led us to undergo further investigations and to initiate new collaborations: we acknowledge Dr. J.-C. Hierso (Ph.D. on Pd and Pt deposition), Dr. B. Caussat (Ph.D. on modelizations on CVD in fluidized beds), Prof. J.-L. Figueiredo and Dr. J.-L. Faria from Porto, Portugal (Pt deposition on carbon), and Dr. Y. Kihn from CEMES, Toulouse (TEM observations). Finally, we are also grateful for financial support from the "Direction de la Recherche, Ministère de la Recherche et de la Technologie", the Région Midi-Pyrénées, The European Economic Community, Engelhard-CLAL, BP Chemicals, and the Agence nationale de la Valorisation et de la Recherche.

VII. References

- (1) *Handbook of Heterogeneous Catalysis*; Ertl, G. et al., Eds, Wiley-VCH: New York, 1997.
- (2) Iwasawa, Y. In *Handbook of Heterogeneous Catalysis*; Ertl, G. et al., Eds, Wiley-VCH: New York, 1997; p 853.
- (3) Impens, N. R. E. N.; van der Voort, P.; Vansant, E. F. *Micro-porous Mater.* **1999**, *28*, 217.
- (4) Psaro, R.; Recchia, S. *Catal. Today* **1998**, *41*, 139.
- (5) Yoo, J. S. *Catal. Today* **1998**, *41*, 409.
- (6) *Advanced Catalysts and Nanostructured Materials*; Möser, W. R., Ed.; Academic Press: New York, 1996.
- (7) Bailey, D. C.; Langer, S. H. *Chem. Rev.* **1981**, *81*, 130.
- (8) Yermakov, Y. I.; Kuznetsov, B. N. *J. Mol. Catal.* **1980**, *9*, 13.
- (9) Yermakov, Y. I. *J. Mol. Catal.* **1983**, *21*, 35.
- (10) Phillips, J.; Dumesic, J. A. *Appl. Catal.* **1984**, *9*, 1.
- (11) Schwartz, J. A. *Chem. Rev.* **1995**, *95*, 477.
- (12) Iwasawa, Y. *Adv. Catal.* **1987**, *35*, 187.
- (13) Lamb, H. H. *Catal. Today* **1993**, *18*, 3.
- (14) Candy, J. P.; Didillon, B.; Smith, E. L.; Shay, T. B.; Bassett, J. M. *J. Mol. Catal.* **1994**, *86*, 179.
- (15) Ichikawa, M. *Adv. Catal.* **1992**, *38*, 283.
- (16) Katada, N.; Niwa, M. *Chem. Vap. Deposition* **1996**, *2*, 125.
- (17) Mond, L.; Langer, C.; Quincke, F. *J. Chem. Soc.* **1890**, *57*, 749.
- (18) Baker, L. L., Jr.; Bernstein, R. B. *J. Am. Chem. Soc.* **1951**, *73*, 4434.
- (19) Gunter, P. L. J.; Niemantsverdriet, W. J. H.; Ribeiro, F. H.; Somorjai, G. A. *Catal. Rev.-Sci. Eng.* **1997**, *39*, 77.
- (20) Paukshtis, E. A.; Yurchenko, E. N. *Russ. Chem. Rev.* **1983**, *52*, 426.
- (21) Chun, W.-J.; Shirai, M.; Tomishige, K.; Asakura, K.; Iwasawa, Y. *J. Mol. Catal.* **1996**, *107*, 55.
- (22) Asakura, K.; Shirai, M.; Iwasawa, Y. *Catal. Lett.* **1993**, *20*, 117.
- (23) Vansant, E. F.; Van Der Voort, P.; Vrancken, K.C. *Characterization and Chemical Modification of the Silica Surface*; Elsevier: New York, 1995.
- (24) Knözinger, H.; Ratnasamy, P. *Catal. Rev.-Sci. Eng.* **1978**, *17*, 31.
- (25) Sohlberg, K.; Pennycook, S. J.; Pantelides, S. T. *Chem. Eng. Commun.* **2000**, *181*, 107.
- (26) Scokart, P. O.; Rouxhet, P. G. *J. Colloid Interface Sci.* **1982**, *86*, 96.
- (27) Hadjiivanov, K. I.; Klissurski, D. G. *Chem. Soc. Rev.* **1996**, *61*.
- (28) Kresge, C. T.; Leonowicz, M. E.; Roth, W. J.; Beck, J. S. *Nature* **1992**, *359*, 710.
- (29) Beck, J. S.; Vartuli, J. C.; Roth, W. J.; Leonowicz, M. E.; Kresge, C. T.; Schmitt, K. D.; Chu, T. W.; Olson, D. H.; Sheppard, E. W.; McCullen, S. B.; Higgins, J. B.; Schlenker, J. L. *J. Am. Chem. Soc.* **1992**, *114*, 10834.
- (30) Corma, A. *Chem. Rev.* **1997**, *97*, 2373.
- (31) Ying, J. Y.; Mehnert, C. P.; Wong, M. S. *Angew. Chem. Int. Ed. Engl.* **1999**, *38*, 56.
- (32) Inagaki, S.; Guan, S.; Fukushima, Y.; Ohsuna, T.; Terasaki, O. *J. Am. Chem. Soc.* **1999**, *121*, 9611.
- (33) Melde, B. J.; Holland, B. T.; Blanford, C. F.; Stein, A. *Chem. Mater.* **1999**, *11*, 3302.
- (34) Asefa, T.; MacLachlan, M. J.; Coombs, N.; Ozin, G. A. *Nature* **1999**, *402*, 867.
- (35) Rodriguez-Reinoso, F. *Carbon* **1998**, *36*, 159.
- (36) Boehm, H. P. *High Temperatures-High Pressures* **1990**, *22*, 275.
- (37) Boehm, H. P. *Carbon* **1994**, *32*, 759.
- (38) Figueiredo, J. L.; Pereira, M. F. R.; Freitas, M. M. A.; Orfao, J. J. M. *Carbon* **1999**, *37*, 1379.
- (39) Coq, B.; Planeix, J. M.; Brotons, V. *Appl. Catal. A* **1998**, *173*, 175.
- (40) Bassett, J. M.; Choplin, A. *J. Mol. Catal.* **1983**, *21*, 95.
- (41) Phillips, J.; Dumesic, J. A. *Appl. Catal.* **1984**, *9*, 1.
- (42) Ugo, R.; Dossi, C.; Psaro, R. *J. Mol. Catal.* **1992**, *77*, 257.
- (43) Lamb, H. H.; Gates, B. C.; Knözinger, H. *Angew. Chem. Int. Ed. Engl.* **1988**, *27*, 1127.
- (44) Bailey, D. C.; Langer, S. H. *Chem. Rev.* **1981**, *81*, 130.
- (45) Reddy, K. P.; Brown, T. L. *J. Am. Chem. Soc.* **1995**, *117*, 2845.
- (46) Gajda, G. J.; Grubbs, R. H.; Weinberg, W. H. *J. Am. Chem. Soc.* **1987**, *109*, 66.
- (47) Howe, R. F. *Inorg. Chem.* **1976**, *15*, 486.
- (48) Brown, T. L. *J. Mol. Catal.* **1981**, *12*, 41.
- (49) Kazusaka, A.; Howe, R. F. *J. Mol. Catal.* **1980**, *9*, 183.
- (50) Kaltchev, M.; Tysoe, W. T. *J. Catal.* **2000**, *193*, 29.
- (51) Walter, T. H.; Thompson, A.; Keniry, M.; Shinoda, S.; Brown, T. L.; Gutowsky, H. S.; Oldfield, E. *J. Am. Chem. Soc.* **1988**, *110*, 1065.
- (52) Kazusaka, A.; Howe, R. F. *J. Mol. Catal.* **1980**, *9*, 199.
- (53) Bilhou, J. L.; Theolier, A.; Smith, A. K.; Bassett, J. M. *J. Mol. Catal.* **1977/78**, *3*, 245.
- (54) Suvanto, M.; Pakkanen, T. A. *J. Mol. Catal.* **1999**, *138*, 211.
- (55) Myllyoja, S.; Pakkanen, T. A. *J. Mol. Catal.* **1998**, *136*, 153.
- (56) Brenner, A.; Hucul, D. A. *J. Catal.* **1980**, *61*, 216.
- (57) Suvanto, M.; Pakkanen, T. A. *Appl. Catal. A* **1998**, *166*, 105.
- (58) Brenner, A.; Burwell, R. L., Jr. *J. Catal.* **1978**, *52*, 353.
- (59) Goldwasser, J.; Fang, S. M.; Houalla, M.; Hall, W. K. *J. Catal.* **1989**, *115*, 34.
- (60) Zecchina, A.; Platero, E. E.; Arean, C. O. *Inorg. Chem.* **1988**, *27*, 102.
- (61) Nakamura, R.; Bowman, R. G.; Burwell, R. L., Jr. *J. Am. Chem. Soc.* **1981**, *103*, 673.

- (62) Jaenicke, S.; Loh, W. L. *Catal. Today* **1999**, *49*, 123.
- (63) Myllyoja, S.; Suvanto, M.; Kuhrinen, M.; Hirva, P.; Pakkanen, T. A. *Surf. Sci.* **1999**, *441*, 454.
- (64) Kurhinen, M.; Venäläinen, T.; Pakkanen, T. A. *J. Phys. Chem.* **1994**, *98*, 10237.
- (65) Hunter, G.; Rochester, C. H.; Wilkinson, A. J.; Paton, J. *J. Chem. Soc., Faraday Trans.* **1996**, *92*, 5093.
- (66) Hunter, G.; Rochester, C. H.; Wilkinson, A. G.; Paton, J. *J. Chem. Soc., Faraday Trans.* **1997**, *93*, 1205.
- (67) Brenner, A.; Hucul, D. A.; Hardwick, S. J. *Inorg. Chem.* **1979**, *18*, 1478.
- (68) Guglielminotti, E. *J. Mol. Catal.* **1981**, *13*, 207.
- (69) Coluccia, S.; Marchese, L.; Martra, G.; Spoto, G.; Zecchina, A. *J. Mol. Catal.* **1990**, *60*, 71.
- (70) Evans, J.; Hayden, B. E.; Lu, G. *J. Chem. Soc., Faraday Trans.* **1996**, *92*, 4733.
- (71) Guglielminotti, E.; Zecchina, A. *J. Chim. Phys.* **1981**, *78*, 891.
- (72) Abdo, S.; Howe, R. F. *J. Phys. Chem.* **1983**, *87*, 1713.
- (73) Okamoto, Y.; Maezawa, A.; Kane, H.; Mitsubishi, I.; Imanaka, T. *J. Chem. Soc., Faraday Trans. I* **1988**, *84*, 851.
- (74) Zecchina, A.; Rao, K. M.; Coluccia, S.; Platero, E. E.; Arean, C. O. *J. Mol. Catal.* **1989**, *53*, 397.
- (75) Zecchina, A.; Bordiga, S.; Escalona Platero, E.; Otero Arean, C. *J. Catal.* **1990**, *125*, 568.
- (76) Okamoto, Y.; Inui, Y.; Onimatsu, H.; Imanaka, T. *J. Phys. Chem.* **1991**, *95*, 4596.
- (77) Özkar, S.; Ozin, G. A.; Moller, K.; Bein, T. *J. Am. Chem. Soc.* **1990**, *112*, 9575.
- (78) Maezawa, A.; Kane, H.; Okamoto, Y.; Imanaka, T. *Chem. Lett.* **1988**, 241.
- (79) Okamoto, Y.; Maezawa, A.; Kane, H.; Imanaka, T. *J. Catal.* **1988**, *112*, 585.
- (80) Tway, L.; Apple, T. M. *Inorg. Chem.* **1992**, *31*, 2885.
- (81) You-Sing, Y.; Howe, R. F. *J. Chem. Soc., Faraday Trans. I* **1986**, *82*, 2887.
- (82) Coudurier, G.; Gallezot, P.; Praliaud, H.; Primet, M.; Imelik, B. *C. R. Acad. Sci. Paris Ser. C* **1976**, *282*, 311.
- (83) Abdo, S.; Howe, R. F. *J. Phys. Chem.* **1983**, *87*, 1722.
- (84) Okamoto, Y.; Kane, H.; Imanaka, T. *Chem. Lett.* **1988**, 2005.
- (85) Okamoto, Y.; Imanaka, T.; Asakura, K.; Iwasawa, Y. *J. Phys. Chem.* **1991**, *95*, 3700.
- (86) Yong, Y. S.; Howe, R. F.; Hughes, A. E.; Jaeger, H.; Sexton, B. A. *J. Phys. Chem.* **1987**, *91*, 6331.
- (87) Coddington, J. M.; Howe, R. F.; Yong, Y. S.; Asakura, K.; Iwasawa, Y. *J. Chem. Soc., Faraday Trans. I* **1990**, *86*, 1015.
- (88) Okamoto, Y.; Kobayashi, Y.; Imanaka, T. *Catal. Lett.* **1993**, *20*, 49.
- (89) Abdo, S.; Gosbee, J.; Howe, R. F. *J. Chim. Phys.* **1981**, *78*, 885.
- (90) Komatsu, T.; Namba, S.; Yashima, T.; Domen, K.; Onishi, T. *J. Mol. Catal.* **1985**, *33*, 345.
- (91) Hugues, F.; Basset, J. M.; Ben Taarit, Y.; Choplin, A.; Primet, M.; Rojas, D.; Smith, A. K. *J. Am. Chem. Soc.* **1982**, *104*, 7020.
- (92) Hugues, F.; Smith, A. K.; Ben Taarit, Y.; Basset, J. M. *J. Chem. Soc., Chem. Commun.* **1980**, 68.
- (93) Jackson, L. J.; Trusheim, M. R. *J. Am. Chem. Soc.* **1982**, *104*, 6590.
- (94) Hugues, F.; Dalmon, J. A.; Smith, A. K.; Basset, J. M.; Olivier, D. *J. Phys. Chem.* **1982**, *86*, 5136.
- (95) Guglielminotti, E.; Zecchina, A. *J. Mol. Catal.* **1984**, *24*, 331.
- (96) Iwasawa, Y.; Yamada, M.; Ogasawara, S.; Sato, Y.; Kuroda, H. *Chem. Lett.* **1983**, 621.
- (97) Phillips, J.; Clausen, B.; Dumesic, J. A. *J. Phys. Chem.* **1980**, *84*, 1814.
- (98) Ballivet-Tkatchenko, D.; Coudurier, G. *Inorg. Chem.* **1979**, *18*, 558.
- (99) Bein, T.; Jacobs, P. A. *J. Chem. Soc., Faraday Trans.* **1983**, *79*, 1819.
- (100) Nagy, J. B.; van Eenoo, M.; Derouane E. G. *J. Catal.* **1979**, *58*, 230.
- (101) Brenner, A. *J. Chem. Soc., Chem. Commun.* **1979**, 251.
- (102) Brenner, A.; Hucul, D. A. *Inorg. Chem.* **1979**, *18*, 2836.
- (103) Bein, T.; Jacobs, P. A. *J. Chem. Soc., Faraday Trans.* **1984**, *80*, 1391.
- (104) Ballivet-Tkatchenko, D.; Coudurier, G.; Mozzanega, H.; Tkatchenko, I.; Kiennemann, A. *J. Mol. Catal.* **1979**, *6*, 293.
- (105) Rao, K. M.; Spoto, G.; Zecchina, A. *J. Catal.* **1988**, *113*, 466.
- (106) Rao, K. M.; Spoto, G.; Guglielminotti, E.; Zecchina, A. *J. Chem. Soc., Faraday Trans.* **1988**, *84*, 2195.
- (107) Schneider, R. L.; Howe, R. F.; Watters, K. L. *Inorg. Chem.* **1984**, *23*, 4593.
- (108) Iwasawa, Y.; Yamada, M.; Sato, Y.; Kuroda, H. *J. Mol. Catal.* **1984**, *23*, 95.
- (109) Asakura, K.; Iwasawa, Y. *Physica B* **1989**, *158*, 152.
- (110) Shirai, M.; Inoue, T.; Onishi, H.; Asakura, K.; Iwasawa, Y. *J. Catal.* **1994**, *145*, 159.
- (111) Asakura, K.; Iwasawa, Y. *J. Phys. Chem.* **1989**, *93*, 4213.
- (112) Suvanto, M.; Pakkanen, T. A.; Backman, L. *Appl. Catal. A* **1999**, *177*, 25.
- (113) Suvanto, S.; Hirva, P.; Pakkanen, T. A. *Surf. Sci.* **2000**, *465*, 277.
- (114) Kurhinen, M.; Pakkanen, T. A. *Langmuir* **1998**, *14*, 6907.
- (115) Schneider, R. L.; Howe, R. F.; Watters, K. L. *Inorg. Chem.* **1984**, *23*, 4600.
- (116) Zecchina, A.; Platero, E. E.; Arean, C. O. *J. Mol. Catal.* **1988**, *45*, 373.
- (117) McKenna, W. P.; Higgins, B. E.; Eyring, E. M. *J. Mol. Catal.* **1985**, *31*, 199.
- (118) Purnell, S. K.; Xu, X.; Goodman, D. W.; Gates, B. C. *J. Phys. Chem.* **1994**, *98*, 4076.
- (119) Papile, C. J.; Gates, B. C. *Langmuir* **1992**, *8*, 74.
- (120) Hu, A.; Neyman, K. M.; Staufer, M.; Belling, T.; Gates, B. C.; Rösch, N. *J. Am. Chem. Soc.* **1999**, *121*, 4522.
- (121) Dossi, C.; Schaefer, J.; Sachtler, W. M. H. *J. Mol. Catal.* **1989**, *52*, 193.
- (122) Keyes, M. P.; Watters, K. L. *J. Catal.* **1986**, *100*, 477.
- (123) Keyes, M. P.; Watters, K. L. *J. Catal.* **1988**, *110*, 96.
- (124) Frederick, B. G.; Apai, G.; Rhodin, T. N. *J. Am. Chem. Soc.* **1987**, *109*, 4797.
- (125) Bowser, W. M.; Weinberg, W. H. *J. Am. Chem. Soc.* **1981**, *103*, 1453.
- (126) Belton, D. N.; Dimaggio, C. L. *Surf. Sci.* **1989**, *220*, 96.
- (127) Belton, D. N.; Schmieg, S. *J. Appl. Surf. Sci.* **1988**, *32*, 173.
- (128) Evans, J.; Hayden, B.; Mosselmans, F.; Murray, A. *J. Am. Chem. Soc.* **1992**, *114*, 6912.
- (129) Evans, J.; Hayden, B.; Mosselmans, F.; Murray, A. *Surf. Sci. Lett.* **1992**, *279*, L159.
- (130) Evans, J.; Hayden, B.; Mosselmans, F.; Murray, A. *Surf. Sci.* **1994**, *301*, 61.
- (131) Hayden, B. E.; King, A.; Newton, M. A. *Chem. Phys. Lett.* **1997**, *269*, 485.
- (132) Hayden, B. E. In *Chemisorption and Reactivity on Supported Clusters and Thin Films*; Kluwer Academic Publishers: Norwell, MA, 1997; p 215.
- (133) Evans, J. *J. Chem. Soc. Rev.* **1997**, 11.
- (134) Hayden, B. E.; King, A.; Newton, M. A. *Surf. Sci.* **1998**, *397*, 306.
- (135) Newton, M. A.; Bennett, R. A.; Smith, R. D.; Bowker, M.; Evans, J. *Chem. Commun.* **2000**, 1677.
- (136) Newton, M. A.; Bennett, R. A.; Smith, R. D.; Bowker, M.; Evans, J. *Surf. Sci.* **2001**, *487*, 223.
- (137) Hayden, B. E.; King, A.; Newton, M. A.; Yoshikawa, N. *J. Mol. Catal.* **2001**, *167*, 33.
- (138) Gelin, P.; Ben Taarit, Y.; Naccache, C. *J. Catal.* **1981**, *59*, 357.
- (139) Evans, J.; Hayden, B. E.; Newton, M. A. *Surf. Sci.* **2000**, *462*, 169.
- (140) Smith, P. B.; Bernasek, S. L.; Schwartz, J.; McNulty, G. S. *J. Am. Chem. Soc.* **1986**, *108*, 5654.
- (141) Chang, T.; Bernasek, S. L.; Schwartz, J. *J. Am. Chem. Soc.* **1989**, *111*, 758.
- (142) Dufour, P.; Houtman, C.; Santini, C. C.; Nédez, C.; Basset, J. M.; Hsu, L. Y.; Shore, S. G. *J. Am. Chem. Soc.* **1992**, *114*, 4248.
- (143) Santini, C. C.; Scott, S. L.; Basset, J. M. *J. Mol. Catal.* **1996**, *107*, 263.
- (144) Iwasawa, Y.; Sato, H. *Chem. Lett.* **1985**, 507.
- (145) Asakura, K.; Iwasawa, Y.; Kuroda, H. *J. Chem. Soc., Faraday Trans.* **1988**, *84*, 1329.
- (146) Dufour, P.; Santini, C. C.; Houtman, C.; Basset, J. M. *J. Mol. Catal.* **1991**, *66*, L23.
- (147) Dufour, P.; Houtman, C.; Santini, C. C.; Basset, J. M. *J. Mol. Catal.* **1992**, *77*, 257.
- (148) Nédez, C.; Theolier, A.; Lefebvre, F.; Choplin, A.; Basset, J. M.; Joly, J. F. *J. Am. Chem. Soc.* **1993**, *115*, 722.
- (149) Quignard, F.; Lecuyer, C.; Bougault, C.; Lefebvre, F.; Choplin, A.; Olivier, D.; Basset, J. M. *Inorg. Chem.* **1992**, *31*, 928.
- (150) Rosier, C.; Niccolai, G. P.; Basset, J. M. *J. Am. Chem. Soc.* **1997**, *119*, 12408.
- (151) Amor Nait Ajjou, J.; Scott, S. L. *Organometallics* **1997**, *16*, 86.
- (152) Ajjou, J. A. N.; Rice, G. L.; Scott, S. L. *J. Am. Chem. Soc.* **1998**, *120*, 13436.
- (153) Dufaud, V.; Niccolai, G. P.; Thivolle-Cazat, J.; Basset, J. M. *J. Am. Chem. Soc.* **1995**, *117*, 4288.
- (154) Farkas, J.; Hampden-Smith, M. J.; Kodas, T. T. *J. Phys. Chem.* **1994**, *98*, 6753.
- (155) Sekine, R.; Kawai, M. *Appl. Phys. Lett.* **1990**, *56*, 1466.
- (156) Sekine, R.; Kawai, M.; Hikita, T.; Hanada, T. *Surf. Sci.* **1991**, *242*, 508.
- (157) Sekine, R.; Kawai, M.; Asakura, K.; Hikita, T.; Kudo, M. *Surf. Sci.* **1992**, *278*, 175.
- (158) Sekine, R.; Kawai, M.; Asakura, K.; Iwasawa, Y. *Mat. Res. Soc. Symp. Proc.* **1991**, *222*, 333.
- (159) Shirai, M.; Asakura, K.; Iwasawa, Y. *Chem. Lett.* **1992**, 1037.
- (160) Haukka, S.; Lakomaa, E.-L.; Suntola, T. *Appl. Surf. Sci.* **1994**, *75*, 220.
- (161) Zecchina, A.; Spoto, G.; Bordiga, S. *J. Chem. Soc., Faraday Trans.* **1989**, *87*, 149.
- (162) Hunter, G.; Rochester, C. H.; Wilkinson, A. J.; Paton, J. *J. Chem. Soc., Faraday Trans.* **1996**, *92*, 4763.

- (163) Hunter, G.; Rochester, C. H.; Wilkinson, A. J.; Paton, J. *J. Chem. Soc., Faraday Trans.* **1997**, *92*, 5093.
- (164) Hunter, G.; Rochester, C. H.; Wilkinson, A. J.; Paton, J. *J. Chem. Soc., Faraday Trans.* **1997**, *93*, 1205.
- (165) Aigler, J. M.; Brito, J. L.; Leach, P. A.; Houalla, M.; Proctor, A.; Cooper, N. J.; Hall, W. K.; Hercules, D. M. *J. Phys. Chem.* **1993**, *97*, 5699.
- (166) Iwasawa, Y.; Yamagishi, M. *J. Catal.* **1983**, *82*, 373.
- (167) Crowfoot, L.; Ozin, G. A.; Özkar, S. *J. Am. Chem. Soc.* **1991**, *113*, 2033.
- (168) Omata, K.; Mazaki, H.; Yagita, H.; Fujimoto, K. *Catal. Lett.* **1990**, *4*, 123.
- (169) Dossi, C.; Bartsch, A.; Losi, P. In *Proceedings of the Congress Advanced Synthesis and Methodologies in Inorganic Chemistry*; Daolio, S. Ed.; 1991, 83.
- (170) Hierso, J.-C.; Serp, P.; Feurer, R.; Kalck, P. *Appl. Organomet. Chem.* **1998**, *12*, 161.
- (171) Suvanto, M.; Pakkanen, T. A. *J. Mol. Catal.* **1997**, *125*, 91.
- (172) Lakomaa, E.-L. *Appl. Surf. Sci.* **1994**, *75*, 185.
- (173) Köhler, S.; Reiche, M.; Frobel, C.; Baerns, M. In *Preparation of Catalysts VI*; Concelet, G. et al., Eds.; Elsevier Science B. V.: New York, 1995; p 1009.
- (174) Hercul, D. A.; Brenner, A. *J. Chem. Soc., Chem. Commun.* **1982**, 830.
- (175) Hercul, D. A.; Brenner, A. *J. Phys. Chem.* **1981**, *85*, 496.
- (176) Thomas, T. J.; Brenner, A. *J. Mol. Catal.* **1983**, *18*, 197.
- (177) Brenner, A.; Hercul, D. A. *J. Am. Chem. Soc.* **1980**, *102*, 2484.
- (178) Brenner, A. *J. Mol. Catal.* **1979**, *5*, 157.
- (179) Gonzalez, P. F.; Villa Garcia, M. A.; Brenner, A. *J. Catal.* **1989**, *118*, 360.
- (180) Masuyama, Y.; Tomatsu, Y.; Ishida, K.; Kurusu, Y.; Segawa, K.-I. *J. Catal.* **1988**, *114*, 347.
- (181) Okamoto, Y.; Maezawa, A.; Kane, H.; Imanaka, T. *J. Chem. Soc., Chem. Commun.* **1988**, 380.
- (182) Suvanto, S.; Hukkamäki, J.; Pakkanen, T. T.; Pakkanen, T. A. *Langmuir* **2000**, *16*, 4109.
- (183) Jaenicke, S.; Loh, W. L. *Catal. Today* **1999**, *49*, 123.
- (184) Wada, Y.; Nakao, C.; Morikawa, A. *Chem. Lett.* **1992**, 1037.
- (185) Bilhou, J. L.; Theolier, A.; Smith, A. K.; Basset, J. M. *J. Mol. Catal.* **1977/78**, *3*, 245.
- (186) Derouane, E. G.; Nagy, J. B.; Védrine, J. C. *J. Catal.* **1977**, *46*, 434.
- (187) Kazusaka, A.; Suzuki, H.; Toyoshima, I. *J. Chem. Soc., Chem. Commun.* **1983**, 150.
- (188) Suvanto, S.; Hukkamäki, J.; Pakkanen, T. T.; Pakkanen, T. A. *Langmuir* **2000**, *16*, 4109.
- (189) Suvanto, S.; Pakkanen, T. A. *J. Mol. Catal.* **2000**, *164*, 273.
- (190) Suvanto, M.; Räty, J.; Pakkanen, T. A. *Appl. Catal. A* **1999**, *181*, 189.
- (191) Suvanto, M.; Räty, J.; Pakkanen, T. A. *Catal. Lett.* **1999**, *62*, 21.
- (192) Kurhinen, M.; Pakkanen, T. A. *Appl. Catal. A* **2000**, *194–195*, 365.
- (193) Myllyjoja, S.; Räty, J.; Pakkanen, T. A. *J. Mol. Catal.* **2000**, *157*, 245.
- (194) Yamaguchi, A.; Asakura, K.; Iwasawa, Y. *J. Mol. Catal.* **1999**, *146*, 65.
- (195) Srinivasan, R.; De Angelis, R. J.; Reucroft, P. J.; Dhore, A. G.; Bentley, J. *J. Catal.* **1989**, *116*, 144.
- (196) Zerger, R. P.; McMahon, K. C.; Seltzer, M. D.; Michel, R. G.; Suib, S. L. *J. Catal.* **1986**, *99*, 498.
- (197) McMahon, K. C.; Suib, S. L.; Johnson, B. G.; Bartholomew, C. H., Jr. *J. Catal.* **1987**, *106*, 47.
- (198) Shen, G.-C.; Liu, A. M.; Ichikawa, M. *J. Chem. Soc., Faraday Trans.* **1998**, *94*, 1353.
- (199) Chen, J. G. C.; Liu, A. M.; Tanaka, T.; Ichikawa, M. *J. Phys. Chem. B* **1998**, *102*, 7782.
- (200) Bando, K. K.; Arakawa, H.; Ichikuni, N. *Catal. Lett.* **1999**, *60*, 125.
- (201) Hirva, P.; Venäläinen, T.; Pakkanen, T. A. *J. Catal.* **1994**, *148*, 722.
- (202) Rizzi, G. A.; Magrin, A.; Granozzi, G. *Surf. Sci.* **1999**, *443*, 277.
- (203) Pinto, P.; Calhorda, M. J.; Straub, T.; Miikkulainen, V.; Räty, J.; Suvanto, M.; Pakkanen, T. A. *J. Mol. Catal.* **2001**, *170*, 209.
- (204) Tsang, C. M.; Augustine, S. M.; Butt, J. M.; Sachtler, W. M. H. *Appl. Catal. A* **1989**, *46*, 45.
- (205) Räty, J.; Pakkanen, T. A. *Appl. Catal. A* **2001**, *208*, 169.
- (206) Räty, J.; Pakkanen, T. A. *J. Mol. Catal.* **2001**, *166*, 275.
- (207) Rizzi, G. A.; Zanoni, R.; Di Siro, S.; Perriello, L.; Granozzi, G. *Surf. Sci.* **2000**, *462*, 187.
- (208) Clowes, S. K.; Seddon, E. A.; McCash, E. M. *Surf. Sci.* **2000**, *464*, L667.
- (209) Close, M. R.; Petersen, J. L.; Kugler, E. L. *Inorg. Chem.* **1999**, *38*, 1535.
- (210) Wei, J.-C. J.; Lo, M.-H. *Appl. Organomet. Chem.* **1998**, *12*, 201.
- (211) Yoo, J. S.; Lin, P. S.; Elfline, S. D. *Appl. Catal. A* **1993**, *106*, 259.
- (212) Yoo, J. S.; Donohue, D. A.; Kleefish, M. S.; Lin, P. S.; Elfline, S. D. *Appl. Catal. A* **1993**, *105*, 83.
- (213) Zajac, G. W.; Choi-Feng, C.; Faber, J.; Yoo, J. S.; Patel, R.; Hochst, H. *J. Catal.* **1995**, *151*, 338.
- (214) Yoo, J. S.; Choi-Feng, C.; Donohue, D. A. *Appl. Catal. A* **1994**, *118*, 87.
- (215) Yoo, J. S.; Sohail, A. R.; Grimmer, S. S.; Choi-Feng, C. *Catal. Lett.* **1994**, *29*, 299.
- (216) Yoo, J. S.; Donohue, D. A.; Kleefish, M. S. *Appl. Catal. A* **1994**, *110*, 75.
- (217) Yoo, J. S. *Appl. Catal. A* **1996**, *135*, 261.
- (218) Centi, G.; Perathoner, S.; Tonini, S. *Catal. Today* **2000**, *61*, 211.
- (219) Chen, H.-Y.; Sachtler, W. M. H. *Catal. Today* **1998**, *42*, 73.
- (220) Voskoboinikov, T. V.; Chen, H.-Y.; Sachtler, W. M. H. *Appl. Catal. B* **1998**, *19*, 279.
- (221) Chen, H.-Y.; Sachtler, W. M. H. *Catal. Lett.* **1998**, *50*, 125.
- (222) Chen, H.-Y.; Voskoboinikov, T.; Sachtler, W. M. H. *Catal. Today* **1999**, *54*, 483.
- (223) El-Malki, El-M.; van Santen, R. A.; Sachtler, W. H. M. *J. Phys. Chem. B* **1999**, *103*, 4611.
- (224) Chen, H.-Y.; Voskoboinikov, T.; Sachtler, W. M. H. *J. Catal.* **1998**, *180*, 171.
- (225) Centi, G.; Vazzana, F. *Catal. Today* **1999**, *53*, 683.
- (226) Centi, G.; Misino, M. *Catal. Today* **1998**, *41*, 287.
- (227) Ma, A.-Z.; Grünert, W. *J. Chem. Soc., Chem. Commun.* **1999**, 71.
- (228) Long, R. Q.; Yang, R. T. *J. Catal.* **1999**, *188*, 332.
- (229) Kucherov, A. V.; Montreuil, C. N.; Kucherova, T. N.; Shelef, M. *Catal. Lett.* **1998**, *56*, 173.
- (230) Uemera, Y.; Hatate, Y.; Ikari, A. *J. Chem. Eng. Jpn.* **1989**, *22*, 48.
- (231) Moene, R.; Makkee, M.; Moulijn, J. A. *Chem. Eng. J.* **1993**, *53*, 13.
- (232) Jacobs, J. P.; Lindfors, L. P.; Reintjes, J. G. H.; Jylhä, O.; Brongersma, H. H. *Catal. Lett.* **1994**, *25*, 315.
- (233) Lindblad, M.; Lindfors, L. P.; Suntola, T. *Catal. Lett.* **1994**, *27*, 323.
- (234) Backman, L. B.; Rautiainen, A.; Krause, A. O. I.; Lindblad, M. *Catal. Today* **1998**, *43*, 11.
- (235) Backman, L. B.; Rautiainen, A.; Lindblad, M.; Jylhä, O.; Krause, A. O. I. *Appl. Catal. A* **2001**, *208*, 223.
- (236) Backman, L. B.; Rautiainen, A.; Lindblad, M.; Krause, A. O. I. *Appl. Catal. A* **2000**, *191*, 55.
- (237) Kainulainen, T. A.; Niemelä, M. K.; Krause, A. O. I. *Catal. Lett.* **1998**, *53*, 97.
- (238) Sonnemanns, J.; Mars, P. *J. Catal.* **1973**, *32*, 209.
- (239) Iwasawa, Y.; Yamagishi, M.; Ogasawara, S. *J. Chem. Soc., Chem. Commun.* **1982**, 246.
- (240) Iwasawa, Y.; Yamagishi, M.; Ogasawara, S. *J. Chem. Soc., Chem. Commun.* **1980**, 871.
- (241) Anpo, M.; Kondo, M.; Coluccia, S.; Louis, C.; Che, M. *J. Am. Chem. Soc.* **1989**, *111*, 8791.
- (242) Anpo, M.; Kondo, M.; Kubokawa, Y.; Louis, C.; Che, M. *J. Chem. Soc., Faraday Trans. 1* **1988**, *84*, 2771.
- (243) Louis, C.; Tatibouët, J. M.; Che, M. *J. Catal.* **1988**, *109*, 354.
- (244) Collart, O.; Van Der Voort, P.; Vansant, E. F.; Gustin, E.; Bouwen, A.; Schoemaker, D.; Rachamandra Rao, R.; Weckhuysen, B. M.; Schoonheydt, R. A. *Phys. Chem. Chem. Phys.* **1999**, *1*, 4099.
- (245) Baltes, M.; Collart, O.; van der Voort, P.; Vansant, E. F. *Langmuir* **1999**, *15*, 5841.
- (246) Miyao, T.; Shishikura, I.; Matsuoka, M.; Nagai, M. *Chem. Lett.* **1996**, 561.
- (247) Patterson, W. R.; Taylor, S. D. *J. Catal.* **1988**, *114*, 460.
- (248) Chien, J. C. W. *J. Am. Chem. Soc.* **1971**, *93*, 4675.
- (249) Bond, G. C.; König, P. J. *Catal.* **1982**, *77*, 309.
- (250) Bond, G. C.; Brückman, K. *Faraday Discuss., Chem. Soc.* **1981**, *72*, 235.
- (251) Grubert, G.; Rathousky, J.; Schulz-Ekloff, G.; Wark, M.; Zukal, A. *Microporous Mater.* **1998**, *22*, 225.
- (252) Hanke, W.; Bienert, R.; Jerschkewitz, H. G. Z. *Anorg. Allg. Chem.* **1975**, *414*, 109.
- (253) Anpo, M.; Sunamoto, M.; Che, M. *J. Phys. Chem.* **1989**, *93*, 1187.
- (254) Inamuru, K.; Okuhara, T.; Misino, M. *Chem. Lett.* **1990**, 1207.
- (255) Inamuru, K.; Okuhara, T.; Misino, M. *J. Phys. Chem.* **1991**, *95*, 4826.
- (256) Okuhara, T.; Inamuru, K.; Misino, M.; Matsubayashi, N.; Shimada, H.; Nishijima, A. *Catal. Lett.* **1993**, *20*, 73.
- (257) Nickl, J.; Dutoit, D.; Baiker, A.; Scharf, U.; Wokaun, A. *Appl. Catal. A* **1993**, *98*, 173.
- (258) Nickl, J.; Dutoit, D.; Baiker, A.; Scharf, U.; Wokaun, A. *Ber. Bunsenges. Phys. Chem.* **1993**, *97*, 217.
- (259) Baltes, M.; Van Der Voort, P.; Collart, O.; Vansant, E. F. *J. Porous Mater.* **1998**, *5*, 317.
- (260) Van Der Voort, P.; Baltes, M.; Vansant, E. F. *J. Phys. Chem. B* **1999**, *103*, 10102.
- (261) Van Der Voort, P.; Morey, M.; Stucky, G. D.; Mathieu, M.; Vansant, E. F. *J. Phys. Chem. B* **1998**, *102*, 585.
- (262) Kytökivi, A.; Jacobs, J.-P.; Hakuli, A.; Meriläinen, J.; Brongersma, H. H. *J. Catal.* **1996**, *162*, 190.

- (263) Hakuli, A.; Kytökivi, A.; Krause, A. O. I. *Appl. Catal. A* **2000**, *190*, 219.
- (264) Babich, I. V.; Plyuto, Y. V.; Van Der Voort, P.; Vansant, E. F. J. *Chem. Soc., Faraday Trans.* **1997**, *93*, 3191.
- (265) Bond, G. C.; Thompson, D. T. *Catal. Rev.-Sci. Eng.* **1999**, *41*, 319.
- (266) Okumura, M.; Tanaka, K.; Ueda, A.; Haruta, M. *Solid State Ionics* **1997**, *95*, 143.
- (267) Haruta, M. *Catal. Today* **1997**, *36*, 153.
- (268) Haruta, M. *Catal. Surv. Jpn.* **1997**, *1*, 61.
- (269) Okumura, M.; Nakamura, S.; Tsubota, S.; Nakamura, T.; Azuma, M.; Haruta, M. *Catal. Lett.* **1998**, *51*, 53.
- (270) Feeley, O. C.; Sachtler, W. M. H. *Appl. Catal. A* **1991**, *75*, 93.
- (271) Dossi, C.; Psaro, R.; Bartsch, A.; Brivio, E.; Galasco, A.; Losi, P. *Catal. Today* **1993**, *17*, 527.
- (272) Dossi, C.; Psaro, R.; Ugo, R.; Zhang, Z. C.; Sachtler, W. M. H. *J. Catal.* **1994**, *149*, 92.
- (273) Sordelli, L.; Martra, G.; Psaro, R.; Dossi, C.; Coluccia, S. *Top. Catal.* **1999**, *8*, 237.
- (274) Dossi, C.; Fusi, A.; Recchia, S.; Anghileri, M.; Psaro, R. *J. Chem. Soc., Chem. Commun.* **1994**, 1245.
- (275) Mehnert, C. P.; Ying, J. Y. *J. Chem. Soc., Chem. Commun.* **1997**, 2215.
- (276) Mehnert, C. P.; Weaver, D. W.; Ying, J. Y. *J. H. Am. Chem. Soc.* **1998**, *120*, 12289.
- (277) Hierso, J.-C.; Satto, C.; Feurer, R.; Kalck, P. *Chem. Mater.* **1996**, *8*, 2481.
- (278) Hierso, J.-C.; Feurer, R.; Kalck, P. *Chem. Mater.* **2000**, *8*, 2481.
- (279) Hierso, J.-C.; Feurer, R.; Kalck, P. *Coord. Chem. Rev.* **1998**, *178*, 8–180, 1811.
- (280) Matsuura, I.; Hashimoto, Y.; Takayasu, O.; Nitta, K.; Yoshida, Y. *Appl. Catal. A* **1991**, *74*, 273.
- (281) Cominos, V.; Gavriliidis, A. *Appl. Catal. A* **2001**, *210*, 381.
- (282) Hong, S. B.; Mielczarski, E.; Davis, M. E. *J. Catal.* **1992**, *134*, 349.
- (283) Dossi, C.; Psaro, R.; Bartsch, A.; Fusi, A.; Sordelli, L.; Ugo, R.; Bellatréccia, M.; Zanoni, R.; Vlaic, G. *J. Catal.* **1994**, *145*, 377.
- (284) Bellatréccia, M.; Zanoni, R.; Dossi, C.; Psaro, R.; Recchia, S.; Vlaic, G. *J. Chem. Soc., Faraday Trans.* **1995**, *91*, 2045.
- (285) Dossi, C.; Psaro, R.; Sordelli, L.; Bellatréccia, M.; Zanoni, R. *J. Catal.* **1996**, *159*, 435.
- (286) Jacobs, G.; Ghadiali, F.; Pisani, A.; Borgna, A.; Alvarez, W. E.; Resasco, D. E. *Appl. Catal. A* **1999**, *23*, 139.
- (287) Feast, S.; Englisch, M.; Jentys, A.; Lercher, J. A. *Appl. Catal. A* **1998**, *174*, 155.
- (288) Serp, P.; Hierso, J.-C.; Feurer, R.; Kihn, Y.; Kalck, P.; Faria, J. L.; Aksyulu, A. E.; Pacheco, A. M. T.; Figueiredo, J. L. *Carbon* **1999**, *37*, 527.
- (289) Serp, P.; Feurer, R.; Kihn, Y.; Kalck, P.; Faria, J. L.; Figueiredo, J. L. *J. Mater. Chem.* **2001**, *11*, 1980.
- (290) Hierso, J.-C.; Feurer, R.; Poujardieu, J.; Kihn, Y.; Kalck, P. *J. Mol. Catal.* **1998**, *135*, 321.
- (291) Serp, P.; Feurer, R.; Kalck, P.; Molinier, J.; Morancho, R.; Guerlet, J. P. *Fr. Patent*, 93.08656, 1993.
- (292) Serp, P.; Feurer, R.; Morancho, R.; Kalck, P. *J. Mol. Catal.* **1995**, *101*, L107.
- (293) Serp, P.; Feurer, R.; Morancho, R.; Kalck, P. *J. Catal.* **1995**, *157*, 294.
- (294) Feurer, R.; Reynes, A.; Serp, P.; Kalck, P.; Morancho, R. *J. Phys. IV Colloque C5* **1995**, *5*, 1037.
- (295) Serp, P.; Château, L.; Feurer, R.; Kiennemann, A.; Kalck, P. *J. Mol. Catal.* **1998**, *136*, 269.
- (296) Serp, P.; Feurer, R.; Morancho, R.; Kalck, P.; Daran, J.-C.; Vaissner, J. *J. Organomet. Chem.* **1995**, 498, 41.
- (297) Locatelli, F.; Didillon, B.; Uzio, D.; Niccolai, G.; Candy, J. P.; Basset, J. M. *J. Catal.* **2000**, *193*, 154.
- (298) Miura, H. *Catal. Today* **1996**, *28*, 215.
- (299) Miura, H.; Taguchi, H.; Sugiyama, K.; Matsuda, T.; Gonzalez, R. D. *J. Catal.* **1990**, *124*, 194.
- (300) Zhou, P. L.; Gates, B. C. *J. Chem. Soc., Chem. Commun.* **1989**, 347.
- (301) Tomishige, K.; Asakura, K.; Iwasawa, Y. *J. Chem. Soc., Chem. Commun.* **1993**, 184.
- (302) Tomishige, K.; Asakura, K.; Iwasawa, Y. *Catal. Lett.* **1993**, *20*, 15.
- (303) Tomishige, K.; Asakura, K.; Iwasawa, Y. *Chem. Lett.* **1994**, 235.
- (304) Tomishige, K.; Asakura, K.; Iwasawa, Y. *J. Catal.* **1994**, *149*, 70.
- (305) Tomishige, K.; Asakura, K.; Iwasawa, Y. *J. Catal.* **1995**, *157*, 472.
- (306) Yoshikawa, K.; Iwasawa, Y. *J. Mol. Catal.* **1995**, *100*, 115.
- (307) Inoue, T.; Tomishige, K.; Iwasawa, Y. *J. Chem. Soc., Chem. Commun.* **1995**, 329.
- (308) Didillon, B.; Houtman, C.; Shay, T.; Basset, J. M. *J. Am. Chem. Soc.* **1993**, *115*, 9380.
- (309) Lessage, P.; Clause, O.; Moral, P.; Didillon, B.; Candy, J. P.; Basset, J. M. *J. Catal.* **1995**, *155*, 238.
- (310) Miura, H.; Itoh, T. *React. Kinet. Catal. Lett.* **1999**, *66*, 189.
- (311) Recchia, S.; Dossi, C.; Fusi, A.; Sordelli, L.; Psaro, P. *Appl. Catal. A* **1999**, *182*, 41.
- (312) Onda, A.; Komatsu, T.; Yashima, T. *J. Chem. Soc., Chem. Commun.* **1998**, 1507.
- (313) Warnken, M.; Lazar, K.; Wark, M. *Phys. Chem. Chem. Phys.* **2001**, *3*, 1870.
- (314) Kwak, B. S.; Sachtler, W. M. H. *J. Catal.* **1993**, *141*, 729.
- (315) Kwak, B. S.; Sachtler, W. M. H. *J. Catal.* **1994**, *145*, 456.
- (316) Sakurai, H.; Sato, S.; Urabe, K.; Izumi, Y. *Chem. Lett.* **1985**, 1783.
- (317) Sato, S.; Sakurai, H.; Urabe, K.; Izumi, Y. *Chem. Lett.* **1985**, 277.
- (318) Sato, S.; Urabe, K.; Izumi, Y. *J. Catal.* **1986**, *102*, 99.
- (319) Sato, S.; Hasegawa, M.; Sodesawa, T.; Nozaki, F. *Bull. Chem. Soc. Jpn.* **1991**, *64*, 516.
- (320) Tavares da Silva, C. L.; Loyola Camorim, V. L.; Zotin, J. L.; Rocco Duarte Pereira, M. L.; da Costa Faro, A., Jr. *Catal. Today* **2000**, *57*, 209.
- (321) Nagai, M.; Suda, T.; Oshikawa, K.; Hirano, N.; Omi, S. *Catal. Today* **1999**, *50*, 29.
- (322) Nagai, M.; Nakauchi, R.; Ono, Y.; Omi, S. *Catal. Today* **2000**, *57*, 297.
- (323) Ramirez Ortiz, J.; Ogura, T.; Medina-Valtierra, J.; Acosta-Ortiz, S. E.; Bosch, P.; de los Reyes, J. A.; Lara, V. H. *Appl. Surf. Sci.* **2001**, *174*, 177.
- (324) Caps, V.; Tsang, S. C. *Catal. Today* **2000**, *61*, 19.
- (325) Burch, R.; Cruiise, N. A.; Gleeson, D.; Tsang, S. C. *J. Mater. Chem.* **1998**, *8*, 227.
- (326) Beutel, T.; Knözinger, H.; Trevino, H.; Zhang, Z. C.; Sachtler, W. M. H.; Dossi, C.; Psaro, R.; Ugo, R. *J. Chem. Soc., Faraday Trans.* **1994**, *90*, 1335.
- (327) Kröger-Laukkonen, M.; Peussa, M.; Leskelä, M.; Niinistö, L. *Appl. Surf. Sci.* **2001**, *183*, 290.
- (328) Izumi, Y.; Asakura, K.; Iwasawa, Y. *J. Catal.* **1991**, *127*, 631.
- (329) Izumi, Y.; Asakura, K.; Iwasawa, Y. *J. Catal.* **1991**, *132*, 566.
- (330) Izumi, Y.; Iwasawa, Y. *J. Phys. Chem.* **1992**, *96*, 10942.
- (331) Komatsu, T.; Mesuda, M.; Yashima, T. *Appl. Catal. A* **2000**, *194*–195, 333.
- (332) Hertl, W.; Hair, M. L. *J. Phys. Chem.* **1971**, *75*, 2181.
- (333) Hair, M. L.; Hertl, W. *J. Phys. Chem.* **1973**, *77*, 1965.
- (334) Hair, M. L.; Hertl, W. *J. Phys. Chem.* **1973**, *77*, 2070.
- (335) Kol'tsov, S. I.; Alekskovskii, V. B. *Russ. J. Chem.* **1968**, *42*, 631.
- (336) Morrow, B. A.; Hardin, A. H. *J. Phys. Chem.* **1979**, *83*, 3135.
- (337) Van der Voort, P.; Gillis-D'Hamers, I.; Vansant, E. F. *J. Chem. Soc., Faraday Trans.* **1990**, *86*, 3751.
- (338) Gillis-D'Hamers, I.; Philipaerts, J.; Van der Voort, P.; Vansant, E. F. *J. Chem. Soc., Faraday Trans.* **1990**, *86*, 3747.
- (339) Niwa, M.; Hibino, T.; Murata, H.; Katada, N.; Murakami, Y. *J. Chem. Soc., Chem. Commun.* **1989**, 289.
- (340) Niwa, M.; Katada, N.; Murakami, Y. *J. Phys. Chem.* **1990**, *94*, 6441.
- (341) Katada, N.; Ishiguro, H.; Muto, K.; Niwa, M. *Chem. Vap. Deposition* **1995**, *1*, 54.
- (342) Katada, N.; Toyama, T.; Niwa, M. *J. Phys. Chem.* **1994**, *98*, 7647.
- (343) Katada, N.; Fukui, H.; Niwa, M. *J. Chem. Eng. Jpn.* **2001**, *34*, 306.
- (344) Katada, N.; Fujii, T.; Iwata, K.; Hibino, H.; Niwa, M. *J. Catal.* **1999**, *186*, 478.
- (345) Sato, S.; Toita, M.; Sodesawa, T.; Nozaki, F. *Appl. Catal. A* **1990**, *62*, 73.
- (346) Imizu, Y.; Tada, A. *Chem. Lett.* **1989**, 1793.
- (347) Sato, S.; Toita, M.; Yu, Y.-Q.; Sodesawa, T.; Nozaki, F. *Chem. Lett.* **1987**, 1535.
- (348) Sato, S.; Hiratsuka, M.; Sodesawa, T.; Nosaki, F. *Bull. Chem. Soc. Jpn.* **1991**, *64*, 2214.
- (349) Muto, K.; Katada, N.; Niwa, M. *Appl. Catal. A* **1996**, *134*, 203.
- (350) Muto, K.; Katada, N.; Niwa, M. *Catal. Today* **1997**, *35*, 145.
- (351) Niwa, M.; Katada, N.; Murakami, Y. *J. Catal.* **1992**, *134*, 340.
- (352) Okuhara, T.; White, J. M. *Appl. Surf. Sci.* **1987**, *29*, 223.
- (353) Jin, T.; Okuhara, T.; White, J. M. *J. Chem. Soc., Chem. Commun.* **1987**, 1248.
- (354) Xu, B.-Q.; Yamaguchi, T.; Tanabe, K. *Chem. Lett.* **1989**, 149.
- (355) Shin, E. W.; Choi, C. H.; Na, Y. H.; Moon, S. H. *Catal. Today* **1998**, *44*, 137.
- (356) Asakura, K.; Ooi, K.; Iwasawa, Y. *J. Mol. Catal.* **1992**, *74*, 345.
- (357) Iiskola, E. I.; Timonen, S.; Pakkanen, T. T.; Häkkinen, O.; Seppälä, J. V. *Appl. Surf. Sci.* **1997**, *121/122*, 372.
- (358) Timonen, S.; Pakkanen, T. T.; Iiskola, E. I. *J. Mol. Catal.* **1999**, *148*, 235.
- (359) Timonen, S.; Pakkanen, T. T.; Iiskola, E. I. *J. Organomet. Chem.* **1999**, *582*, 273.
- (360) Okumura, K.; Asakura, K.; Iwasawa, Y. *Langmuir* **1998**, *14*, 3607.
- (361) Okumura, K.; Asakura, K.; Iwasawa, Y. *J. Phys. Chem. B* **1997**, *101*, 9984.
- (362) Asakura, K.; Okumura, K.; Inoue, T.; Kubota, T.; Chun, W. H.; Iwasawa, Y. *Mat. Res. Soc. Symp. Proc.* **1998**, *497*, 99.
- (363) Okumura, K.; Asakura, K.; Iwasawa, Y. *Catal. Today* **1998**, *39*, 343.

- (364) Okumura, K.; Ichikuni, N.; Asakura, K.; Iwasawa, Y. *J. Chem. Soc., Faraday Trans.* **1997**, *93*, 3217.
- (365) Nariman, K. E.; Lerou, J. J.; Bischoff, K. B.; Foley, H. C. *Ind. Eng. Chem. Res.* **1993**, *32*, 263.
- (366) Niwa, M.; Itoh, H.; Kato, S.; Hattori, T.; Murakami, Y. *J. Chem. Soc., Chem. Commun.* **1982**, 819.
- (367) Niwa, M.; Kato, M.; Hattori, T.; Murakami, Y. *J. Chem. Soc., Faraday Trans.* **1984**, *80*, 3135.
- (368) Niwa, M.; Kawashima, Y.; Hibino, T.; Murakami, Y. *J. Chem. Soc., Faraday Trans.* **1988**, *84*, 4327.
- (369) Hibino, T.; Niwa, M.; Hattori, A.; Murakami, Y. *Appl. Catal. A* **1988**, *44*, 95.
- (370) Sawa, M.; Kato, K.; Hirota, K.; Niwa, M.; Murakami, Y. *Appl. Catal. A* **1990**, *64*, 297.
- (371) Niwa, M.; Kawashima, Y.; Murakami, Y. *J. Chem. Soc., Faraday Trans.* **1985**, *81*, 2757.
- (372) Yan, Y.; Vansant, E. F. *J. Phys. Chem. B* **1990**, *94*, 2582.
- (373) Niwa, M.; Kato, M.; Hattori, T.; Murakami, Y. *J. Phys. Chem.* **1986**, *90*, 6233.
- (374) Hibino, T.; Niwa, M.; Murakami, Y. *J. Catal.* **1991**, *128*, 551.
- (375) Kim, J.-H.; Ishida, A.; Okajima, M.; Niwa, M. *J. Catal.* **1996**, *161*, 387.
- (376) Kim, J.-H.; Ikoma, Y.; Niwa, M. *Microporous Mesoporous Mater.* **1999**, *32*, 37.
- (377) Weber, R. W.; Möller, K. P.; Unger, M.; O'Connor, C. T. *Microporous Mater.* **1998**, *23*, 179.
- (378) Röger, H. P.; Krämer, M.; Möller, K. P.; O'Connor, C. T. *Microporous Mater.* **1998**, *21*, 607.
- (379) Shaikh, R. A.; Hedge, S. G.; Behlekar, A. A.; Rao, B. S. *Catal. Today* **1999**, *49*, 201.
- (380) Wang, I.; Ay, C.-L.; Lee, B.-J.; Chen, M.-H. *Appl. Catal. A* **1989**, *54*, 257.
- (381) Bhat, Y. S.; Das, J.; Halgeri, A. B. *J. Catal.* **1995**, *155*, 154.
- (382) Shimizu, S.; Abe, N.; Iguchi, A.; Dohba, M.; Sato, H.; Hirose, K. *Microporous Mater.* **1998**, *21*, 447.
- (383) Zheng, J.; Chun, Y.; Dong, J.; Xu, Q. *J. Mol. Catal.* **1998**, *130*, 271.
- (384) Lin, C. H.; Lee, K. C.; Wan, B.-Z. *Appl. Catal. A* **1997**, *164*, 59.
- (385) Baeck, S. H.; Lee, K. M.; Lee, W. H. *Catal. Lett.* **1998**, *52*, 221.
- (386) Kuno, H.; Shibagaki, M.; Takahashi, K.; Honda, I.; Matsushita, H. *Bull. Chem. Soc. Jpn.* **1991**, *64*, 2508.
- (387) Kuno, H.; Shibagaki, M.; Takahashi, K.; Honda, I.; Matsushita, H. *Bull. Chem. Soc. Jpn.* **1992**, *65*, 1240.
- (388) Bhat, Y. S.; Das, J.; Halgeri, A. B. *Bull. Chem. Soc. Jpn.* **1996**, *69*, 469.
- (389) Niwa, M.; Kawashima, Y.; Murakami, Y. *J. Chem. Soc., Faraday Trans.* **1985**, *81*, 2757.
- (390) Suzuki, M.; Amano, J.; Niwa, M. *Microporous Mater.* **1998**, *21*, 541.
- (391) Hibino, T.; Niwa, M.; Murakami, Y.; Sano, M.; Shin-ichi, K.; Hanaichi, T. *J. Phys. Chem.* **1989**, *93*, 7847.
- (392) Hibino, T.; Niwa, M.; Murakami, Y.; Sano, M. *J. Chem. Soc., Faraday Trans.* **1989**, *85*, 2327.
- (393) Tynjälä, P.; Pakkanen, T. T. *J. Mol. Catal.* **1997**, *122*, 159.
- (394) Asakura, K.; Aoki, M.; Iwasawa, Y. *Catal. Lett.* **1988**, *1*, 395.
- (395) Pozzo, R. L.; Baltanas, M. A.; Cassano, A. E. *Catal. Today* **1997**, *39*, 219.
- (396) Gao, X.; Wachs, I. E. *Catal. Today* **1999**, *51*, 233.
- (397) Kinney, J. B.; Staley, R. H. *J. Phys. Chem.* **1983**, *87*, 3735.
- (398) Schrijnemakers, K.; van der Voot, P.; Vansant, E. F. *Phys. Chem. Chem. Phys.* **1999**, *1*, 2569.
- (399) Schrijnemakers, K.; Impens, N. R. E. N.; Vansant, E. F. *Langmuir* **1999**, *15*, 5807.
- (400) Haukka, S.; Lakomaa, E.-L.; Root, A. *J. Phys. Chem. B* **1993**, *97*, 5085.
- (401) Lakomaa, E.-L.; Haukka, S.; Suntola, T. *Appl. Surf. Sc.* **1992**, *60/61*, 742.
- (402) Yang, Q.; Wang, S.; Lu, J.; Xiong, G.; Feng, Z.; Xin, Q.; Li, C. *Appl. Catal. A* **2000**, *194*, 507.
- (403) Wang, S.; Yang, Q.; Wu, Z.; Li, M.; Lu, J.; Tan, Z.; Li, C. *J. Mol. Catal.* **2001**, *172*, 219.
- (404) Klaas, J.; Schulz-Eckloff, G.; Jaeger, N. I. *J. Phys. Chem. B* **1997**, *101*, 1305.
- (405) Anpo, M.; Chiba, K. *J. Mol. Catal.* **1992**, *74*, 207.
- (406) Jackson, N. B.; Wang, C. M.; Schwitzgebel, J.; Ekerdt, J. G.; Brock, J. R.; Heller, A. *J. Electrochem. Soc.* **1991**, *138*, 3660.
- (407) Anpo, M.; Aikawa, N.; Kubokawa, Y.; Che, M.; Louis, C.; Giannello, E. *J. Phys. Chem.* **1985**, *89*, 5017.
- (408) Anpo, M.; Aikawa, N.; Kubokawa, Y.; Che, M.; Louis, C.; Giannello, E. *J. Phys. Chem.* **1985**, *89*, 5689.
- (409) Ding, Z.; Hu, X.; Lu, G. Q.; Yue, P.-L.; Greenfield, P. F. *Langmuir* **2000**, *16*, 6216.
- (410) Kirkbir, F.; Komiyama, H. *Can. J. Chem. Eng.* **1987**, *65*, 759.
- (411) Segawa, K.; Katsuta, M.; Kameda, F. *Catal. Today* **1996**, *29*, 215.
- (412) Pophal, C.; Kameda, F.; Hoshino, K.; Yoshinaka, S.; Segawa, K. *Catal. Today* **1997**, *39*, 21.
- (413) Yoshinaka, S.; Segawa, K. *Catal. Today* **1998**, *45*, 293.
- (414) Segawa, K.; Takahashi, K.; Satoh, S. *Catal. Today* **2000**, *63*, 123.
- (415) Foger, K.; Anderson, J. R. *Appl. Catal. A* **1986**, *23*, 139.
- (416) Asakura, K.; Inukai, J.; Iwasawa, Y. *J. Phys. Chem.* **1992**, *96*, 829.
- (417) Coronas, J.; Santamaría, J. *Catal. Today* **1999**, *51*, 377.
- (418) Tsapatsis, M.; Kim, S.; Nam, S. W.; Gavalas, G. *Ind. Eng. Chem. Res.* **1991**, *30*, 2152.
- (419) Megiris, C.; Glezer, J. H. E. *Ind. Eng. Chem. Res.* **1992**, *31*, 1293.
- (420) Sea, B. K.; Watanabe, M.; Kusakabe, K.; Morooka, S.; Kim, S. S. *Gas. Sep. Purif.* **1996**, *10*, 187.
- (421) Nijmeijer, A.; Bladergroen, B. J.; Verweij, H. *Microporous Mater.* **1998**, *25*, 179.
- (422) Cameron, M. A.; Gartland, I. P.; Smith, J. A.; Diaz, S. F.; George, S. M. *Langmuir* **2000**, *16*, 7435.
- (423) Yan, S.; Maeda, H.; Kusakabe, K.; Morooka, S. *Ind. Eng. Chem. Res.* **1994**, *33*, 616.
- (424) Morooka, S.; Yan, S.; Yokoyama, S.; Kusakabe, K. *Sep. Sci. Technol.* **1995**, *30*, 2877.
- (425) Xomeritakis, G.; Lin, Y. S. *J. Membr. Sci.* **1996**, *120*, 261.
- (426) Xomeritakis, G.; Lin, Y. S. *AIChE J.* **1998**, *44*, 174.
- (427) Uemiya, S.; Kajiwara, M.; Kojima, T. *AIChE J.* **1997**, *43*, 2715.
- (428) Uemiya, S.; Kato, W.; Uyama, A.; Kajiwara, M.; Kojima, T.; Kikuchi, E. *Sep. Purif. Technol.* **2001**, *22–23*, 309.
- (429) Kikuchi, E.; Nemoto, Y.; Kajiwara, M.; Uemiya, S.; Kojima, T. *Catal. Today* **2000**, *56*, 75.
- (430) Yano, M.; Ohno, K.; Imanaka, H. *J. Phys. IV Colloque C5* **1995**, *5*, 1069.
- (431) Daub, K.; Wunder, V. K.; Dittmeyer, R. *Catal. Today* **2001**, *67*, 257.
- (432) Daub, K.; Emig, G.; Chollier, M.-J.; Callant, M.; Dittmeyer, R. *Chem. Eng. Sci.* **1999**, *54*, 1577.
- (433) Dittmeyer, R.; Höllerin, V.; Daub, K. *J. Mol. Catal.* **2001**, *173*, 135.
- (434) Pina, M. P.; Irusta, S.; Menéndez, M.; Santamaría, J.; Hughes, R.; Boag, N. *Ind. Eng. Chem. Res.* **1997**, *36*, 4557.
- (435) De Jong, K. P. *Curr. Opin. Solid State Mater. Sci.* **2001**, *4*, 55.

CR9903508

Utilização de Materiais Carbonáceos, obtidos pelo processo CVD a partir da sílica MCM-41, para a adsorção de etinilestradiol

Luisa E. Milagre (IC)¹, Tatiana A. Ribeiro-Santos (PG)¹, Ana Paula C. Teixeira (PQ)¹, Maria Helena Araujo (PQ)^{1*}

¹Departamento de Química, Universidade Federal de Minas Gerais, UFMG, Belo Horizonte, MG 31270-901, Brasil.

*maria.araujo@pq.cnpq.br

Palavras Chave: MCM-41, CVD, etinilestradiol

Abstract

Utilization of carbonaceous materials, obtained by CVD process using the MCM-41 silica for the ethinylestradiol adsorption

Carbonaceous materials were synthesized from MCM-41 by CVD process and used as adsorbent to etinilestradiol.

Introdução

Os nanotubos de carbono têm sido muito utilizados como componentes de compósitos híbridos, os quais formam a parte hidrofóbica do material e a matriz, que é utilizada na síntese dos mesmos, atuam como a parte hidrofílica. Estes materiais podem ser produzidos por diferentes métodos, mas o processo CVD (*chemical vapor deposition*) está ganhando cada vez mais importância e é considerado o método mais prático e econômico para a produção de nanotubos de carbono em larga escala.^[1,2] Neste trabalho, a MCM-41 foi utilizada como matriz inorgânica e o CTA⁺Br⁻, presente na matriz, como fonte de carbono para a produção de materiais carbonáceos via processo CVD. Em seguida, os materiais sintetizados foram testados na remoção do hormônio 17α-etinilestradiol (EE).

Resultados e Discussão

Para a síntese dos materiais, a MCM-41/CTAB foi impregnada com FeCl₃, para obter 10% de Fe como catalisador. Então o sólido foi tratado termicamente a 600°C em dois meios: apenas com fluxo de N₂ (MCM_N6) e com fluxo de N₂/etanol (MCM_E6). Os materiais obtidos foram caracterizados por análise térmica, espectroscopia Raman (Fig. 1a.), difração de raios X (Fig. 1b.) e microscopia eletrônica de varredura (Fig. 2.). Pela análise térmica, estimou o teor de carbono para as amostras MCM_N6 (11%) e MCM_E6 (16%).

Fig. 1. (a) Espectros Raman **(b)** Difração de raios X dos materiais obtidos pelo processo CVD.

Na Fig. 1a é possível observar que as duas amostras sintetizadas apresentaram bandas típicas

de materiais de carbono: Bandas D e G. A razão I_G/I_D foi maior para o material produzido na presença de etanol o que pode indicar uma maior qualidade do tipo de carbono produzido. Pelos difratogramas, observa-se um pico largo na região de 2θ entre 20° e 30°, que está associada com a sílica amorfa, além de picos em aproximadamente 26°, típica das estruturas de carbono grafítico e picos referentes à fase Fe₃C na região entre 30 – 40°.^[3,4]

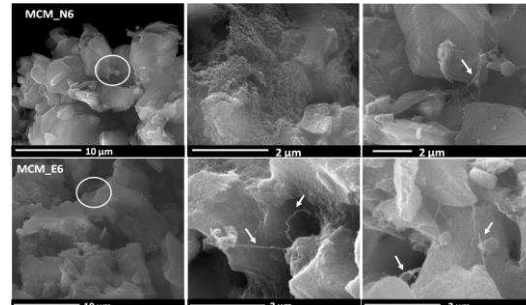


Fig. 2. Microscopia eletrônica de varredura dos materiais obtidos pelo método CVD.

Por meio das imagens de MEV, é possível observar que houve formação de uma superfície rugosa com alguns filamentos de carbono, evidenciando a formação de carbono no material de sílica. Os materiais obtidos, após o processo CVD foram utilizados para a sorção de EE. Para que os materiais MCM_N6 e MCM_E6 atinjam o equilíbrio durante a adsorção do EE, são necessários 90 minutos e suas capacidades de adsorção são aproximadamente 7,0 e 5,0 mg_{EE} g⁻¹, respectivamente.

Conclusões

Os resultados obtidos pelo processo CVD sugerem uma via alternativa para a síntese de materiais carbonáceos, utilizando MCM-41 como matriz inorgânica e o surfactante CTA⁺Br⁻ como fonte de carbono. Além disso, os materiais obtidos podem ser utilizados como adsorventes de contaminantes.

Agradecimentos

CNPq, CAPES, FAPEMIG, Centro de Microscopia

¹ Baddour, C.E. and C. Briens. A Review. International Journal of Chemical Reactor Engineering, **2005**. 3(1).

² Douven, S., et al. Chemical Engineering Journal, **2012**. 188: p. 113-125.

³Dupuis, A.-C. Progress in Materials Science, 2005. **50**(8): p. 929-961.

⁴Rechenberg, H.R., et al.. **226–230, Part 2**: p. 1930-1932.



US 20050150819A1

(19) **United States**

(12) **Patent Application Publication** (10) **Pub. No.: US 2005/0150819 A1**
Wachs (43) **Pub. Date:** **Jul. 14, 2005**

(54) **OXIDATIVE DESULFURIZATION OF
SULFUR-CONTAINING HYDROCARBONS**

(75) Inventor: **Israel E Wachs**, Bridgewater, NJ (US)

Correspondence Address:
BANNER & WITCOFF
1001 G STREET N W
SUITE 1100
WASHINGTON, DC 20001 (US)

(73) Assignee: **LEHIGH UNIVERSITY**, Bethlehem,
PA (US)

(21) Appl. No.: **10/498,362**

(22) PCT Filed: **Dec. 11, 2002**

(86) PCT No.: **PCT/US02/37600**

Related U.S. Application Data

(60) Provisional application No. 60/339,162, filed on Dec.
13, 2001.

Publication Classification

(51) **Int. Cl.⁷** **C10G 27/04**; C10G 29/16

(52) **U.S. Cl.** **208/208 R**; 208/244; 208/243;
208/249

(57) ABSTRACT

A method for desulfurizing a hydrocarbon stream (10) containing heterocyclic sulfur compounds, which process comprises contacting the heterocyclic sulfur compounds in the gas phase (60) in the presence of oxygen (70) with a supported metal oxide catalyst, or with a bulk metal oxide catalyst (600) to convert at least a portion of the heterocyclic sulfur compounds to oxygenated products as well as sulfur-deficient hydrocarbons and separately recovering the oxygenated products separately from a hydrocarbon stream with substantially reduced sulfur.

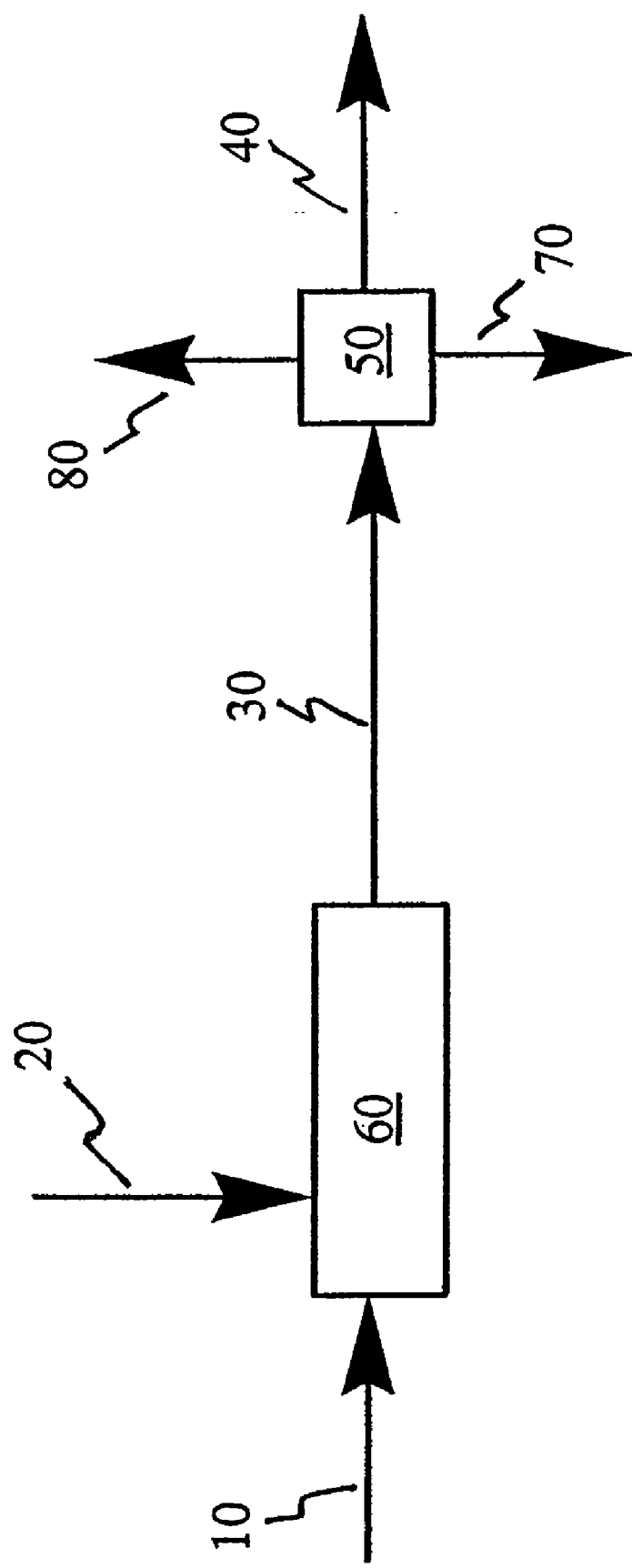


FIGURE 1

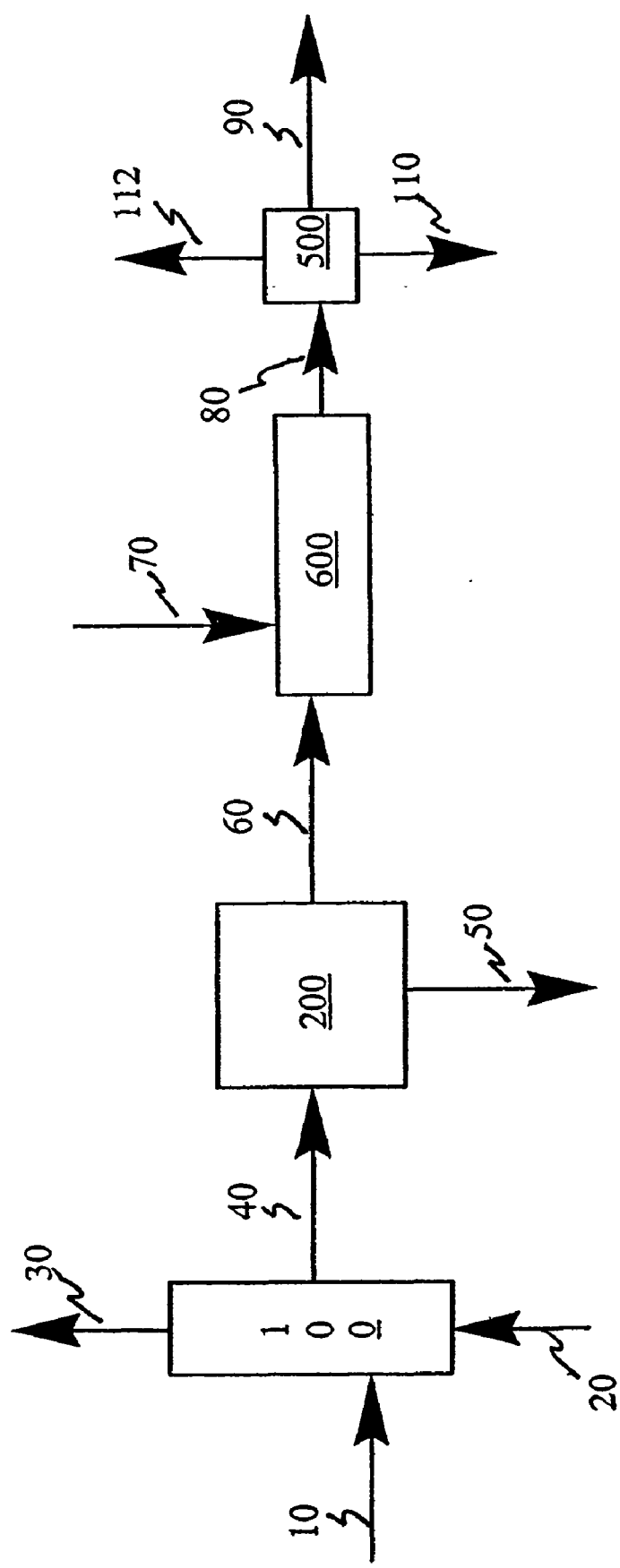


FIGURE 2

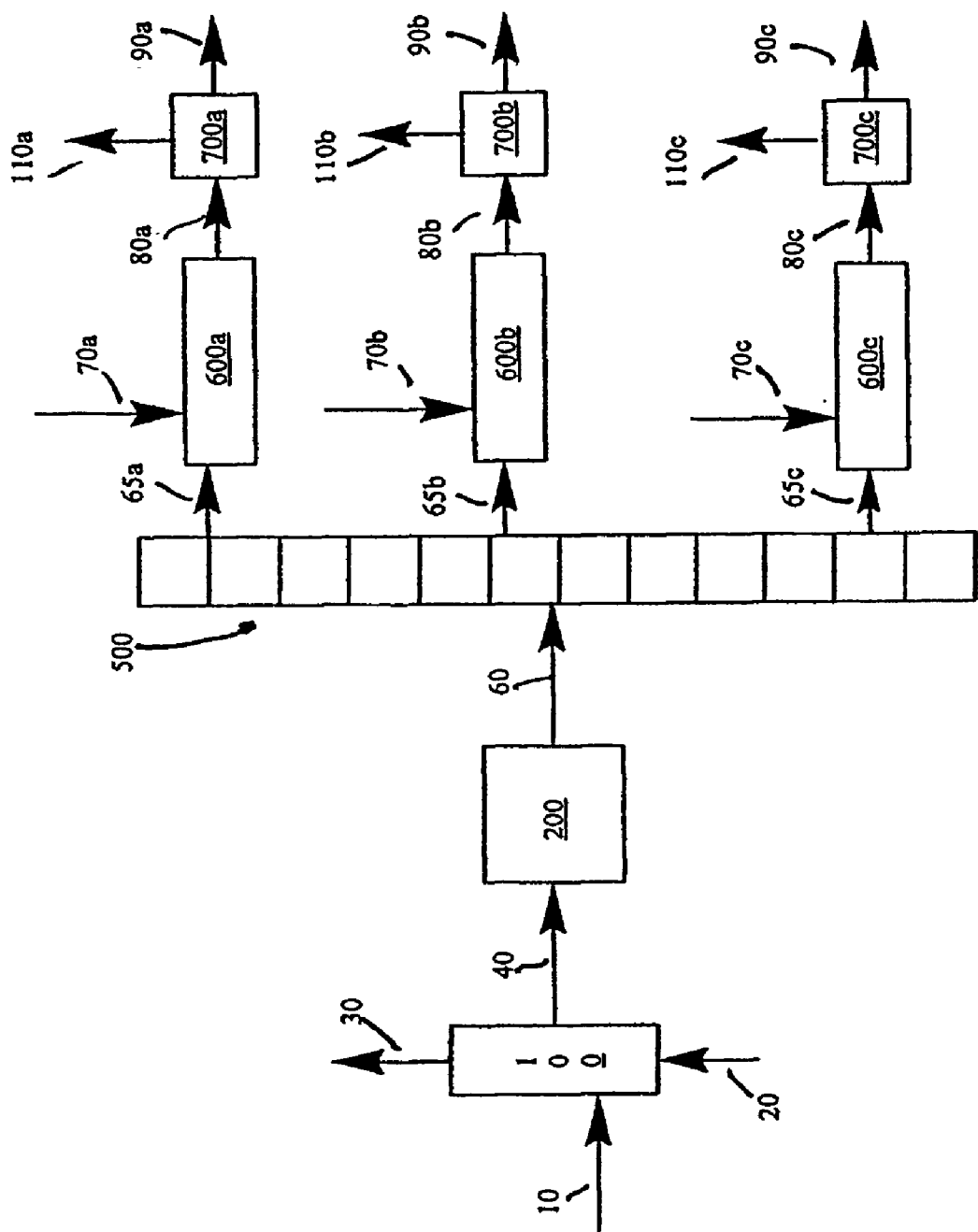
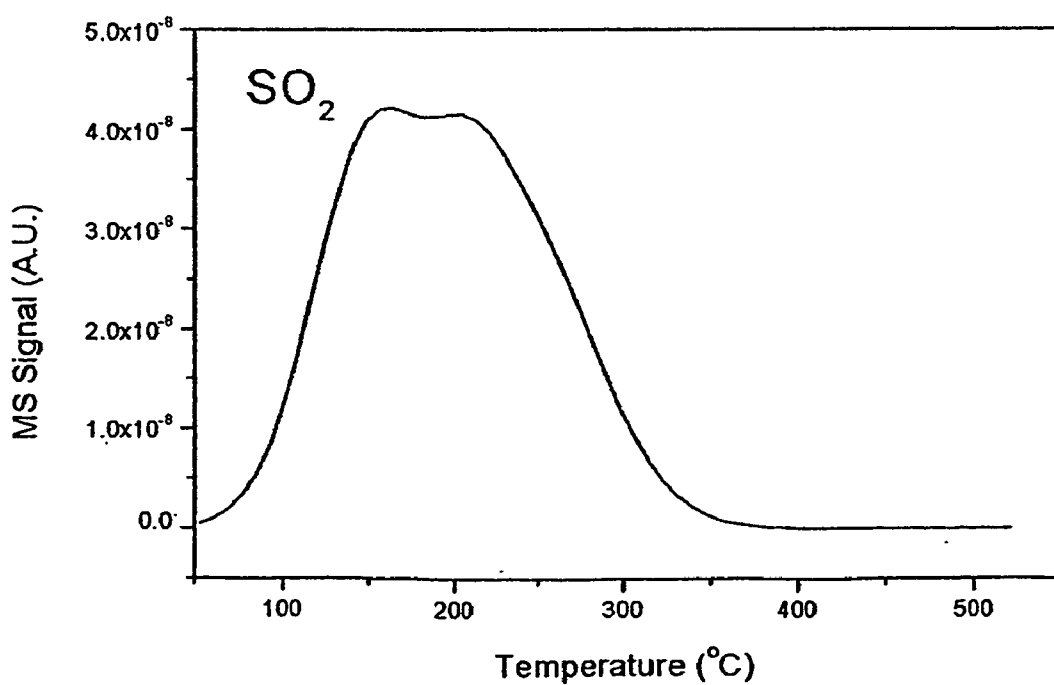
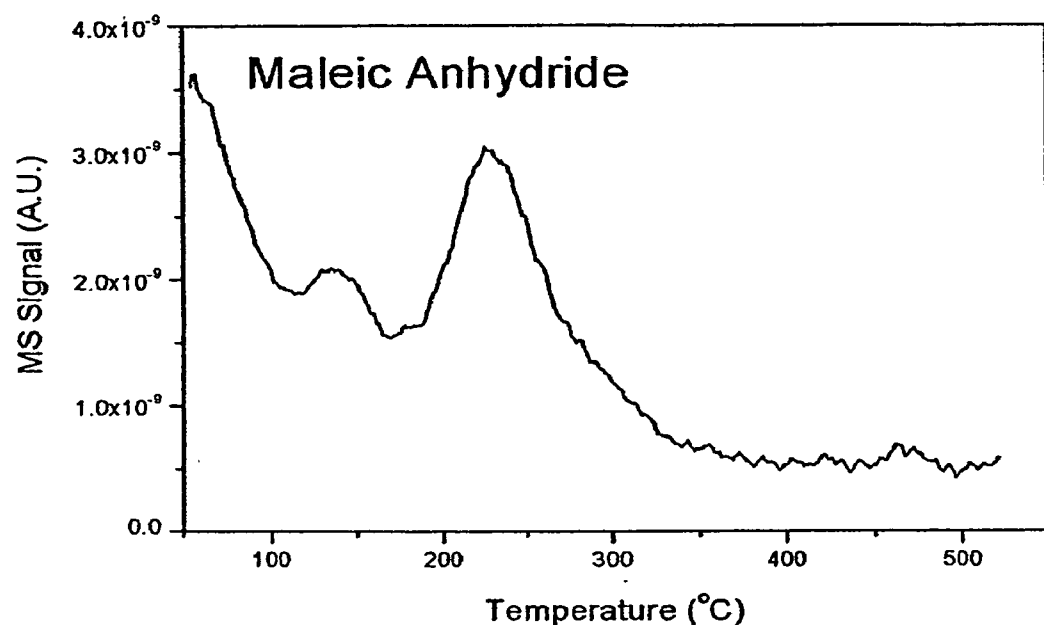
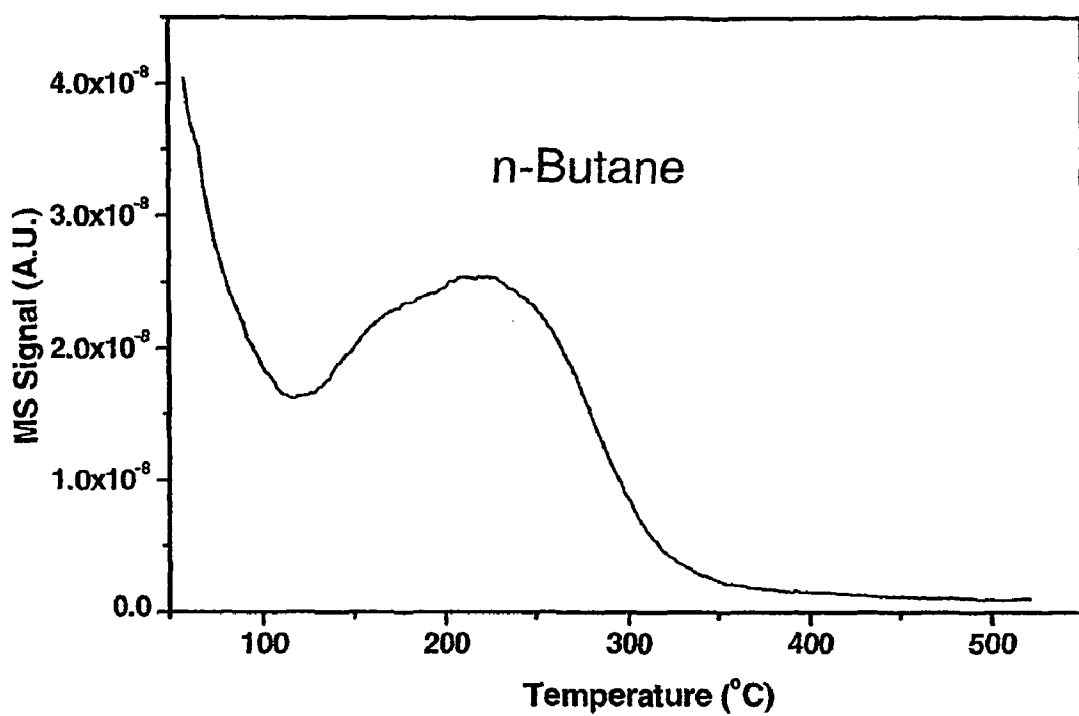


FIGURE 3

FIGURE 4

**TPSR-MS Profiles after Thiophene adsorbed at 50 °C on 5% V₂O₅/TiO₂
(5% O₂/He FLOW)**



**FIGURE 5**

**TPSR-MS Profile after Thiophene adsorbed at 50 °C on 5% V₂O₅/TiO₂
(5% O₂/He FLOW)**

OXIDATIVE DESULFURIZATION OF SULFUR-CONTAINING HYDROCARBONS

CROSS-REFERENCE TO RELATED APPLICATIONS

[0001] This application claims the benefit of U.S. Provisional application Ser. No. 60/339,162.

BACKGROUND OF THE INVENTION

[0002] 1. Field of the Invention

[0003] This invention broadly relates to a process for the removal and subsequent conversion of sulfur compounds found in hydrocarbons, especially refractory sulfur compounds found in petroleum streams (blend stocks) used to make gasoline and diesel fuel, to useful oxygenated hydrocarbon products and sulfur dioxide. Thus, the invention broadly relates to producing a hydrocarbon stream of a lowered sulfur content. The invention particularly relates to a catalytic gas phase oxidation process using a supported metal oxide catalyst or a bulk metal oxide catalyst for treating refractory sulfur compounds found in petroleum streams, such as used to make gasoline and diesel fuel, and converting them to useful oxygenated hydrocarbon products, such as maleic acid (anhydride), phenol, benzyl aldehyde and benzoic acid, and to sulfur dioxide. This method can also be extended to the removal of sulfur typically present in such sulfur containing hydrocarbons as gasoline and diesel fuels to yield sulfur dioxide and sulfur-deficient hydrocarbons.

[0004] 2. Description of Related Art

[0005] Diverse types of petroleum feedstocks and streams contain sulfur compounds whose removal often is indispensable for commercial utilization of the feedstock or stream and/or for subsequent processing of the feedstock. In the face of ever-tightening sulfur specifications in transportation fuels, such as gasoline and diesel fuel, sulfur removal from petroleum feedstocks used to makes such fuels and from the petroleum fuel products themselves will become increasingly more important in years to come. In this regard, there have been several studies by the EPA concluding that the presence of sulfur in gasoline has an adverse impact on catalytic converters and, thus, tailpipe emissions from automobiles.

[0006] Sulfur deactivates conventional three-way Pt/Pd/Rh/Al₂O₃ catalytic converters designed to reduce hydrocarbon, CO and NOx emissions. Sulfur also degrades automobile diagnostic systems. Gasoline sulfur also prevents the introduction of more advanced catalytic technologies, such as Pt/BaO-based catalysts as NOx traps. For diesel fuels, the presence of sulfur produces an additional problem since particulate emissions created during combustion are increased in the presence of sulfur. There is special concern for particulates less than 2.5 microns since the EPA has concluded that there is a stronger link than ever between the tiniest soot particles and thousands of premature deaths each year. Consequently, both the EPA and the DOE have recommended that significantly limiting the level of sulfur in gasoline (15 ppm) and diesel fuels (30 ppm) would be essential for meeting lower vehicle emission standards in the future (by 2007). It is no surprise that substantial efforts have been expended to eliminate sulfur compounds from petroleum products.

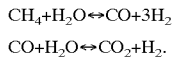
[0007] Sulfur compounds routinely found in petroleum feedstocks and products include thiols (RSH), sulfides (RSR), disulfides (RSSR), saturated cyclic sulfides (C₂-C₅-cyclic sulfur-compounds, which incorporate sulfur into the saturated ring structure), thiophenes (primarily unsaturated C₄-cyclic sulfur compounds, where sulfur is incorporated into the unsaturated ring structure) and thiophene derivatives such as benzothiophene and dibenzothiophene (benzene rings that are fused to the sides of the thiophene (unsaturated C₄-cyclic sulfur compound) and various substituted benzothiophenes and dibenzothiophenes. Sulfur is the most abundant heteroatom impurity in petroleum crude and varies from 0.1 to 5 wt % depending on the geographic origin of the petroleum. After distillation of the crude oil, the sulfur content increases with the fraction's boiling point: naphtha (0.01-0.05% sulfur), kerosene (0.1-0.3% sulfur), gas oil (0.5-1.5% sulfur), atmospheric residue (2.5-5% sulfur), vacuum gas oil (1.5-3% sulfur), and vacuum residue (3-6% sulfur).

[0008] For the low boiling naphtha fraction, sulfur is mainly present as thiols, sulfides, disulfides or thiophene. For the middle boiling kerosene and gas oil fractions and especially the higher boiling fractions, thiophenic compounds, particularly benzothiophenes, dominate.

[0009] As a general rule, simple aliphatic, naphthenic, and aromatic mercaptans, sulfides, di- and polysulfides and the like surrender their sulfur more readily than the class of heterocyclic sulfur compounds comprised of thiophene and its higher homologs and analogs. Within the generic thiophenic class, desulfurization reactivity decreases with increasing molecular structure and complexity. While simple thiophenes represent the more labile sulfur types, the other extreme, sometimes referred to as "hard sulfur" or "refractory sulfur," is represented by the derivatives of benzothiophene and dibenzothiophene, especially those mono- and di-substituted and condensed ring dibenzothiophenes bearing substituents on the carbons beta to the sulfur atom. These highly refractory sulfur heterocycles resist desulfurization.

[0010] Conventional technology removes sulfur from petroleum feedstocks via catalytic hydrodesulfurization (HDS). Hydrodesulfurization is one of the fundamental processes of the refining and petrochemical industries. In HDS, sulfur removal is typically achieved by reaction of the sulfur compounds with hydrogen over non-noble metal sulfides, especially those of Co/Mo/Al₂O₃ and Ni/Mo/Al₂O₃ catalysts, operating at elevated temperatures (~400° C.) and extremely high pressures (~100 atmospheres). Under these somewhat severe reaction conditions, (1) RSH, RSR and RSSR react to form hydrocarbons (RH), (2) saturated cyclic sulfides are converted to alkanes, (3) thiophene reacts largely to mixed isomers of butene (C₄H₈), (4) benzothiophene and its derivatives are initially hydrogenated to thiophane derivatives before removal of the sulfur atom to finally yield ethylbenzene (Bz-CH₂CH₃) and (5) dibenzothiophene is mainly converted to biphenyl with small amounts of phenylcyclohexene. The sulfur itself, along with the H₂, is ultimately converted to hydrogen sulfide. This H₂S is subsequently reacted with O₂ in the Claus process to H₂O and elemental sulfur, which is disposed in special landfills. An overall hydrogen balance for the HDS process reveals that the very valuable and expensive H₂ ultimately gets converted to invaluable H₂O.

[0011] Hydrogen consumption, thus, is an important consideration in these hydrodesulfurization (HDS) reactions because many of the components present in the feedstocks are more valuable as unsaturates, especially aromatics and olefins, and the hydrogenolysis of such components results in the production of light gases with marginal fuel values. In addition, during the manufacture of H₂ a significant amount of global warming CO₂ is generated during the very energy intensive steam reforming of methane, or steam reforming of lower hydrocarbons. The H₂ is typically generated by steam reforming of CH₄, or lower hydrocarbons, and the water-gas shift reaction as follows:



[0012] Thus, the current HDS process technology converts valuable H₂ to invaluable H₂O, reduces the octane of the gasoline feedstocks, generates global warming CO₂ and elemental sulfur that needs to be disposed and is extremely energy intensive.

[0013] Notwithstanding these drawbacks, the petroleum industry has stated that HDS will be the preferred approach they will use to reduce sulfur levels in response to tighter regulatory controls because, HDS is a well-established and proven technology.

[0014] While HDS, as currently practiced, is known to provide nearly complete removal of mercaptans, sulfides and disulfides from liquid hydrocarbons, use of the current designs for reducing the level of thiophenes and other refractory sulfur compounds to a level of 30 ppm or below is problematic. In order to meet this very low level of sulfur, petroleum refiners will have to build additional capacity for generating additional hydrogen and will have to increase the reactor capacities of their HDS units or develop significantly more active HDS catalysts. Furthermore, efforts to drive the current HDS processes to increased sulfur removal is likely to lead to increased hydrogenation of the valuable fuel components and degradation in the fuel value (octane reduction) of the treated petroleum feedstock.

[0015] While HDS remains the predominant commercial approach for desulfurizing petroleum products, particularly petroleum feedstocks for making gasoline, the prior art has continued to develop and examine alternative processes. For example, various oxidative processes are known for removal of mercaptans by converting them to disulfides; such as the Merox™ process (see Handbook of Petroleum Refining Processes, R. A. Meyers, editor-in-chief, chapter 9.1, McGraw-Hill Book Company (1986)). It is also known to remove mercaptans and disulfides from petroleum feedstocks by adsorption with clays. U.S. Pat. No. 5,360,536 uses an adsorbent of a solid solution of metal oxides.

[0016] U.S. Pat. No. 5,935,422 describes a process for removal of organic sulfur compounds, particularly heterocyclic sulfur compounds, from petroleum feedstocks, and especially FCC feedstocks, by adsorption using zeolite Y exchanged with an alkali or alkaline earth metal cation and preferably impregnated with a group VIII metal. Regeneration of the sorbent is achieved by beating the sulfur-laden adsorbent in a hydrogen atmosphere.

[0017] The prior art also is exploring the use of biological removal processes (biodesulfurization). For example, U.S. Pat. No. 6,130,081 relates to a method of degrading organic

sulfur compounds such as benzothiophene, dibenzothiophene and the like, by use of microorganisms belonging to the genus *Paenibacillus* and having the ability to decompose organic sulfur compounds, especially heterocyclic sulfur compounds, by specifically cleaving their C—S bonds under elevated temperature conditions.

[0018] Te et al., "Oxidative reactivities of dibenzothiophenes in polyoxometalate/H₂O₂ and formic acid/H₂O₂ systems," *Applied Catalysts A: General*, 219(2001) 267-280 describes a liquid phase oxidation process potentially useful for removing refractory sulfur compounds from liquid hydrocarbon feed steams. The sulfur compounds are oxidized to sulfones and sulfoxides, which then can be extracted from the hydrocarbon. Other liquid phase oxidative approaches are described in EP 565 324 and U.S. Pat. No. 5,910,440 (biocatalytic).

[0019] I. G. Fedorchenko, N. N. Nechiporenko, V. I. Mitryaeva and E. N. Dubranovskaya, "Catalytic Activity of Certain Metal Oxides in Oxidation of Sulfur Compounds," *Vestn. Khar'kov. Politekh. Inst.* 13 (1966):44-47 describes work involving the oxidation of thiophene over active metal oxides mixed with pumice, 1/4 ratio. Best results were obtained with Fe₂O₃, MoO₃ and Al₂O₃, but the reaction products obtained under the chosen reaction conditions were CO_x, SO₂ and H₂O. A similar combustion study of thiophene was reported by V. A. Sslavinskaaya, D. Kreile, D. Eglite and I. Geimane, "Formation of Carbon Monoxide and Carbon Dioxide in the Vapor-Phase Oxidation of Heterocyclic Compounds on Vanadium-Molybdenum-Phosphorous Catalysts," *Latv. PSR Zinat. Akad. Vestis, Kim. Ser.* 6 (1971): 735-738. These investigators employed a V—Mo—P catalyst.

[0020] Another interesting investigation of thiophene oxidation over a 10% MoO₃ and TiO₂ mixed metal oxide catalyst is reported by M. Blanchard and J. Goichon, "Heterogeneous Catalytic Oxidation of Aromatic Sulfur Compounds: Thiophene and Benzothiophene," *Bull. Soc. Chim. Fr.* 1-2/Pt. 2 (1975): 289-290. The oxidation yielded 75% selectivity towards maleic anhydride and thiomaleic anhydride at moderate conversions. Supported MoO₃/TiO₂ and bulk V₂O₅ were also found to be efficient catalysts for the selective oxidation of thiophene to maleic products. In addition, oxidation of benzothiophene over the 10% MoO₃—TiO₂ catalyst quantitatively yielded phenol with 100% selectivity.

[0021] U.S. Pat. No. 5,969,191 describes a catalytic thermochemical process, which can be used for converting by-products from pulp and paper mills (TRS compounds including mercaptans) to a valuable chemical intermediate (H₂CO), which is consumed in the pulp and paper Industry. A key catalytic reaction step in the thermochemical process scheme is the selective catalytic oxidation of organosulfur compounds (e.g., CH₃SH+2O₂→H₂CO+SO₂+H₂O) over certain supported (mono-layered) metal oxide catalysts. The preferred commercial catalyst employed in this process consists of a specially engineered V₂O₅/TiO₂ catalyst that minimizes the adverse effects of heat and mass transfer limitations that can result in the over oxidation of the desired H₂CO to CO_x and H₂O.

BRIEF DESCRIPTION OF THE DRAWINGS

[0022] FIG. 1 is a schematic drawing of a process of the present invention.

[0023] FIG. 2 is another schematic drawing of a process of the present invention.

[0024] FIG. 3 is still another schematic drawing of a particularly preferred process of the present invention.

[0025] FIG. 4 illustrates the results of Temperature Programmed Surface Reaction-Mass Spectrometry experiments.

[0026] FIG. 5 illustrates another result of the Temperature Programmed Surface Reaction-Mass Spectrometry experiment.

BRIEF DESCRIPTION OF THE INVENTION

[0027] The present invention is directed to a process for removing sulfur compounds found in a hydrocarbon stream, e.g., in a petroleum feedstock or petroleum product, and converting such sulfur compounds, or sulfinyl (=SO) or sulfonyl (=SO₂) derivatives thereof, to sulfur dioxide and to useful oxygenated products as well as sulfur-deficient hydrocarbons by vapor phase oxidative desulfurization of the sulfur compounds, or the sulfinyl (=SO) or sulfonyl (=SO₂) derivatives thereof, removed from such hydrocarbon stream. The sulfur compounds, or sulfinyl (=SO) or sulfonyl (=SO₂) derivatives thereof in the gas phase are contacted with a supported metal oxide catalyst, or with a bulk metal oxide catalyst in the presence of oxygen for a time sufficient to convert at least a portion of the heterocyclic sulfur compounds, or the sulfinyl (=SO) or sulfonyl (=SO₂) derivatives thereof, to oxygenated products and sulfur-deficient hydrocarbons and recovering a hydrocarbon stream with substantially reduced sulfur separately from the oxygenated products. The process not only results in the removal of sulfur compounds from such petroleum feedstocks, such as gasoline and diesel feedstocks, but actually provides for the efficient upgrading of various cyclic sulfur compounds found in these petroleum feedstocks (e.g., C₂-C₅ saturated cyclic-sulfur compounds, thiophenes, benzothiophenes and dibenzothiophenes) to valuable chemical products (C₂-C₅ hydrocarbons and/or oxygenated hydrocarbons, maleic anhydride, phenol, benzoic acid and H₂SO₄ or elemental sulfur). The oxidative desulfurization process thus reduces the sulfur content of hydrocarbon streams without the need for additional hydrogen consumption.

[0028] According to the present invention, the sulfur compound impurities found in a gaseous hydrocarbon feed stream containing such sulfur impurities, especially refractory sulfur compounds such as thiophenes, benzothiophenes, and dibenzothiophenes and their higher boiling derivatives, or the sulfinyl (=SO) or sulfonyl (=SO₂) derivatives thereof, are contacted in the presence of oxygen with a supported metal oxide catalyst. A supported metal oxide catalyst comprises a metal oxide support having supported thereon a layer, preferably only a monolayer, of a catalytic metal oxide. The catalytic metal oxide layer supported by the metal oxide support used in the process of the present invention is typically based on a metal selected from the group consisting of titanium (Ti), zirconium (Zr), molybdenum (Mo), rhenium (Re), vanadium (V), chromium (Cr), tungsten (W), manganese (Mn), niobium (Nb), tantalum (Ta) and mixtures thereof. The metal oxide support for the supported metal oxide catalyst generally is selected from titania (TiO₂), silica (SiO₂), zirconia (ZrO₂), alumina (Al₂O₃), ceria (CeO₂), magnesia (MgO), niobia (Nb₂O₅),

tantala (Ta₂O₅), manganates (MnO_x), lanthanum oxide (La₂O₃), tin oxide (SnO₂) and mixtures thereof. Generally, a support of titania, zirconia, ceria, niobia, tin oxide or their mixture is preferred.

[0029] As a general rule, titanium (Ti), zirconium (Zr), niobium (Nb), tantalum (Ta) and tungsten (W) should not be used as the sole catalytic species with a silica support, nor should the metal oxide support and the supported metal oxide of the catalyst be the same.

[0030] In a generally less preferred alternative embodiment of the present invention, the process also can be carried out using a bulk metal oxide catalyst wherein the bulk metal oxide, and especially the bulk mixed metal oxide, is based on molybdates (Mo), chromates (Cr), vanadates (V), rhenates (Re), titanates (Ti), niobates (Nb), tantalates (Ta), tungstates (W), manganates (Mn) and mixtures thereof. Bulk metal oxide catalysts based on molybdenum, chromium and vanadium are preferred.

[0031] The preferred supported metal oxide catalyst compositions (mono-layered catalysts) and the bulk metal oxide catalyst compositions, useful for practicing the present invention, are known in the prior art, as are their methods of production.

DETAILED DESCRIPTION OF THE INVENTION

[0032] Hydrocarbon feedstocks suitable for treatment using the present invention are those petroleum-based feedstocks, which contain condensed ring sulfur heterocyclic compounds. Such compounds are typically found in petroleum streams boiling in the distillate range and higher. Non-limiting examples of such feedstocks include a catalytically cracked gasoline stream (e.g., cracked naphtha), generally from a fluid catalytic cracker (FCC gasoline) or thermal catalytic cracker (TCC), a heavy straight run gasoline stream, generally obtained by atmospheric distillation of a crude, an aromatic saturated gasoline stream, diesel fuels and jet fuels. Such feeds typically have a boiling range from about 150 to about 600° C., usually from about 175 to about 400° C. In the broad practice of this invention, any hydrocarbon stream containing refractory sulfur compounds can be treated, since their boiling point temperatures at atmospheric pressure are: thiophene (84° C.), 2,5-dimethylthiophene (134° C.), 1-benzothiophene (222° C.), dibenzothiophene (333° C.), 4-methyldibenzothiophene (298° C.) and 4,6-dimethyldibenzothiophene (estimated to be ~250-380° C.).

[0033] There is a well-established hierarchy in the ease of sulfur removal from the various organo-sulfur compounds common to petroleum streams. Simple aliphatic mercaptans, naphthenic mercaptans, and aromatic mercaptans, sulfides, di-sulfides and polysulfides and the like generally surrender their sulfur content more readily than the class of heterocyclic sulfur compounds comprised of thiophene and its higher homologs and analogs. Within the generic thiophenic class, desulfurization reactivity also decreases with increasing molecular structure and complexity. While simple thiophenes represent the more labile sulfur types in this class, the other extreme, which is sometimes referred to as "hard sulfur" or "refractory sulfur," is represented by the derivatives of benzothiophene and dibenzothiophene, especially those mono-substituted and di-substituted and con-

densed ring dibenzothiophenes. An example of a typical three-ring "hard" sulfur compound found in petroleum streams is 4,6-dimethylbenzothiophene, or 4,6-DMDBT for short. These highly refractory sulfur heterocycles resist desulfurization as a consequence of steric inhibition. For this reason, these materials often survive traditional desulfurization processes, e.g. hydrodesulfurization, and remain in the hydrocarbon stream as a potential poison for subsequent processes whose operability is dependent upon a sulfur sensitive catalyst. Destruction of these "hard sulfur" types can be accomplished under relatively severe process conditions in HDS, but this is undesirable owing to the onset of harmful side reactions leading to feed and/or product degradation and excessive hydrogen consumption.

[0034] While the desulfurization process of the present invention is potentially applicable to all sulfur bearing compounds common to petroleum streams, it is particularly suitable for the oxidative desulfurization of the least reactive, more highly refractory sulfur species, such as those derived from thiophenes, benzothiophenes and dibenzothiophenes. As used throughout the specification and claims, therefore, the term "refractory sulfur" and similar terms is intended to embrace thiophene, benzothiophene, dibenzothiophene, and the higher boiling derivatives of these sulfur compounds. In addition, to these sulfur compounds, the present invention also embraces the sulfinyl ($=\text{SO}$) or sulfonyl ($=\text{SO}_2$) derivatives of thiophene, benzothiophene, dibenzothiophene, and their higher boiling derivatives.

[0035] The process of the present invention generally will result in a hydrocarbon stream with substantially reduced sulfur, a sulfur dioxide stream and separate streams of oxygenated hydrocarbon products. For purposes of this invention, the term, "substantially reduced sulfur", depends upon the overall process being considered, but can be defined as a sulfur content less than about 100 wppm, preferably less than about 50 wppm, more preferably less than about 30 wppm, and most preferably less than about 10 wppm as measured by existing, conventional analytical technology.

[0036] In accordance with the present invention, and with reference to FIG. 1, a sulfur-containing hydrocarbon gas stream **10**, preferably containing and enriched amount of refractory sulfur compounds such as thiophene, benzothiophene, dibenzothiophene and their higher boiling derivatives, is introduced into a reactor **60**. The level of such sulfur compounds can be enriched in such steam using known techniques of absorption, adsorption, extraction and the like. Air or an oxygen-enriched gas generally is added via stream **20** to establish oxidizing conditions in reactor **60**. Reactor **60** contains a supported metal oxide catalyst (preferably mono-layered), or a bulk metal oxide catalyst, in a form suitable for conducting the oxidation reactions. The selective oxidation that occurs in reactor **60** produces a gas stream containing the oxygenated hydrocarbon products, sulfur dioxide, H_2O , CO_x and unreacted hydrocarbons and sulfur compounds, which exits reactor **60** in gas stream **30**. The oxygenated products may include maleic anhydride, phenol, benzyl aldehyde, benzoic acid and the like depending upon the nature of the sulfur compounds in gas stream **10**.

[0037] As noted, the oxidizing agent used in the selective oxidation can usually be oxygen or air. The contacting of

the, sulfur-containing hydrocarbon gas stream with the supported metal oxide catalyst or bulk metal oxide catalyst under an oxidizing atmosphere, e.g., in the presence of oxygen, and at an appropriate temperature, causes a selective oxidation of the sulfur compounds to the valuable oxygenated products and sulfur deficient hydrocarbons.

[0038] The optimum reaction time in reaction zone **60** (space velocity) varies with temperature, pressure and the molar ratio of the reactants. The space velocity likely will be maintained below about 4800 V/V/hr. As a general rule, higher conversions are associated with lower space velocities, e.g., a space velocity of 5 to 200 volume of gas (STP) per volume of catalyst per hour. In the broad practice of the invention, space velocities of up to 2000 volumes of gas (STP) per volume of catalyst per hour are generally contemplated.

[0039] A variety of oxygenated species, such as maleic anhydride, phenol, benzyl aldehyde and benzoic acid, are the intended products of the present process and can be recovered from the gaseous reaction product via stream **40**, separate from byproduct SO_2 and the CO_x via stream **80** and separate from unreacted (sulfur depleted) hydrocarbons and unconverted sulfur-containing compounds via stream **70**, using any one of a number of separation options (zone **50**) known to those skilled in the art.

[0040] The selectivity of the oxidation of the organosulfur compounds to the valuable oxygenated products and the sulfur-deficient hydrocarbons has its origin in the preferential attack of oxygen at the C—S bonds of the organosulfur compounds, in the vicinity of the catalytic surface sites, because of the weak C—S bonds relative to strong C—O bonds. The nature of the products resulting from the gas phase oxidation suggests that the initial oxygen atoms are attached to the carbon atoms adjacent to the sulfur atom and that the thiomaleic anhydride can be completely converted to maleic anhydride at conversions approaching 100%. Over-oxidation of maleic anhydride to CO_x and H_2O should not be a significant problem since anhydrides are known to be relatively stable (especially compared to the reactive C—S—C bond in thiomaleic anhydride).

[0041] Maleic anhydride, expected to be produced by the selective oxidation of thiophene and some of the higher refractory sulfur compounds, is an important chemical intermediate that is currently produced by selective oxidation of n-butane over bulk VPO catalysts, with annual production ~2 billion pounds. Phenol, another of the expected products from the selective oxidation of benzothiophene, ranks third among the secondary products of benzene, one of the world's ten top bulk organic chemicals, and annual synthetic phenol production is ~5 billion pounds. The current technology to synthesize phenol from benzene is very complicated and consumes much energy and produces significant waste by-products. For example, phenol production via the classical benzenesulfonic acid process yields 1.35 pounds of Na_2SO_3 and 2.1 pounds Na_2SO_4 as by-products for every pound of phenol. Moreover, a three-stage distillation is required for phenol purification. The present process, thus provides a useful alternative source of this valuable chemical. Benzyl aldehyde, benzoic acid and maleic anhydride may also form from benzothiophene.

[0042] Saturated cyclic sulfides are expected to be converted to dialdehydes and glycols (via hydrogenation),

which also are valuable chemical intermediates. Of special interest is the saturated C₂ cyclic sulfide, which should be oxidized to C₂-dialdehyde and can be hydrogenated to ethylene glycol, ~7 billion pounds annual production. The saturated C₅ cyclic sulfide also is expected to be oxidized to maleic anhydride since n-pentane is oxidized to maleic anhydride.

[0043] As will be recognized by those skilled in the art, the gas stream 30 leaving the reactor will contain the hydrocarbon feedstock and may contain unreacted sulfur compounds, as well as the oxygenated products, sulfur dioxide, carbon oxides and water. Principal by-products of the oxidative desulfurization that may be formed are carbon monoxide, which may be accompanied by carbon dioxide (possibly in a minor amount) and sulfur dioxide. COS may also be a minor product.

[0044] The reaction mixture leaving the reactor 60 in gas stream 30 is generally subject to further processing in zone 50 in a conventional manner. For example, a concentrated stream of the oxygenated products 40 can be recovered in a washer, or by indirect cooling, or also by fractional cooling. For example, the washing can be performed with an aqueous stream, in which case a multi-stage washer can be used. An aqueous stream 40 containing the oxygenated products can be obtained in this manner separate from the sulfur dioxide and carbon oxides in stream 80. An advantage of the vapor-phase route is the ease with which SO₂ and CO_x can be separated from the reaction products because of their very high vapor pressure and any residual SO₂ can be readily removed with an ion exchange column. With judicious selection of metal oxide catalyst, the sulfur-containing compounds that are typically present in petroleum feedstocks and other petroleum products are expected to be selectively oxidized to valuable chemical intermediates or sulfur-deficient hydrocarbons.

[0045] The sulfur dioxide can be disposed of by any technique known in the art. For example, the sulfur oxide (from stream 80) can be oxidized and converted to sulfuric acid. The sulfuric acid can then be used directly in the petroleum refinery for purposes well known to those skilled in the art. The crude stream 40 of the oxygenated products then can be treated, such as by distillation, for recovering a purified stream of, for example, maleic anhydride and other oxygenated species. Fractional condensation also can be used to obtain a desired oxygenated product. Other ways for individually isolating the oxygenated products will be apparent to those skilled in this art. The residual gas 80, likely containing carbon monoxide as well, may be treated (so as to recover sulfur oxides). The remaining fraction in stream 70 containing the original hydrocarbon fraction and any unreacted sulfur compounds can be recycled to the oxidative desulfurization reactor 60 (not shown) following any heating that may be needed to convert the stream into a gas, or may be sufficiently low in sulfur to be returned to the refinery for use as a gasoline feed stock.

[0046] For obtaining higher yields and selectivities, the conditions of the oxidative desulfurization can be varied. For example, the pressure, temperature, composition of the starting gas mixture, the amount of catalyst and/or the rate of flow can be varied. The reactor effluent remaining after separation of the oxygenated products and by-products can then be recycled (not shown) into the reactor 60.

[0047] A key feature of the present invention is the use of a heterogeneous gas phase reaction conducted in the presence of certain metal oxide supported catalysts (preferably mono-layered catalysts), or bulk metal oxide catalysts, between the sulfur compounds and oxygen. The metal oxide of the supported metal oxide catalyst is accommodated in the support primarily as a two-dimensional metal oxide overlayer (preferably a mono-layer), with the oxide having a non-crystalline form. Supported metal oxide catalysts useful in the process of this invention generally comprise a metal oxide substrate, or support, such as titania, silica, zirconia, alumina, niobia, tantalum, ceria, magnesia, manganese, lanthanum oxide, tin oxide and mixtures thereof, whose surface has been modified with a layer (preferably no more than a monolayer) of an oxide of a catalytic metal or a mixture of catalytic metal oxides as identified above (e.g., preferably an oxide of vanadium, and oxide mixtures containing vanadium) in an amount such that the catalyst exhibits properties different from the metal oxide substrate whose surface has not been modified. The support and the supported metal should not be the same.

[0048] Consequently, in this preferred embodiment of the invention, the metal oxide loading (preferably vanadium oxide) on the metal oxide support or substrate, e.g., a titania support, must be sufficient to modify the metal oxide surface. The metal oxide loading on the metal oxide support or substrate broadly ranges between about 0.5 to 35 wt % of the total catalyst weight.

[0049] The preferred vanadia (vanadium oxide) on titania, supported metal oxide catalyst used in this process has at least a portion, preferably at least about 25 wt %, and most preferably substantially all of said supported vanadium oxide in a non-crystalline form.

[0050] A preferred metal oxide support for use in the process of this invention is titania (titanium dioxide), which can be employed in the anatase or rutile form. For example at least about 25 wt % (and generally from about 50 to about 100 wt %) of the titanium dioxide (TiO₂) can be in the anatase form. As recognized by those skilled in the catalytic art, the titania support material needs to be judiciously evaluated since certain grades may have impurities that interfere with the catalytic activity. Normally, with recognition of the previous caveat, the titanium dioxide may be prepared by any conventional technique. The titanium dioxide used in the catalyst of this invention may be composed of substantially porous particles of a diameter of from about 0.4 to about 0.7 micron and preferably has a specific surface area of at least about 1 m²/g, more usually at least about 5 m²/g, preferably at least about 40 m²/mg and sometimes at least about 100 m²/g.

[0051] The metal oxide supported catalysts used in the process of this invention may be prepared by impregnation techniques well-known in the art, such as incipient wetness, grafting, equilibrium adsorption, vapor deposition, thermal spreading, etc. When using an incipient wetness impregnation technique, an aqueous or non-aqueous solution containing a metal oxide precursor compound is contacted with the metal oxide support or substrate material, e.g., titania, for a time sufficient to deposit a metal oxide precursor material onto the support such as by selective adsorption or alternatively, excess solvent may be evaporated leaving behind the precursor compound or salt. If an incipient wetness impreg-

nation technique is used to prepare a catalyst of this invention, the metal oxide precursor (e.g., salt) solution used may be aqueous or organic, the only requirement being that an adequate amount of a precursor compound for the selected metal oxide be soluble in the solvent used in preparing this solution. Other impregnation techniques, such as vapor deposition and thermal spreading, do not require use of a solvent as does incipient wetness, and may be desirable in some circumstances to avoid the problem of volatile organic carbon (VOC) emissions.

[0052] One way to disperse vanadium oxide, tungsten oxide or a combination of the two oxides onto a titania metal oxide support or substrate is to impregnate titania spheres or powder (spheres or powder are used as representative examples of shapes of titania) with a solution containing a vanadium or a tungsten compound. When impregnating a substrate with both oxides, the tungsten and vanadium are introduced in a stepwise manner, tungsten first, followed by vanadium, with appropriate intermediate drying and calcining steps. Each solution may be an aqueous solution, one using an organic solvent or a mixture of the two. Generally, an aqueous solution is preferred. Criteria used to choose the vanadium and tungsten compounds include whether the compounds are soluble in the desired solvent and whether the compounds decompose at an acceptable rate at a high, calcination temperature to give the appropriate metal oxide overlayer. Illustrative of suitable compounds of vanadium and tungsten are the halides of vanadium and tungsten, oxyacids, oxyacid salts and oxysalts of vanadium and tungsten. Specific examples or precursors are tungsten dibromide, tungsten pentabromide, tungsten tetrachloride, tungsten dioxydichloride, tungstic acid, ammonium metatungstate, vanadium tribromide, vanadium dichloride, vanadium trichloride, vanadium oxychloride, vanadium oxydichloride, vanadic acid, vanadyl sulfate, vanadium alkoxides, vanadium oxalate (which may be formed in situ by reaction of V_2O_5 and an aqueous solution of oxalic acid), and ammonium meta-vanadate. Suitable metal oxide precursor compounds for the other metal species suitable for making the supported metal oxide catalysts of this invention are well recognized by those skilled in the catalysis art.

[0053] The impregnation of the metal oxide support or substrate, e.g., titania support in the form of spheres or powder, with the metal oxide precursor compound solution may be carried out, as noted above, in ways well known in the art using either wet or dry impregnation techniques. One convenient method is to place the metal oxide support or substrate, e.g., titania particles, into a rotary evaporator, which is equipped with a steam jacket. An impregnating solution of a precursor compound which contains an amount of the desired metal to be included in the finished catalyst (as the metal oxide) is added to the support particles and the mixture is cold rolled (no steam) for a time from about 10 to 60 minutes sufficient to impregnate the support with the precursor compound solution. Next, steam is introduced and the solvent is evaporated from the impregnated solution. This usually takes from about 1 to about 4 hours. The impregnated support will normally be dried at temperatures ranging from about 50°-300° C. to remove excess solvent.

[0054] Water-soluble precursor compounds are generally preferred for industrial applications because of the environmental concern about VOC emissions. Nonetheless, when using an organic solvent, initial heating may be done in a

nitrogen atmosphere to remove any flammable solvent. Finally, the support particles are removed from the rotary evaporator and calcined in a suitable oxidizing atmosphere such as air, oxygen, etc. at a temperature of about 150° to 800° C., and more usually from 400°-600° C., preferably for about 1 to about 3 hours, sufficient to decompose the precursor compound to the corresponding metal oxide. In other cases, as recognized by those skilled in the art, calcining conditions need to be adjusted to avoid undesirably reducing the surface area of the metal oxide support.

[0055] Because some precursor compounds are air/moisture sensitive, they are prepared under a nitrogen atmosphere as is recognized by those skilled in this art. The time required to calcine the composite will, of course, depend on the temperature and in general will range from about 0.5-7 hours. Calcination at 450° C. for about 2 hours has proven to be suitable for 1% vanadia on titania catalysts. The precise time and temperature for calcination depends on the particular metal oxide overlayer and should be selected, as well-recognized by those skilled in the art, to avoid adversely affecting the metal oxide support, e.g. in the case of a titania metal oxide support, to avoid substantial crystal phase transformation of the anatase into another crystalline form, e.g., rutile, and degradation of extended surface area.

[0056] Reducing atmospheres may also be used to decompose the transition metal oxide precursors. To avoid potential safety concerns, the resulting composite should be calcined to convert the reduced metal component to the oxide form. If the support is to be provided with an overlayer of a combination of metal oxides, e.g., if an overlayer containing both vanadium oxide and tungsten oxide is desired, then the metal oxide precursor compounds may be impregnated on the metal oxide support simultaneously, but preferably are impregnated sequentially. The metal oxide supported catalysts used in the process of this invention will generally have surface metal oxide loadings of from about 0.5 to 35 wt. % metal oxide based on the total active catalyst composition, preferably from about 1 to 20 wt. %, more usually from about 1-15 wt. %, and most preferably 1-10 wt. % based on the total active catalyst composition. The intent, generally, is to provide no more than a monolayer of the catalytic oxide overlayer on the metal oxide support.

[0057] Titania, silica, zirconia, alumina, niobia, tantalum, ceria, magnesia, manganates, lanthanum oxide and tin oxide are conveniently referred to as supports or substrates in the description of the preferred embodiment of the present invention, based to a large degree on the way the catalyst is prepared. Nonetheless, it should be noted that these metal oxides also provide important roles as active catalytic components in the supported metal oxide catalyst. Combination supports may also be advantageous for use in catalysts suitable for practicing the process of this invention. For example, substrates constituting a mixture of titania and zirconia, or titania and silica can be used.

[0058] Further details on the preparation and structure of such metal oxide supported catalysts useful in the practice of the present invention can be found, inter alia, in Jehng et al., *Applied Catalysis A*, 83, (1992) 179-200; Kim and Wachs, *Journal of Catalysis*, 142, 166-171; Jehng and Wachs, *Catalysis Today*, 16, (1993) 417-426; Kim and Wachs, *Journal of Catalysis*, 141, (1993) 419-429; Deo et al., *Applied Catalysis A*, 91, (1992) 27-42; Deo and Wachs,

Journal of Catalysis, 146, (1994) 323-334; Deo and Wachs, *Journal of Catalysis*, 146, (1994) 335-345; Jehng et al., *J. Chem. Soc. Faraday Trans.*, 91(5), (1995) 953-961; Kim et al. *Journal of Catalysis*, 146, (1994) 268-277; Banares et al., *Journal of Catalysis*, 150, (1994) 407-420 and Jehng and Wachs, *Catalyst Letters*, 13, (1992) 9-20, the disclosures of which are incorporated herein by reference.

[0059] For the supported metal oxide catalyst, the preferred vanadium oxide may preferably be used in mixture with an oxide of one of molybdenum (Mo), tungsten (W), chromium (Cr), rhenium (Re), and manganese (Mn), supported on titania or silica. In the case of a vanadia on silica catalyst, an adjuvant selected from the group consisting of an oxide of titanium, zirconium, cerium, tin, niobium and tantalum, should generally be present to enhance catalytic activity. A particularly preferred supported metal oxide catalyst is one comprising a vanadia overlayer (monolayer) on a titania support.

[0060] It often is desired that the metal oxide support, such as titania, silica, zirconia, alumina, niobia, tantalum, magnesia, ceria, manganates, lanthanum oxide, tin oxide, and their mixtures, used as a catalyst support component in accordance with the present invention have a surface area in the range of about 1 to about 150 m²/g and higher. These materials may be used in any configuration, shape or size, which exposes their surface and any metal oxide overlayer dispersed thereon, to the gaseous stream passed in contact therewith. For example, these oxide supports, such as titania can conveniently be employed in a particulate form or deposited (before or after impregnation with the metal oxide overlayer) on a monolithic carrier or onto ceramic rings or pellets. As particles, the support, such as titania, can be formed in the shape of pills, pellets, granules, rings, spheres and the like. Use of free particulates might be desirable when large catalyst volumes are needed or if the catalyst bed is operated in a fluidized state. A monolithic form, or deposition of the active catalyst on an inert ceramic support might be preferred in applications where catalyst movement is to be avoided because of concerns about catalyst attrition and dusting, and a possible increase in pressure drop across a particulate catalyst bed. In a preferred approach, a metal oxide supported catalyst, such as a vanadia on titania catalyst, may be deposited on a ceramic carrier such as silicon carbide, silicon nitride, carborundum steatite, alumina and the like, provided in the shape of rings or pellets. Typically, the active catalyst will be applied to the inert ceramic support in an amount to provide 1 to 15% by weight of the supported catalyst.

[0061] As noted, the present invention also contemplates the use of bulk metal oxides as the catalyst for converting petroleum sulfur compounds into oxygenated products. Such bulk metal oxide catalysts generally constitute molybdates (Mo), chromates (Cr), vanadates (V), rhenates (Re), titanates (Ti), niobates (Nb), tantalates (Ta), tungstates (W), manganates (Mn) and mixtures thereof. Such metal oxides also contain a wide variety of other metal species such as alkali metals (e.g., sodium (Na), lithium (Li), potassium (K) and cesium (Cs)), alkaline earth metals (e.g., calcium (Ca), barium (Ba), and magnesium (Mg)) and transition metals (e.g., copper (Cu), nickel (Ni), cobalt (Co), aluminum (Al), lead (Pb), bismuth (Bi), iron (Fe), zinc (Zn), cadmium (Cd),

tellurium (Te), manganese (Mn)). Those skilled in the art recognize the wide variety of available bulk metal oxide catalysts.

[0062] Methods for making bulk metal oxide catalysts used in the present invention also are well known to those skilled in the art. In particular, the active catalyst can be prepared by physically blending the metal oxides, by coprecipitation from aqueous solutions containing soluble compounds of the catalyst components in the desired molar ratio or by any other technique, which provides an intimate mixture of the metal oxide constituents. For example, an aqueous solution of a water-soluble molybdenum compound (ammonium heptamolybdate) is mixed with a water-soluble iron compound (ferric chloride) to cause coprecipitation of both molybdenum and iron, using procedures well known to those skilled in the art. The coprecipitate is washed, to eliminate the soluble salts formed during the coprecipitation reactions, filtered, dried and calcined to convert the metal constituents to their active iron molybdate (oxide) form. Those skilled in the art recognize a variety of water-soluble metal compounds that can be used to prepare the active bulk metal catalyst. Alternatively, oxides of the respective metals may be ground together and calcined. Additional details on bulk metal oxides and bulk metal oxide catalysis can be found in Arora et al., *Journals of Catalysis*, 159, (1996) 1-13, which is incorporated herein by reference.

[0063] Those skilled in the art recognize that there exists a wide range of compounds, generally used in admixture, suitable for preparing bulk metal oxide catalysts. The following is a representative, though not exhaustive, list of possible constituents: bulk vanadates such as PbV₂O₆, NaVO₃, Na₃VO₄, BiVO₄ and other Bi—V—O family members, AlVO₄, FeVO₄, Mg₃(VO₄)₂, Mg₂V₂O₇, CeVO₄, Zn₃(VO₄)₂, CdV₂O₇, Zn₂V₂O₇, VOPO₄ and other V—P—O family members, KVO₃, Pb₂V₂O₇, and TiVO₄; bulk molybdates such as PbMoO₄, CaMoO₄, Bi₂Mo₂O₉, Bi₃(FeO₄)(MoO₄)₃ and other Bi—Mo—O family members, Na₂MoO₄, MnMoO₄, Gd₂(MoO₄)₃, MgMoO₄, CuMoO₄, CoMoO₄, Fe₂(MoO₄)₃, Te₂MoO₇, NiMoO₄, Al₂(MoO₄)₃, Cr₂(MoO₄)₃, and Na₂Mo₂O₇; bulk niobates such as YNbO₄, YbNbO₄, LiNbO₃, NaNbO₃, KNbO₃, AlNbO₄, K₈Nb₆O₁₉, BiNbO₄, and other Bi—Nb—O family members, SbNbO₄, NbOPO₄, CaNb₂O₆, K₁Nb₆O₁₇, and KCa₂Nb₃O₁₀; bulk tungstates such as Li₆WO₆, FeWO₄, CoWO₄, MnWO₄, NiWO₄, CuWO₄, CaWO₄, Cs₂WO₄, Na₂WO₄, B_aWO₄, Fe₂(WO₄)₃, Al₂(WO₄)₃, SrWO₄, K₂WO₄, Na₂W₂O₇, Li₂WO₄, CsLuW₂O₈, BiWO₄, and other Bi—W—O family members; bulk chromates such as Na₂CrO₄, Na₂Cr₂O₇, Na₂Cr₃O₁₀, Na₂Cr₄O₁₃, K₂CrO₄, K₂Cr₂O₇, K₂Cr₃O₁₀, K₂Cr₄O₁₃, Fe₂(CrO₄)₃, CaCrO₄, Cs₂CrO₄; BiCrO₄ and other Bi—Cr—O family members; bulk rhenates such as NaReO₄, Li₆ReO₄, and Mg(ReO₄)₂; bulk titanates such as Na₂TiO₄, NaTiO₃, BaTiO₄, BaTiO₃, and other Ba—Ti—O as well as Bi—Ti—O family members and bulk manganates such as Mn₃(VO₄)₂, MnAl₂O₄, KMnO₄, MnO, MnO₂, Mn₂O₃, and Mn₃O₄.

[0064] To achieve high selectivity in the conversion of the petroleum sulfur compounds to the oxygenated compounds, it is important to maintain the flow rate of reactant gas per unit mass of catalyst in the range of 10⁻² to 10⁴ cubic centimeters (STP) of reactants per gram of active catalyst per minute (excluding inert ceramic components or other inert support material). Generally, higher reaction tempera-

tures permit higher flow rates. Usually, the process can be operated at 10^{-1} to 10^2 , cubic centimeters (STP) of reactants per gram of catalyst per minute.

[0065] The oxidation reaction involving the noted refractory sulfur compounds is exothermic. As recognized by those skilled in the art a variety of reactor designs may be employed, such as a tubular reactor, to accommodate the necessary mass and heat transfer processes for effective operation on a continuous basis, semi-continuous or batch basis. Packed catalyst beds and fluid bed operation are contemplated as possible embodiments. The oxidation reaction may be conducted at atmosphere pressure, and above or below atmospheric pressure.

[0066] Among the aromatic heterocyclic sulfur compounds of particular interest in this application are thiophene, 2-methylthiophene, 3-methylthiophene, 2-ethylthiophene, benzothiophene, and dimethylbenzothiophene, as well as higher boiling derivatives. Mercaptans which can also be removed by the process of this invention often contain from 3-10 carbon atoms, and are illustrated by materials such as 1-mercaptopropane, 2-mercaptopropane, 1-mercaptopentane, 2-mercaptopentane, 2-methyl-2-mercaptopropane, mercaptopentanes, mercaptohexanes, mercaptoheptanes, mercaptooctanes, mercaptononanes, and mercaptoodecane. The total sulfur content in hydrocarbon feedstocks usually is in the range from about 150 ppm to as much as several thousand ppm and higher. Indeed, hydrocarbon streams containing as much as 5% sulfur are often encountered. After treatment according to the invention the sulfur content of the hydrocarbon stream is desirably no more than about 100 ppm, and more desirably under about 50 ppm.

[0067] In another embodiment of the invention, the hydrocarbon stream, containing the organo-sulfur compounds may first be treated to reduce its sulfur content using an alternative technology, as shown in FIG. 2, before employing the oxidative desulfurization of the present invention. The stream may be treated to reduce its sulfur content preferably to less than about 1,000 ppm, more preferably to less than about 500 ppm, and most preferably to less than about 200 ppm before subjecting the hydrocarbon to the oxidative desulfurization of the present invention. It may be advantageous for the refiner to upgrade the sulfur-containing petroleum feedstocks before treatment using the present invention by first removing as much as possible of the easy-to-remove sulfur using conventional processes such as HDS.

[0068] In accordance with this embodiment of the present invention, and with reference to FIG. 2, a sulfur-containing hydrocarbon gas stream 10 containing organo-sulfur compounds is first treated using an alternative sulfur removal system, such as conventional HDS, in treatment zone 100. As recognized by those skilled in the art, when using HDS the sulfur-containing petroleum feedstock is treated with a stream of hydrogen (stream 20) to convert the easy-to-remove sulfur compounds to hydrogen sulfide (stream 30). Suitable processes for desulfurizing hydrocarbons, particularly gasoline feedstocks, include technologies described in the following U.S. Pat Nos. 5,340,466; 5,346,609; 5,409,596; 5,411,658; 5,482,617; 5,500,108; 5,510,016; 5,510,568; 5,525,210; 5,595,634; 5,597,476; 5,770,46; 5,807,477; 5,906,730; 6,042,719; 6,103,105; 6,120,679; 6,153,089 and

6,162,352. Still other techniques will be apparent to those skilled in the art of sulfur removal. The easy-to-remove sulfur compounds include aliphatic mercaptans, naphthenic mercaptans, and aromatic mercaptans, sulfides, di-sulfides and polysulfides

[0069] The petroleum feedstock discharged from treatment zone 100, having a reduced sulfur content, but retaining most, if not all, of the refractory sulfur compounds such as thiophene, benzothiophene, dibenzothiophene and their higher boiling derivatives, in stream 40 is then preferably introduced into a concentration zone 200 for increasing the concentration of such refractory sulfur compounds. For example, in a preferred approach the refractory sulfur compounds would be concentrated from the major portion of the petroleum feedstock, possibly via complexation with ammonium complexes or by use of another known extraction or absorption technology, and distilled, or otherwise separated into a sulfur-concentrated hydrocarbon stream 60 and a sulfur-depleted petroleum feedstock 50.

[0070] The sulfur concentrated hydrocarbon stream 60 then is introduced into a reactor 600 for oxidative desulfurization. Air or an oxygen-enriched gas generally is added to the reactor via stream 70 to establish oxidizing conditions in reactor 600. Reactor 600 contains a supported metal oxide catalyst, or a bulk metal oxide catalyst, in a form suitable for conducting the oxidation reactions. The selective oxidation that occurs in reactor 600 produces a gas stream containing the oxygenated products, sulfur dioxide, H_2O , CO_x and unreacted hydrocarbons and sulfur compounds, which exits reactor 600 in gas stream 80. The oxygenated products may include maleic anhydride, phenol, benzyl aldehyde, benzoic acid and the like depending upon the nature of the sulfur compounds in gas stream 60 and sulfur-deficient hydrocarbons may also be produced.

[0071] As noted, the oxidizing agent used in the selective oxidation can usually be oxygen or air. The contacting of the sulfur-containing hydrocarbon gas stream with the supported metal oxide catalyst or bulk metal oxide catalyst under an oxidizing atmosphere, e.g., in the presence of oxygen, and at an appropriate temperature, causes a selective oxidation of the sulfur compounds to the valuable oxygenated products.

[0072] The optimum reaction time in reaction zone 600 (space velocity) varies with temperature, pressure and the molar ratio of the reactants. The space velocity likely will be maintained below about 4800 V/V/hr. As a general rule, higher conversions are associated with lower space velocities, e.g., a space velocity of 5 to 200 volume of gas (STP) per volume of catalyst per hour. In the broad practice of the invention, space velocities of up to 2000 volumes of gas (STP) per volume of catalyst per hour are generally contemplated.

[0073] A variety of oxygenated species, such as maleic anhydride, phenol, benzyl aldehyde and benzoic acid, are the intended products of the present process and can be recovered from the gaseous reaction product stream 80, separate from byproduct SO_2 and the CO_x and from unreacted hydrocarbons, sulfur-deficient hydrocarbons and unconverted sulfur-containing compounds (stream 110), using any one of a number of separation options known to those skilled in the art.

[0074] As will be recognized by those skilled in the art, the gas stream 80 leaving the reactor will contain the hydrocar-

bon feedstock and may contain unreacted sulfur compounds, sulfur-deficient hydrocarbons as well as the oxygenated products, sulfur dioxide, carbon oxides and water. Principal by-products of the oxidative desulfurization that may be formed are carbon monoxide, which may be accompanied by carbon dioxide (often in a minor amount) and sulfur dioxide.

[0075] The reaction mixture leaving the reactor **600** in gas stream **80** is generally subject to further processing in zone **500** in a conventional manner. For example, a concentrated stream of the oxygenated products **90** can be recovered in a washer, or by indirect cooling, or also by fractional cooling. For example, the washing can be performed with an aqueous stream, in which case a multi-stage washer can be used. An aqueous stream **90** containing the oxygenated products can be obtained in this manner separate from the sulfur dioxide and carbon oxides in stream **112**. An advantage of the vapor-phase route is the ease with which SO₂ and CO_x can be separated from the reaction products because of their very high vapor pressure and any residual SO₂ can be readily removed with an ion exchange column. With judicious selection of metal oxide catalyst, the sulfur-containing compounds that are typically present in petroleum feed stocks are expected to be selectively oxidized to valuable chemical intermediates and sulfur-deficient hydrocarbons.

[0076] The sulfur dioxide can be disposed of by any technique known in the art. For example, the sulfur oxide (from stream **112**) can be oxidized and converted to sulfuric acid. The sulfuric acid can then be used directly in the petroleum refinery for purposes well known to those skilled in the art. The crude stream of the oxygenated products then can be treated, such as by distillation, for recovering a purified stream of, for example, maleic anhydride. Fractional condensation also can be used to obtain a desired oxygenated product. Other ways for isolating the oxygenated products will be apparent to those skilled in this art. The residual gas **112**, likely containing carbon monoxide as well may be treated (so as to recover sulfur oxides). The remaining fraction in stream **110** containing the hydrocarbon fraction and any unreacted sulfur compounds and sulfur-deficient hydrocarbons can be recycled to the oxidative desulfurization reactor **600** (not shown) following any heating that may be needed to convert the stream into a gas, or may be sufficient low in sulfur impurities to be returned to the refinery as for blending with other feedstocks for making gasoline.

[0077] For obtaining higher yields and selectivities, the conditions of the oxidative desulfurization can be varied. For example, the pressure, temperature, composition of the starting gas mixture, the amount of catalyst and/or the rate of flow can be varied. The reactor effluent remaining after separation of the oxygenated products and by-products can then be recycled (not shown) into the reactor **600**.

[0078] In accordance with this invention, the refractory sulfur compounds are separated and then isolated from a petroleum feedstock by distillation, solvent extraction and/or adsorption-desorption and then they are oxidized by gas phase oxidation over a supported metal oxide catalyst. In a particularly preferred embodiment of the present invention, shown schematically in FIG. 3, a sulfur-containing hydrocarbon gas stream **10** containing organo-sulfur compounds is first treated using an alternative sulfur removal system,

such as conventional HDS, in treatment zone **100**. As recognized by those skilled in the art, when using HDS the, sulfur-containing petroleum feedstock is treated with a stream of hydrogen (stream **20**) to convert the easy-to-remove sulfur compounds to hydrogen sulfide (stream **30**). Suitable processes for desulfurizing hydrocarbons, particularly gasoline feedstocks, include technologies described in the following U.S. Pat. Nos. 5,340,466; 5,346,609; 5,409,596; 5,411,658; 5,482,617; 5,500,108; 5,510,016; 5,510,568; 5,525,210; 5,595,634; 5,597,476; 5,770,46; 5,807,477; 5,906,730; 6,042,719; 6,103,105; 6,120,679; 6,153,089 and 6,162,352. Still other techniques will be apparent to those skilled in the art of sulfur removal. The easy-to-remove sulfur compounds include aliphatic mercaptans, naphthenic mercaptans, and aromatic mercaptans, sulfides, di-sulfides and polysulfides. Alternatively, the easy-to-remove sulfur compounds may also be desulfurized by oxidative desulfurization.

[0079] The petroleum feedstock discharged from treatment zone **100**, having a reduced sulfur content, but retaining most, if not all, of the refractory sulfur compounds such as thiophene, benzothiophene, dibenzothiophene and any higher boiling derivatives, in stream **40** is then preferably introduced into a concentration zone **200** for isolating the sulfur compounds from the hydrocarbon stream. For a petroleum feedstock that is already substantially free of the easy-to-remove organo-sulfur compounds, i.e., contains only refractory sulfur compounds, the stream can by-pass treatment zone **100** and be introduced directly into concentration zone **200**.

[0080] For example, in a preferred approach for concentration zone **200** the refractory sulfur compounds could be isolated from the major portion of the petroleum feedstock, possibly via reversible complexation with ammonium complexes or by use of another known extraction or absorption technology, such as the extraction technique described in U.S. Pat. No. 5,753,103 (the full disclosure of which is incorporated herein by reference), the ionic liquid extraction technique described by Bösmann et al., in *Chem. Commun.*, 2001, 2492-2495 (the full disclosure of which is incorporated herein by reference), or by a reversible olefin complexation, such as by modifying the OATS process (for Olefinic Alkylation of Thiophenic Sulphur) developed and commercialized by BP.

[0081] The OATS process facilitates the separation of the thiophenes (and other refractory sulfur compounds) by catalytically causing them to react with olefins present in a hydrocarbon stream to produce heavier compounds with boiling points above 200° C. In such modification, the sulfur-olefin complex would be broken, likely by heating the complex to isolate the organo-sulfur compounds.

[0082] In any event, following such processing in concentration zone **200**, a stream containing principally the refractory sulfur compounds such as thiophene, benzothiophene, dibenzothiophene and their higher boiling derivatives, is produced within concentration zone **200** and exits that zone in stream **60**.

[0083] In an alternate approach, the organo-sulfur compounds, principally including refractory sulfur compounds such as thiophene, benzothiophene, dibenzothiophene and their higher boiling derivatives, may first be treated using a mild selective oxidation, such as a liquid phase oxidation, to

convert such organo-sulfur compounds to their sulfinyl (=SO) (sulfone) or sulfonyl (=SO_2) (sulfoxide) derivatives. Such mild oxidation processes are well known in the art. These sulfinyl (=SO) (sulfone) or sulfonyl (=SO_2) (sulfoxide) derivatives then could be isolated, such as by extraction using dimethyl sulfoxide, or by distillation or adsorption, and then would be subjected to further processing in accordance with the present invention.

[0084] Aside from the sulfur-containing feed stream **40** and the concentrated sulfur product stream **60**, other feed streams and by-product streams entering and exiting concentration zone **200** are not shown.

[0085] In yet another alternative arrangement, the OATS process could be used to treat the original hydrocarbon stream **10** and then the lower boiling sulfur fraction recovered from that processing operation (e.g., mercaptans, sulfides and the like) could be removed by fractionation and added to other refinery streams, slated to be treated only by conventional hydrotreatment. The remaining fraction would lead to stream **60** containing principally the refractory sulfur compounds such as thiophene, benzothiophene, dibenzothiophene, their higher boiling derivatives, or the sulfinyl (=SO) (sulfone) or sulfonyl (=SO_2) (sulfoxide) derivatives thereof.

[0086] The refractory sulfur compounds, or the sulfinyl (=SO) (sulfone) or sulfonyl (=SO_2) (sulfoxide) derivatives thereof, in stream **60** are then introduced into a distillation zone **500** within which the various fractions of the stream are separated using standard rectification techniques. For illustrative purposes only, stream **60** is shown being separated into three fractions **65a**, **65b** and **65c**, respectively containing primarily thiophene, benzothiophene and higher boiling compounds and derivatives, or their corresponding sulfinyl (=SO) (sulfone) or sulfonyl (=SO_2) (sulfoxide) derivatives. Each purified stream then is introduced respectively into a reactor **600a** through **600c** for oxidative desulfurization in accordance with the present invention. Air or an oxygen-enriched gas generally is added to each of the reactors via streams **70a** through **70c** respectively to establish oxidizing conditions in each respective reactor **600a** through **600c**. Each reactor preferably contains a supported metal oxide catalyst (monolayer catalyst), or alternatively a bulk metal oxide catalyst, in a form suitable for conducting the oxidation reactions. Each reactor can be similar to those described above.

[0087] The selective oxidation that occurs in each reactor produces a gas stream containing the oxygenated product generated by oxidation of each of the respective sulfur compounds, sulfur dioxide, H_2O , and CO_x , which exits each reactor **600a** through **600c** in gas streams **80a**, **80b** and **80c** respectively. The oxygenated products may include maleic anhydride in stream **80a**, phenol in stream **80b**, benzyl aldehyde and benzoic acid in stream **80c** and the like, depending upon the nature of the sulfur compounds in each of the gas streams **60a** through **60c**.

[0088] As noted, the oxidizing agent used in the selective oxidation can usually be oxygen or air. The contacting of the organo-sulfur compounds, in the gaseous phase, with the supported metal oxide catalyst or bulk metal oxide catalyst under an oxidizing atmosphere, e.g., in the presence of oxygen, and at an appropriate temperature, causes a selective oxidation of the sulfur compounds to the valuable oxygenated products.

[0089] Each oxidized product stream **80a** through **80c** then is treated in a separation zone **700a** through **700c** to remove sulfur dioxide and other light boiling fractions from the desired oxygenated products in stream **90a** through **90c** respectively.

[0090] The only significant emission from the process of the present invention would be undesirable greenhouse gas CO_2 due to minor unselective oxidation reaction pathways, as the sulfur dioxide can be recovered and used in the refinery as described above. Furthermore, the oxidative desulfurization of the present invention removes the need for additional hydrogen production from the costly and energy intensive methane reforming reaction, which would be required to support the planned expansion of the current hydrodesulfurization (HDS) technology to obtain the higher level of sulfur removal required by the more stringent regulatory limits.

[0091] The vapor-phase organo-sulfur oxidation route of the present invention is generally preferred relative to the known liquid oxidation approaches given the potential for large-scale production of the previously described oxygenated compounds, which are useful chemical intermediates. In addition, vapor-phase routes also avoid problems with solvents and catalyst recovery usually encountered with liquid-phase oxidation processes and the mild temperatures employed in liquid-phase oxidation, which tend to yield only sulfoxides and sulfones.

[0092] The advantages offered by this oxidative desulfurization process are: (1) the use of free O_2 , rather than expensive H_2 to drive the desulfurization, (2) the elimination of, or diminution of the need for costly reactor units for methane steam reforming and water-gas shift for added hydrogen generation and for additional Claus reactions, (3) the production of significantly lower amounts of global warming CO_2 due to the minor unselective oxidation reaction pathways, (4) the direct production of H_2SO_4 that can be used in the alkylation processes in the petroleum refinery and (5) the production of a supply of relatively inexpensive sulfur-containing feedstocks for the production of valuable chemical intermediates as well as sulfur-deficient olefinic and aromatic hydrocarbons. Thus, the oxidative desulfurization process of the invention is able to remove sulfur from fuels in a way that approaches the ultimate pollution control strategy: an environmentally benign process with zero emissions.

EXAMPLES

[0093] To facilitate a more complete understanding of the invention, a number of examples showing catalyst preparation are provided below. The scope of the invention, however, is not limited to specific embodiments disclosed in these examples, which are for purposes of illustration only.

[0094] Catalyst Preparation and Characterization—Supported metal oxide catalysts can be prepared as follows:

Preparation Example 1

Vanadia on Titania

[0095] A vanadia on titania metal oxide supported catalyst can be prepared in accordance with the following procedure. A vanadia-titania catalyst can be prepared by using TiO_2

(Degussa P25) as the support. The TiO_2 support (~10% rutile and ~90% anatase) possesses a surface area of $\sim 55 \text{ m}^2/\text{g}$. It is calcined in air at 500° C . and cooled to room temperature before impregnation with the vanadium oxide precursor. The vanadium oxide overlayer on the TiO_2 support is prepared from vanadium triisopropoxide oxide (Alfa, 95-98% purity) by the incipient wetness impregnation method. The preparation is performed under a nitrogen environment and in nonaqueous solutions, since the alkoxide precursor is air and moisture sensitive. Solutions of known amounts of vanadium triisopropoxide oxide and propanol-2, corresponding to the incipient wetness impregnation volume and the final amount of vanadium required, are prepared in a glove box filled with nitrogen. The solutions of the vanadium precursor and propanol-2 are then thoroughly mixed with the titania support and dried at room temperature in the glove box for 24 hr. The impregnated samples are heated to 300° C . in flowing nitrogen and the final calcination is performed in O_2 (Linde, 99.9% pure) at 500° C . for 15 hours. The catalyst is then pelletized, crushed and sieved to obtain catalyst particles sizes between 100 to $200 \mu\text{m}$.

Preparation Example 1A

Vanadia on Titania

[0096] Another vanadia on titania metal oxide supported catalyst can be prepared using the general procedure of Preparation Example 1 except that the final calcination is conducted at 450° C . for 2 hours.

Preparation Example 2

Molybdenum Oxide on Titania

[0097] An aqueous solution of ammonium heptamolybdate ($(\text{NH}_4)_6\text{Mo}_7\text{O}_{24} \cdot 4\text{H}_2\text{O}$) (Alfa) is deposited onto TiO_2 (Degussa P25) as the support (~10% rutile and ~90% anatase) by the incipient wetness technique. As in Example 1, the support is calcined in air at 500° C . and cooled to room temperature before impregnation with the molybdenum oxide precursor. The support possesses a surface area of $\sim 55 \text{ m}^2/\text{g}$. After impregnation, the wet samples are dried at room temperature for 16 hours, further dried at $110\text{-}120^\circ \text{ C}$. for 16 hours and calcined at 450° C . for 12 hours. The catalyst is then pelletized, crushed and sieved to obtain catalyst particles sizes between 100 to $200 \mu\text{m}$.

Preparation Example 3

Chromia on Titania

[0098] An aqueous solution of chromium nitrate ($\text{Cr}(\text{NO}_3)_3 \cdot 9\text{H}_2\text{O}$) (Allied Chemical Co.) is deposited onto TiO_2 (Degussa P25) as the support using the incipient wetness technique. As in the previous Examples, the TiO_2 support (~10% rutile and ~90% anatase) is calcined in air at 500° C . and cooled to room temperature before impregnation with the chromium precursor. The support possesses a surface area of $\sim 55 \text{ m}^2/\text{g}$. After impregnation, the wet samples are dried at room temperature for 16 hours, further dried at $110\text{-}120^\circ \text{ C}$. for 16 hours and calcined at 450° C . for 13 hours. The catalyst is then pelletized, crushed and sieved to obtain catalyst particles sizes between 100 to $200 \mu\text{m}$.

Preparation Example 4

Rhenium Oxide on Titania

[0099] An aqueous solution of perrhenic acid (HReO_4) (Aldrich) is deposited onto TiO_2 (Degussa P25) as the

support using the incipient wetness technique. As before, the TiO_2 support (~10% rutile and ~90% anatase) is calcined in air at 500° C . and cooled to room temperature before impregnation with the rhenium oxide precursor. The support possesses a surface area of $\sim 55 \text{ m}^2/\text{g}$. After impregnation, the wet samples are dried at room temperature for 16 hours, further dried at $110\text{-}120^\circ \text{ C}$. for 16 hours and calcined at 450° C . for 13 hours. The catalyst is then pelletized, crushed and sieved to obtain catalyst particles sizes between 100 to $200 \mu\text{m}$.

Preparation Example 5

Vanadia on Zirconia

[0100] A vanadium oxide overlayer is deposited onto a zirconium oxide (ZrO_2) support (Degussa) having a surface area $\sim 39 \text{ m}^2/\text{g}$ using an organic solution of vanadium triisopropoxide oxide (Alfa, 95-98% purity). In particular, the vanadium overlayer is prepared by the incipient wetness impregnation method using a solution of vanadium triisopropoxide oxide and propanol-2 in a glove box filled with nitrogen. The solutions of the vanadium precursor and propanol-2 are thoroughly mixed with the zirconia support and dried at room temperature for 16 hours, further dried at $110\text{-}120^\circ \text{ C}$. for 16 hours and calcined at 450° C . for 16 hours. The catalyst is then pelletized, crushed and sieved to obtain catalyst particles sizes between 100 to $200 \mu\text{m}$.

Preparation Example 6

Vanadia on Niobia

[0101] A vanadium oxide overlayer is deposited on a niobia (Nb_2O_5) support ($55 \text{ m}^2/\text{g}$) using vanadium triisopropoxide oxide (Alfa, 95-98% purity) and the incipient wetness technique. The niobia support is prepared by calcining niobic acid (Niobia Products Co.) at 500° C . for two hours. A solution of vanadium triisopropoxide oxide and propanol-2 is thoroughly mixed with the niobia support in a glove box filled with nitrogen, dried at room temperature for 16 hours, further dried at $110\text{-}120^\circ \text{ C}$. for 16 hours and calcined at 450° C . for 16 hours. The catalyst is then pelletized, crushed and sieved to obtain catalyst particles sizes between 100 to $200 \mu\text{m}$.

Preparation Example 7

Vanadia on Alumina

[0102] A vanadium oxide overlayer is deposited on an alumina (Al_2O_3) support (Harshaw, $180 \text{ m}^2/\text{g}$) using an organic solution of vanadium triisopropoxide oxide (Alfa, 95-98% purity) and the incipient wetness impregnation. A solution of the vanadium precursor and propanol-2 is thoroughly mixed with the alumina support, in a glove box filled with nitrogen, dried at room temperature for 16 hours, further dried at $110\text{-}120^\circ \text{ C}$. for 16 hours and calcined at 500° C . for 16 hours. The catalyst is then pelletized, crushed and sieved to obtain catalyst particles sizes between 100 to $200 \mu\text{m}$.

Preparation Example 8

Vanadia on Silica

[0103] A vanadium oxide overlayer is deposited on a silica (SiO_2) support (Cab-O-Sil, $300 \text{ m}^2/\text{g}$) using an organic

solution of vanadium triisopropoxide oxide (Alfa, 95-98% purity) and the incipient wetness impregnation. A solution of the vanadium precursor and propanol-2 is thoroughly mixed in a glove box filled with nitrogen with the SiO_2 support, the wet silica was dried at room temperature for 16 hours, further dried at 110-120° C. for 16 hours and calcined at 500° C. for 16 hours. The catalyst is then pelletized, crushed and sieved to obtain catalyst particles sizes between 100 to 200 μm .

Preparation Example 9

Tungsten Oxide on Silica

[0104] An aqueous solution of ammonium metatungstate ($(\text{NH}_4)_6\text{H}_2\text{W}_{12}\text{O}_{40} \cdot x\text{H}_2\text{O}$) (Pfaltz & Bauer, 99.9% purity) is deposited as an oxide overlayer onto a silica (SiO_2) support (Cab-O-Sil, 300 m^2g^{-1}) using the incipient wetness technique. After impregnation, the silica support is dried at room temperature for 16 hours, further dried at 110-120° C. for 16 hours and calcined at 500° C. for 16 hours. The catalyst is then pelletized, crushed and sieved to obtain catalyst particles sizes between 100 to 200 μm .

Preparation Example 10

Niobia on Silica

[0105] An aqueous solution of niobium oxalate (Niobium Products Co.) is deposited onto a silica (SiO_2) support (Cab-O-Sil, 300 m^2g^{-1}) using the incipient wetness technique. After impregnation, the silica support is dried at room temperature for 16 hours, further dried at 110-120° C. for 16 hours and calcined at 500° C. for 16 hours. The catalyst is then pelletized, crushed and sieved to obtain catalyst particles sizes between 100 to 200 μm .

Preparation Example 11

Titania on Silica

[0106] Titanium isopropoxide (Aldrich) in a toluene solution is impregnated onto a silica (SiO_2) support (Cab-O-Sil, 300 m^2g^{-1}) under a nitrogen blanket to form a titania overlayer using the incipient wetness technique. After impregnation, the wet silica is dried at room temperature for 16 hours, further dried at 110-120° C. for 16 hours and calcined at 500° C. for 16 hours. The catalyst is then pelletized, crushed and sieved to obtain catalyst particles sizes between 100 to 200 μm .

Preparation Example 12

Vanadia and Tungsten Oxide on Titania

[0107] A vanadia and tungsten oxide on titania catalyst is prepared by a two step incipient wetness impregnation method. A vanadium oxide overlayer is deposited first on the TiO_2 support using a solution of vanadium triisopropoxide oxide (Alfa, 95-98% purity) and propanol-2 by the incipient wetness impregnation method in a glove box filled with nitrogen. The solution of the vanadium precursor and propanol-2 are thoroughly mixed with the TiO_2 (Degussa P25) as the support. The TiO_2 support (~10% rutile and ~90% anatase) is prepared by previous calcination in air at 500° C. and cooled to room temperature before impregnation with the vanadium oxide precursor. The support possesses a

surface area of ~55 m^2/g . After impregnation, the wet TiO_2 is dried at room temperature for 16 hours, further dried at 110-120° C. for 16 hours and calcined at 450° C. for 12 hours. Subsequently, an aqueous solution of ammonium metatungstate ($(\text{NH}_4)_6\text{H}_2\text{W}_{12}\text{O}_{40} \cdot x\text{H}_2\text{O}$) is deposited as an oxide overlayer onto the TiO_2 support, again using the incipient wetness technique. After impregnation, the wet samples are dried at room temperature for 16 hours, further dried at 110-120° C. for 16 hours and calcined at 500° C. for 16 hours. The catalyst is then pelletized, crushed and sieved to obtain catalyst particles sizes between 100 to 200 μm .

Preparation Example 13

Vanadia and Titania on Silica

[0108] A vanadia and titania on silica catalyst is prepared by a two step incipient wetness impregnation method. The silica support used for this study was Cabosil EH-5 (380 m^2/g). This fluffy material is treated with water in order to condense its volume for easier handling. Then the wet SiO_2 is dried at 120° C. and subsequently calcined at 500° C. overnight. A titanium oxide overlayer is deposited first on the silica (SiO_2) support under a nitrogen blanket using titanium isopropoxide (Aldrich) in a toluene solution by the incipient wetness impregnation method in a glove box filled with nitrogen. After impregnation, the loaded sample is dried at room temperature for 16 hours, further dried at 110-120° C. for 16 hours and calcined at 500° C. for 4 hours. Subsequently, a solution of vanadium triisopropoxide oxide (Alfa, 95-98% purity) and propanol-2 is impregnated onto the silica (SiO_2) support containing titania again using the incipient wetness technique. The solution of the vanadium precursor and propanol-2 is thoroughly mixed with the SiO_2 support containing titania. After impregnation, the wet SiO_2 is dried at room temperature for 16 hours, further dried at 110-120° C. for 16 hours and calcined at 450° C. for 2 hours. The catalyst is then pelletized, crushed and sieved to obtain catalyst particles sizes between 100 to 200 μm .

Example 1

[0109] Temperature Programmed Surface Reaction Mass Spectrometry (TPSR-MS) was carried out with an AMI-100 system (Zeton Altamira Instruments) equipped with an online mass spectrometer (Dycor DyMaxion, Ametek Process Instruments). The catalyst sample (200 mg of a 5% $\text{V}_2\text{O}_5/\text{TiO}_2$) was loaded in an U-type quartz tube and pre-treated at 450° C. in flowing dry air for 1 h to remove moisture and ensure the catalyst was fully oxidized, and then cooled down to the adsorption temperature in He (Air gas, ultrahigh purity) flow. The temperature was probed using a thermocouple placed ~5 mm above the top portion of the catalyst bed. The adsorption was performed at 50° C. for thiophene by flowing a certified mixture of 1000 ppm Thiophene/He (Scott Specialty Gases) for 30 minutes at a flow rate of 30 mL/min. After the reactor was purged of any excess adsorbents with He for 30 minutes the catalyst was then ramped from the adsorption temperature to 500° C. at a constant heating rate of 10° C./min in He or 5% O_2/He (Scott Specialty Gases) with a flow rate of 30 mL/min. The desorbed gases were analyzed by a quadrupole mass spectrometer linked via a capillary tube from the exiting gas stream of the reactor at m/e=26 (Maleic Anhydride) and m/e=64 (SO_2), respectively. Pure gases of He and Ar were used to verify the calibration of the mass spectrometer prior to any analysis.

[0110] The results are shown in **FIG. 4**. The separate figures show the desorption of maleic anhydride and SO₂ after adsorption of thiophene on a 5% V₂O₅/TiO₂ catalyst at 100 C. The sample is heated at a rate of 10 C/minute in flowing oxygen/He and the reaction products are monitored by a mass spectrometer. This transient experiment proves that maleic anhydride can be formed from thiophene oxidesulfurization on supported vanadia on titania catalyst. The first plot (for maleic anhydride) shows the formation of maleic anhydride from thiophene under the stated conditions. The second plot (for SO₂) shows that the sulfur contained in the thiophene ring has been removed as SO₂ during the formation of maleic anhydride mentioned earlier.

[0111] Another product from the oxidation was n-butane, a sulfur-deficient hydrocarbon, as is shown in **FIG. 5**.

[0112] It will be understood that while the invention has been described in conjunction with specific embodiments thereof, the foregoing description and examples are intended to illustrate, but not limit the scope of the invention. Other aspects, advantages and modifications will be apparent to those skilled in the art to which the invention pertains, and these aspects and modifications are within the scope of the invention, which is limited only by the appended claims.

I claim:

1. A process for desulfurizing a hydrocarbon stream containing heterocyclic sulfur compounds, which process comprises contacting said heterocyclic sulfur compounds, or sulfinyl (=SO) or sulfonyl (=SO₂) derivatives thereof, in the gas phase and in the presence of oxygen with a supported metal oxide catalyst, or with a bulk metal oxide catalyst.

2. The process of claim 1 wherein the contacting converts at least a portion of the heterocyclic sulfur compounds, or the sulfinyl (=SO) or sulfonyl (=SO₂) derivatives thereof, to oxygenated products.

3. The process of claim 1 wherein the contacting converts at least a portion of the heterocyclic sulfur compounds, or the sulfinyl (=SO) or sulfonyl (=SO₂) derivatives thereof, to oxygenated products and then recovering a hydrocarbon stream with substantially reduced sulfur separately from the oxygenated products.

4. The process of claim 1 wherein the contacting converts at least a portion of the heterocyclic sulfur compounds, or the sulfinyl (=SO) or sulfonyl (=SO₂) derivatives thereof, to sulfur-deficient hydrocarbons.

5. The process of claim 1 wherein the contacting converts at least a portion of the heterocyclic sulfur compounds, or

the sulfinyl (=SO) or sulfonyl (=SO₂) derivatives thereof, to oxygenated products and sulfur-deficient hydrocarbons.

6. The process of claim 1 wherein the contacting converts at least a portion of the heterocyclic sulfur compounds, or the sulfinyl (=SO) or sulfonyl (=SO₂) derivatives thereof, to oxygenated products and sulfur-deficient hydrocarbons and then recovering a hydrocarbon stream with substantially reduced sulfur separately from the oxygenated products.

7. The process of claim 1, 2, 3, 4, 5 or 6 wherein the supported metal oxide catalyst comprises a metal oxide substrate, or support, such as titania, silica, zirconia, alumina, niobia, tantalum, ceria, magnesia, manganates, lanthanum oxide, tin oxide and mixtures thereof, whose surface has been modified with a monolayer of an oxide of a catalytic metal selected from the group consisting of titanium (Ti), zirconium (Zr), molybdenum (Mo), rhenium (Re), vanadium (V), chromium (Cr), tungsten (W), manganese (Mn), niobium (Nb), tantalum (Ta) and mixtures thereof.

8. The process of claim 7 wherein the catalytic metal is vanadium and mixtures containing vanadium.

9. The process of claim 1, 2, 3, 4, 5 or 6 wherein the bulk metal oxide catalyst comprises a compound selected from molybdates (Mo), chromates (Cr), vanadates (V), rhenates (Re), titanates (Ti), niobates (Nb), tantalates (Ta), tungstates (W), manganates (Mn) and mixtures thereof.

10. The process of claim 8 wherein the bulk metal oxide catalyst is selected from PbV₂O₆, NaVO₃, Na₃VO₄, BiVO₄, AlVO₄, FeVO₄, Mg₃(VO₄)₂, Mg₂V₂O₇, CeVO₄, Zn₃(VO₄)₂, CdV₂O₇, Zn₂V₂O₇, VOPO₄, KVO₃, Pb₂V₂O₇, TiVO₄, PbMoO₄, CaMoO₄, Bi₂Mo₂O₉, Bi₃(FeO₄)(MoO₄)₃, Na₂MoO₄, MnMoO₄, Gd₂(MoO₄)₃, MgMoO₄, CuMoO₄, CoMoO₄, Fe₂(MoO₄)₃, Te₂MoO₇, NiMoO₄, Al₂(MoO₄)₃, Cr₂(MoO₄)₃, Na₂Mo₂O₇, YNbO₄, YbNbO₄, LiNbO₃, NaNbO₃, KNbO₃, AlNbO₄, K₈Nb₆O₁₉, BiNbO₄, SbNbO₄, NbOPO₄, CaNb₂O₆, K₄Nb₆O₁₇, KCa₂Nb₃O₁₀, Li₆WO₆, FeWO₄, CoWO₄, MnWO₄, NiWO₄, CuWO₄, CaWO₄, Cs₂WO₄, Na₂WO₄, B_aWO₄, Fe₂(WO₄)₃, Al₂(WO₄)₃, SrWO₄, K₂WO₄, Na₂W₂O₇, Li₂WO₄, CsLuW₂O₈, BiWO₄, Na₂CrO₄, Na₂Cr₂O₇, Na₂Cr₃O₁₀, Na₂Cr₄O₁₃, K₂CrO₄, K₂Cr₂O₇, K₂Cr₃O₁₀, K₂Cr₄O₁₃, Fe₂(CrO₄)₃, CaCrO₄, Cs₂CrO₄, BiCrO₄, NaReO₄, Li₆ReO₄, Mg(ReO₄)₂, Na₂TiO₄, NaTiO₃, BaTiO₄, BaTiO₃, Mn₃(VO₄)₂, MnAl₂O₄, KMnO₄, MnO, MnO₂, Mn₂O₃ and Mn₃O₄.

* * * * *